

NSEL Report Series
Report No. NSEL-023
March 2010

Nonlinear Seismic Analysis of Circular Concrete-Filled Steel Tube Members and Frames



**Mark D. Denavit
and
Jerome F. Hajjar**



Department of Civil and Environmental Engineering
University of Illinois at Urbana-Champaign

UILU-ENG-2010-1803



ISSN: 1940-9826

The Newmark Structural Engineering Laboratory (NSEL) of the Department of Civil and Environmental Engineering at the University of Illinois at Urbana-Champaign has a long history of excellence in research and education that has contributed greatly to the state-of-the-art in civil engineering. Completed in 1967 and extended in 1971, the structural testing area of the laboratory has a versatile strong-floor/wall and a three-story clear height that can be used to carry out a wide range of tests of building materials, models, and structural systems. The laboratory is named for Dr. Nathan M. Newmark, an internationally known educator and engineer, who was the Head of the Department of Civil Engineering at the University of Illinois [1956-73] and the Chair of the Digital Computing Laboratory [1947-57]. He developed simple, yet powerful and widely used, methods for analyzing complex structures and assemblages subjected to a variety of static, dynamic, blast, and earthquake loadings. Dr. Newmark received numerous honors and awards for his achievements, including the prestigious National Medal of Science awarded in 1968 by President Lyndon B. Johnson. He was also one of the founding members of the National Academy of Engineering.

Contact:

Prof. B.F. Spencer, Jr.
Director, Newmark Structural Engineering Laboratory
2213 NCEL, MC-250
205 North Mathews Ave.
Urbana, IL 61801
Telephone (217) 333-8630
E-mail: bfs@illinois.edu

The authors would like to thank the following individuals for their contributions to this work. Cenk Tort from Skidmore, Owings & Merrill assisted in model development. Professor Roberto T. Leon and Tiziano Perea from the Georgia Institute of Technology have provided advice and data for the experiments presented in Section 5.8. Ana Lucuta from the University of Illinois at Urbana-Champaign has assisted in the preparation of figures. The support and advice of Tom Schlaflly from the American Institute of Steel Construction is appreciated. This material is based upon work supported by the National Science Foundation under Grant No. CMMI-0619047, the American Institute of Steel Construction, and the University of Illinois at Urbana-Champaign. Any opinions, findings, and conclusions or recommendations expressed in this material are those of the author and do not necessarily reflect the views of the National Science Foundation or other sponsors.

The cover photographs are used with permission. The Trans-Alaska Pipeline photograph was provided by Terra Galleria Photography (<http://www.terragalleria.com/>).

ABSTRACT

Accurate nonlinear formulations are necessary for the assessment of structures under seismic and other extreme loading. In this work, a three-dimensional distributed plasticity beam element formulation for circular concrete-filled steel tubes has been developed for nonlinear static and dynamic analyses of composite seismic force resisting systems. A mixed basis for the formulation was chosen to allow for accurate modeling of both material and geometric nonlinearities. The formulation utilizes uniaxial cyclic constitutive models for the concrete core and steel tube that account for the salient features of each material, as well as the interaction between the two, including concrete confinement and local buckling of the steel tube. The accuracy of the formulation was verified against a wide variety of analytical and experimental results. The verification confirms the capability of the formulation to accurately produce realistic simulations of element and frame behavior.

CONTENTS

Chapter 1: Introduction.....	1
1.1 Motivation.....	1
1.1 Finite Element Formulations.....	2
1.2 Uniaxial Constitutive Models for CCFT Members.....	4
1.3 Outline and Scope of Report.....	7
Chapter 2: Three-Dimensional Mixed Beam Finite Element.....	9
2.1 Introduction.....	9
2.2 Finite Element Formulation.....	10
Chapter 3: Uniaxial Cyclic Concrete Constitutive Model for CCFT Members.....	27
3.1 Introduction.....	27
3.2 Monotonic Compressive Response.....	27
3.3 Monotonic Tensile Response.....	44
3.4 Cyclic Response.....	45
Chapter 4: Uniaxial Cyclic Steel Constitutive Model for CCFT Members.....	55
4.1 Introduction.....	55
4.2 Plasticity Model.....	55
4.3 Local Buckling of the Steel Tube.....	63
Chapter 5: Verification of the Finite Element Formulation.....	73
5.1 Introduction.....	73
5.2 Elastic Geometrically Nonlinear Problems.....	73
5.3 Monotonic Stub Column Experiments.....	79
5.4 Monotonic Bending Experiments.....	87
5.5 Monotonic Proportionally Loaded Beam-Column Experiments.....	95
5.6 Monotonic Non-Proportionally Loaded Beam-Column Experiments.....	103
5.7 Cyclic Pure Bending Experiments.....	111
5.8 Cyclic Slender Beam-Column Experiments.....	119
5.9 Comparison to Existing Models.....	133
Chapter 6: Conclusions.....	138
References.....	139

INTRODUCTION

1.1 Motivation

In steel and concrete composite construction, the two materials are integrated in structural members to combine the advantages of both materials. Composite beam-columns come in several forms (Figure 1-1). The most common are either steel-encased concrete (SRC) where a steel shape is encased within a concrete column or concrete-filled steel tubes (CFT) where an outer tube is filled with concrete. Concrete-filled tubes are generally designated by the shape of steel tube, i.e., rectangular and square (RCFT) or circular (CCFT).

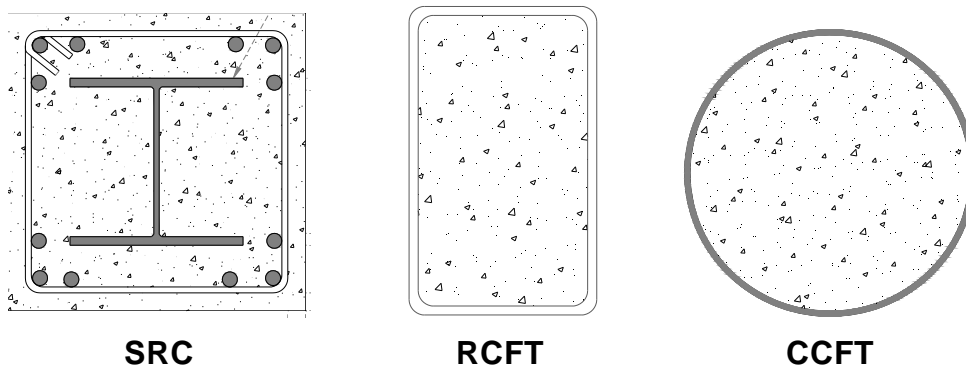


Figure 1-1. Typical Steel and Concrete Composite Sections

Steel has high strength and ductility; it also facilitates connections with steel girders and braces in a steel framing system. Concrete is economical, durable, and fire resistant. For CCFT columns in particular, the steel tube confines the concrete core leading to an increase in both strength and ductility of the concrete. The concrete core, in turn, restricts inward local buckling of the steel tube. Applications of CCFTs within the United States include columns in braced frames of high-rise buildings. CCFT columns with diameters ranging up to one to three meters and with a D/t ratio of approximately 100 are often used (Roeder et al., 1999).

Composite columns have been shown to have high strength, stiffness, and ductility. However, little data is available to justify the structural system response factors (e.g., R , C_d , and Ω_o) given in the specifications for seismic design of structures utilizing composite lateral force resisting frames. Accurate nonlinear static and dynamic computational formulations are required for developing rational system response factors. The models should directly simulate all predominate inelastic effects from the onset of yielding through strength and stiffness degradation causing collapse, while being sufficiently robust to track inelastic force redistribution without convergence problems up to the point of collapse (FEMA 2008). Such a model would also aid in investigations of

beam-column strength and establishing guidelines for the computation of equivalent composite beam-column rigidity to be used in seismic analysis and design of composite frames. To these ends, an advanced distributed plasticity mixed beam finite element formulation has been developed for investigation of composite beam-column and frame behavior. This work presents the development of a new finite element and material models for the steel and concrete geared especially for circular concrete-filled steel tube beam-columns. Validation is provided versus more than one hundred experiments from the literature for a range of geometries and includes both normal and high strength materials.

1.1 Finite Element Formulations

Structural analyses using nonlinear finite element formulations are performed to quantify demand, optimize design, among other purposes. There are a number of different types of finite element formulations that could be applied to frame structures using CCFT members. Beam elements reduce the three-dimensional behavior to one-dimension, utilizing a kinematic assumption (e.g., initially plane sections remain plane) to describe the deformations of any point within the member by the deformations of cross sections along the length of the member. Three-dimensional continuum analysis allows for detailed simulation of CCFT members. In this type of analysis, the concrete core is commonly modeled with brick elements, while the steel tube is modeled with shell elements (Schneider 1998; Johansson and Gylltoft 2002; Varma et al. 2002; Hu et al. 2003). The interface between the two materials may be modeled with gap and friction elements. Phenomena that are simplified for analysis using beam elements may be modeled explicitly. For example, confinement of the concrete core can be modeled through the use of three-dimensional constitutive relations and local buckling of the steel tube can be modeled through geometrical nonlinear behavior. Despite the improved accuracy and rationality, the computational expense prevents continuum analysis from being a viable option for analysis of complete three-dimensional frames.

Concentrated plasticity formulations model material nonlinearity only at hinges, usually of zero length, at the element ends while assuming the element remains elastic in between the hinges (Hajjar and Gourley 1997; El-Tawil and Deierlein 2001; Inai et al. 2004). Distributed plasticity formulations allow material nonlinearity throughout the element, monitoring inelasticity at specific integration points along the length of the element (Hajjar et al. 1998; Aval et al. 2002; Varma et al. 2002; Tort and Hajjar 2007). In comparison to concentrated plasticity, distributed plasticity is more accurate and more computationally expensive, since inelasticity is traced at multiple points along the length of the element rather than just the element ends. While in several cases (e.g., double curvature of a beam-column) material nonlinearity is mostly limited to the element ends, the distributed plasticity approach is appealing because of its accuracy and generality.

In both the concentrated and distributed plasticity approaches, initiation and evolution of cross sectional behavior needs to be modeled. This may be accomplished in several ways. One option models section behavior through multiple surfaces and flow rules defined in stress-resultant space (Hajjar and Gourley 1996; El-Tawil and Deierlein 2001). For

example, elastic response is maintained if the loading point remains within the loading surface. Plastic deformation commences when the loading surface is breached with the level of deformation related to the distance between the loading surface and bounding surface. A second option, subdivides the two-dimensional cross section into many fibers that are each assigned a uniaxial material model (Hajjar et al. 1998; Aval et al. 2002; Varma et al. 2002; Tort and Hajjar 2007). A kinematic assumption (e.g., initially plane sections remain plane) is used to determine the longitudinal strain at the centroid of each fiber. Based on this strain, the stress and modulus of each fiber are computed and aggregated to obtain the sectional response. The fiber approach is appealing because of the ability to account either explicitly or implicitly for all the salient features of CCFT members (e.g., concrete cracking, confinement, local buckling, etc.) through relatively simple uniaxial stress-strain models.

A further classification of beam elements relates to what variables are taken as the primary unknowns. This classification distinguishes displacement-based, force-based and mixed elements. Mixed, in this case, indicates that both element displacements and stress resultants as taken as primary state variables. However, the term could also indicate other combinations of primary state variables (Hjelmstad and Taciroglu 2003). Displacement-based, also termed stiffness-based, elements regard nodal displacements as the primary unknowns (Hajjar and Gourley 1997; Aval et al. 2002; Alemdar and White 2005). Element deformations are computed using interpolation functions. Element equilibrium is satisfied only in a variational sense, i.e., element internal forces computed from the assumed displacement field do not strictly satisfy equilibrium. This type of formulation is considered easy to implement and to extend to geometric nonlinear behavior. However, the interpolation functions typically used for the deformations only model a linear curvature distribution along the length of the element. This is a significant limitation especially in the case where plastic hinges develop, causing severely nonlinear curvature distributions. Force-based, also termed flexibility-based, elements regard element forces as the primary unknowns (de Souza 2000; El-Tawil and Deierlein 2001; Alemdar and White 2005). Stress resultants along the length of the element are computed using interpolation functions. Element equilibrium is strictly satisfied; however, the compatibility of deformations within the element is satisfied only in a variational sense. In comparison to displacement-based elements, force-based elements are often more computationally expensive and have more elaborate state determination procedures. Mixed elements regard both element forces and nodal displacements as primary unknowns, allowing interpolation functions for both element deformations and stress resultants along the length of the element (Nukala and White 2004a; Alemdar and White 2005; Tort and Hajjar 2007). Despite the complexity of the state determination procedure, which is typically greater than for displacement- or force-based elements, the mixed method provides a favorable balance of accurate assessment of nonlinear curvatures along the length of the element and capability to include geometric nonlinearity directly. In this work, a mixed distributed plasticity fiber-based beam element formulation for CCFT beam-columns is implemented within OpenSees.

OpenSees is an object-oriented software framework for the analysis of structural systems (OpenSees 2009). Software patterns, implemented within the framework, represent the

fundamental relationships necessary for nonlinear finite element analysis. The main abstractions include: *ModelBuilder*, which constructs objects and adds them to the domain; *Domain*, which is the aggregation of all nodes, elements, loads and constraints and contains the state of the structure; *Recorder*, which monitors and outputs defined parameters in the model; and *Analysis*, which moves the model from one state to another. These abstractions interact with specific elements through the common interface of the of the abstract *Element* class, in most cases eliminating the need for special nodes, constraints, solution algorithms, etc., for any particular element. The flexible, reusable, and extensible nature of the framework allows a minimum amount of new code that needs to be written for a new element or material to be implemented.

A beam implementation is simply the state determination procedure within the natural coordinate system (Scott et al. 2008). Separate objects exist to define the geometric transformations and cross section constitutive relations otherwise necessary. In typical cases the existing implementations of these objects are sufficient. Similarly, a uniaxial material implementation is simply the state determination procedure for the given a strain.

A number of elements already exist within the OpenSees framework ranging from brick and quadrilateral elements for continuum analysis, to truss and zero-length elements. Beam elements include: two- and three-dimensional elastic elements, concentrated plasticity elements, displacement-based distributed plasticity elements, and force-based distributed plasticity elements (OpenSees 2009). A wide variety of uniaxial materials used in fiber sections to define sectional response also already exist. Materials include: elastic, elastically perfectly plastic, hardening, and several models specifically for concrete and steel, among others.

The finite element formulation presented in this work is a mixed fiber-based distributed plasticity beam element. It is derived in the corotational frame (described in Section 2.2.1) and implemented within OpenSees utilizing existing software patterns to allow for general analyses of CCFT members and frames.

1.2 Uniaxial Constitutive Models for CCFT Members

Accurate constitutive models are necessary for the analysis of structural members. Analyses that use a fiber discretization to define section behavior rely on uniaxial material models that govern the behavior of the subdivisions of the cross sections. The need for uniaxial constitutive models for specifically CCFT members arises from the multi-dimensional nature of the composite interaction. Even in uniaxial loading, the concrete core is under a three-dimensional state of stress while the steel tube is under two-dimensional state of stress. While this not unique to CCFT members, the extent to which these multi-dimensional aspects effect the uniaxial (along the longitudinal axis of the member) behavior is. Several researchers have proposed different constitutive models for CCFT members (Shams and Saadeghvaziri 1999; Susantha et al. 2001; Elremaily and Azizinamini 2002; Sakino et al. 2004; Hatzigeorgiou 2008). Each of these models uses

different assumptions and methods of calibration, but they generally strive to mimic the response of concentrically loaded short CCFT columns.

For clarity and consistency in notation, a few expressions common to the constitutive relations will be presented here. It is typical to utilize the idealized stress distribution shown in the free body diagram in Figure 1-2 to derive a relation between the hoop stress in the steel tube and the confining pressure in the concrete core. Such a relation is presented in Equations 1.1 and 1.2, where f_l is the confining pressure in the concrete core, D is the outside diameter of the steel tube, t is the thickness of the steel tube, and $\alpha_\theta F_y$ is the hoop stress in the steel tube expressed as the product of the ratio of hoop stress to steel yield stress and steel yield stress.

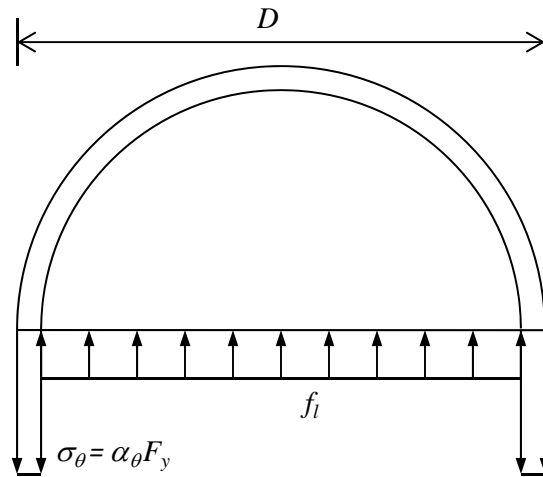


Figure 1-2. Idealized Free Body Diagram of a CCFT Section

$$\sum F = 2t\alpha_\theta F_y - (D - 2t)f_l = 0 \quad [1.1]$$

$$f_l = \alpha_\theta F_y \frac{2}{D/t - 2} \quad [1.2]$$

The von Mises yield criterion is also commonly employed. For the biaxial state of stress assumed to exist in the steel tubes of CCFT members, the yield criteria is written as in Equation 1.3, where α_θ is the ratio of hoop stress to steel yield stress and α_z is the ratio of axial stress to steel yield stress.

$$\alpha_\theta^2 - \alpha_\theta \alpha_z + \alpha_z^2 = 1 \quad [1.3]$$

For the case of a given hoop stress ratio, yield occurs at different axial stress ratios in the positive and negative direction. These can be computed as Equation 1.4 for positive stress and Equation 1.5 for negative stress.

$$\alpha_{z,\text{criticalpositive}} = 0.5 \left(\alpha_{\theta} + \sqrt{4 - 3\alpha_{\theta}^2} \right) \quad [1.4]$$

$$\alpha_{z,\text{criticalnegative}} = 0.5 \left(\alpha_{\theta} - \sqrt{4 - 3\alpha_{\theta}^2} \right) \quad [1.5]$$

The concrete core experiences a strength increase due to the confinement pressure acting on it. Numerous relations have been proposed to estimate the increase in strength. Two of the most common are those proposed by Richart et al. (1929) (Equation 1.6) and Mander et al. (1988) (Equation 1.7).

$$f'_{cc} = f'_c + 4.1f_l \quad [1.6]$$

$$f'_{cc} = f'_c \left(-1.254 + 2.254 \sqrt{1 + \frac{7.94f_l}{f'_c}} - 2 \frac{f_l}{f'_c} \right) \quad [1.7]$$

Sakino et al. (2004) presents constitutive relations for CCFT members calibrated to a series of tests of on short concentrically loaded columns. Based on a regression analysis using the experimental strength of the columns, an estimation of the steel hoop stress is made as 19% of the yield stress of the steel (i.e., $\alpha_{\theta} = 0.19$). The hoop stress is related to the confinement pressure in the concrete core using Equation 1.2, which is in turn related to the confined concrete strength using Equation 1.6. A nonlinear function is used to describe the stress-strain relation of the concrete core. An elastic-perfectly plastic model, with the positive and negative yield stresses adjusted in accordance with the von Mises yield criterion to account for the hoop stress (Equations 1.4 and 1.5), is used to describe the stress-strain relation of the steel tube.

Elremaily and Azizinamini (2002) present similar constitutive relations to Sakino (2004). Using a different set of calibration set (although there was overlap) and different model for the confined concrete strength (Equation 1.7), the hoop stress was estimated as 10% of the yield stress of the steel (i.e., $\alpha_{\theta} = 0.10$). A nonlinear function was used for the stress-strain relation of the concrete and an adjusted elastic-perfectly plastic relation was used for the steel tube.

Hatzigeorgiou (2008) similarly bases the confined concrete strength on the hoop stress in the steel tube. However, rather than a constant ratio value for all CCFT members, the ratio of hoop stress to yield stress is assumed to follow a function of the yield stress and the D/t ratio (Equation 1.8).

$$\alpha_{\theta} = \exp \left[\ln(D/t) + \ln(F_y) - 11 \right] \leq 1.0 \quad [1.8]$$

The stress-strain relationship is made up of three branches: the pre-peak branch described by a cubic function, a post-peak linear descending branch, and a constant residual strength branch. A hardening model is used for the steel tube, where again, the positive and negative yield stresses are adjusted for the presence of hoop stress.

Susantha et al. (2001) also uses the steel hoop stress as a main parameter in the computation of the confined concrete strength. The ratio of hoop stress to yield stress is posed as a difference between the Poisson's ratio the steel tube and that of the concrete core, empirical relations are given for these values which are based on the ratio of concrete strength to steel yield stress and the D/t ratio (Equations 1.9 through 1.11).

$$\alpha_\theta = (\nu_e - 0.5) \quad [1.9]$$

$$\nu_e = 0.2312 + 0.3582\nu'_e - 0.1524(f'_c / F_y) + 4.843\nu'_e(f'_c / F_y) - 9.169(f'_c / F_y)^2 \quad [1.10]$$

$$\nu'_e = 0.881 \times 10^{-6}(D/t)^3 - 2.58 \times 10^{-4}(D/t)^2 + 1.953 \times 10^{-2}(D/t) + 0.4011 \quad [1.11]$$

A three branch model is used for the stress-strain relation of the concrete core with a nonlinear pre-peak branch, linear descending branch, and constant residual branch. A model for the steel tube was not presented.

The models posed by Shams and Saadeghvaziri (1999) differ from the others in that they were calibrated to the results of finite element analyses rather than experimental tests. The confined concrete strength is determined using a function of the concrete strength and the D/t ratio. A nonlinear equation is used for the stress-strain relation of the steel tube. Two parameters were defined to adjust the compressive strength of the steel tube. The first accounts for the biaxial effect of the hoop stress and is a function of the D/t ratio. The second accounts for the length of the column and is a function of the L/D ratio.

The similarities between these models identify the main material and geometric parameters that govern the behavior of CCFT members: the concrete compressive strength, the steel yield strength, and D/t ratio. In each of the models, these three parameters primarily dictate the response of the materials. This prior work also shows that the confinement of the concrete core provided by hoop stress in the steel tube is a dominate phenomenon is the response of CCFT members. However, additional behavioral features also affect the response of CCFT members and were largely ignored in these models, including local buckling of the steel tube, hardening of the steel tube, and tensile capacity of the concrete core (Gourley et al. 2008). The constitutive relations presented in this work follow the same trends as in the prior work while modeling a more comprehensive range of behavior.

1.3 Outline and Scope of Report

Chapter 2 presents the development of a three-dimensional distributed plasticity beam element formulation for circular concrete-filled steel tubes. Chapter 3 and Chapter 4 present the development uniaxial cyclic constitutive models for the concrete core and steel tube respectively. These models account for the salient features of each material, as well as the interaction between the two, including concrete confinement and local buckling of the steel tube. Chapter 5 contains a comprehensive verification study to assess the accuracy of the formulation. Comparisons between analytical or experimental

results and computational results confirm the capability of the formulation to accurately produce realistic simulations of element and frame behavior. Conclusions are drawn and future research recommendations are made in Chapter 6.

THREE-DIMENSIONAL MIXED BEAM FINITE ELEMENT

2.1 Introduction

For steel and concrete composite members, material nonlinearity and inelasticity arises from both constituent materials. Changes in the geometry of the structure under loading induce geometric nonlinearities that also need to be modeled. The mixed formulation allows for accurate modeling of both geometric and material nonlinearities. Further, frame analyses using distributed-plasticity beam-column elements strike a favorable balance of computational efficiency and accuracy.

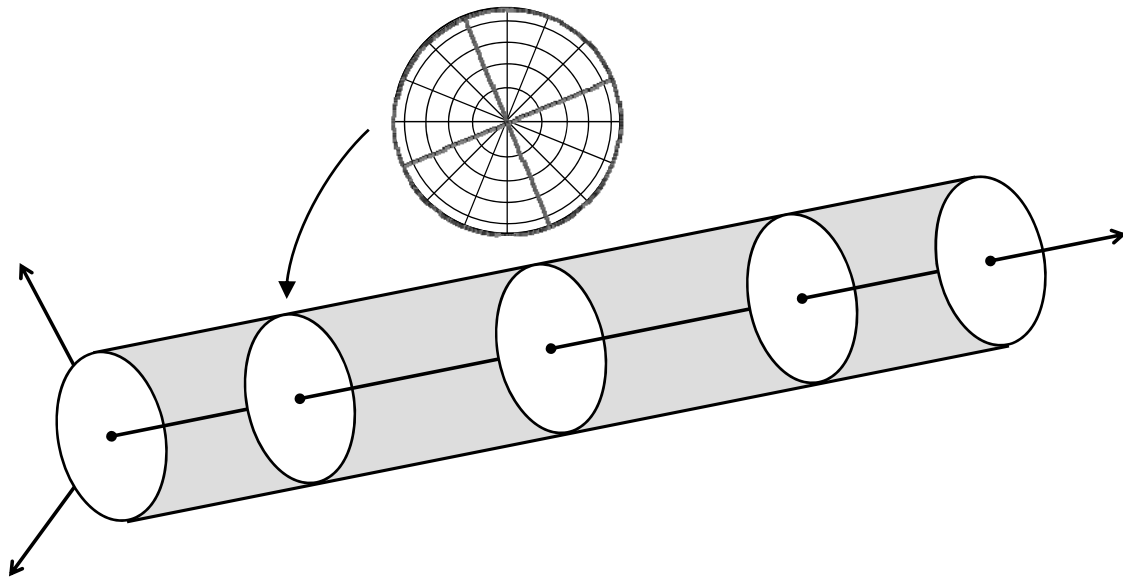


Figure 2-1. Distributed Plasticity Finite Element Formulation Showing Integration Points and Material Fibers

Distributed plasticity mixed beam finite element formulations have been developed previously (Nukala and White 2004a; Alemdar and White 2005; Tort and Hajjar 2007). The formulation by Nukala and White (2004a) was intended for the analysis of steel structures and included section warping. The formulation by Tort and Hajjar (2007) was intended for the analysis of rectangular CFT members and included slip between the steel tube and concrete core. The formulation presented here is in many ways similar to these models, particularly with respect to the general form of the governing equations. However, each of these models has slightly different state determination algorithms, a possibility arising from the multiple fields introduced in the formulation (Alemdar and White 2005). The previous formulations, nonetheless, serve as a guide to the current

formulation and provide indication of the extensibility of the formulation procedure to model other phenomena. In the following sections, a finite element formulation for analysis of CCFT members is derived.

2.2 Finite Element Formulation

2.2.1 Corotational Frame

The deformation of an element can be separated into two components, rigid body modes and deformational modes. There are several advantages to representing the element deformations in this way. First, the element displacements can be described with fewer degrees-of-freedom (DOF). This allows for a simplification in computation of the element stiffness matrix and internal forces. Second, since the deformational modes are relatively small, simplifications can be made in determining strains.

The frame in which the rigid body modes have been removed is referred to as the corotational or natural frame. For a three-dimensional beam without the effects of torsion, there exist five natural DOFs. Two rotational deformations at each end and an axial elongation at a single end (Figure 2-2) are sufficient to represent the element deformation completely. The deformations in the natural frame are expressed with respect to the initial undeformed configuration. In this sense, the model is a Total-Lagrangian formulation. This is in contrast to an Updated-Lagrangian formulation in which the deformations are expressed with respect to the last converged state.

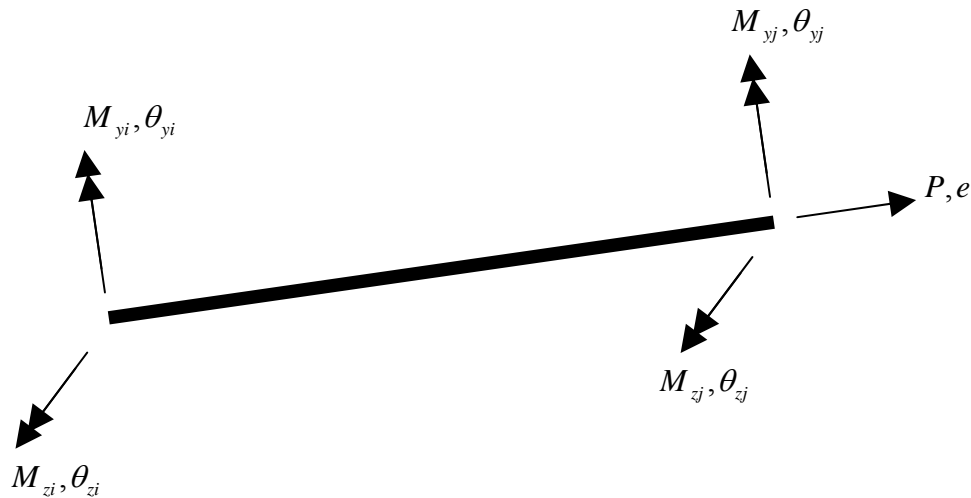


Figure 2-2. Degrees-of-Freedom and Forces in the Corotational Frame

2.2.2 Governing Differential Equation

The governing differential equation is obtained by examining equilibrium of a beam-column of infinitesimal length (Figure 2-3). A linear torsional response is assumed. For that reason, torsional moments are decoupled and excluded from the equilibrium

equations and will be incorporated into the formulation later. The beam is loaded only through end forces. The consequence of this simplification is that during analyses, loads may only be applied at nodes. Through equilibrium the following relations (Equations 2.1 through 2.4) are derived.

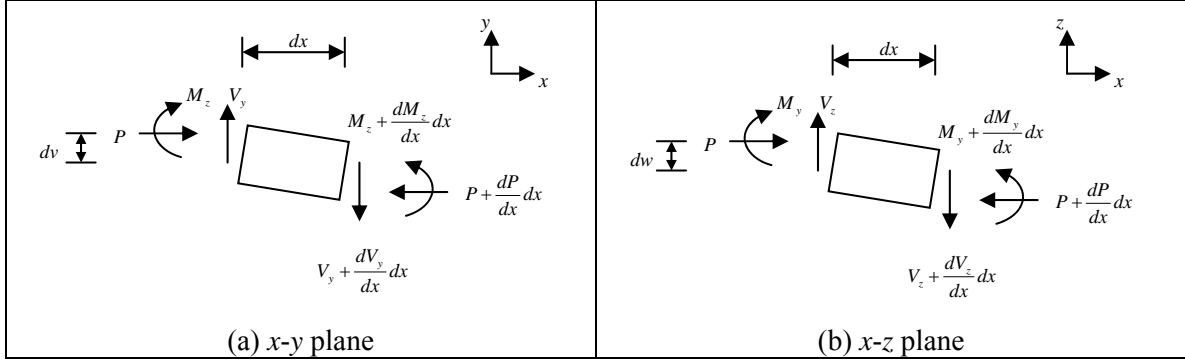


Figure 2-3. Internal Forces of an Infinitesimal Element

$$P \frac{dv}{dx} - \frac{dM_z}{dx} + V_y = 0 \quad [2.1]$$

$$P \frac{dw}{dx} - \frac{dM_y}{dx} + V_z = 0 \quad [2.2]$$

$$\frac{dV_y}{dx} = 0 \quad \frac{dV_z}{dx} = 0 \quad [2.3]$$

$$\frac{dP}{dx} = 0 \quad [2.4]$$

Differentiating Equations 2.1 and 2.2 with respect to x and noting the relations of Equations 2.3 and 2.4 results in the governing differential equations.

$$-P \frac{d^2v}{dx^2} + \frac{d^2M_z}{dx^2} = 0 \quad [2.5]$$

$$-P \frac{d^2w}{dx^2} + \frac{d^2M_y}{dx^2} = 0 \quad [2.6]$$

To obtain the weak form of the governing differential equations, Equations 2.4, 2.5, and 2.6 are multiplied by appropriate weighting functions and integrated over the length of the element (Equation 2.7). Note that in keeping with the Total-Lagrangian approach, the integral is performed over the initial length of the element.

$$\int_0^{L_0} \delta v \left(-P \frac{d^2v}{dx^2} + \frac{d^2M_z}{dx^2} \right) dx + \int_0^{L_0} \delta w \left(-P \frac{d^2w}{dx^2} + \frac{d^2M_y}{dx^2} \right) dx - \int_0^{L_0} \delta u \frac{dP}{dx} dx = 0 \quad [2.7]$$

Equation 2.8 is obtained by applying integration by parts to Equation 2.7.

$$\begin{aligned}
& \int_0^{L_0} \delta v_{,x} P v_{,x} dx - [\delta v P v_{,x}]_0^{L_0} + \int_0^{L_0} \delta v_{,xx} M_z dx + [\delta v M_{z,x}]_0^{L_0} - [\delta v_{,x} M_z]_0^{L_0} \\
& + \int_0^{L_0} \delta w_{,x} P w_{,x} dx - [\delta w P w_{,x}]_0^{L_0} + \int_0^{L_0} \delta w_{,xx} M_y dx + [\delta w M_{y,x}]_0^{L_0} - [\delta w_{,x} M_y]_0^{L_0} \quad [2.8] \\
& + \int_0^{L_0} \delta u_{,x} P dx - [\delta u P]_0^{L_0} = 0
\end{aligned}$$

where the notation “ $_{,x}$ ” and “ $_{,xx}$ ” following a variable indicates the first and second derivative of that variable with respect to x respectively. This notation will be used throughout the rest of this discussion. Collecting terms, Equation 2.8 is simplified to

$$\begin{aligned}
& \int_0^{L_0} (\delta u_{,x} + \delta v_{,x} v_{,x} + \delta w_{,x} w_{,x}) P + \delta v_{,xx} M_z + \delta w_{,xx} M_y dx \\
& - [(\delta u + \delta v v_{,x} + \delta w w_{,x}) P - \delta v M_{z,x} + \delta v_{,x} M_z - \delta w M_{y,x} + \delta w_{,x} M_y]_0^{L_0} = 0 \quad [2.9]
\end{aligned}$$

Noting that the virtual displacements (δu , δv , and δw) satisfy the essential boundary conditions, specifically that they are zero where the displacements are zero in the natural frame, Equation 2.9 can be further simplified to

$$\int_0^{L_0} [\delta u_{,x} + \delta v_{,x} v_{,x} + \delta w_{,x} w_{,x} \quad \delta v_{,xx} \quad \delta w_{,xx}] \mathbf{D} dx - \delta \mathbf{q}^T \mathbf{Q}_{\text{ext}} = 0 \quad [2.10]$$

where \mathbf{D} is vector of section forces given later in Equation 2.16b; \mathbf{q} is a vector of natural displacements given later in Equation 2.12c; and \mathbf{Q}_{ext} is a vector of applied element end forces given by Equation 2.11.

$$\mathbf{Q}_{\text{ext}} = [P \quad M_{z_i} \quad M_{y_i} \quad M_{z_j} \quad M_{y_j}]^T \quad [2.11]$$

2.2.3 Finite Element Discretization

In this mixed formulation, both element displacements and forces are taken as primary state variables. Interpolation functions are thus necessary for both fields. A linear interpolation function was chosen for the axial deformations and cubic interpolation functions were chosen for the transverse deformations (Equation 2.12).

$$\mathbf{u} = \mathbf{N}_u \mathbf{q} \quad [2.12a]$$

$$\mathbf{u} = [u \quad v \quad w]^T \quad [2.12b]$$

$$\mathbf{q} = [e \quad \theta_{z_i} \quad \theta_{y_i} \quad \theta_{z_j} \quad \theta_{y_j}]^T \quad [2.12c]$$

$$\mathbf{N}_u = \begin{bmatrix} \frac{x}{L} & 0 & 0 & 0 & 0 \\ 0 & x - \frac{2x^2}{L} + \frac{x^3}{L^2} & 0 & -\frac{x^2}{L} + \frac{x^3}{L^2} & 0 \\ 0 & 0 & x - \frac{2x^2}{L} + \frac{x^3}{L^2} & 0 & -\frac{x^2}{L} + \frac{x^3}{L^2} \end{bmatrix} \quad [2.12d]$$

For compactness of notation, the following equations will be defined.

$$A(x) = x - \frac{2x^2}{L} + \frac{x^3}{L^2} \quad [2.13]$$

$$B(x) = -\frac{x^2}{L} + \frac{x^3}{L^2} \quad [2.14]$$

The first variation of the element deformation can be shown to utilize the same interpolation functions (Equation 2.15).

$$\delta \mathbf{u} = \mathbf{N}_u \delta \mathbf{q} \quad [2.15]$$

The stress resultants can be described by an axial force (P) and two bending moments (M_z, M_y) about two orthogonal axes. A constant interpolation function was chosen for the axial force and linear interpolation functions with additional P - δ terms were chosen for the bending moments.

$$\mathbf{D} = \mathbf{N}_{D1} \mathbf{Q} \quad [2.16a]$$

$$\mathbf{D} = \begin{bmatrix} P & M_z & M_y \end{bmatrix}^T \quad [2.16b]$$

$$\mathbf{Q} = \begin{bmatrix} P & M_{zi} & M_{yi} & M_{zj} & M_{yj} \end{bmatrix}^T \quad [2.16c]$$

$$\mathbf{N}_{D1} = \begin{bmatrix} 1 & 0 & 0 & 0 & 0 \\ v(x) & 1 - \frac{x}{L} & 0 & \frac{x}{L} & 0 \\ w(x) & 0 & 1 - \frac{x}{L} & 0 & \frac{x}{L} \end{bmatrix} \quad [2.16d]$$

The first variation of the section forces may be expressed as

$$\delta \mathbf{D} = \delta \mathbf{N}_{D1} \mathbf{Q} + \mathbf{N}_{D1} \delta \mathbf{Q} \quad [2.17]$$

or, through a rearrangement of terms

$$\delta \mathbf{D} = \mathbf{N}_{D2} \delta \mathbf{q} + \mathbf{N}_{D1} \delta \mathbf{Q} \quad [2.18]$$

where

$$\mathbf{N}_{\mathbf{D2}} = \begin{bmatrix} 0 & 0 & 0 & 0 & 0 \\ 0 & PA & 0 & PB & 0 \\ 0 & 0 & PA & 0 & PB \end{bmatrix} \quad [2.19]$$

2.2.4 Kinematic Equations

The cross-sectional deformations of a three-dimensional beam element without torsional effect can be represented by an axial strain (ε) and two curvatures (κ_z, κ_y) about two orthogonal axes.

$$\hat{\mathbf{d}} = [\varepsilon \quad \kappa_z \quad \kappa_y]^T \quad [2.20]$$

The axial component of Green-Lagrange strain is defined by Equation 2.21

$$\varepsilon = u_{,x} + 1/2(v_{,x})^2 + 1/2(w_{,x})^2 \quad [2.21]$$

It is important to note that the description of the Green-Lagrange strain in Equation 2.21 is not complete. The term $1/2(u_{,x})^2$ was omitted since the axial deformation of the element chord is assumed to be small (Alemdar and White 2005). Curvatures are defined as

$$\kappa_z = v_{,xx} \quad \kappa_y = w_{,xx} \quad [2.22]$$

Utilizing the interpolation functions of the finite element discretization (Equation 2.12) the strains can be written as

$$\varepsilon = \frac{e}{L} + \frac{1}{2} \left(A_{,x} \theta_{yi} + B_{,x} \theta_{yj} \right)^2 + \frac{1}{2} \left(A_{,x} \theta_{zi} + B_{,x} \theta_{zj} \right)^2 \quad [2.23]$$

$$\kappa_z = A_{,xx} \theta_{zi} + B_{,xx} \theta_{zj} \quad [2.24]$$

$$\kappa_y = A_{,xx} \theta_{yi} + B_{,xx} \theta_{yj} \quad [2.25]$$

The first variation of the cross section strains may be written as

$$\delta\varepsilon = \delta u_{,x} + v_{,x} \delta v_{,x} + w_{,x} \delta w_{,x} \quad [2.26]$$

$$\delta\kappa_z = \delta v_{,xx} \quad \delta\kappa_y = \delta w_{,xx} \quad [2.27]$$

Utilizing the interpolation functions of the finite element discretization (Equation 2.12) the first variation of the strains can be written as

$$\delta\varepsilon = \frac{\delta e}{L} + (A_{,x}\theta_{yi} + B_{,x}\theta_{yj})(A_{,x}\delta\theta_{yi} + B_{,x}\delta\theta_{yj}) + (A_{,x}\theta_{zi} + B_{,x}\theta_{zj})(A_{,x}\delta\theta_{zi} + B_{,x}\delta\theta_{zj}) \quad [2.28]$$

$$\delta\kappa_z = A_{,xx}\delta\theta_{zi} + B_{,xx}\delta\theta_{zj} \quad [2.29]$$

$$\delta\kappa_y = A_{,xx}\delta\theta_{yi} + B_{,xx}\delta\theta_{yj} \quad [2.30]$$

These equations are written in matrix form as

$$\delta\hat{\mathbf{d}} = \mathbf{N}_{\delta\hat{\mathbf{d}}} \delta\mathbf{q} \quad [2.31]$$

$$\mathbf{N}_{\delta\hat{\mathbf{d}}} = \begin{bmatrix} 1/L & A_{,x}^2\theta_{zi} + A_{,x}B_{,x}\theta_{zj} & A_{,x}^2\theta_{yi} + A_{,x}B_{,x}\theta_{yj} & A_{,x}B_{,x}\theta_{zi} + B_{,x}^2\theta_{zj} & A_{,x}B_{,x}\theta_{yi} + B_{,x}^2\theta_{yj} \\ 0 & A_{,xx} & 0 & B_{,xx} & 0 \\ 0 & 0 & A_{,xx} & 0 & B_{,xx} \end{bmatrix} \quad [2.32]$$

2.2.5 Compatibility Equation

The mixed finite element formulation requires satisfaction of equilibrium and compatibility equations simultaneously based on the selected variation principle. Element strains are obtained along the length of the element from displacements ($\hat{\mathbf{d}}$). They are also obtained from forces (\mathbf{d}). The compatibility equation (Equation 2.33) ensures that the cross section strains obtained from element displacement are equal to those obtained from element forces in a variational sense.

$$\int_0^{L_0} \delta\mathbf{D}^T (\hat{\mathbf{d}} - \mathbf{d}) dx = 0 \quad [2.33]$$

2.2.6 The Hellinger-Reissner Principle

The Hellinger-Reissner principle is stated by combining the weak form of the equilibrium equation (Equation 2.10) and the compatibility equation (Equation 2.33).

$$\int_0^{L_0} \delta\hat{\mathbf{d}}^T \mathbf{D} dx - \delta\mathbf{q}^T \mathbf{Q}_{\text{ext}} + \int_0^{L_0} \delta\mathbf{D}^T (\hat{\mathbf{d}} - \mathbf{d}) dx = 0 \quad [2.34]$$

Equation 2.35 is obtained by substituting Equations 2.18 and 2.31 into 2.34 and collecting terms.

$$\delta\mathbf{q}^T \left(\int_0^{L_0} \mathbf{N}_{\delta\hat{\mathbf{d}}}^T \mathbf{D} dx - \mathbf{Q}_{\text{ext}} + \int_0^{L_0} \mathbf{N}_{\mathbf{D}2}^T (\hat{\mathbf{d}} - \mathbf{d}) dx \right) + \delta\mathbf{Q}^T \left(\int_0^{L_0} \mathbf{N}_{\mathbf{D}1}^T (\hat{\mathbf{d}} - \mathbf{d}) dx \right) = 0 \quad [2.35]$$

Since $\delta\mathbf{q}^T$ and $\delta\mathbf{Q}^T$ are arbitrary, two equations are obtained.

$$\mathbf{g} = \int_0^{L_0} \mathbf{N}_{\hat{\mathbf{d}}}^T \mathbf{D} dx - \mathbf{Q}_{\text{ext}} + \int_0^{L_0} \mathbf{N}_{\mathbf{D}2}^T (\hat{\mathbf{d}} - \mathbf{d}) dx = 0 \quad [2.36]$$

$$\mathbf{V} = \int_0^{L_0} \mathbf{N}_{\mathbf{D}1}^T (\hat{\mathbf{d}} - \mathbf{d}) dx = 0 \quad [2.37]$$

2.2.7 Section Equilibrium Equation

A third equation is obtained noting section equilibrium. One set of section forces is obtained through interpolation of the element forces (Equation 2.16). Another set of section forces, \mathbf{D}_Σ , is obtained through integration of the individual fiber stresses. These two sets of forces are maintained equal to each other through Equation 2.38.

$$\mathbf{U} = \mathbf{D}_\Sigma - \mathbf{D} \quad [2.38]$$

2.2.8 Consistent Linearization of the Element Compatibility Equation

Linearized versions of the governing equations are necessary in the element state determination and stiffness formulation process. First, the element compatibility equation will be linearized about the solution variables. A Taylor series expansion is used to perform the linearization.

$$\mathbf{V}^{i+1} \approx \mathbf{V}^i + \left. \frac{d}{d\alpha} \right|_{\alpha, \gamma=0} \mathbf{V}(\mathbf{q} + \alpha \Delta \mathbf{q}, \mathbf{Q} + \gamma \Delta \mathbf{Q}) + \left. \frac{d}{d\gamma} \right|_{\alpha, \gamma=0} \mathbf{V}(\mathbf{q} + \alpha \Delta \mathbf{q}, \mathbf{Q} + \gamma \Delta \mathbf{Q}) \quad [2.39]$$

This can be expanded such that the terms can be evaluated individually.

$$\begin{aligned} \mathbf{V}^{i+1} \approx & \mathbf{V}^i + \int_0^{L_0} \left(\left. \frac{d}{d\alpha} \right|_{\alpha, \gamma=0} \mathbf{N}_{\mathbf{D}1}^T \right) (\hat{\mathbf{d}} - \mathbf{d}) dx + \int_0^{L_0} (\mathbf{N}_{\mathbf{D}1}^T) \left(\left. \frac{d}{d\alpha} \right|_{\alpha, \gamma=0} \hat{\mathbf{d}} \right) dx \\ & - \int_0^{L_0} (\mathbf{N}_{\mathbf{D}1}^T) \left(\left. \frac{d}{d\alpha} \right|_{\alpha, \gamma=0} \mathbf{d} \right) dx + \int_0^{L_0} \left(\left. \frac{d}{d\gamma} \right|_{\alpha, \gamma=0} \mathbf{N}_{\mathbf{D}1}^T \right) (\hat{\mathbf{d}} - \mathbf{d}) dx \\ & + \int_0^{L_0} (\mathbf{N}_{\mathbf{D}1}^T) \left(\left. \frac{d}{d\gamma} \right|_{\alpha, \gamma=0} \hat{\mathbf{d}} \right) dx - \int_0^{L_0} (\mathbf{N}_{\mathbf{D}1}^T) \left(\left. \frac{d}{d\gamma} \right|_{\alpha, \gamma=0} \mathbf{d} \right) dx \end{aligned} \quad [2.40]$$

The second term of the right hand side of Equation 2.40 is evaluated as

$$\begin{aligned}
& \int_0^{L_o} \left(\frac{d}{d\alpha} \Big|_{\alpha,\gamma=0} \mathbf{N}_{\mathbf{D1}}^T \right) (\hat{\mathbf{d}} - \mathbf{d}) dx \\
&= \int_0^{L_o} \begin{bmatrix} 0 & 0 & 0 & 0 & 0 \\ A\Delta\theta_{zi} + B\Delta\theta_{zj} & 0 & 0 & 0 & 0 \\ A\Delta\theta_{yi} + B\Delta\theta_{yj} & 0 & 0 & 0 & 0 \end{bmatrix}^T (\hat{\mathbf{d}} - \mathbf{d}) dx \\
&= \int_0^{L_o} \begin{bmatrix} 0 & A(\hat{\mathbf{d}} - \mathbf{d})[2] & A(\hat{\mathbf{d}} - \mathbf{d})[3] & B(\hat{\mathbf{d}} - \mathbf{d})[2] & B(\hat{\mathbf{d}} - \mathbf{d})[3] \\ 0 & 0 & 0 & 0 & 0 \\ 0 & 0 & 0 & 0 & 0 \\ 0 & 0 & 0 & 0 & 0 \\ 0 & 0 & 0 & 0 & 0 \end{bmatrix} dx \Delta \mathbf{q} \\
&= \mathbf{M}_d \Delta \mathbf{q}
\end{aligned} \tag{2.41}$$

The third term of the right hand side of Equation 2.40 is evaluated as

$$\begin{aligned}
& \int_0^{L_o} (\mathbf{N}_{\mathbf{D1}}^T) \left(\frac{d}{d\alpha} \Big|_{\alpha,\gamma=0} \hat{\mathbf{d}} \right) dx = \int_0^{L_o} (\mathbf{N}_{\mathbf{D1}}^T) (\mathbf{N}_{\hat{\mathbf{d}}} \Delta \mathbf{q}) dx \\
&= \int_0^{L_o} \mathbf{N}_{\mathbf{D1}}^T \mathbf{N}_{\hat{\mathbf{d}}} dx \Delta \mathbf{q} = \mathbf{G}_1 \Delta \mathbf{q}
\end{aligned} \tag{2.42}$$

The fourth term of the right hand side of Equation 2.40 is evaluated as

$$\begin{aligned}
& \int_0^{L_o} (\mathbf{N}_{\mathbf{D1}}^T) \left(\frac{d}{d\alpha} \Big|_{\alpha,\gamma=0} \mathbf{d} \right) dx \\
&= \int_0^{L_o} (\mathbf{N}_{\mathbf{D1}}^T) \frac{\partial \mathbf{d}}{\partial \mathbf{D}_\Sigma} \frac{\partial \mathbf{D}_\Sigma}{\partial \mathbf{D}} \left(\frac{d}{d\alpha} \Big|_{\alpha,\gamma=0} \mathbf{D} \right) dx \\
&= \int_0^{L_o} (\mathbf{N}_{\mathbf{D1}}^T) \mathbf{f} \mathbf{I} \left(\begin{bmatrix} 0 & 0 & 0 & 0 & 0 \\ A\Delta\theta_{zi} + B\Delta\theta_{zj} & 0 & 0 & 0 & 0 \\ A\Delta\theta_{yi} + B\Delta\theta_{yj} & 0 & 0 & 0 & 0 \end{bmatrix} \mathbf{Q} \right) dx \\
&= \int_0^{L_o} (\mathbf{N}_{\mathbf{D1}}^T) \mathbf{f} \begin{bmatrix} 0 & 0 & 0 & 0 & 0 \\ 0 & PA & 0 & PB & 0 \\ 0 & 0 & PA & 0 & PB \end{bmatrix} \Delta \mathbf{q} dx \\
&= \int_0^{L_o} \mathbf{N}_{\mathbf{D1}}^T \mathbf{f} \mathbf{N}_{\mathbf{D2}} dx \Delta \mathbf{q} = \mathbf{H}_{12} \Delta \mathbf{q}
\end{aligned} \tag{2.43}$$

The fifth and sixth terms of the right hand side of Equation 2.40 is evaluated as

$$\int_0^{L_0} \left(\frac{d}{d\gamma} \Big|_{\alpha, \gamma=0} \mathbf{N}_{\mathbf{dI}}^T \right) (\hat{\mathbf{d}} - \mathbf{d}) dx = 0 \quad [2.44]$$

$$\int_0^{L_0} (\mathbf{N}_{\mathbf{dI}}^T) \left(\frac{d}{d\gamma} \Big|_{\alpha, \gamma=0} \hat{\mathbf{d}} \right) dx = 0 \quad [2.45]$$

The seventh term of the right hand side of Equation 2.40 is evaluated as

$$\begin{aligned} \int_0^{L_0} (\mathbf{N}_{\mathbf{dI}}^T) \left(\frac{d}{d\gamma} \Big|_{\alpha, \gamma=0} \mathbf{d} \right) dx &= \int_0^{L_0} (\mathbf{N}_{\mathbf{dI}}^T) \frac{\partial \mathbf{d}}{\partial \mathbf{D}_\Sigma} \frac{\partial \mathbf{D}_\Sigma}{\partial \mathbf{D}} \left(\frac{d}{d\gamma} \Big|_{\alpha, \gamma=0} \mathbf{D} \right) dx \\ &= \int_0^{L_0} (\mathbf{N}_{\mathbf{dI}}^T) \mathbf{f} \mathbf{I} \mathbf{N}_{\mathbf{dI}} \Delta \mathbf{Q} dx = \int_0^{L_0} \mathbf{N}_{\mathbf{dI}}^T \mathbf{f} \mathbf{N}_{\mathbf{dI}} dx \Delta \mathbf{Q} = \mathbf{H}_{11} \Delta \mathbf{Q} \end{aligned} \quad [2.46]$$

where \mathbf{f} is the flexibility of the section.

Combining the results of Equations 2.41 through 2.46 back into Equation 2.40 yields

$$\begin{aligned} \mathbf{V}^{i+1} &\approx \mathbf{V}^i + \mathbf{M}_d \Delta \mathbf{q} + \mathbf{G}_1 \Delta \mathbf{q} - \mathbf{H}_{12} \Delta \mathbf{q} - \mathbf{H}_{11} \Delta \mathbf{Q} \\ &\approx \mathbf{V}^i + (\mathbf{M}_d + \mathbf{G}_1 - \mathbf{H}_{12}) \Delta \mathbf{q} - \mathbf{H}_{11} \Delta \mathbf{Q} \end{aligned} \quad [2.47]$$

The final linearized form of the element compatibility equation (Equation 2.47) will be used in the state determination and stiffness formulation procedure as described in Section 2.2.12.

2.2.9 Consistent Linearization of the Element Equilibrium Equation

Linearization of the element equilibrium equation follows a similar process.

$$\begin{aligned} \mathbf{g}^{i+1} &\approx \mathbf{g}^i + \frac{d}{d\alpha} \Big|_{\alpha, \gamma, \beta=0} \mathbf{g}(\mathbf{q} + \alpha \Delta \mathbf{q}, \mathbf{Q} + \gamma \Delta \mathbf{Q}, \mathbf{Q}_{\text{ext}} + \beta \Delta \mathbf{Q}_{\text{ext}}) \\ &+ \frac{d}{d\gamma} \Big|_{\alpha, \gamma, \beta=0} \mathbf{g}(\mathbf{q} + \alpha \Delta \mathbf{q}, \mathbf{Q} + \gamma \Delta \mathbf{Q}, \mathbf{Q}_{\text{ext}} + \beta \Delta \mathbf{Q}_{\text{ext}}) \\ &+ \frac{d}{d\beta} \Big|_{\alpha, \gamma, \beta=0} \mathbf{g}(\mathbf{q} + \alpha \Delta \mathbf{q}, \mathbf{Q} + \gamma \Delta \mathbf{Q}, \mathbf{Q}_{\text{ext}} + \beta \Delta \mathbf{Q}_{\text{ext}}) \end{aligned} \quad [2.48]$$

The second term of the right hand side of Equation 2.48 can be expanded such that the terms can be evaluated individually.

$$\begin{aligned}
& \left. \frac{d}{d\alpha} \right|_{\alpha,\gamma,\beta=0} \mathbf{g}(\mathbf{q} + \alpha\Delta\mathbf{q}, \mathbf{Q} + \gamma\Delta\mathbf{Q}, \mathbf{Q}_{\text{ext}} + \beta\Delta\mathbf{Q}_{\text{ext}}) \\
&= \int_0^{L_0} \left(\left. \frac{d}{d\alpha} \right|_{\alpha,\gamma,\beta=0} \mathbf{N}_{\delta\hat{\mathbf{d}}}^T \right) \mathbf{D} dx + \int_0^{L_0} \mathbf{N}_{\delta\hat{\mathbf{d}}}^T \left(\left. \frac{d}{d\alpha} \right|_{\alpha,\gamma,\beta=0} \mathbf{D} \right) dx \\
&\quad - \left(\left. \frac{d}{d\alpha} \right|_{\alpha,\gamma,\beta=0} \mathbf{Q}_{\text{ext}} + \beta\Delta\mathbf{Q}_{\text{ext}} \right) + \int_0^{L_0} \left(\left. \frac{d}{d\alpha} \right|_{\alpha,\gamma,\beta=0} \mathbf{N}_{\mathbf{D}2}^T \right) (\hat{\mathbf{d}} - \mathbf{d}) dx \\
&\quad + \int_0^{L_0} \mathbf{N}_{\mathbf{D}2}^T \left(\left. \frac{d}{d\alpha} \right|_{\alpha,\gamma,\beta=0} \hat{\mathbf{d}} \right) dx - \int_0^{L_0} \mathbf{N}_{\mathbf{D}2}^T \left(\left. \frac{d}{d\alpha} \right|_{\alpha,\gamma,\beta=0} \mathbf{d} \right) dx
\end{aligned} \tag{2.49}$$

The first term of the right hand side of Equation 2.49 is evaluated as

$$\begin{aligned}
& \int_0^{L_0} \left(\left. \frac{d}{d\alpha} \right|_{\alpha,\gamma,\beta=0} \mathbf{N}_{\delta\hat{\mathbf{d}}}^T \right) \mathbf{D} dx \\
&= \int_0^{L_0} P \begin{bmatrix} 0 \\ A_{,x}^2 \Delta\theta_{zi} + A_{,x} B_{,x} \Delta\theta_{zj} \\ A_{,x}^2 \Delta\theta_{yi} + A_{,x} B_{,x} \Delta\theta_{yj} \\ A_{,x} B_{,x} \Delta\theta_{zi} + B_{,x}^2 \Delta\theta_{zj} \\ A_{,x} B_{,x} \Delta\theta_{yi} + B_{,x}^2 \Delta\theta_{yj} \end{bmatrix} dx \\
&= \int_0^{L_0} P \begin{bmatrix} 0 & 0 & 0 & 0 & 0 \\ 0 & A_{,x}^2 & 0 & A_{,x} B_{,x} & 0 \\ 0 & 0 & A_{,x}^2 & 0 & A_{,x} B_{,x} \\ 0 & A_{,x} B_{,x} & 0 & B_{,x}^2 & 0 \\ 0 & 0 & A_{,x} B_{,x} & 0 & B_{,x}^2 \end{bmatrix} dx \Delta\mathbf{q} \\
&= \mathbf{K}_g \Delta\mathbf{q}
\end{aligned} \tag{2.50}$$

The second term of the right hand side of Equation 2.49 is evaluated as

$$\int_0^{L_0} \mathbf{N}_{\delta\hat{\mathbf{d}}}^T \left(\left. \frac{d}{d\alpha} \right|_{\alpha,\gamma,\beta=0} \mathbf{D} \right) dx = \int_0^{L_0} \mathbf{N}_{\delta\hat{\mathbf{d}}}^T \mathbf{N}_{\mathbf{D}2} dx \Delta\mathbf{q} = \mathbf{G}_2 \Delta\mathbf{q} \tag{2.51}$$

The third term of the right hand side of Equation 2.49 is evaluated as

$$\left. \frac{d}{d\alpha} \right|_{\alpha,\gamma,\beta=0} \mathbf{Q}_{\text{ext}} + \beta\Delta\mathbf{Q}_{\text{ext}} = 0 \tag{2.52}$$

The fourth term of the right hand side of Equation 2.49 is evaluated as

$$\int_0^{L_0} \left(\frac{d}{d\alpha} \Big|_{\alpha,\gamma,\beta=0} \mathbf{N}_{\mathbf{D2}}^T \right) (\hat{\mathbf{d}} - \mathbf{d}) dx = 0 \quad [2.53]$$

The fifth term of the right hand side of Equation 2.49 is evaluated as

$$\int_0^{L_0} \mathbf{N}_{\mathbf{D2}}^T \left(\frac{d}{d\alpha} \Big|_{\alpha,\gamma,\beta=0} \hat{\mathbf{d}} \right) dx = \int_0^{L_0} \mathbf{N}_{\mathbf{D2}}^T \mathbf{N}_{\hat{\mathbf{d}}} dx \Delta \mathbf{q} = \mathbf{G}_2^T \Delta \mathbf{q} \quad [2.54]$$

The sixth term of the right hand side of Equation 2.49 is evaluated as

$$\int_0^{L_0} \mathbf{N}_{\mathbf{D2}}^T \left(\frac{d}{d\alpha} \Big|_{\alpha,\gamma,\beta=0} \mathbf{d} \right) dx = \int_0^{L_0} \mathbf{N}_{\mathbf{D2}}^T \mathbf{f} \mathbf{N}_2 dx \Delta \mathbf{q} = \mathbf{H}_{22} \Delta \mathbf{q} \quad [2.55]$$

The third term of the right hand side of Equation 2.48 can be expanded such that the terms can be evaluated individually.

$$\begin{aligned} & \frac{d}{d\gamma} \Big|_{\alpha,\gamma,\beta=0} \mathbf{g}(\mathbf{q} + \alpha \Delta \mathbf{q}, \mathbf{Q} + \gamma \Delta \mathbf{Q}, \mathbf{Q}_{\text{ext}} + \beta \Delta \mathbf{Q}_{\text{ext}}) \\ &= \int_0^{L_0} \left(\frac{d}{d\gamma} \Big|_{\alpha,\gamma,\beta=0} \mathbf{N}_{\hat{\mathbf{d}}}^T \right) \mathbf{D} dx + \int_0^{L_0} \mathbf{N}_{\hat{\mathbf{d}}}^T \left(\frac{d}{d\gamma} \Big|_{\alpha,\gamma,\beta=0} \mathbf{D} \right) dx \\ & \quad - \left(\frac{d}{d\gamma} \Big|_{\alpha,\gamma,\beta=0} \mathbf{Q}_{\text{ext}} + \beta \Delta \mathbf{Q}_{\text{ext}} \right) + \int_0^{L_0} \left(\frac{d}{d\gamma} \Big|_{\alpha,\gamma,\beta=0} \mathbf{N}_{\mathbf{D2}}^T \right) (\hat{\mathbf{d}} - \mathbf{d}) dx \\ & \quad + \int_0^{L_0} \mathbf{N}_{\mathbf{D2}}^T \left(\frac{d}{d\gamma} \Big|_{\alpha,\gamma,\beta=0} \hat{\mathbf{d}} \right) dx - \int_0^{L_0} \mathbf{N}_{\mathbf{D2}}^T \left(\frac{d}{d\gamma} \Big|_{\alpha,\gamma,\beta=0} \mathbf{d} \right) dx \end{aligned} \quad [2.56]$$

The first term of the right hand side of Equation 2.56 is evaluated as

$$\int_0^{L_0} \left(\frac{d}{d\gamma} \Big|_{\alpha,\gamma,\beta=0} \mathbf{N}_{\hat{\mathbf{d}}}^T \right) \mathbf{D} dx = 0 \quad [2.57]$$

The second term of the right hand side of Equation 2.56 is evaluated as

$$\int_0^{L_0} \mathbf{N}_{\hat{\mathbf{d}}}^T \left(\frac{d}{d\gamma} \Big|_{\alpha,\gamma,\beta=0} \mathbf{D} \right) dx = \int_0^{L_0} \mathbf{N}_{\hat{\mathbf{d}}}^T \mathbf{N}_{\mathbf{D1}} dx \Delta \mathbf{Q} = \mathbf{G}_1^T \Delta \mathbf{Q} \quad [2.58]$$

The third term of the right hand side of Equation 2.56 is evaluated as

$$\left. \frac{d}{d\gamma} \right|_{\alpha,\gamma,\beta=0} \mathbf{Q}_{\text{ext}} + \beta \Delta \mathbf{Q}_{\text{ext}} = 0 \quad [2.59]$$

The fourth term of the right hand side of Equation 2.56 is evaluated as

$$\begin{aligned} & \int_0^{L_o} \left(\left. \frac{d}{d\gamma} \right|_{\alpha,\gamma,\beta=0} \mathbf{N}_{\mathbf{D2}}^T \right) (\hat{\mathbf{d}} - \mathbf{d}) dx \\ &= \int_0^{L_o} \begin{bmatrix} 0 & 0 & 0 \\ 0 & A\Delta P & 0 \\ 0 & 0 & A\Delta P \\ 0 & B\Delta P & 0 \\ 0 & 0 & B\Delta P \end{bmatrix} (\hat{\mathbf{d}} - \mathbf{d}) dx \\ &= \int_0^{L_o} \begin{bmatrix} 0 & 0 & 0 & 0 & 0 \\ A\Delta P(\hat{\mathbf{d}} - \mathbf{d})[2] & 0 & 0 & 0 & 0 \\ A\Delta P(\hat{\mathbf{d}} - \mathbf{d})[3] & 0 & 0 & 0 & 0 \\ B\Delta P(\hat{\mathbf{d}} - \mathbf{d})[2] & 0 & 0 & 0 & 0 \\ B\Delta P(\hat{\mathbf{d}} - \mathbf{d})[3] & 0 & 0 & 0 & 0 \end{bmatrix} dx \Delta \mathbf{Q} \\ &= \mathbf{M}_d^T \Delta \mathbf{Q} \end{aligned} \quad [2.60]$$

The fifth term of the right hand side of Equation 2.56 is evaluated as

$$\int_0^{L_o} \mathbf{N}_{\mathbf{D2}}^T \left(\left. \frac{d}{d\gamma} \right|_{\alpha,\gamma,\beta=0} \hat{\mathbf{d}} \right) dx = 0 \quad [2.61]$$

The sixth term of the right hand side of Equation 2.56 is evaluated as

$$\int_0^{L_o} \mathbf{N}_{\mathbf{D2}}^T \left(\left. \frac{d}{d\gamma} \right|_{\alpha,\gamma,\beta=0} \mathbf{d} \right) dx = \int_0^{L_o} \mathbf{N}_{\mathbf{D2}}^T \mathbf{f} \mathbf{N}_{\mathbf{D1}} dx \Delta \mathbf{Q} = \mathbf{H}_{12}^T \Delta \mathbf{Q} \quad [2.62]$$

The fourth term of the right hand side of Equation 2.48 is evaluated as

$$\left. \frac{d}{d\beta} \right|_{\alpha,\gamma,\beta=0} \mathbf{g}(\mathbf{q} + \alpha \Delta \mathbf{q}, \mathbf{Q} + \gamma \Delta \mathbf{Q}, \mathbf{Q}_{\text{ext}} + \beta \Delta \mathbf{Q}_{\text{ext}}) = -\Delta \mathbf{Q}_{\text{ext}} \quad [2.63]$$

Combining the results of Equations 2.49 through 2.63 back in to Equation 2.48 yields

$$\mathbf{g}^{i+1} \approx \mathbf{g}^i + (\mathbf{K}_g + \mathbf{G}_2 + \mathbf{G}_2^T - \mathbf{H}_{22}) \Delta \mathbf{q} + (\mathbf{G}_1 + \mathbf{M}_d - \mathbf{H}_{12})^T \Delta \mathbf{Q} - \Delta \mathbf{Q}_{\text{ext}} \quad [2.64]$$

The final linearized form of the element equilibrium equation (Equation 2.64) will be used in the state determination and stiffness formulation procedure as described in Section 2.2.12.

2.2.10 Consistent Linearization of the Section Equilibrium Equation

Linearization of the section equilibrium equation follows a similar process. By expanding the section equilibrium equation about \mathbf{d} , holding \mathbf{D} constant

$$\mathbf{U}^{i+1} \approx \mathbf{U}^i + \left. \frac{d}{d\alpha} \right|_{\alpha=0} \mathbf{U}(\mathbf{d} + \alpha\Delta\mathbf{d}) \quad [2.65]$$

The second term on the right hand side of Equation 2.65 is evaluated as

$$\left. \frac{d}{d\alpha} \right|_{\alpha=0} \mathbf{U}(\mathbf{d} + \alpha\Delta\mathbf{d}) = \left. \frac{d}{d\alpha} \right|_{\alpha=0} \mathbf{D}_{\Sigma}(\mathbf{d} + \alpha\Delta\mathbf{d}) = \mathbf{k} \Delta\mathbf{d} \quad [2.66]$$

Substituting into the result of Equation 2.66 back into Equation 2.65 yields

$$\mathbf{U}^{i+1} \approx \mathbf{U}^i + \mathbf{k} \Delta\mathbf{d} \quad [2.67]$$

The final linearized form of the section equilibrium equation (Equation 2.67) will be used in the state determination and stiffness formulation procedure as described in Section 2.2.12.

2.2.11 Consistent Element Tangent Stiffness Matrix

The consistent tangent stiffness matrix is obtained using the linearized equations. Setting Equation 2.47 to zero and solving for $\Delta\mathbf{Q}$ yields

$$\Delta\mathbf{Q} = \mathbf{H}_{11}^{-1} \mathbf{V}^i + \mathbf{H}_{11}^{-1} (\mathbf{M}_d + \mathbf{G}_1 - \mathbf{H}_{12}) \Delta\mathbf{q} \quad [2.68]$$

Setting Equation 2.64 to zero and substituting in the result of Equation 2.68 yields

$$\begin{aligned} & \left[(\mathbf{K}_g + \mathbf{G}_2 + \mathbf{G}_2^T - \mathbf{H}_{22}) + (\mathbf{G}_1 + \mathbf{M}_d - \mathbf{H}_{12})^T \mathbf{H}_{11}^{-1} (\mathbf{G}_1 + \mathbf{M}_d - \mathbf{H}_{12}) \right] \Delta\mathbf{q} \\ & = \Delta\mathbf{Q}_{\text{ext}} - \mathbf{g}^i - (\mathbf{G}_1 + \mathbf{M}_d - \mathbf{H}_{12})^T \mathbf{H}_{11}^{-1} \mathbf{V}^i \end{aligned} \quad [2.69]$$

Substituting in the definition of \mathbf{g} yields

$$\begin{aligned} & \left[(\mathbf{K}_g + \mathbf{G}_2 + \mathbf{G}_2^T - \mathbf{H}_{22}) + (\mathbf{G}_1 + \mathbf{M}_d - \mathbf{H}_{12})^T \mathbf{H}_{11}^{-1} (\mathbf{G}_1 + \mathbf{M}_d - \mathbf{H}_{12}) \right] \Delta\mathbf{q} \\ & = \Delta\mathbf{Q}_{\text{ext}} - \mathbf{G}_1^T \mathbf{Q} + \mathbf{Q}_{\text{ext}}^i - \int_0^{L_0} \mathbf{N}_{D2}^T (\hat{\mathbf{d}}^i - \mathbf{d}^i) dx - (\mathbf{G}_1 + \mathbf{M}_d - \mathbf{H}_{12})^T \mathbf{H}_{11}^{-1} \mathbf{V}^i \end{aligned} \quad [2.70]$$

Simplifying

$$\mathbf{K} \Delta \mathbf{q} = \mathbf{Q}_{\text{ext}}^{i+1} - \mathbf{Q}_{\text{int}}^i \quad [2.71]$$

where,

$$\mathbf{K} = (\mathbf{K}_g + \mathbf{G}_2 + \mathbf{G}_2^T - \mathbf{H}_{22}) + (\mathbf{G}_1 + \mathbf{M}_d - \mathbf{H}_{12})^T \mathbf{H}_{11}^{-1} (\mathbf{G}_1 + \mathbf{M}_d - \mathbf{H}_{12}) \quad [2.72]$$

$$\mathbf{Q}_{\text{int}}^i = \mathbf{G}_1^T \mathbf{Q} + \int_0^{L_e} \mathbf{N}_{D2}^T (\hat{\mathbf{d}}^i - \mathbf{d}^i) dx + (\mathbf{G}_1 + \mathbf{M}_d - \mathbf{H}_{12})^T \mathbf{H}_{11}^{-1} \mathbf{V}^i \quad [2.73]$$

In this form, \mathbf{K} is the tangent stiffness matrix of the element and the right hand side of Equation 2.71 can be interpreted as the residual force, equal to the difference between the externally applied load and the element internal force corresponding to the previous element state, $\mathbf{Q}_{\text{int}}^i$.

2.2.12 Element State Determination

In typical incremental nonlinear analyses, trial displacements are computed based on external loading and the prior state of the structure. This stage is also called the predictor phase (Yang and Leu 1991) and is followed by the state determination, or corrector phase. The accuracy of the formulation is predominantly governed by this latter stage (Yang and Leu 1991). The state determination of mixed elements is often more complex than either displacement-based or force-based elements (Alemdar and White 2005).

The three nonlinear governing equations (Equations 2.36, 2.37, and 2.38) which may be seen to operate at the global, element, and section levels respectively, allow for different methods of state determination. Global equilibrium is solved iteratively. Element compatibility and section equilibrium may be solved iteratively or, alternatively, linearized equations may be utilized and the errors converted to residual forces that may be eliminated through iterations at the global or element level (Nukala and White 2004b). With the option of nonlinear iterations or linearized approximation at both the element and section level, four possible algorithms may be developed. It should be noted that the nonlinear iteration option, as compared to the linearized approximation option, generally requires fewer global iterations at the expense of more costly element or section computations. In this work, as in that of others (Alemdar and White 2005 and Tort and Hajjar 2007), the linearized approximation option is chosen at both the element and section levels.

Integration along the length of the element needs to be performed to compute many of the key element matrices and vectors. Gauss-Lobatto quadrature is utilized to perform the integration numerically. In this integration scheme, the location of the integration points and their associated weights are selected in a manner such that an integration point is located at each element end. This is beneficial, noting that the force and deformation values are often the largest at the element ends (e.g., reverse curvature flexure).

To begin the process of state determination, the total natural element deformations are obtained from the *GeometricTransformation* object associated with the element. The strain and curvature at each integration point are then calculated.

The shape function matrices are then computed and natural forces are updated using Equation 2.68. Then for each integration point the section forces are computed from the shape function. Using Equation 2.74, the section strains are updated.

$$\mathbf{d}^{i+1} = \mathbf{d}^i + \mathbf{f} \left[\mathbf{D}^{i+1} - \mathbf{D}_\Sigma^i \right] \quad [2.74]$$

The strains at each section are sent to their associated *section* object, which will update the uniaxial material models assigned to each fiber, aggregate the sectional response, and return the new section stresses and section stiffnesses.

The element matrices are then computed using Gauss-Lobatto quadrature as described in Equations 2.75 through 2.83.

$$\mathbf{G}_1 = \sum_{\text{allsections}} L_o W_k \mathbf{N}_{D1}^T \mathbf{N}_{\delta \hat{\mathbf{d}}} \quad [2.75]$$

$$\mathbf{G}_2 = \sum_{\text{allsections}} L_o W_k \mathbf{N}_{D2}^T \mathbf{N}_{\delta \hat{\mathbf{d}}} \quad [2.76]$$

$$\mathbf{V} = \sum_{\text{allsections}} L_o W_k \mathbf{N}_{D1}^T (\hat{\mathbf{d}} - \mathbf{d} - \mathbf{f}(\mathbf{D} - \mathbf{D}_\Sigma)) \quad [2.77]$$

$$\mathbf{V}_2 = \sum_{\text{allsections}} L_o W_k \mathbf{N}_{D2}^T (\hat{\mathbf{d}} - \mathbf{d}) \quad [2.78]$$

$$\mathbf{H}_{11} = \sum_{\text{allsections}} L_o W_k \mathbf{N}_{D1}^T \mathbf{f} \mathbf{N}_{D1} \quad [2.79]$$

$$\mathbf{H}_{12} = \sum_{\text{allsections}} L_o W_k \mathbf{N}_{D1}^T \mathbf{f} \mathbf{N}_{D2} \quad [2.80]$$

$$\mathbf{H}_{22} = \sum_{\text{allsections}} L_o W_k \mathbf{N}_{D2}^T \mathbf{f} \mathbf{N}_{D2} \quad [2.81]$$

$$\mathbf{K}_g = \sum_{\text{allsections}} L_o W_k P \begin{bmatrix} 0 & 0 & 0 & 0 & 0 \\ 0 & A_{,x}^2 & 0 & A_{,x} B_{,x} & 0 \\ 0 & 0 & A_{,x}^2 & 0 & A_{,x} B_{,x} \\ 0 & A_{,x} B_{,x} & 0 & B_{,x}^2 & 0 \\ 0 & 0 & A_{,x} B_{,x} & 0 & B_{,x}^2 \end{bmatrix} \quad [2.82]$$

$$\mathbf{M}_d = \sum_{\text{allsections}} L_o W_k \begin{bmatrix} 0 & A(\hat{\mathbf{d}}-\mathbf{d})[2] & A(\hat{\mathbf{d}}-\mathbf{d})[3] & B(\hat{\mathbf{d}}-\mathbf{d})[2] & B(\hat{\mathbf{d}}-\mathbf{d})[3] \\ 0 & 0 & 0 & 0 & 0 \\ 0 & 0 & 0 & 0 & 0 \\ 0 & 0 & 0 & 0 & 0 \\ 0 & 0 & 0 & 0 & 0 \end{bmatrix} \quad [2.83]$$

where, W_k is the integration weight.

The element internal force and stiffness matrix are computed using Equations 2.73 and 2.72 respectively. The extra terms in the computation of the vector \mathbf{V} (Equation 2.77) arise from the choice of algorithm noted earlier, they represent the error at the section level that has been pushed to this level to be eliminated by iteration. Note that the vector \mathbf{V}_2 is equivalent to the second term on the right hand side of Equation 2.73. At this point it is necessary to add the torsional force and stiffness that were assumed to exhibit a linear response (Equations 2.84 and 2.85)

$$\mathbf{Q}_{\text{int,with torsion}} = \begin{bmatrix} \mathbf{Q}_{\text{int}} \\ \frac{GJ}{L}\theta \end{bmatrix} \quad [2.84]$$

$$\mathbf{K}_{\text{with torsion}} = \begin{bmatrix} \mathbf{K} & 0 \\ 0 & \frac{GJ}{L} \end{bmatrix} \quad [2.85]$$

where, GJ/L is the torsional stiffness, and θ is the twist in natural coordinates.

Equations 2.84 and 2.85 represent the complete internal element force and tangent stiffness matrix in the natural coordinate system. Transformation of these quantities to the local and global coordinate systems for assembly and solution at the global level is performed by the *GeometricTransformation* object associated with the element.

2.2.13 Transformation of Element Force, Displacements, and Stiffness between Natural and Global Coordinate Systems

Three coordinate systems are relevant to each element. First, the natural coordinate system has the rigid body modes removed and rotates with the motion of the element. Second, the local coordinate system is aligned with the natural coordinate system but has the rigid body modes. Third, the global coordinate system is common for all elements and is fixed throughout the analysis.

The accuracy of the transformation between the three coordinate systems has a significant effect on the accuracy of the geometric nonlinearity. In the OpenSees framework, the abstract class, *GeometricTransformation*, is defined to provide multiple definitions of the force, deformation, and stiffness transformations necessary between the global and

natural coordinate systems (Scott et al. 2008). There are various subclasses that contain implementations of specific transformation procedures with various kinematic and equilibrium assumptions. One subclass, *LinearTransformation*, would be suitable for analyses without geometric nonlinearities. Other subclasses, *PDeltaTransformation* and *CorotationalTransformation*, utilize nonlinear transformations suitable for analyses with large deformations. These two subclasses differ in their accuracy and complexity, with the *CorotationalTransformation* being the more accurate and more complex (de Souza 2000). Despite the added complexity, the interface of the *CorotationalTransformation* is identical to that of the other transformations, thus adding no complexity to the element itself, only additional computation during analyses. In the OpenSees framework, the choice of geometric transformations is made by the analyst when defining the structure, not by the developer of the finite element. For all analyses presented in this work, the *CorotationalTransformation* was used.

UNIAXIAL CYCLIC CONCRETE CONSTITUTIVE MODEL FOR CCFT MEMBERS

3.1 Introduction

The accuracy of the mixed beam formulation presented in Chapter 2 depends strongly on the ability of the constitutive relations to provide realistic estimations of the behavior of CCFT members. Using the fiber method, the response of a cross section is governed by the aggregation of response from individual fibers and the uniaxial constitutive relations associated with them. Further, the possibility of cyclic loading during static and dynamic loading requires the constitutive relations to be applicable to arbitrary strain histories.

In this work, the stress-strain response of the concrete core is modeled with a set of empirical nonlinear curves calibrated with respect to experimental studies available in the literature.

3.2 Monotonic Compressive Response

When CCFT members are subjected to compression, both the steel tube and the concrete core expand laterally due to Poisson's effect. In the early stages, the steel tube expands at a greater rate than the concrete core (i.e., the Poisson's ratio is larger for the steel tube). However, as the loading continues the rate of lateral expansion of the concrete core increases due to micro-cracking and eventually a radial interaction occurs. The result of this interaction is a confinement pressure on the concrete and a hoop stress in the steel.

The concrete material model is based largely on recommendations by Chang and Mander (1994). The equation proposed by Tsai (1988) is used to model pre- and post- peak behavior (Equations 3.1 through 3.7). This equation defines the stress-strain response based on four parameters: the initial tangent stiffness, the peak stress, the strain at peak stress, and r , a parameter that controls the post-peak behavior.

$$y = \frac{nx}{D(x)} \quad [3.1]$$

$$z = \frac{(1-x^r)}{D(x)^2} \quad [3.2]$$

$$D(x) = \begin{cases} 1 + \left(n - \frac{r}{r-1}\right)x + \frac{x^r}{r-1} & \text{for } r \neq 1 \\ 1 + (n-1 + \ln x)x & \text{for } r = 1 \end{cases} \quad [3.3]$$

$$x^- = \left| \frac{\varepsilon}{\varepsilon'_{cc}} \right| \quad [3.4]$$

$$n^- = \left| \frac{E_c \varepsilon'_{cc}}{f'_{cc}} \right| \quad [3.5]$$

$$\sigma^- = f'_{cc} y \quad [3.6]$$

$$E^- = E_c z \quad [3.7]$$

where, the “-” superscripts in Equations 3.4 through 3.7 indicate that these values are applicable for the compressive response.

Since there is little interaction between the concrete core and steel tube for low loads, the initial tangent stiffness is based the response of unconfined concrete and is given by Equation 3.8, as recommended by Chang and Mander (1994).

$$E_c [\text{MPa}] = 8,200 f'_c [\text{MPa}]^{3/8} \quad [3.8]$$

The peak stress, strain at peak stress, and post-peak parameter r , all depend on the interaction of the steel tube and the concrete core, specifically the level of confinement provided by the steel tube.

3.2.1 Confinement Model for CCFT Beam-Columns

The level of confinement experienced by the concrete core has a significant impact on the behavior of CCFT members. A set of 24 well-documented experiments on concentrically load short columns were selected for calibration of the constitutive relations (Table 3.1). These tests were selected to have combinations of high and low values of steel yield stress, concrete compressive strength, and D/t ratio. Among other uses described later, the calibration set was used to determine an expression for the confinement pressure, f_l , assumed to be acting on the concrete core of CCFT members. From equilibrium of an assumed stress pattern within CCFT section (Figure 1-2), the confinement pressure is written in terms of the hoop stress in the steel tube, expressed in terms of the yield stress (i.e., $\alpha_\theta F_y$, where α_θ is the ratio of hoop stress to yield stress), and the D/t ratio (Equation 3.9).

$$f_l = \alpha_\theta F_y \frac{2}{D/t - 2} \quad [3.9]$$

Increasing levels of hoop stress in the steel tube induce increasing levels of confinement in the concrete core. The increasing confinement has the effect of strengthening the concrete core, while the increasing hoop stress has the effect of weakening the steel tube noting the von Mises failure criterion. Noting this relationship, an expression for the hoop stress, or rather the ratio of hoop stress to yield stress, α_θ , in the steel tube is developed based on an optimization to match experimental results. The hoop stress ratio in the steel tube does not remain constant over the course of loading of CCFT members but it is taken as such for simplicity.

To determine an expression for the hoop stress ratio, α_θ , a least squares optimization was performed to reduce the error between computed strength and experimental strength for the calibration set. The experimental strength was taken as the peak load attained during the test or, for specimens that display continual hardening behavior, an estimation was made of the load at which the cross section was fully inelastic. The maximum load attained during the test, P_{max} , and the load used for calibration, P_{cal} , are listed in Table 3.2. The computed strength was taken as the sum of the concrete strength noting strength enhancement from confinement and the steel strength noting degradation from biaxial stresses.

The confined concrete strength is computed using the model of Mander et al. (1988) for symmetric states of confinement (Equation 3.10).

$$f'_{cc} = f'_c \left(-1.254 + 2.254 \sqrt{1 + \frac{7.94 f_l}{f'_c}} - 2 \frac{f_l}{f'_c} \right) \quad [3.10]$$

The von Mises failure criterion is used to determine the longitudinal strength of the steel tube, expressed in terms of the yield stress (i.e., $\alpha_z F_y$) (Equation 3.11). This model is used to calibrate the expression for the hoop stress ratio despite the fact that the steel model presented in Chapter 4 does not explicitly provide this stress at the peak concrete strength, as is implied by this procedure. As will be seen, the results are sufficiently accurate to justify the procedure presented here.

$$\alpha_z F_y = \left(\frac{1}{2} \left(\alpha_\theta + \sqrt{4 - 3\alpha_\theta^2} \right) \right) F_y \quad [3.11]$$

Using these two expressions for concrete stress and steel stress, the respective cross sectional areas, and a value for the ratio of hoop stress to yield stress, α_θ , the strength of the column may be computed. If the form of the equation for the hoop stress ratio is assumed (e.g., linear function of D/t ratio) the coefficients of that equation can be determined though a least squares minimization of the error between the experimental and computed strengths. The best correspondence between computed and experimental strength was found when using a linear function of the D/t ratio for the hoop stress ratio (Equation 3.12). The hoop stress ratio is limited to zero since a compressive hoop stress will not exist for CCFT members. Computed values of the hoop stress ratio for the calibration set are listed in Table 3.2.

$$\alpha_{\theta} = 0.138 - 0.00174(D/t) \geq 0 \quad [3.12]$$

Using this expression for the hoop stress ratio (Equation 3.12) and the confinement model (Equation 3.10) the peak concrete stress to be used in the stress-strain relationship is obtained. The strain at peak stress is also determined based on this assumed level of confinement. The strain at peak stress for unconfined concrete is expressed using Equation 3.13, following recommendations by Chang and Mander (1994).

$$\varepsilon_c = \frac{f'_c [\text{MPa}]^{1/4}}{28} \quad [3.13]$$

The increase in strain at peak stress due to confinement follows the model by Richart et al. (1929) (Equation 3.14).

$$\varepsilon'_{cc} = \varepsilon_c (1 + 5(f'_{cc}/f'_c - 1)) \quad [3.14]$$

Table 3.1. Material and Geometric Properties of the Calibration Set

Test #	Author	Year	Specimen	D (mm)	t (mm)	D/t	f _c (MPa)	F _y (MPa)	L (mm)	L/D
1	Yoshioka et al.	1995	CC6-C-8	238.0	4.54	52.4	76.98	578.6	714	3.00
2	Yoshioka et al.	1995	CC6-D-8	360.0	4.54	79.3	85.12	578.6	1080	3.00
3	Yoshioka et al.	1995	CC8-D-8	336.0	6.47	51.9	85.12	834.5	1008	3.00
4	O'Shea & Bridge	2000	S12CS80A	190.0	1.13	168.1	80.20	185.7	663	3.49
5	O'Shea & Bridge	2000	S12CS10A	190.0	1.13	168.1	108.00	185.7	660	3.47
6	O'Shea & Bridge	2000	S20CS80B	190.0	1.94	97.9	74.80	256.4	664	3.49
7	Yoshioka et al.	1995	CC6-C-2	238.0	4.54	52.4	25.40	578.6	714	3.00
8	Yoshioka et al.	1995	CC6-D-2	360.0	4.54	79.3	25.40	578.6	1080	3.00
9	Yoshioka et al.	1995	CC8-D-2	336.0	6.47	51.9	25.40	834.5	1008	3.00
10	Yoshioka et al.	1995	CC8-A-8	108.0	6.47	16.7	76.98	834.5	324	3.00
11	Yoshioka et al.	1995	CC6-A-8	121.5	4.54	26.8	76.98	578.6	365	3.00
12	Giakoumelis & Lam	2004	C8	115.0	4.92	23.4	104.90	365.0	300	2.61
13	Yoshioka et al.	1995	CC4-A-2	149.2	2.96	50.4	25.40	283.4	448	3.00
14	Yoshioka et al.	1995	CC4-D-2	450.0	2.96	152.0	25.40	283.4	1350	3.00
15	Yoshioka et al.	1995	CC4-C-2	300.5	2.96	101.5	25.40	283.4	902	3.00
16	Han & Yao	2004	scv1-1	100.0	3.00	33.3	58.50	303.5	300	3.00
17	Han & Yao	2004	sch1-2	100.0	3.00	33.3	58.50	303.5	300	3.00
18	Sakino et al.	1985	S6HA	101.8	5.70	17.9	37.36	305.0	200	1.96
19	Yoshioka et al.	1995	CC6-A-2	122.0	4.54	26.9	25.40	578.6	366	3.00
20	Yoshioka et al.	1995	CC8-A-2	108.0	6.47	16.7	25.40	834.5	324	3.00
21	Yamamoto et al.	2002	C20A-2A	216.4	6.66	32.5	24.30	452.0	649	3.00
22	Sakino et al.	1985	S6LA	101.8	5.70	17.9	17.95	305.0	200	1.96
23	Schneider	1998	C1	140.8	3.00	46.9	28.81	285.0	605	4.30
24	Schneider	1998	C2	141.4	6.50	21.8	28.81	313.0	608	4.30

Table 3.2. Calibration Load Data and Hoop Stress Ratio

Test #	P_o (kN)	P_{max} (kN)	P_{cal} (kN)	α_θ
1	5,095	5,578	5,578	0.047
2	11,166	11,505	11,521	0.000
3	12,567	13,776	13,701	0.048
4	2,345	2,295	2,309	0.000
5	3,114	3,040	3,051	0.000
6	2,329	2,592	2,592	0.000
7	2,972	3,035	3,025	0.047
8	5,390	5,633	5,605	0.000
9	7,672	8,475	8,407	0.048
10	2,269	2,713	2,713	0.109
11	1,729	2,100	2,100	0.091
12	1,533	1,787	1,793	0.097
13	795	941	845	0.050
14	5,112	4,415	4,435	0.000
15	2,515	2,382	2,384	0.000
16	683	780	783	0.080
17	683	820	814	0.080
18	765	971	845	0.107
19	1,224	1,500	1,334	0.091
20	1,903	2,275	2,046	0.109
21	2,771	3,568	3,247	0.081
22	640	953	667	0.107
23	781	881	756	0.056
24	1,235	1,825	1,334	0.100

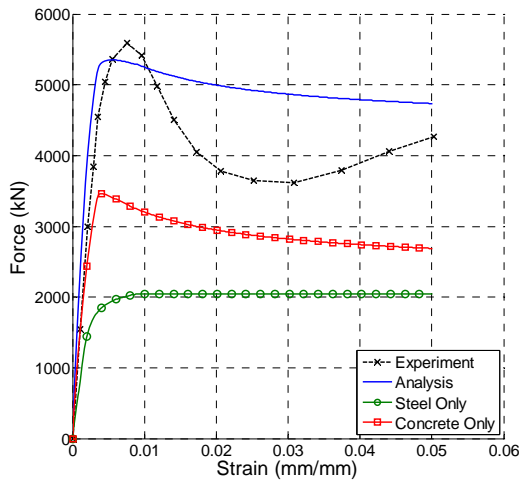
3.2.2 Post-peak behavior

The r factor in Equations 3.2 and 3.3, which controls the nonlinear descending branch, was calibrated such that the energy represented by the computed force-deformation response was equal to the corresponding energy obtained from the experiments. The expression for r based on concentrically loaded short columns was then adjusted to attain better correspondence for other testing configurations, including beams and beam-columns (presented in Sections 5.4 through 5.6). The value of r that yields good results in the post-peak range causes a sporadic hardening behavior (i.e., stiffness values larger than the initial stiffness) in the pre-peak range. To correct for this, two separate value of r are used, one in the pre-peak range and one in the post-peak range. The value of r in the pre-peak range is based on recommendations by Chang and Mander (1994) for unconfined concrete. Since the transition between the two values of r is made at the point peak compressive stress, continuity in both stress and stiffness is guaranteed. The final expression for r is shown in Equation 3.15.

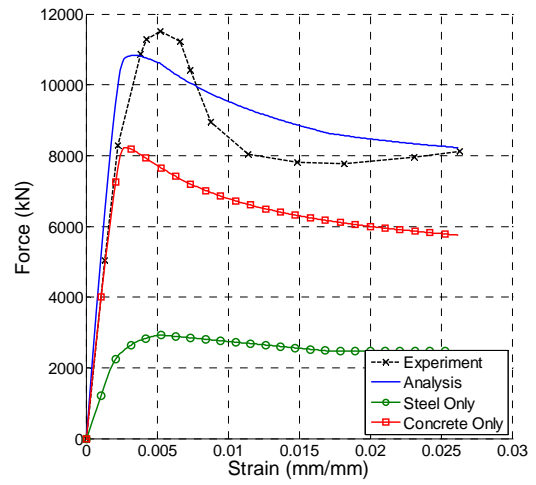
$$r^- = \begin{cases} f'_c [\text{MPa}] / 5.2 - 1.9 & \text{for } \varepsilon > \varepsilon'_{cc} \\ 0.4 + 0.016(D/t)(f'_c / F_y) & \text{for } \varepsilon \leq \varepsilon'_{cc} \end{cases} \quad [3.15]$$

3.2.3 Comparison of Experimental and Computational Results

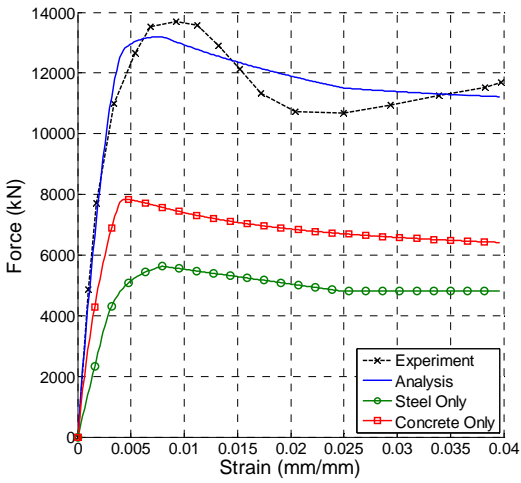
To illustrate the stress-strain response of the concrete model, analyses were performed for each experiment in the calibration set. The composite load deformation response obtained from the experiment and the analysis for each test is shown in Figure 3-1. The steel and concrete components are also plotted (details of the steel model is discussed in Chapter 4). Various metrics were computed for comparison between experimental and computational results (Table 3.3). These include: peak load, strain at peak load, initial stiffness, and area under the curve. The average error in peak load and area under the curve are less than 10 percent each, indicating good correspondence. The average error in strain at peak load and initial stiffness are higher, at approximately 30 percent and 55 percent respectively. It is noted that among the 24 tests there are tests where the metrics are underestimated and also tests where the metrics are overestimated. Since the modulus of steel is relatively constant, the errors in stiffness may be caused by inaccurate estimation of the concrete modulus; also, undesirable elastic deformations in the experimental apparatus may be a cause of an apparent overestimation of the specimen stiffness.



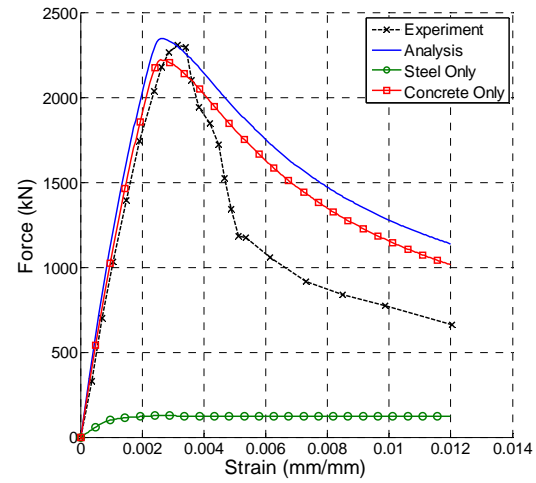
(a) Test #1; Yoshioka et al. 1995; Specimen: CC6-C-8



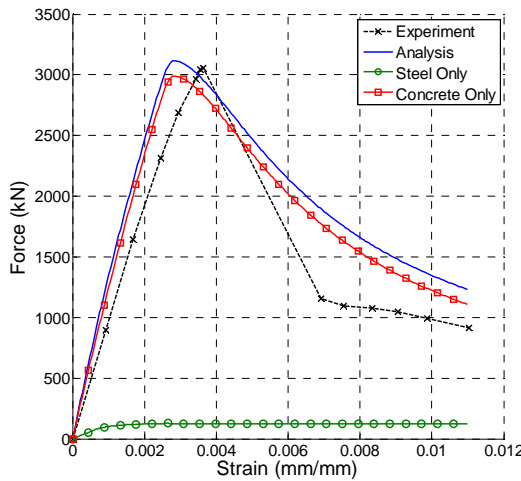
(b) Test #2; Yoshioka et al. 1995; Specimen: CC6-D-8



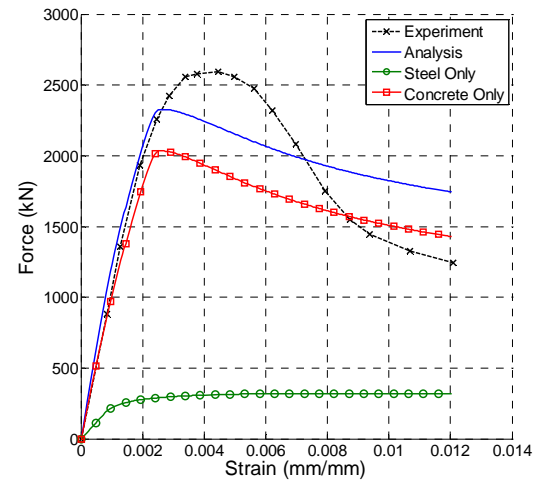
(c) Test #3; Yoshioka et al. 1995; Specimen: CC8-D-8



(d) Test #4; O'Shea & Bridge 2000; Specimen: S12CS80A

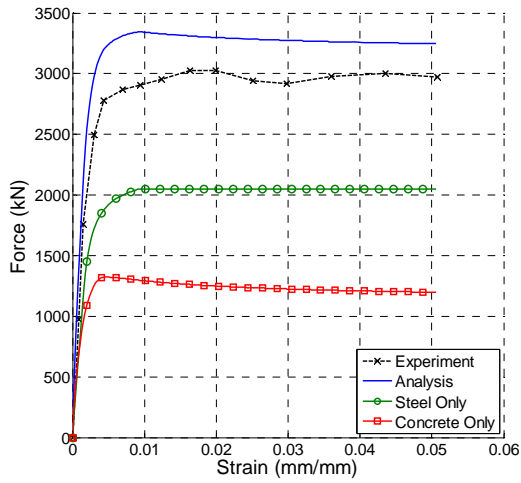


(e) Test #5; O'Shea & Bridge 2000; Specimen: S12CS10A

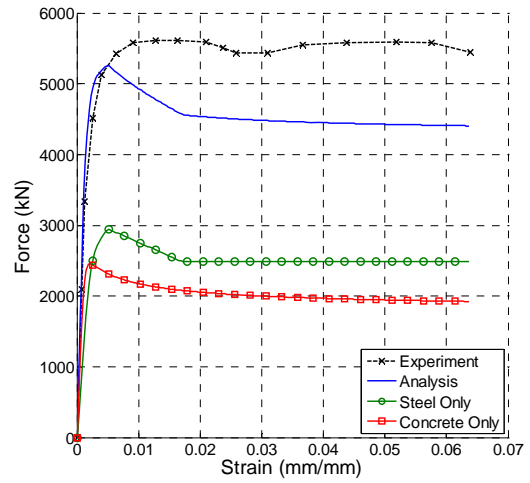


(f) Test #6; O'Shea & Bridge 2000; Specimen: S20CS80B

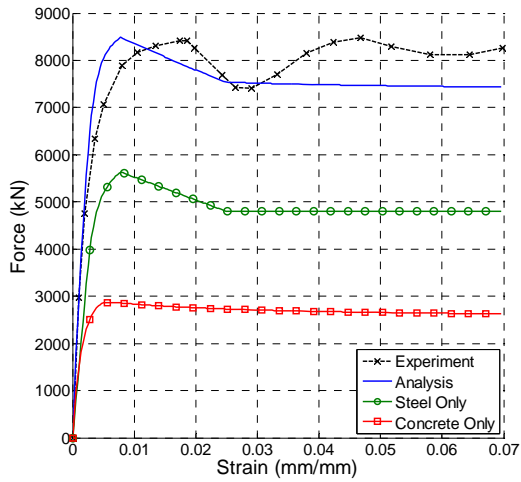
Figure 3-1. Experimental and Computational Results for the Calibration Set



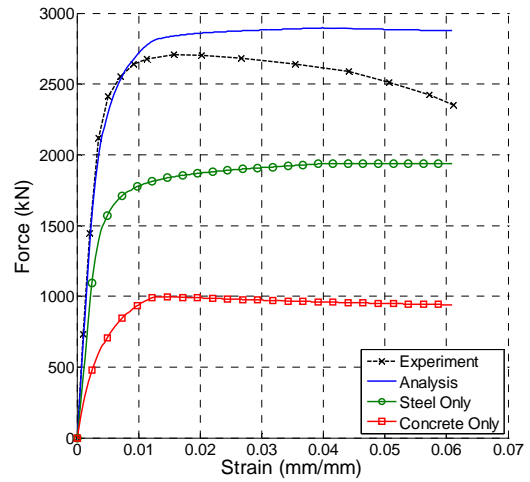
(g) Test #7; Yoshioka et al. 1995; Specimen: CC6-C-2



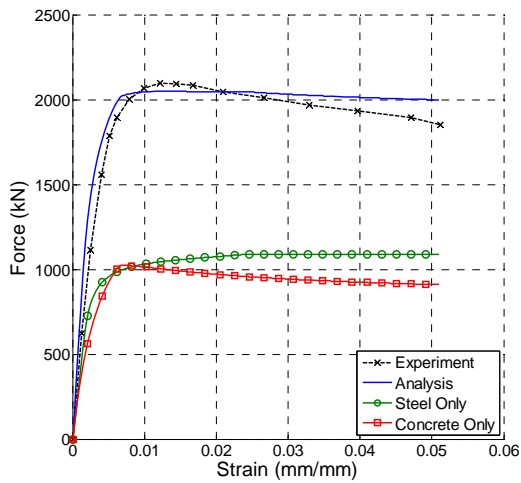
(h) Test #8; Yoshioka et al. 1995; Specimen: CC6-D-2



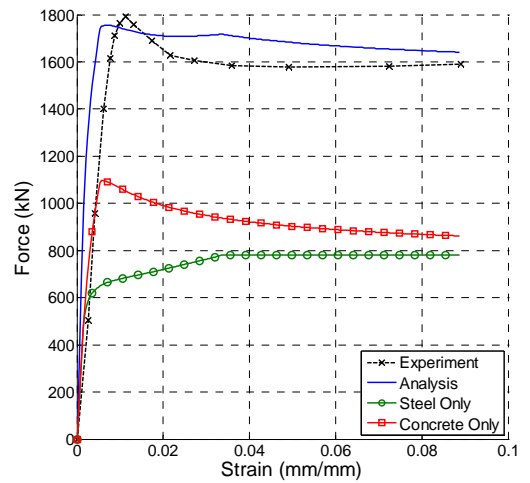
(i) Test #9; Yoshioka et al. 1995; Specimen: CC8-D-2



(j) Test #10; Yoshioka et al. 1995; Specimen: CC8-A-8

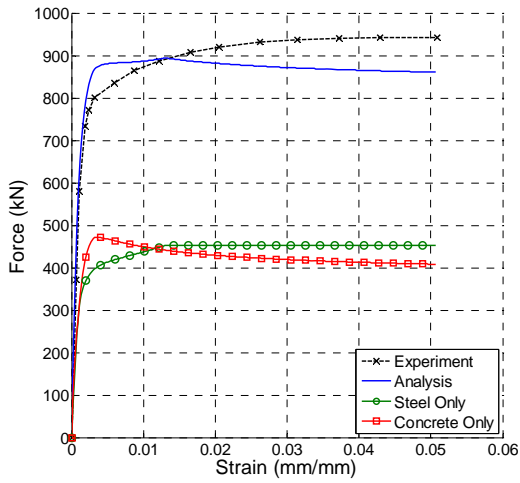


(k) Test #11; Yoshioka et al. 1995; Specimen: CC6-A-8

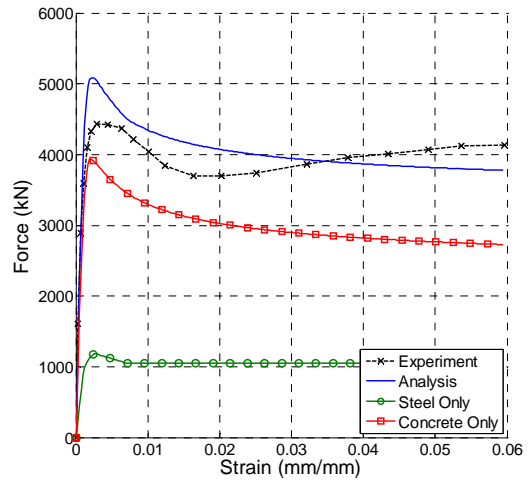


(l) Test #12; Giakoumelis & Lam 2004; Specimen: C8

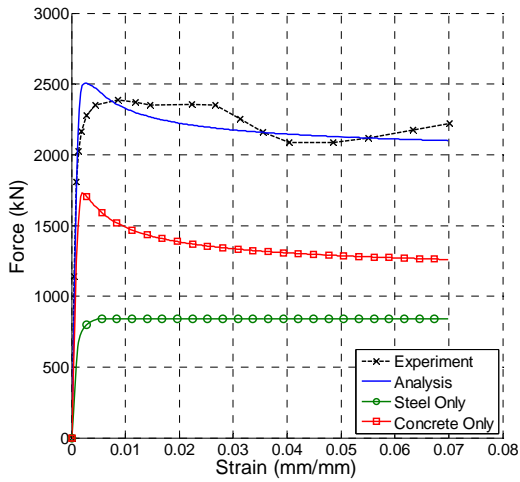
Figure 3-1. Experimental and Computational Results for the Calibration Set (continued)



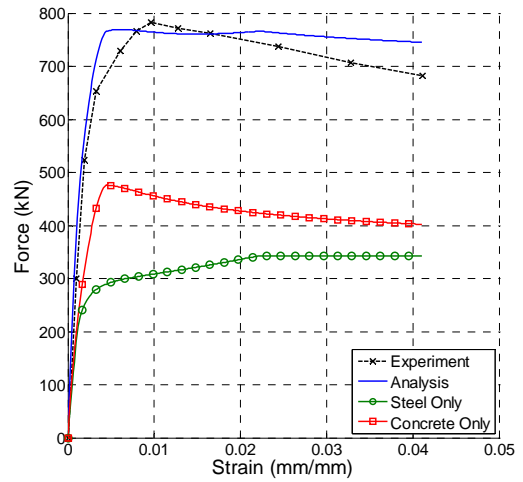
(m) Test #13; Yoshioka et al. 1995; Specimen: CC4-A-2



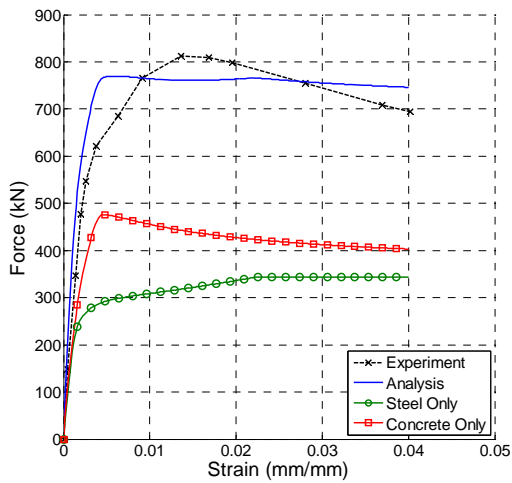
(n) Test #14; Yoshioka et al. 1995; Specimen: CC4-D-2



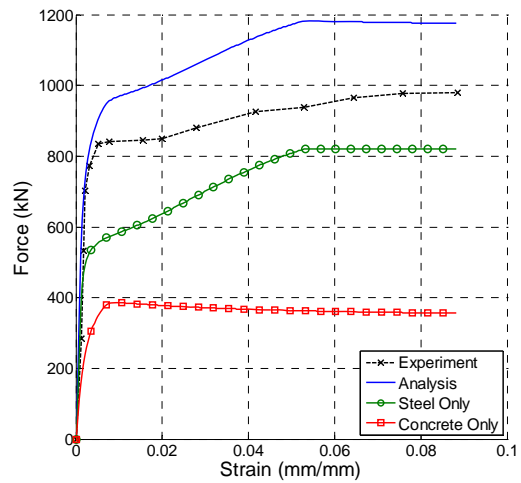
(o) Test #15; Yoshioka et al. 1995; Specimen: CC4-C-2



(p) Test #16; Han & Yao 2004; Specimen: scv1-1

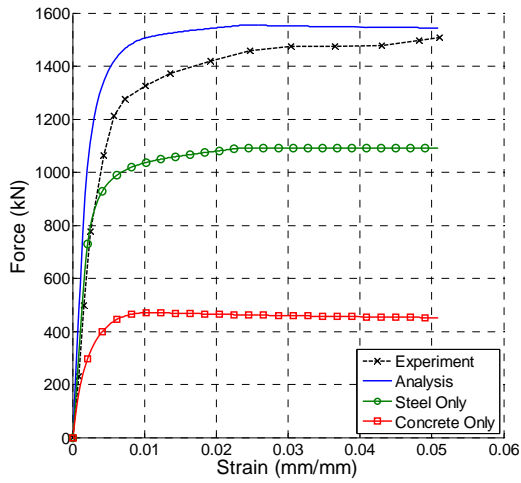


(q) Test #17; Han & Yao 2004; Specimen: sch1-2

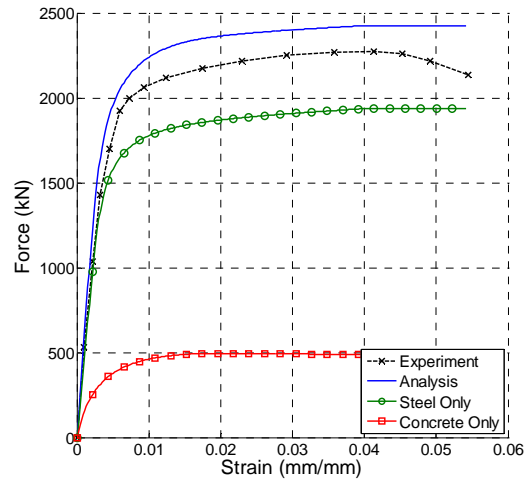


(r) Test #18; Sakino et al. 1985; Specimen: S6HA

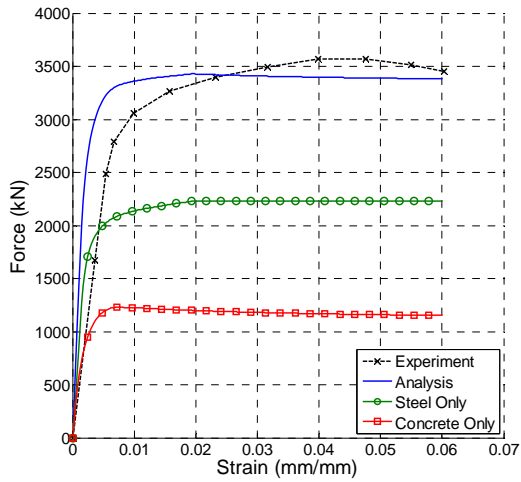
Figure 3-1. Experimental and Computational Results for the Calibration Set (continued)



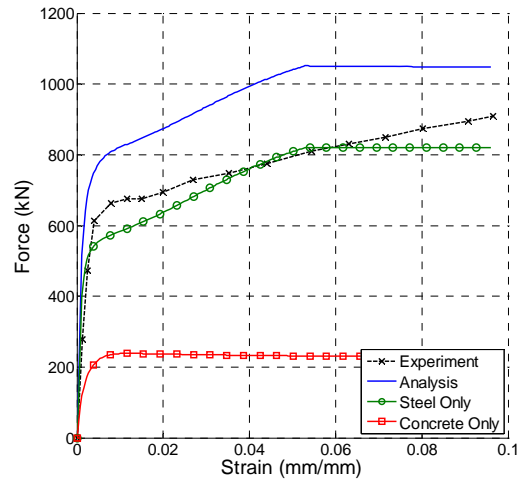
(s) Test #19; Yoshioka et al. 1995; Specimen: CC6-A-2



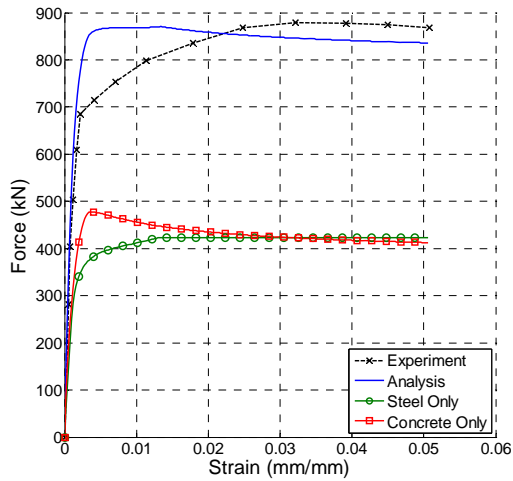
(t) Test #20; Yoshioka et al. 1995; Specimen: CC8-A-2



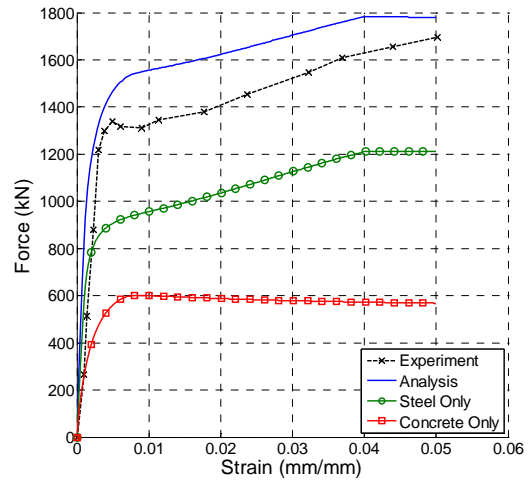
(u) Test #21; Yamamoto et al. 2002; Specimen: C20A-2A



(v) Test #22; Sakino et al. 1985; Specimen: S6LA



(w) Test #23; Schneider 1998; Specimen: C1



(x) Test #24; Schneider 1998; Specimen: C2

Figure 3-1. Experimental and Computational Results for the Calibration Set (continued)

Table 3.3. Comparison Metrics for the Calibration Set

Test #	Peak Load (kN)			Strain at Peak Load			Initial Stiffness (kN)			Area under Curve (kN)		
	Expt.	Model	% Error	Expt.	Model	% Error	Expt.	Model	% Error	Expt.	Model	% Error
1	5,595	5,353	-4.33%	0.007619	0.005430	-28.72%	1,460,760	2,237,170	53.15%	203.7	242.3	18.92%
2	11,508	10,834	-5.86%	0.005206	0.003369	-35.29%	3,768,710	5,079,650	34.78%	217.9	232.6	6.74%
3	13,701	13,201	-3.65%	0.009271	0.007957	-14.17%	4,861,980	4,430,050	-8.88%	449.1	456.5	1.64%
4	2,308	2,347	1.70%	0.003140	0.002602	-17.12%	987,422	1,218,750	23.43%	13.9	19.0	36.25%
5	3,054	3,116	2.03%	0.003640	0.002825	-22.39%	975,521	1,375,380	40.99%	17.3	21.5	24.08%
6	2,594	2,327	-10.27%	0.004463	0.002660	-40.41%	1,054,320	1,283,400	21.73%	21.9	22.5	3.07%
7	3,026	3,346	10.59%	0.019882	0.009343	-53.01%	1,110,050	1,583,010	42.61%	145.6	161.6	10.98%
8	5,613	5,260	-6.29%	0.016392	0.005115	-68.80%	2,813,470	3,437,460	22.18%	346.0	287.8	-16.84%
9	8,474	8,488	0.17%	0.046813	0.007825	-83.28%	2,968,040	2,961,300	-0.23%	547.5	520.9	-4.87%
10	2,707	2,897	7.02%	0.015714	0.039852	153.60%	711,501	676,921	-4.86%	153.4	166.0	8.22%
11	2,098	2,048	-2.39%	0.012205	0.013107	7.38%	469,392	715,519	52.44%	96.8	99.5	2.81%
12	1,791	1,755	-1.98%	0.011324	0.006764	-40.27%	207,103	693,536	234.88%	137.3	146.9	6.98%
13	942	894	-5.13%	0.050923	0.013036	-74.40%	524,671	665,931	26.92%	45.5	43.6	-4.21%
14	4,435	5,085	14.65%	0.002891	0.002387	-17.45%	5,809,640	4,722,070	-18.72%	235.2	239.4	1.78%
15	2,387	2,507	5.03%	0.008632	0.002526	-70.74%	2,670,210	2,280,600	-14.59%	155.1	152.4	-1.77%
16	782	770	-1.61%	0.009658	0.006093	-36.91%	295,798	409,731	38.52%	29.1	30.2	3.76%
17	812	770	-5.25%	0.013587	0.005952	-56.19%	260,592	409,882	57.29%	29.0	29.4	1.70%
18	979	1,183	20.78%	0.088620	0.052818	-40.40%	242,609	500,425	106.27%	79.8	96.1	20.36%
19	1,508	1,555	3.09%	0.051117	0.023923	-53.20%	319,284	579,386	81.46%	69.3	75.3	8.67%
20	2,275	2,426	6.66%	0.041310	0.039824	-3.60%	494,008	585,753	18.57%	113.7	122.4	7.63%
21	3,568	3,429	-3.89%	0.039868	0.019285	-51.63%	466,977	1,514,730	224.37%	193.0	198.2	2.65%
22	908	1,051	15.72%	0.096466	0.052863	-45.20%	202,772	460,596	127.15%	74.3	92.7	24.80%
23	878	871	-0.90%	0.032104	0.013418	-58.21%	522,327	576,608	10.39%	41.8	42.3	1.27%
24	1,696	1,784	5.20%	0.050174	0.040139	-20.00%	368,204	851,662	131.30%	71.9	80.9	12.53%
Mean			1.71%			-32.10%			54.21%			7.38%
Standard Deviation			7.78%			45.71%			67.47%			11.27%
Median			-0.37%			-40.34%			36.65%			5.25%

3.2.4 Size effect on the concrete compressive strength

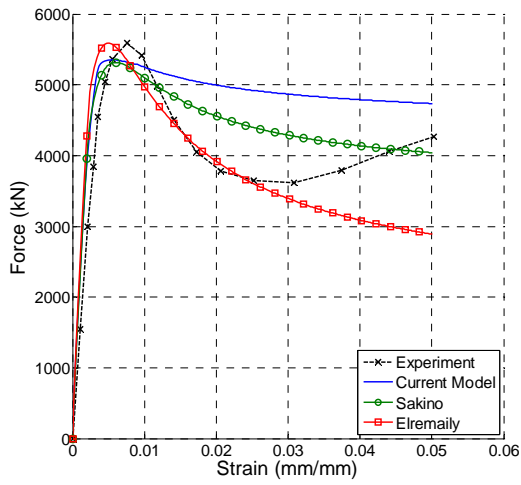
In the concrete material model proposed by Sakino et al. (2004) a factor was included to account for size effect on the concrete compressive strength. This factor was a power function of the diameter of the concrete core based on the test results of Blanks and McNamara (1935). The test specimens in this investigation were unreinforced and showed that compressive strength tends to decrease as the size of the specimen increases. However, it is expected that as confining stress is applied to the concrete the size effect is less than that of plain concrete and there is a reinforcement level at which the size effect is eliminated because the concrete will behave plastically (Kim et al. 1999). Kim et al. (1999) developed an equation for the strength of spirally reinforced concrete cylinders accounting for size effects and also proposed a limit at which size effects are mitigated. Applying this limit to CCFTs, by assuming zero spacing and using an equivalent area of transverse reinforcement, would result in the following limit at which the size effect is mitigated.

$$\frac{D}{t} < \frac{\alpha_0 8000}{f'_c [\text{MPa}]} + 2 \quad [3.16]$$

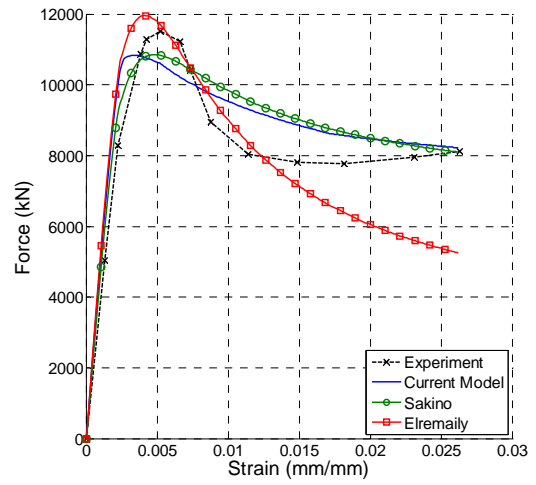
For normal strength concrete ($f'_c \approx 30\text{MPa}$), Equation 3.16 yields a D/t limit of approximately 24, with stockier tubes exhibiting no size effect and more slender tubes experiencing some. Noting that 24 is within the normal range of D/t ratios, albeit on the low end, applying a correction for size effect to CCFT members based on the results of experiments unconfined concrete may be inaccurate. Additionally, an experimental study by Yamamoto et al. (2002) on the concrete compressive strength of short CFT columns indicated that CCFT columns do not exhibit size effects. The range of column diameters considered in the study by Yamamoto et al. (2002) was approximately 100 mm to 450 mm. The calibration set presented in Section 3.2.1 contains a similar range of diameters. In current practice, however, it is common to have CCFT members with diameters ranging up to one to three meters (Roeder et al., 1999). This is in contrast to the ranges of steel yield strength, concrete compressive strength, and D/t ratio in the calibration set which better represent the range of material and geometric properties used in current practice. Without applicable experimental results over the range of material and geometric properties necessary to formulate an appropriate correction, size effect in CCFT members is neglected.

3.2.5 Comparison of Material Models

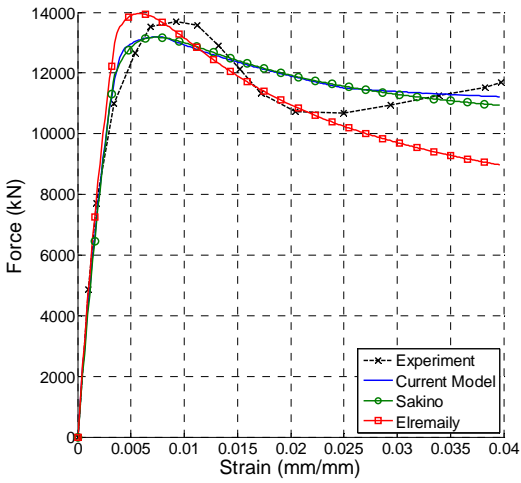
It is interesting to examine the difference between the proposed material model and two comprehensive material models developed in prior studies. Sakino et al. (2004) and Elremaily and Azizinamini (2002) developed constitutive relations for the steel tube and concrete core of CCFT members. Figure 3-2 shows experimental load deformation results for the 24 CCFT columns in the calibration set used previously. Computational results from the proposed model (including the steel model to be discussed in Chapter 4), the model developed by Sakino et al. (2004) (denoted “Sakino”) and the model developed by Elremaily and Azizinamini (2002) (denoted “Elremaily”) are overlaid.



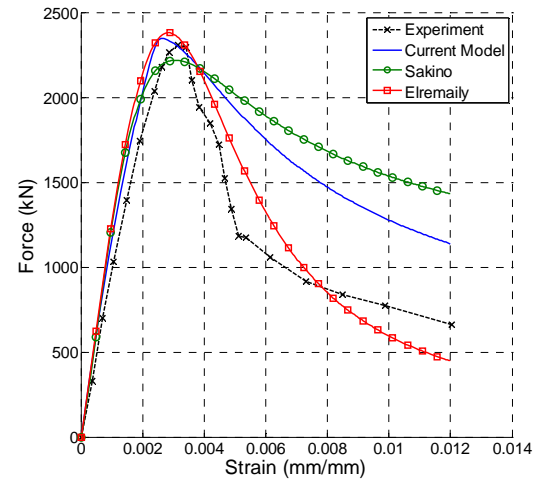
(a) Test #1; Yoshioka et al. 1995; Specimen: CC6-C-8



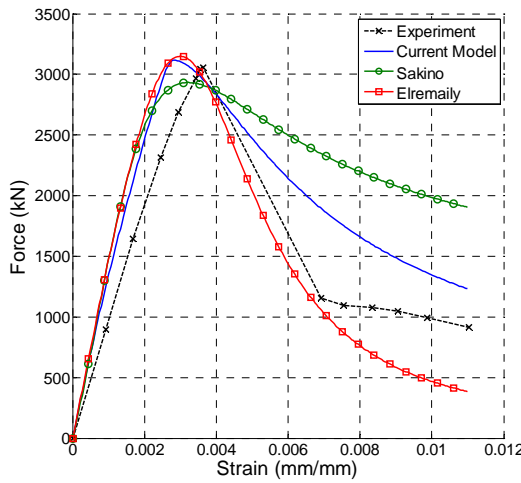
(b) Test #2; Yoshioka et al. 1995; Specimen: CC6-D-8



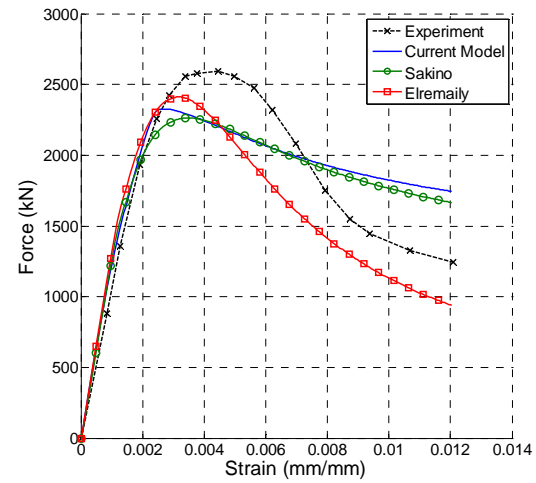
(c) Test #3; Yoshioka et al. 1995; Specimen: CC8-D-8



(d) Test #4; O'Shea & Bridge 2000; Specimen: S12CS80A

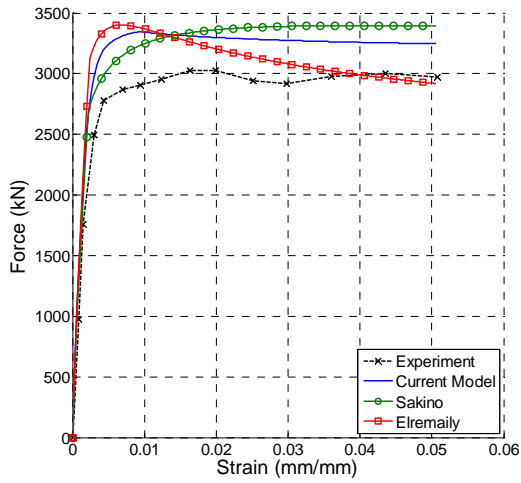


(e) Test #5; O'Shea & Bridge 2000; Specimen: S12CS10A

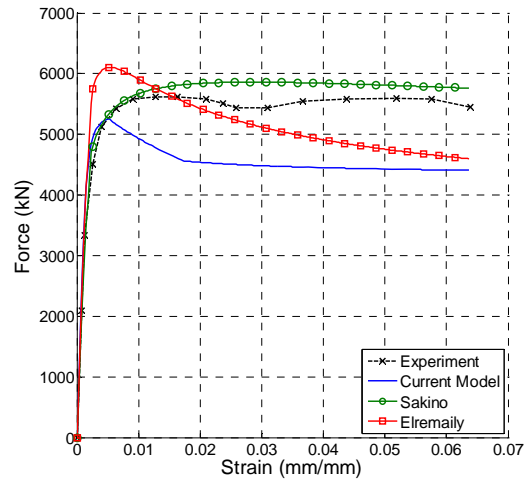


(f) Test #6; O'Shea & Bridge 2000; Specimen: S20CS80B

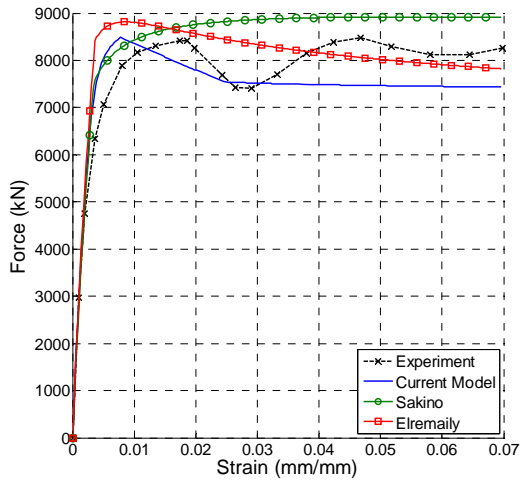
Figure 3-2. Comparison of Material Models for the Calibration Set



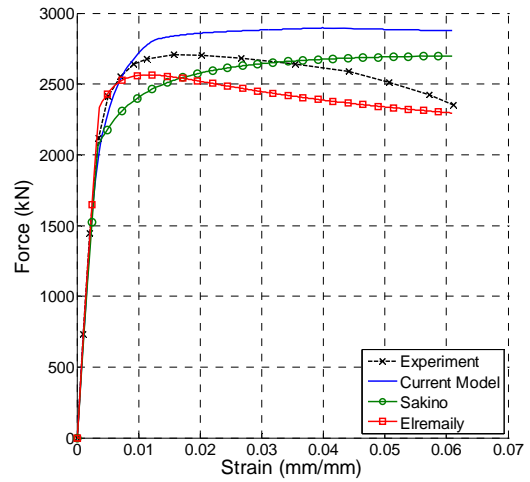
(g) Test #7; Yoshioka et al. 1995; Specimen: CC6-C-2



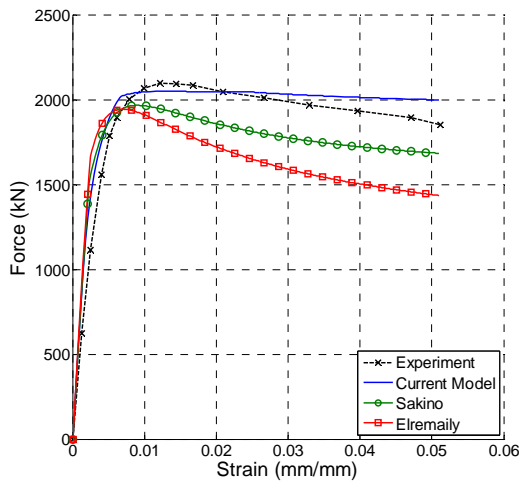
(h) Test #8; Yoshioka et al. 1995; Specimen: CC6-D-2



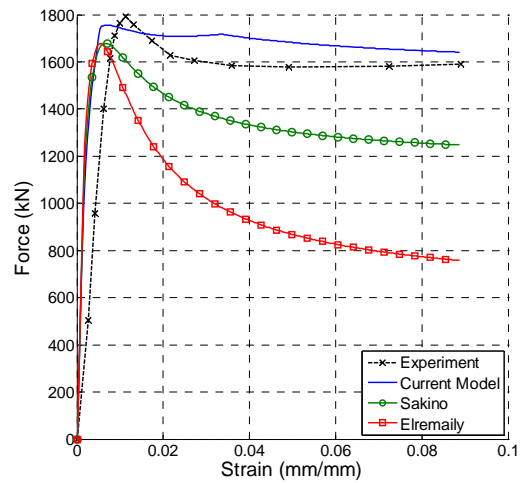
(i) Test #9; Yoshioka et al. 1995; Specimen: CC8-D-2



(j) Test #10; Yoshioka et al. 1995; Specimen: CC8-A-8

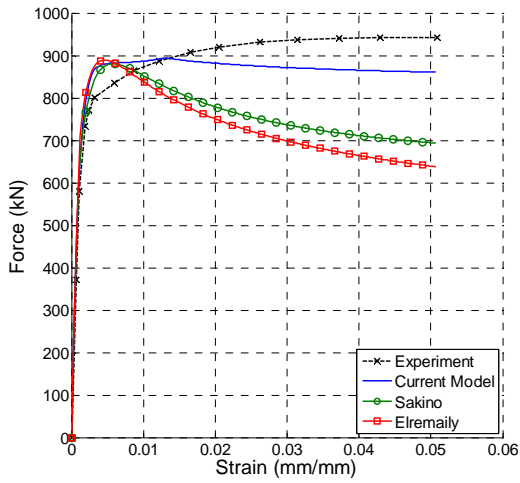


(k) Test #11; Yoshioka et al. 1995; Specimen: CC6-A-8

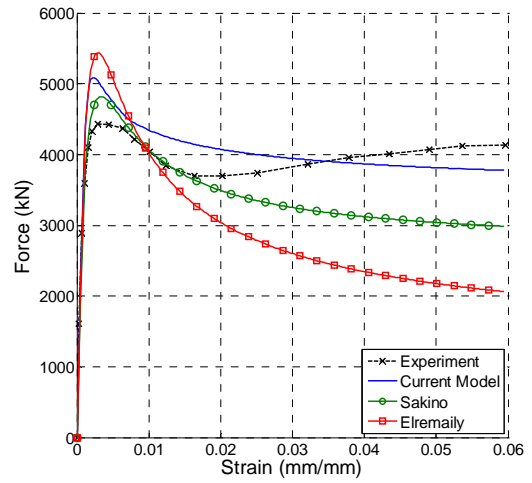


(l) Test #12; Giakoumelis & Lam 2004; Specimen: C8

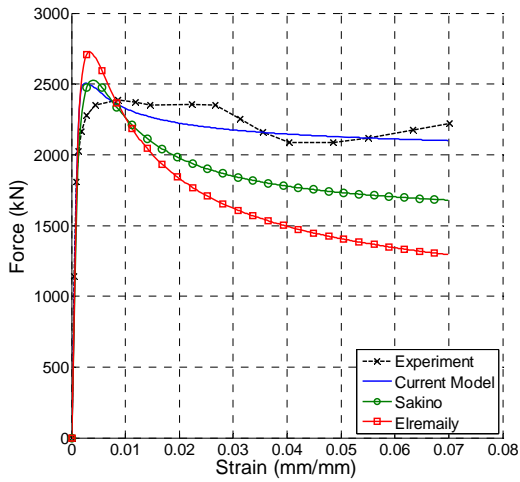
Figure 3-2. Comparison of Material Models for the Calibration Set (continued)



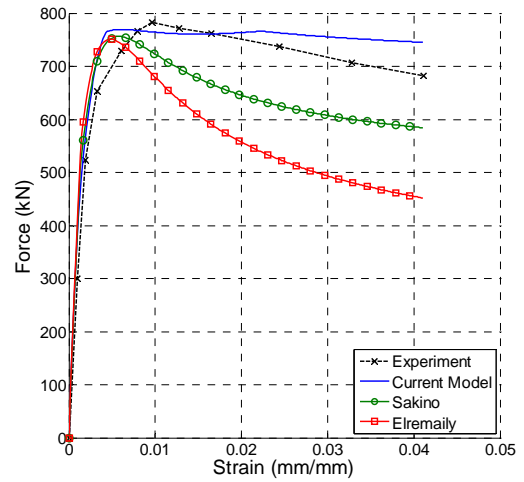
(m) Test #13; Yoshioka et al. 1995; Specimen: CC4-A-2



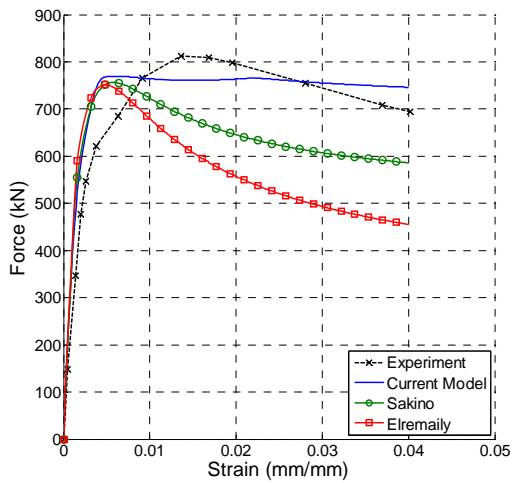
(n) Test #14; Yoshioka et al. 1995; Specimen: CC4-D-2



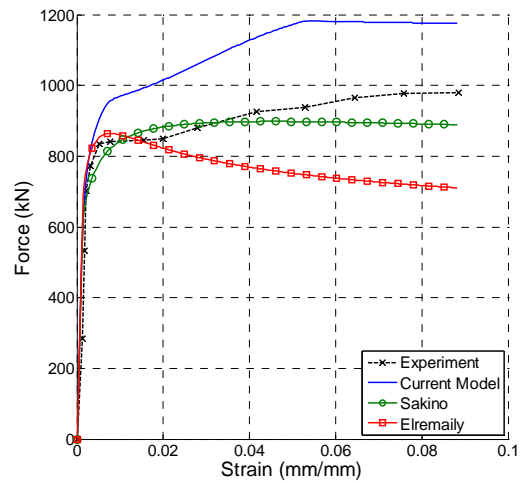
(o) Test #15; Yoshioka et al. 1995; Specimen: CC4-C-2



(p) Test #16; Han & Yao 2004; Specimen: scv1-1

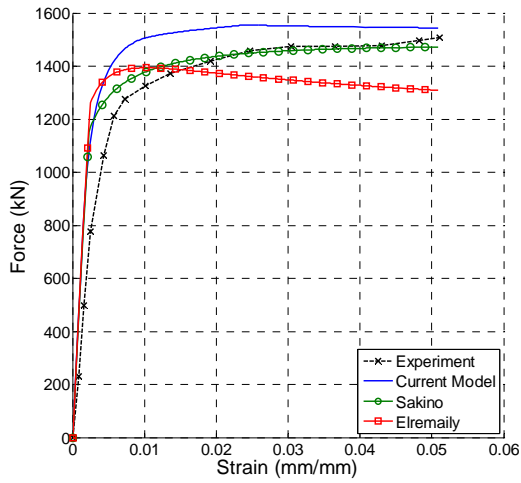


(q) Test #17; Han & Yao 2004; Specimen: sch1-2

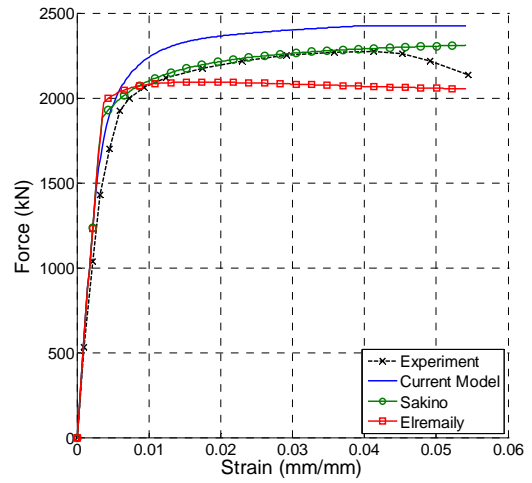


(r) Test #18; Sakino et al. 1985; Specimen: S6HA

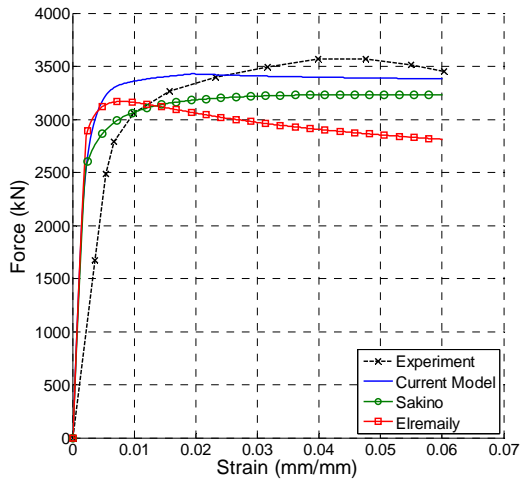
Figure 3-2. Comparison of Material Models for the Calibration Set (continued)



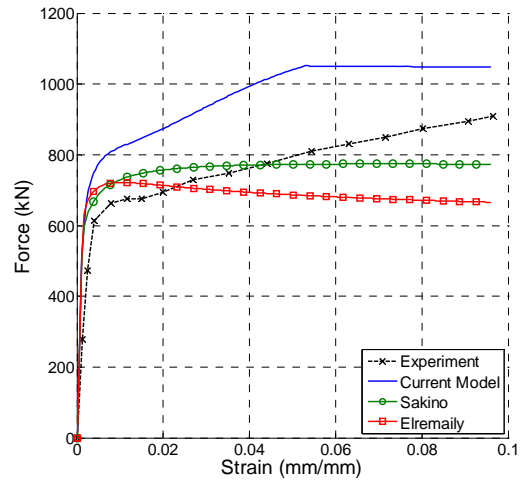
(s) Test #19; Yoshioka et al. 1995; Specimen: CC6-A-2



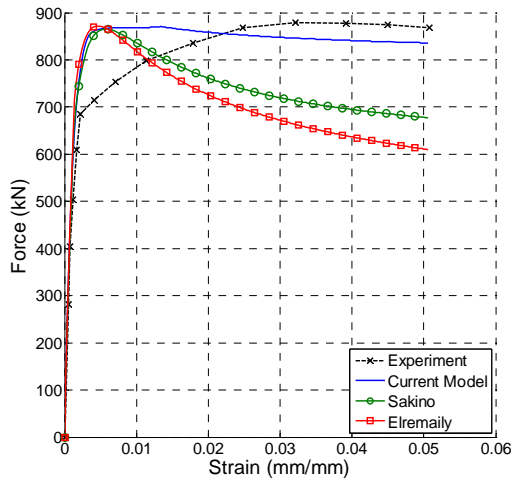
(t) Test #20; Yoshioka et al. 1995; Specimen: CC8-A-2



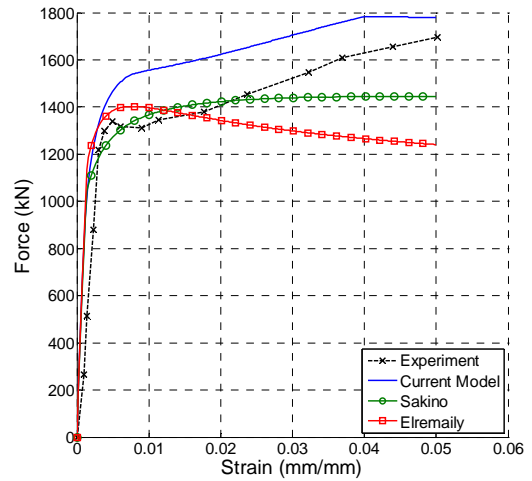
(u) Test #21; Yamamoto et al. 2002; Specimen: C20A-2A



(v) Test #22; Sakino et al. 1985; Specimen: S6LA



(w) Test #23; Schneider 1998; Specimen: C1



(x) Test #24; Schneider 1998; Specimen: C2

Figure 3-2. Comparison of Material Models for the Calibration Set (continued)

The comparison shows that the pre-peak response and peak load for all three models are similar. The major differences lie in the post-peak response where significant variation between models can be observed. In general, the model by Elremaily and Azizinamini (2002) shows the most post-peak descent, followed by the model developed by Sakino et al. (2004), and the current model. The lower descent observed in the current model is due to the fact that it is the only one, among the three, that models hardening in the steel tube, and that the post-peak parameter r was adjusted so that better correspondence is achieved with various loading cases, not just centrally-loaded short CCFT columns.

3.3 Monotonic Tensile Response

Many uniaxial constitutive relations for CCFT members neglect the tensile response of the concrete (Shams and Saadeghvaziri 1999; Susantha et al. 2001; Elremaily and Azizinamini 2002; Sakino et al. 2004; Hatzigeorgiou 2008). However, modeling the tensile response of concrete has been shown to improve the accuracy of nonlinear finite element models for composite members (Gourley and Hajjar 1994).

The shape of the stress-strain response of concrete in tension is similar to that of concrete in compression. Noting that, Chang and Mander (1994) recommended the using the same shape equations as the compressive response for the tensile response of concrete (Equations 3.1 through 3.3) but with different normalized variables (Equations 3.17 through 3.18).

$$x^+ = \left| \frac{\varepsilon_c - \varepsilon_o}{\varepsilon_t} \right| \quad [3.17]$$

$$n^+ = \frac{E_c f'_t}{\varepsilon_t} \quad [3.18]$$

$$\sigma^+ = f_t y \quad [3.19]$$

$$E^+ = E_c z \quad [3.20]$$

where, the “+”superscripts indicate that these values are applicable for the tensile response and the term ε_o is used to shift the tensile response as described later.

The initial tangent is taken as the elastic modulus. The peak tensile stress, strain at peak tensile stress, and post-peak parameter r follow recommendations by Tort and Hajjar (2007).

$$f'_t [\text{MPa}] = 0.5 \sqrt{f'_c [\text{MPa}]} \quad [3.21]$$

$$\varepsilon_t = 1.23 \frac{f'_t}{E_t} \quad [3.22]$$

$$r^+ = 4 \quad [3.23]$$

In contrast to the compressive response, which has non-zero stress for all compressive strains, the tensile response is assumed to reach a critical strain at which the material experiences linear degradation until zero stress is reached, at which point the concrete is said to have cracked and is no longer capable of sustaining tensile stress. Specifically, for tensile strains below the critical strain ($x^+ < x_{cr}^+$), the stress-strain response is modeled with the equation by Tsai as described above; for tensile strains between the critical strain and cracking strain ($x_{cr}^+ \leq x^+ < x_{crack}^+$) the stress-strain response is modeled by a linear equation (Equations 3.25 and 3.26); and for tensile strain greater than the cracking strain ($x^+ \geq x_{crack}^+$), the stress-strain response is zero.

$$x_{crack}^+ = x_{cr}^+ - \frac{y(x_{cr}^+)}{n^+ z(x_{cr}^+)} \quad [3.24]$$

$$\sigma = f_t \left[y(x_{cr}^+) + n^+ z(x_{cr}^+) (x^+ - x_{cr}^+) \right] \quad [3.25]$$

$$E = E_c z(x_{cr}^+) \quad [3.26]$$

3.4 Cyclic Response

3.4.1 Cyclic Rule Descriptions and Determination Process

The cyclic rule-based model of Chang and Mander (1994) is adopted in this work. It consists of three types of curves: envelope curves, connecting curves, and transition curves. Envelope curves are also referred to as the backbone of the cyclic response. Connecting curves represent the unloading and subsequent loading stress-strain path between envelope curves. Transition curves describe the path between connecting curves of opposite directions.

The stress-strain response of the envelope curves in tension and compression are described in previous sections. The stress-strain response for the connecting curves and transition curves, as will be seen, is described by the stress, strain, and tangent modulus at two states. An appropriate function to describe the stress-strain relationship would provide a continuous, smooth, and monotonic transition. Chang and Mander (1994) derive a smooth curve that monotonically transitions from one point and slope to another. This curve was used for all rules in the model with exception of the positive and negative envelopes and zero stress rules. This curve is defined by Equations 3.27 through 3.31. The definition of R (Equation 3.30) has been modified from the original to not allow the result of a negative number. If R is computed as negative, then a smooth transition is not possible without a change in curvature and the resulting stress-strain relation given by Equation 3.27 is not as intended. For this reason, R is limited to a minimum value of zero.

It should be noted that an R of zero reduces the nonlinear transition curve to a linear transition.

$$\sigma = \sigma_i + (\varepsilon - \varepsilon_i)[E_i + A] \quad [3.27]$$

$$E = E_i + (R + 1)A \quad [3.28]$$

$$A = (E_{sec} - E_i) \left| \frac{\varepsilon - \varepsilon_i}{\varepsilon_f - \varepsilon_i} \right|^R \quad [3.29]$$

$$R = \frac{E_f - E_{sec}}{E_{sec} - E_i} \geq 0 \quad [3.30]$$

$$E_{sec} = \frac{\sigma_f - \sigma_i}{\varepsilon_f - \varepsilon_i} \quad [3.31]$$

In the force recovery stage of the nonlinear analysis, the uniaxial strain of each fiber is updated. To determine the updated stress and tangent, a state determination process is performed that includes determination of the new rule and update of state variables. Each rule is described below:

Rule 0: The initial state of all material fibers is Rule 0. The fiber remains in this state until it is subjected to a non-zero strain at which point it transitions to either the tensile or compressive backbone curve depending on the sign of the strain. In this state, the stress is zero and the tangent is equal to the initial tangent.

Rule 1: The compressive envelope is described by Rule 1. In this state, the stress and strain follow the compressive backbone curve presented above.

Rule 2: The non-zero portion of the tensile envelope is described by Rule 2. In this state, the stress and strain follow the tensile backbone curve presented above.

Rule 3: Unloading from the compressive backbone (Rule 1) is described by Rule 3. Initiation of this rule is detected by a positive (towards tension) strain increment while on the compressive backbone curve. The stress-strain response of the material is described by the transition curve, which is defined by an initial and final stress, strain, and tangent. The initial stress and strain are equal to the stress and strain at the reversal from Rule 1. The initial tangent is taken as the elastic modulus. The final stress is taken as zero. The final strain (ε_{pl}^-) and tangent (E_{sec}^-) are computed based on the recommendations of Chang and Mander (1994).

$$E_{\text{sec}}^- = E_c \left(\frac{\left| \frac{f_{r1}}{E_c \varepsilon'_{cc}} \right| + 0.57}{\left| \frac{\varepsilon_{r1}}{\varepsilon'_{cc}} \right| + 0.57} \right) \quad [3.32]$$

$$E_{pl}^- = 0.1 E_c \exp \left(-2 \left| \frac{\varepsilon_{r1}}{\varepsilon'_{cc}} \right| \right) \quad [3.33]$$

$$\varepsilon_{pl}^- = \varepsilon_{r1} - \frac{f_{r1}}{E_{\text{sec}}^-} \quad [3.34]$$

where the subscript “ $r\#$ ” on the variables f (stress) and ε (strain) indicate that the variable represents the state at last reversal from Rule # (e.g., f_{r1} represents the stress at which the last reversal from Rule 1 occurred).

Rule 4: Unloading from the tensile backbone (Rule 2) is described by Rule 4. Initiation of this rule is detected by a negative (towards compression) strain increment while on the tension backbone curve. The stress-strain response of the material is described by the transition curve, which is defined by an initial and final stress, strain, and tangent. The initial stress and strain are equal to the stress and strain at the reversal from Rule 2. The initial tangent is taken as the elastic modulus. The final stress is taken as zero. The final strain (ε_{pl}^+) and tangent (E_{sec}^+) are computed based on the recommendations of Chang and Mander (1994).

$$E_{\text{sec}}^+ = E_c \left(\frac{\left| \frac{f_{r2}}{E_c \varepsilon_t} \right| + 0.67}{\left| \frac{\varepsilon_{r2} - \varepsilon_o}{\varepsilon_t} \right| + 0.67} \right) \quad [3.35]$$

$$E_{pl}^+ = \frac{E_c}{\left| \frac{\varepsilon_{r2} - \varepsilon_o}{\varepsilon_t} \right|^{1.1} + 1} \quad [3.36]$$

$$\varepsilon_{pl}^+ = \varepsilon_{r2} - \frac{f_{r2}}{E_{\text{sec}}^+} \quad [3.37]$$

Rule 6: The zero valued portion of the tensile envelope is described by Rule 6. In this state, the stress and tangent are equal to zero. Upon reaching this Rule, the material is said to have cracked.

Rule 7: A return to the compressive backbone curve is defined by Rule 7. The response of Rule 7 depends on whether it was arrived at after a full reversal (from Rule 10) or after a partial reversal (from Rule 16). Thus, the initial stress and tangent, as well as the final stress, for this rule are computed upon a reversal from the compressive envelope (Rule 1) and updated if a partial reversal (i.e., a reversal from Rule 3) occurs. In either case, the initial strain is equal to the reversal strain from Rule 1, ε_{r1} , and the final stress and tangent lie on the compressive envelope, which is determined based on the final strain. The following is computed upon a reversal from Rule 1.

$$\Delta f^- = 0.09 f_{r1} \sqrt{\left| \frac{\varepsilon_{r1}}{\varepsilon'_{cc}} \right|} \quad [3.38]$$

$$\Delta \varepsilon^- = \frac{\varepsilon_{r1}}{1.15 + 2.75 \left| \frac{\varepsilon_{r1}}{\varepsilon'_{cc}} \right|} \quad [3.39]$$

$$f_{new}^- = f_{r1} - \Delta f^- \quad [3.40]$$

$$\varepsilon_{re}^- = \varepsilon_{r1} + \Delta \varepsilon^- \quad [3.41]$$

$$E_{new}^- = \frac{f_{new}^-}{\varepsilon_{r1} - \varepsilon_{pl}^-} \quad [3.42]$$

where f_{new}^- and E_{new}^- are the initial stress and tangent respectively and ε_{re}^- is the final stress of Rule 7 if arrived at from a full reversal.

The following is computed upon a reversal from Rule 3 (i.e., a partial reversal)

$$f_{new*}^- = f_{r1} - \Delta f^- \left(\frac{\varepsilon_{r1} - \varepsilon_{r3}}{\varepsilon_{r1} - \varepsilon_{pl}^-} \right) \quad [3.43]$$

$$\varepsilon_{re*}^- = \varepsilon_{r1} + \Delta \varepsilon^- \left(\frac{\varepsilon_{r1} - \varepsilon_{r3}}{\varepsilon_{r1} - \varepsilon_{pl}^-} \right) \quad [3.44]$$

$$E_{new*}^- = \frac{f_{new*}^- - f_{r3}}{\varepsilon_{r1} - \varepsilon_{r3}} \quad [3.45]$$

where f_{new*}^- and E_{new*}^- are the initial stress and tangent respectively and ε_{re*}^- is the final stress of Rule 7 if arrived at from a partial reversal.

Rule 8: A return to the tension backbone curve is defined by Rule 8. The response of Rule 8 depends on whether it was arrived at after a full reversal (from Rule 9) or after a partial reversal (from Rule 17). Thus, the initial stress and tangent, as well as the final stress, for this rule are computed upon a reversal from the tension envelope (Rule 2) and updated if a partial reversal (i.e., a reversal from Rule 4) occurs. In either case, the initial strain is equal to the reversal strain from Rule 2, ε_{r2} , and the final stress and tangent lie on the tension envelope, which is determined based on the final strain. The following is computed upon a reversal from Rule 2.

$$\Delta f^+ = 0.15 f_{r2} \quad [3.46]$$

$$\Delta \varepsilon^+ = 0.22 \varepsilon_{r2} \quad [3.47]$$

$$f_{new}^+ = f_{r2} - \Delta f^+ \quad [3.48]$$

$$\varepsilon_{re}^+ = \varepsilon_{r2} + \Delta \varepsilon^+ \quad [3.49]$$

$$E_{new}^+ = \frac{f_{new}^+}{\varepsilon_{r2} - \varepsilon_{pl}^+} \quad [3.50]$$

where f_{new}^+ and E_{new}^+ are the initial stress and tangent respectively and ε_{re}^+ is the final stress of Rule 8 if arrived at from a full reversal.

The following is computed upon a reversal from Rule 4 (i.e., a partial reversal)

$$f_{new*}^+ = f_{r2} - \Delta f^+ \left(\frac{\varepsilon_{r2} - \varepsilon_{r2}}{\varepsilon_{r2} - \varepsilon_{pl}^+} \right) \quad [3.51]$$

$$\varepsilon_{re*}^+ = \varepsilon_{r2} + \Delta \varepsilon^+ \left(\frac{\varepsilon_{r2} - \varepsilon_{r4}}{\varepsilon_{r2} - \varepsilon_{pl}^+} \right) \quad [3.52]$$

$$E_{new*}^+ = \frac{f_{new*}^+ - f_{r4}}{\varepsilon_{r2} - \varepsilon_{r4}} \quad [3.53]$$

where f_{new*}^+ and E_{new*}^+ are the initial stress and tangent respectively and ε_{re*}^+ is the final stress of Rule 8 if arrived at from a partial reversal.

Rule 9: Loading in the tension region after a full unloading from compression is defined by Rule 9. The starting stress, strain, and tangent are the final stress, strain, and tangent from the compression unloading (Rule 3). The final stress, strain, and tangent are either taken as calculated upon unloading from Rule 2 for a full reversal or recomputed as described in the following. The criteria for recomputing is expressed in Equation 3.54.

$$\frac{\varepsilon_{r2} - \varepsilon_o}{\varepsilon_t} < \frac{\varepsilon_{r1}}{\varepsilon'_{cc}} \quad [3.54]$$

If a recomputation is necessary, the process is as described in Equations 3.46 through 3.50, but using a value of ε_{r2} given by Equation 3.55.

$$\varepsilon_{r2} = \varepsilon_{r1} \frac{\varepsilon_t}{\varepsilon'_{cc}} \quad [3.55]$$

Rule 10: Loading in the compression region after a full unloading from tension is defined by Rule 10. The starting stress, strain, and tangent are the final stress, strain, and tangent from the tension unloading (Rule 4). The final stress, strain, and tangent are taken as calculated upon unloading from Rule 1 for a full reversal.

Rule 11: The transition between reloading in the tension range (Rule 9) and reloading in the compression range (Rule 10) is defined by Rule 11. The initial stress and strain are defined as the unloading stress and strain from Rule 9. The initial tangent is taken as the elastic modulus. The final strain is given by Equation 3.56.

$$\varepsilon_b = \varepsilon_{r1} - (\varepsilon_{r1} - \varepsilon_{pl}^+) \left(\frac{\varepsilon_{r9} - \varepsilon_{pl}^-}{\varepsilon_{r2} - \varepsilon_{pl}^-} \right) \quad [3.56]$$

The final stress and tangent are the stress and tangent corresponding to the final strain on Rule 10.

Rule 12: The transition between reloading in the compression range (Rule 10) and reloading in the tension range (Rule 9) is defined by Rule 12. The initial stress and strain are defined as the unloading stress and strain from Rule 10. The initial tangent is taken as the elastic modulus. The final strain is given by Equation.

$$\varepsilon_a = \varepsilon_{pl}^- + (\varepsilon_{r2} - \varepsilon_{pl}^-) \left(\frac{\varepsilon_{r1} - \varepsilon_{r10}}{\varepsilon_{r1} - \varepsilon_{pl}^+} \right) \quad [3.57]$$

The final stress and tangent are the stress and tangent corresponding to the final strain on Rule 9.

Rule 13: Reloading in compression from zero stress after cracking has occurred (Rule 6) is defined by Rule 13. The initial stress, strain, and tangent are equal to their values upon reversal from Rule 6. The final stress, strain, and tangent are the values computed upon the last unloading from the compression envelope.

Rule 14: Unloading from the compressive reloading curve (Rule 13) post-cracking is described by Rule 14. The initial stress, strain, and tangent are equal to their values upon reversal from Rule 13. The final stress and tangent taken as zero, while the final strain is computed as in Equation 3.58.

$$\varepsilon_b = \varepsilon_{r13} - \frac{f_{r13}}{E_{\text{sec}}} \quad [3.58]$$

Rule 15: Reloading from the unloading curve (Rule 14) from the compressive reloading curve (Rule 13) post-cracking is described by Rule 15. The initial stress, strain, and tangent are equal to their values upon reversal from Rule 14. The final stress, strain, and tangent values are taken as the stress, strain, and tangent upon unloading from Rule 13.

Rule 16: Reloading from the unloading curve (Rule 3) from the compressive envelope is defined by Rule 16. In the work of Chang and Mander (1994) this rule was treated as a branch of Rule 7. The initial stress and strain are taken at their values upon reversal from Rule 3. The initial tangent is taken as the elastic modulus. The final strain is equal to the strain at reversal from the compression envelope. The final stress and tangent are as calculated in Equations 3.43 and 3.45 respectively.

Rule 17: Reloading from the unloading curve (Rule 4) from the tension envelope is defined by Rule 17. In the work of Chang and Mander (1994) this rule was treated as a branch of Rule 8. The initial stress and strain are taken at their values upon reversal from Rule 4. The initial tangent is taken as the elastic modulus. The final strain is equal to the strain at reversal from the compression envelope. The final stress and tangent are as calculated in Equations 3.51 and 3.53 respectively.

A summary of the initial and final strains used in the transition curve for each of the rules is given in Table 3.4.

Table 3.4. Summary of Initial and Final Rule Values

Rule	Strain	Initial Stress	Tangent	Strain	Final Stress	Tangent
0			$\sigma = 0, E = E_c$			
1			Compression Envelope			
2			Tension Envelope			
3	ε_{r1}	f_{r1}	E_c	ε_{pl}^-	0	E_{pl}^-
4	ε_{r2}	f_{r2}	E_c	ε_{pl}^+	0	E_{pl}^+
6			$\sigma = 0, E = 0$			
7	ε_{r1}	f_{new}^- or f_{new*}^-	E_{new}^- or E_{new*}^-	ε_{re}^- or ε_{re*}^-	Computed from final strain	
8	ε_{r2}	f_{new}^+ or f_{new*}^+	E_{new}^+ or E_{new*}^+	ε_{re}^+ or ε_{re*}^+	Computed from final strain	
9	ε_{pl}^-	0	E_{pl}^-	ε_{r2}	f_{new}^+	E_{new}^+
10	ε_{pl}^+	0	E_{pl}^+	ε_{r1}	f_{new}^-	E_{new}^-
11	ε_{r9}	f_{r9}	E_c	ε_b	Computed from final strain	
12	ε_{r10}	f_{r10}	E_c	ε_a	Computed from final strain	
13	ε_{r6}	0	0	ε_{r1}	f_{new}^-	E_{new}^-
14	ε_{r13}	f_{r13}	E_c	ε_b	0	0
15	ε_{r14}	f_{r14}	E_c	ε_a	Computed from final strain	
16	ε_{r3}	f_{r3}	E_c	ε_{r1}	f_{new*}^-	E_{new*}^-
17	ε_{r4}	f_{r4}	E_c	ε_{r2}	f_{new*}^+	E_{new*}^+

3.4.2 Shifting of the Tensile Envelope

Before cracking has occurred and upon reversals from the compressive envelope, the tensile envelope is shifted such that tensile stress is achieved immediately after the compressive stress vanishes upon unloading. The shift is defined by a single parameter, ε_o , and is calculated as follows. Two different methods are employed depending on the whether the criteria of Equation 3.54 is satisfied. If the criteria is satisfied, then a new value for ε_{r2} is forced and new points are calculated just as if a reversal from Rule 2 has occurred, the value of ε_o is reset as in Equation 3.59.

$$\varepsilon_o = \varepsilon_{pl}^- - \varepsilon_{r2} + \frac{2f_{r2}}{E_{sec}^+ + E_{pl}^+} \quad [3.59]$$

If the criteria of Equation 3.54 is not satisfied, the change in the parameter describing the shift of the tensile branch is computed as in Equation 3.60.

$$\Delta \varepsilon_o = \varepsilon_{pl}^- - \varepsilon_{r2} + \frac{2f_{r2}}{E_{sec}^+ + E_{pl}^+} \quad [3.60]$$

For both cases, it is necessary for continuity to shift all referenced strains (e.g., ε_{r2} , ε_a , etc.) by the change in value of ε_o .

UNIAXIAL CYCLIC STEEL CONSTITUTIVE MODEL FOR CCFT MEMBERS

4.1 Introduction

Experimental research on CCFT members have exhibited several features that can be attributed to the cyclic response of the steel tube. These features include: elastic unloading following a load reversal, decreasing elastic zone, and local buckling of the steel tube (Gourley et al. 2008). The ability of the constitutive relation to capture these effects these is thus important. Effects from the cold-forming process of the steel tubes should also be included in a comprehensive constitutive relation, notably the smooth transaction between elastic and plastic response, rather than the formation of a significant yield plateau. In this work, fracture of the steel tube is neglected, as it typically does not occur until very late in loading histories.

Constitutive models recommended for CCFT in prior studies have often consisted of simple elastic-perfectly plastic or hardening models shifted for the effect of biaxial stress (Elremaily and Azizinamini 2002; Sakino et al. 2004; Hatzigeorgiou 2008). These effectively ignore any effect of residual stress or local buckling.

Constitutive relations may be derived either as explicit functions of stress and strain, as the concrete constitute relation was derived in the previous chapter. Alternatively, the relation may be derived based on a set of hardening and flow rules that act on the incremental strain. A tangent stiffness is computed based on the incremental strain, material parameters, and state variables that depend on the prior loading history. The latter option is used as the basis for the proposed steel constitutive relation.

4.2 Plasticity Model

The steel constitutive relation is formulated in an incremental form based on a bounding surface plasticity formulation by Shen et al. (1995).

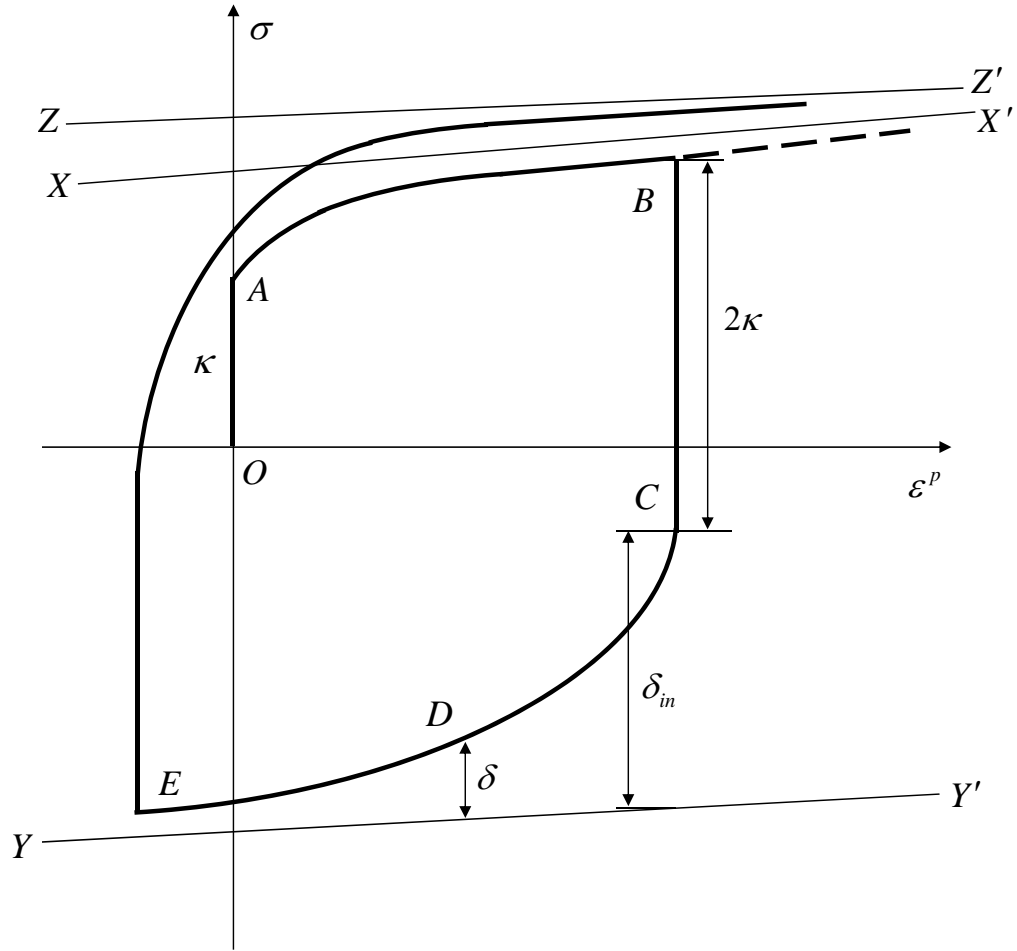


Figure 4-1. Uniaxial Cyclic Stress-Plastic Strain Curve

The total strain increment is decomposed into an elastic component and plastic component (Equation 4.1).

$$\Delta \varepsilon^t = \Delta \varepsilon^e + \Delta \varepsilon^p \quad [4.1]$$

The stress increment is defined as the product of the strain increment and a modulus (Equations 4.2 through 4.4). The appropriate modulus depends on which component (elastic, plastic, or total) of the strain is utilized. Further, the tangent modulus, E^t , may be written in terms of the elastic modulus, E^e , and the plastic modulus, E^p , (Equation 4.5).

$$\Delta \sigma = E^t \Delta \varepsilon^t \quad [4.2]$$

$$\Delta \sigma = E^e \Delta \varepsilon^e \quad [4.3]$$

$$\Delta \sigma = E^p \Delta \varepsilon^p \quad [4.4]$$

$$E^t = \frac{E^p E^e}{E^p + E^e} \quad [4.5]$$

The elastic component is assumed to hold a linear relationship (Equation 4.6).

$$\sigma = E^e \varepsilon^e \quad [4.6]$$

When the stress lies within the elastic range, the tangent modulus is assumed to be equal to the elastic modulus (the plastic modulus is taken as infinity). The size of the elastic range is described by Equation 4.7.

$$\frac{\kappa}{\kappa_o} = \alpha - a \exp(-100b\bar{\varepsilon}^p) - (\alpha - a - 1) \exp(-100c\bar{\varepsilon}^p) \quad [4.7]$$

where, κ is the half of the current size of the elastic range; κ_o is half the initial size of the elastic range, taken as the yield strength of the steel (F_y); $\bar{\varepsilon}^p$ is the effective plastic strain range, defined as the difference between the maximum and minimum plastic strains the material has experienced; and α, a, b, c are material constants,

If the stress lies outside of the elastic range, the plastic modulus takes a finite value given by Equations 4.8 and 4.9.

$$E^p = E_o^p + h \frac{\delta}{\delta_{in} - \delta} \quad [4.8]$$

$$h = e\delta + f \quad [4.9]$$

where, E_o^p is the slope of the bounding line; δ is the distance between the bounding surface and the current (loading) point; δ_{in} is the value of δ at the point of initial yield in the current loading path; and e and f , are material constants.

The bounding line does not remain constant throughout the strain history. The slope of the bounding line is assumed to decrease with the plastic work (Equation 4.10).

$$E_o^p = \frac{E_{oi}^p}{1 + \omega W^p} \quad [4.10]$$

where, E_{oi}^p is the initial slope of the bounding line, a material constant; W^p is the plastic work (Equation 4.11); and ω is a material constant.

$$W^p(t) = \int_0^t \sigma(s) \varepsilon^p(s) ds \quad [4.11]$$

where, t is a time parameter and s is the variable of integration. Equation 4.11 is computed as the sum of the product of the stress and change in plastic strain for all previous steps.

Further, the position of the bounding is assumed to increase with plastic strain (Equation 4.12).

$$\bar{\kappa} = \bar{\kappa}_\infty + (\bar{\kappa}_o - \bar{\kappa}_\infty) \exp(-\zeta \rho^2) \quad [4.12]$$

where, $\bar{\kappa}$ is the current size of the bounding line; $\bar{\kappa}_\infty$ is the limiting value of the bounding line, taken at the ultimate tensile strength of the steel (F_u); $\bar{\kappa}_o$ is the initial size of the bounding line, a material constant; ρ is half of the effective plastic strain range ($\frac{1}{2}\bar{\varepsilon}^p$); and ζ is a material constant.

For better correlation to cyclic behavior that does not include full reversals, the virtual bounding line and memory line are introduced (Figure 4-2).

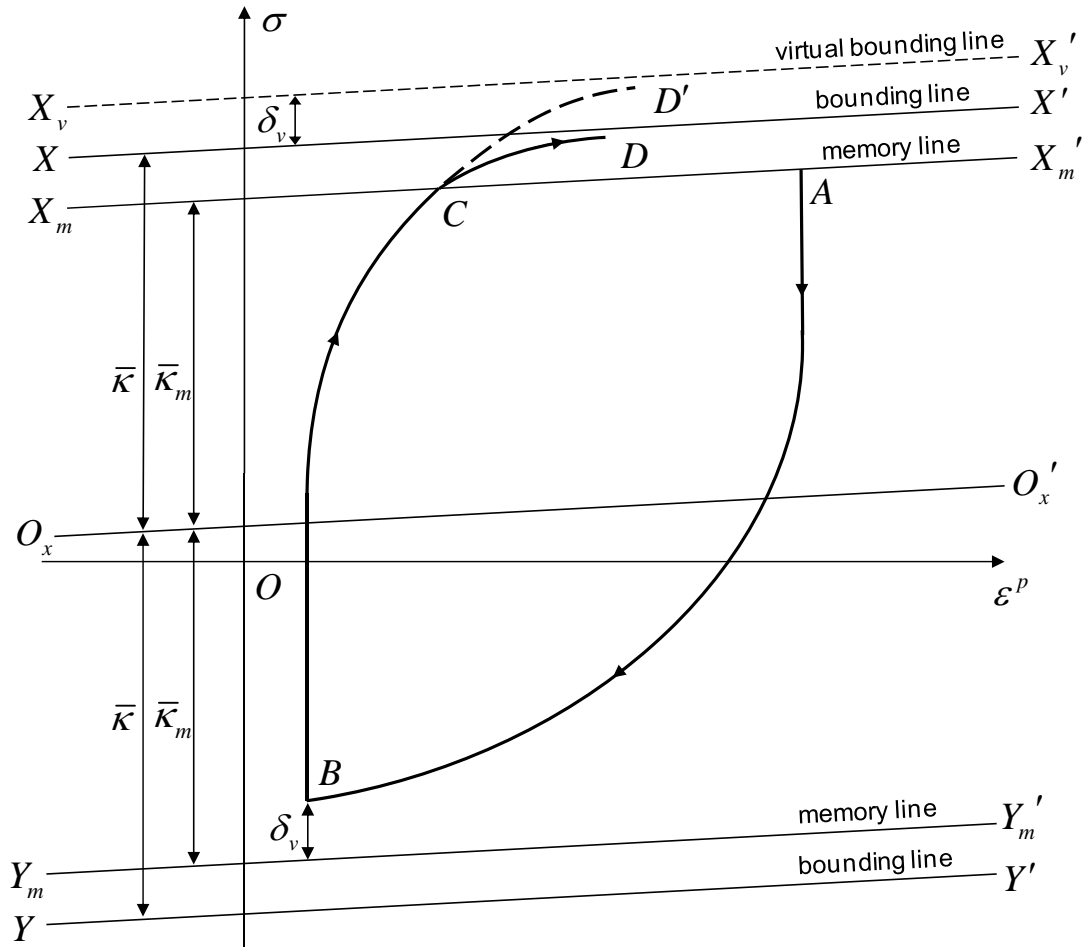


Figure 4-2. Definition of Virtual Bounding Line and Memory Line

Both the virtual bounding line and the memory line are assumed to lie parallel to the bounding line. The initial size of the memory line is taken as the yield strength of the steel and the size grows symmetrically with the loading point (i.e., the size of the memory line is the largest stress attained by the material). If a loading path reverses before

reaching the memory line (e.g., Point B in Figure 4-2), the virtual bounding line is created outside the bounding line by the same amount the loading path was short of the memory line (e.g., line $X_v-X'_v$ in Figure 4-2). Along the reversed path, until the memory line on the opposite side is reached (e.g., Point C in Figure 4-2), the plastic modulus is computed with respect to the virtual bounding line, not the bounding line, as described by Equation 4.13, where δ_v is the distance between the virtual bounding line and the bounding line.

$$E^p = E_o^p + h \frac{\delta + \delta_v}{\delta_{in} - \delta} \quad [4.13]$$

This section describes the uniaxial bounding surface model as proposed by Shen et al. (1995) for structural steel. As discussed in Sections 4.2.2, 4.2.3 and 4.3, modifications to this model were made to better describe the stress-strain response of cold-formed circular steel tubes used in CCFT members.

4.2.1 Material Properties

The material parameters required for the steel material model are given in Table 4.1 as reported in Mamaghani et al. (1996) with minor changes as noted later.

Table 4.1. Steel Model Material Parameters

Parameter	$F_y \leq 357 \text{ MPa}$	$357 \text{ MPa} < F_y \leq 524 \text{ MPa}$	$F_y \geq 524 \text{ MPa}$
$\bar{\kappa}_o$	$1.06 F_y$	$1.06 F_y$	$1.06 F_y$
a	-0.505	-0.528	-0.553
b	2.17	1.88	6.47
c	14.4	18.7	34.8
e	500	316	300
f	$0.300 E^e$	$0.484 E^e$	$0.361 E^e$
α	0.191	0.217	0.175
w	$3.08 / F_y$	$4.00 / F_y$	$2.67 / F_y$
E_{oi}^p	$8.96 \times 10^{-3} E^e$	$1.01 \times 10^{-2} E^e$	$7.85 \times 10^{-3} E^e$
ζ	$9.89 \times 10^{-4} / \varepsilon_y^2$	$1.52 \times 10^{-3} / \varepsilon_y^2$	$8.04 \times 10^{-3} / \varepsilon_y^2$

The majority of experimental reporting includes documentation of the ultimate strength of steel tube. For the cases for which it is not reported, an empirical relation was developed to estimate the ultimate strength. This relation (Equation 4.14) was based on the yield strength and ultimate strength reported for steel tubes from other CCFT members.

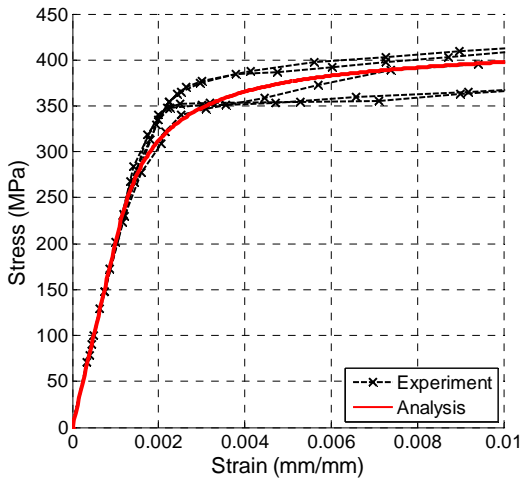
$$F_u = F_y \left(1 + 7.306 F_y [\text{MPa}]^{-1.674} \right) \quad [4.14]$$

4.2.2 Initial Plastic Strain

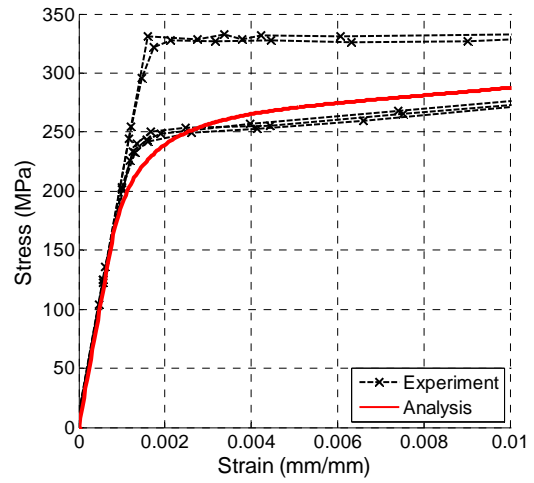
Due to the residual stresses generated during fabrication, cold-formed steel tubes have a low proportional limit with no distinct yield plateau or transition region to hardening. In this study, as in the prior studies of Tort and Hajjar (2007) and Hajjar et al. (1998) an initial plastic strain, ε^p_o , is used to model the effect of the cold-forming process. A value of $\varepsilon^p_o = 0.0006$ provides the best fit a suite of tensile tests performed on coupons cut from circular steel tubes (Table 4.2 and Figure 4-3). Also, to better match the tensile coupon tests and to be consistent with the typical 0.2% offset definition of yield, the value of the size of the initial bounding lines was taken as $1.06 F_y$ for the entire range of materials considered. This is in contrast to the values reported by Mamaghani et al. (1996), who used alternative values that varied between grades of steel and were based on experimental results.

Table 4.2. Material Properties of Tensile Coupon Tests

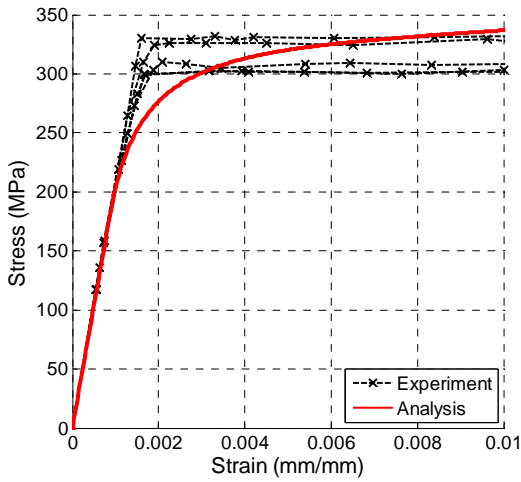
Test #	Author	Year	Specimen	F_y (MPa)	F_u (MPa)	E_s (MPa)
1	Bridge & O'Shea	1997	165x3.0	363.3	466.9	200,600
2	Bridge & O'Shea	1997	190x2.0	252.4	368.4	204,500
3	Bridge & O'Shea	1997	190x1.6	303.4	380.2	206,600
4	Bridge & O'Shea	1997	190x1.2	185.7	307.6	178,400
5	Bridge & O'Shea	1997	190x1.2"R"	203.1	299.0	188,300
6	Bridge & O'Shea	1997	190x1.0	210.7	322.1	177,000
7	Marson & Bruneau	2000	CFST 64	449.0	562.0	199,700
8	Marson & Bruneau	2000	CFST 34	415.0	515.0	177,500
9	Marson & Bruneau	2000	CFST 42	505.0	595.0	228,801



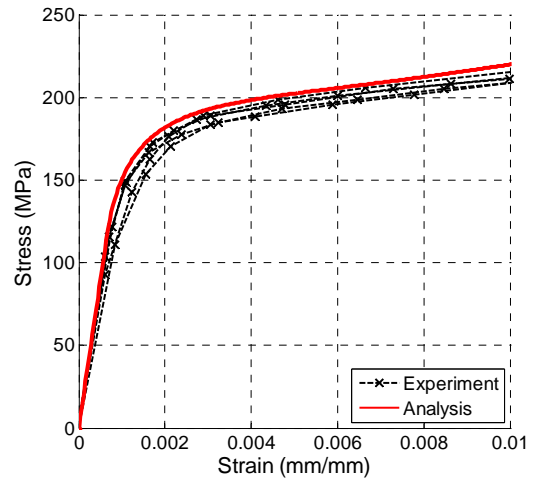
(a) Test #1; Bridge & O'Shea 1997; Specimen: 165x3.0



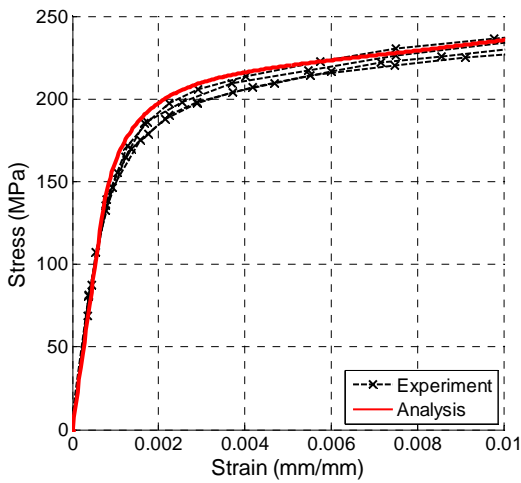
(b) Test #2; Bridge & O'Shea 1997; Specimen: 190x2.0



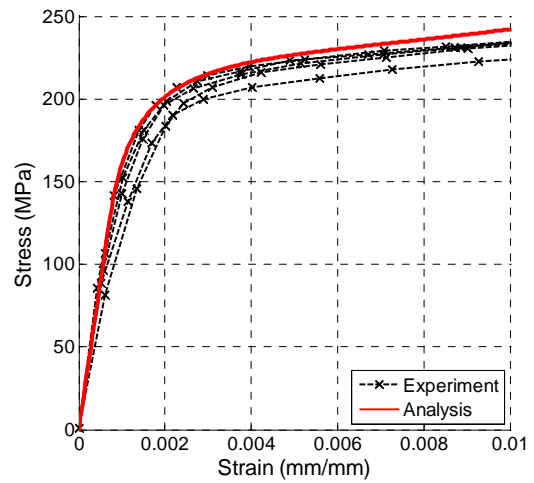
(c) Test #3; Bridge & O'Shea 1997; Specimen: 190x1.6



(d) Test #4; Bridge & O'Shea 1997; Specimen: 190x1.8

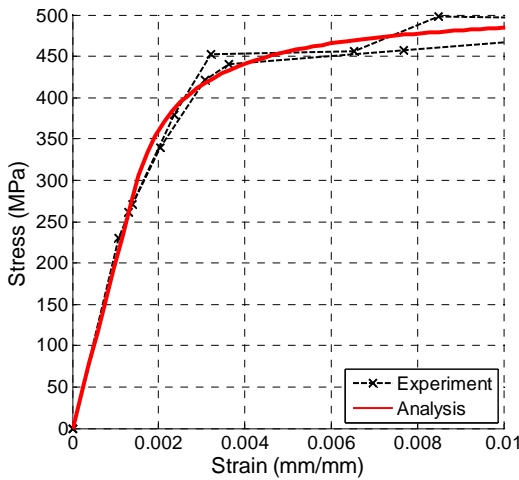


(e) Test #5; Bridge & O'Shea 1997; Specimen: 190x1.2"R

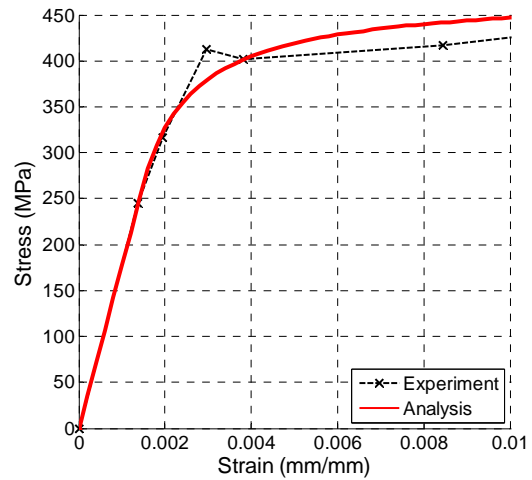


(f) Test #6; Bridge & O'Shea 1997; Specimen: 190x1.0

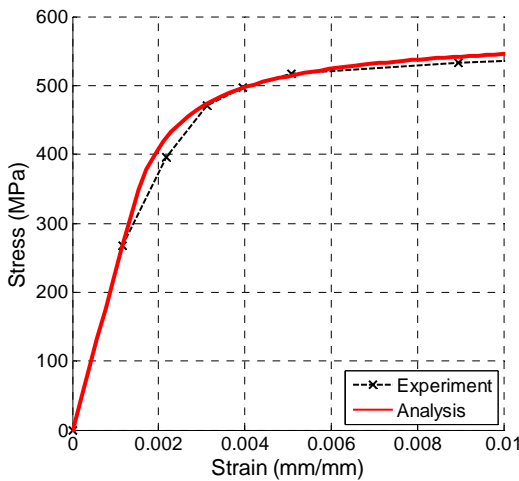
Figure 4-3. Comparison of Experimental and Computational Tensile Coupon Results



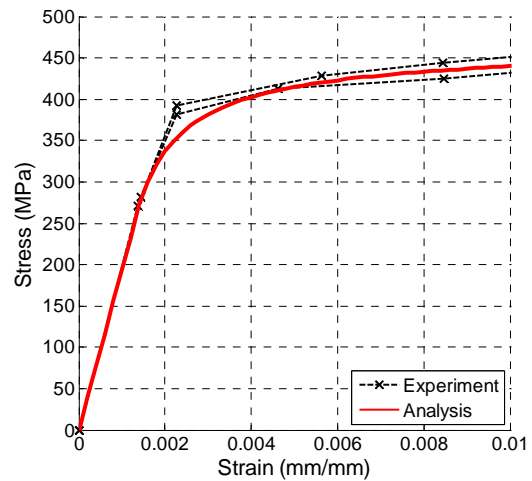
(g) Test #7; Marson & Bruneau 2000; Specimen: CFST 64



(h) Test #8; Marson & Bruneau 2000; Specimen: CFST 34



(i) Test #9; Marson & Bruneau 2000; Specimen: CFST 42



(j) Test #10; Marson & Bruneau 2000; Specimen: CFST 5

Figure 4-3. Comparison of Experimental and Computational Tensile Coupon Results (continued)

4.2.3 Adjustment for Biaxial State of Stress

Due to lateral expansion of the concrete core the steel tube is under a state of biaxial stress. To account for this, the initial yield range is adjusted based on the level of hoop stress assumed to be present in the steel tube. The size of the initial yield surface, κ , is computed using Equation 4.7, noting the initial plastic strain. The size is then multiplied by the results of Equations 1.4 and 1.5 for the positive stress and negative stress yield limits respectively to obtain the size of the initial yield surface accounting for the biaxial state of stress. This adjustment is made only for the initial yield surface. A similar adjustment is made in the steel models of other researchers (Elremaily and Azizinamini 2002; Sakino et al. 2004; Hatzigeorgiou 2008).

4.3 Local Buckling of the Steel Tube

Under compressive loading the steel tube of CCFT members is susceptible to local buckling. Due to the concrete core, the steel tube only has the ability to locally buckle outward. In contrast to hollow tubular members that may also buckle inward, this is a higher mode of buckling that both delays the onset of local buckling and increases the compressive capacity (Bradford et al. 2002).

4.3.1 Monotonic Response

The monotonic compressive response of the proposed constitutive model is modified from the model of Shen et al. (1995) to consist of three regions. The first region is the model as described previously, beginning with the elastic branch and continuing with the smooth plastic response. The second region is commences after the initiation of local buckling, where the response is assumed to be linear strength degradation. The third region is a constant residual stress.

Strain may be used to determine the initiation of local buckling in steel tubes (Tort and Hajjar 2007). Based on experimental observations that explicitly denote the local buckling of the steel tube, an expression for the strain at which local buckling occurs has been derived. The results from two studies are used to calibrate the equation (Table 4.3 and Figure 4-4). Schneider (1998) indicates the initiation of local buckling for typical concentrically loaded short columns. Bridge and O'Shea (1997) present the results of concentrically loaded short CCFT tests where only the steel tube was loaded and was unbonded from the concrete core. For these tests, the entire load is assumed to be taken by the steel tube and local buckling is assumed to initiate at the occurrence of the peak load. These experimental results were analyzed and a power function was found to provide a strong correlation to the data (correlation of $R^2 = 0.925$) (Equations 4.15 and 4.16).

$$\varepsilon_{lb} = \varepsilon_y (0.2139R^{-1.413}) \quad [4.15]$$

$$R = \frac{D F_y}{t E_s} \quad [4.16]$$

If the strain at local buckling, ε_{lb} , is computed as less than the yield strain, ε_y , then the local buckling can be considered elastic. This only occurs for values of R greater than 0.3357.

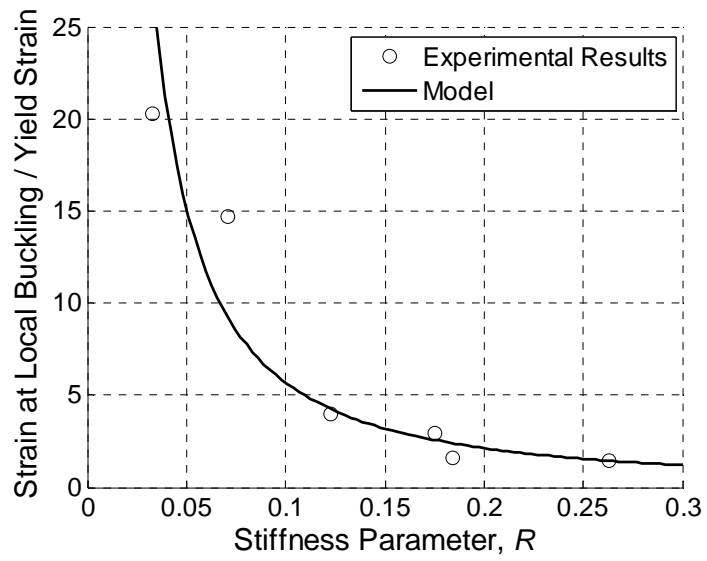


Figure 4-4. Calibration of Strain at Local Buckling

Table 4.3. Properties of Specimens Used for Calibration of Strain at Local Buckling

Test #	Author	Year	Specimen Name	F_y (MPa)	E_s (MPa)	D (mm)	t (mm)	D/t	L (mm)	R	e_{lb} (mm/mm)	e_y (mm/mm)	e_{lb}/e_y
1	Schneider	1998	C1	285.0	189,475	140.8	3.00	46.93	635.0	0.071	0.02211	0.001504	14.70
2	Schneider	1998	C2	313.0	206,011	141.4	6.50	21.75	635.0	0.033	0.03083	0.001519	20.29
3	O'Shea & Bridge	1997	S10BSC	210.7	177,000	190.0	0.86	220.93	658.5	0.263	0.00171	0.00119	1.44
4	O'Shea & Bridge	1997	S12BSC	185.7	178,400	190.0	1.13	168.14	659.5	0.175	0.00308	0.001041	2.96
5	O'Shea & Bridge	1997	S16BSC	306.1	207,400	190.0	1.52	125.00	657.5	0.184	0.00238	0.001476	1.61
6	O'Shea & Bridge	1997	S20BSC	256.4	204,700	190.0	1.94	97.94	657.0	0.123	0.00500	0.001253	3.99

Once local buckling has initiated, the stress-strain response is assumed to experience a linear degradation region followed by a region of constant residual stress. The calibration of the parameters defining the slope of the linear descending branch and the constant residual stress was done in conjunction with the calibration of the post-peak compression region of the concrete constitutive relation described in Section 3.2.2. The form of the equation governing the constant residual stress is based on the work of Bradford, Loh, and Uy (2002) (Equation 4.18). The parameter, R_{crit} , in Equation 4.18 was calibrated along with the r factor, which governs the post-peak behavior of the concrete (Equations 3.2 and 3.3). The two parameters were calibrated such that the energy represented by the computed force-deformation response was equal to the corresponding energy obtained from the experiments for the calibration set of stub columns presented in Section 3.2.1. The r factor was later altered to provide better correspondence to specimens with other loading conditions, however, R_{crit} was left unaltered. A constant value is assumed for all steel tubes for the slope of the linear descending branch (Equation 4.17). The value was chosen to provide the best correspondence between the computed and experimental force-deformation response in the region where softening of the steel tube is predicted to occur.

$$K_s = -\frac{E_s}{30} \quad [4.17]$$

$$f_{rs} = \begin{cases} f_{lb} (R_{crit} / R) & \text{for } R > R_{crit} = 0.17 \\ f_{lb} & \text{otherwise} \end{cases} \quad [4.18]$$

where f_{lb} is the stress at local buckling.

4.3.2 Cyclic Response

Further modifications are necessary to model the response of cyclic local buckling of the steel tube. Local buckling is first triggered by the strain limit given by Equation 4.15. The reference strain to which this value is compared needs to be updated based on plasticity experience by the material. Upon unloading from tensile plasticity the strain at zero stress, $\varepsilon_{lb,ref}$, is computed assuming a linear relationship. It is then this strain that serves as the reference to determine the initiation of local buckling, (Equation 4.19).

$$\text{Local Buckling} = \begin{cases} \text{yes} & \text{if } (\varepsilon < \varepsilon_{lb,ref} - \varepsilon_{lb}) \\ \text{no} & \text{otherwise} \end{cases} \quad [4.19]$$

After the first initiation of local buckling, later local buckling is triggered by a stress limit. The stress at which local buckling occurs is defined as the last stress attained while local buckling was occurring. This behavior was observed experimentally by Fukumoto and Kusama (1985) for rectangular steel tubes. Further, to provide a smooth transition to this limiting stress, the bounding line in the compressive region (i.e., Line Y-Y' in Figure 4-1) is defined to be equal to the critical local buckling stress.

To approximate the response of unloading of the buckled steel tube, both the size of the elastic range and the plastic modulus are reduced as a function of the tube slenderness and the plastic work of the material. Equations 4.20 and 4.21 were derived to attain good correlation between the experimental and analytical results for the cyclic non-proportionally loaded cantilever beam-column tests by Marson and Bruneau (2004) (Table 4.3 and Figure 4-5 through Figure 4-8). In these tests, a constant axial load was applied to a cantilever column. Increasing cyclic transverse displacements were then applied to the free end of the column. Two elements with three sections each were used to model the column. Noting the two-dimensional nature of the loading, the fiber discretization took the form of strips, with 50 strips along the height of the section for each the steel and concrete. The steel and concrete stress-strain response shown in Figure 4-5 through Figure 4-8 is obtained from the extreme fiber for each material at the base of the column. Comparisons are made between experimental and computational results for both the horizontal force at the free end of the column and the moment at the base of the column.

$$K_{reduced} = \gamma_k K \quad [4.20a]$$

$$\gamma_k = \left(1 - 15R \sqrt{\frac{W^p}{F_y}} \right) \geq 0.05 \quad [4.20b]$$

$$E_{reduced}^p = \gamma_{E^p} E^p \quad [4.21a]$$

$$\gamma_{E^p} = \left(1 - 10R \sqrt{\frac{W^p}{F_y}} \right) \geq 0.05 \quad [4.21b]$$

Table 4.4. Material and Geometric Properties of Cyclic Local Buckling Calibration Set

Test #	Author	Year	Specimen	D (mm)	t (mm)	D/t	f'_c (MPa)	F_y (MPa)	L (mm)	L/D	P (kN)	P/P _o
1	Marson & Bruneau	2004	CFST 51	323.9	5.50	58.9	35.00	405.0	2200	6.8	1,600	0.33
2	Marson & Bruneau	2004	CFST 34	323.9	7.50	43.2	40.00	415.0	2200	6.8	1,920	0.32
3	Marson & Bruneau	2004	CFST 64	406.4	5.50	73.9	37.00	449.0	2200	5.4	1,000	0.13
4	Marson & Bruneau	2004	CFST 42	406.4	9.50	42.8	35.00	505.0	2200	5.4	1,920	0.19

Test #1; Marson & Bruneau 2004; Specimen: CFST 51

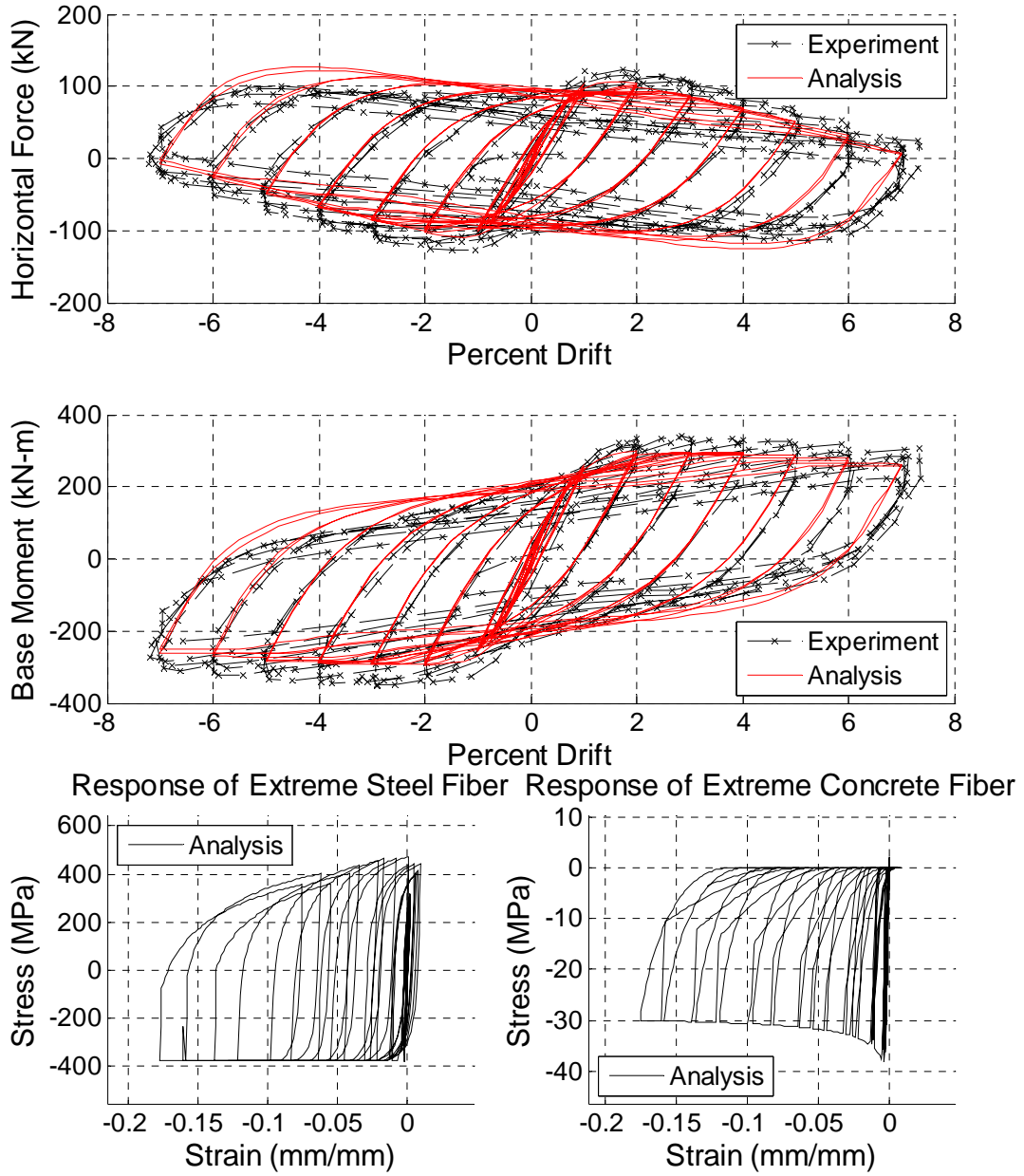
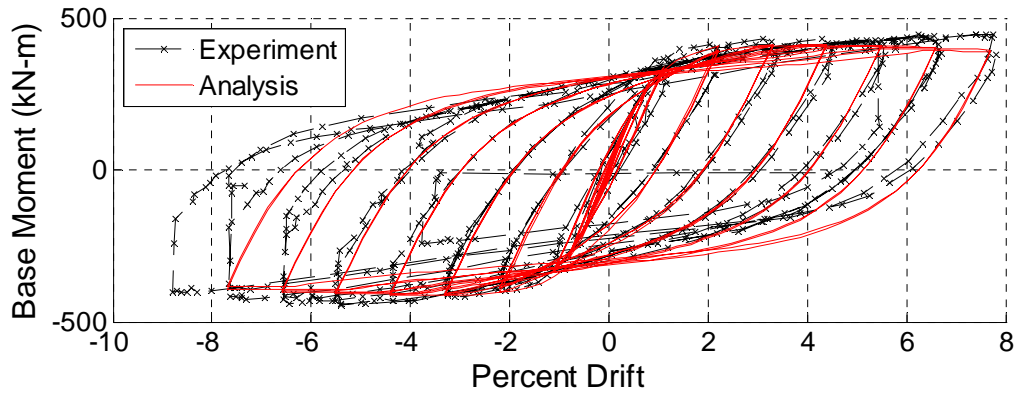
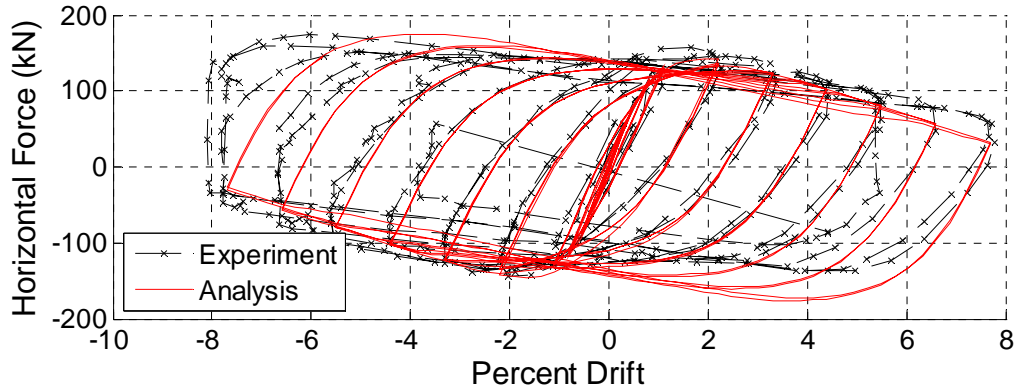


Figure 4-5. Cyclic Local Buckling Calibration Results of Specimen CFST 51

Test #2; Marson & Bruneau 2004; Specimen: CFST 34



Response of Extreme Steel Fiber Response of Extreme Concrete Fiber

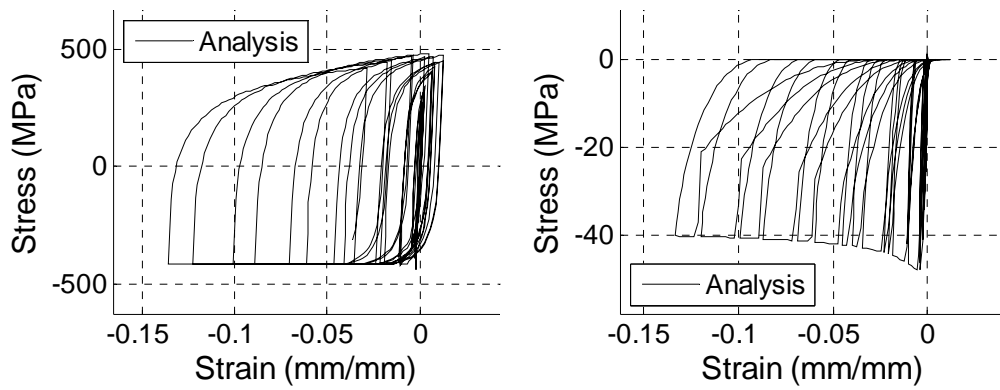


Figure 4-6. Cyclic Local Buckling Calibration Results of Specimen CFST 34

Test #3; Marson & Bruneau 2004; Specimen: CFST 64

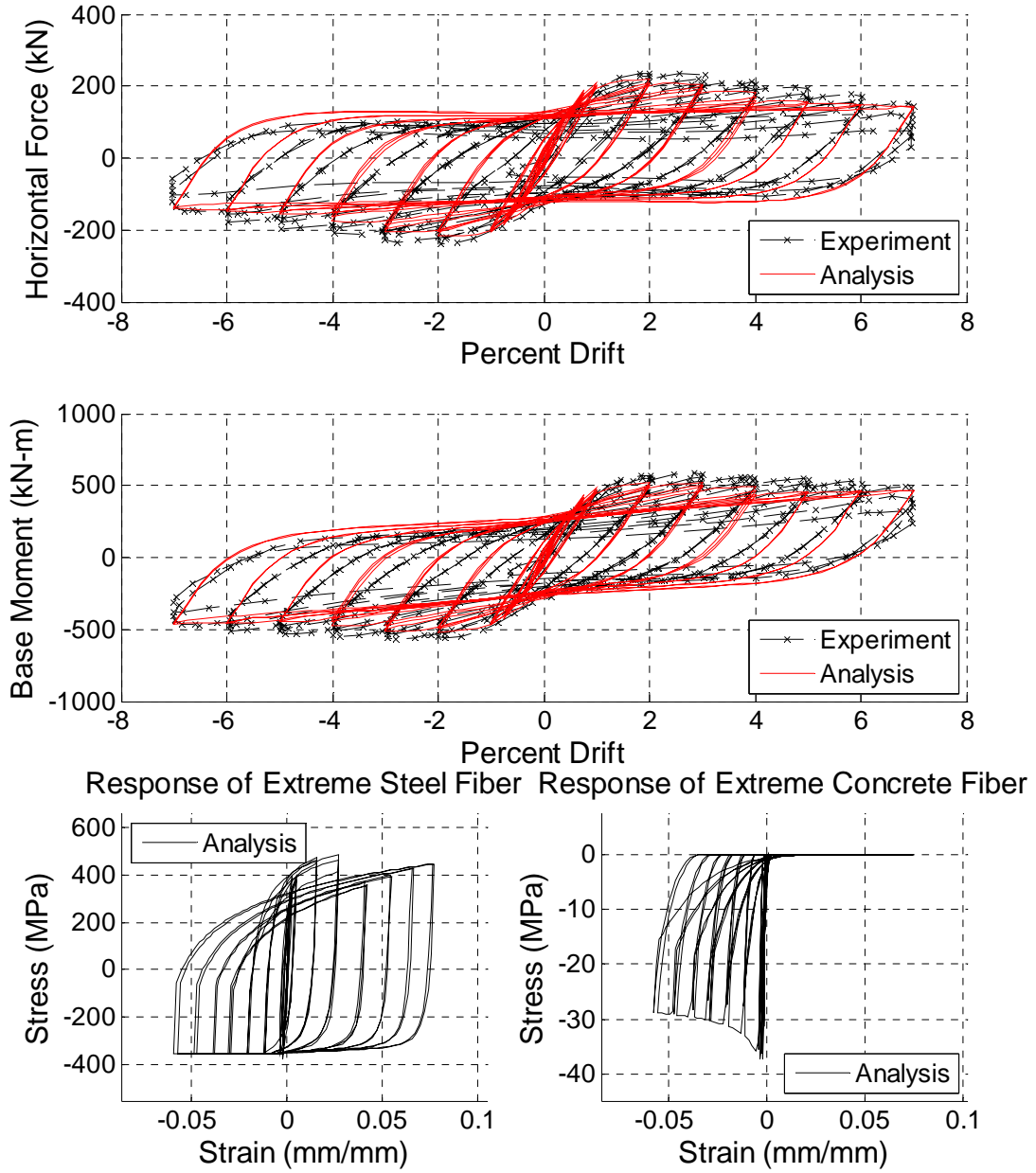


Figure 4-7. Cyclic Local Buckling Calibration Results of Specimen CFST 64

Test #4; Marson & Bruneau 2004; Specimen: CFST 42

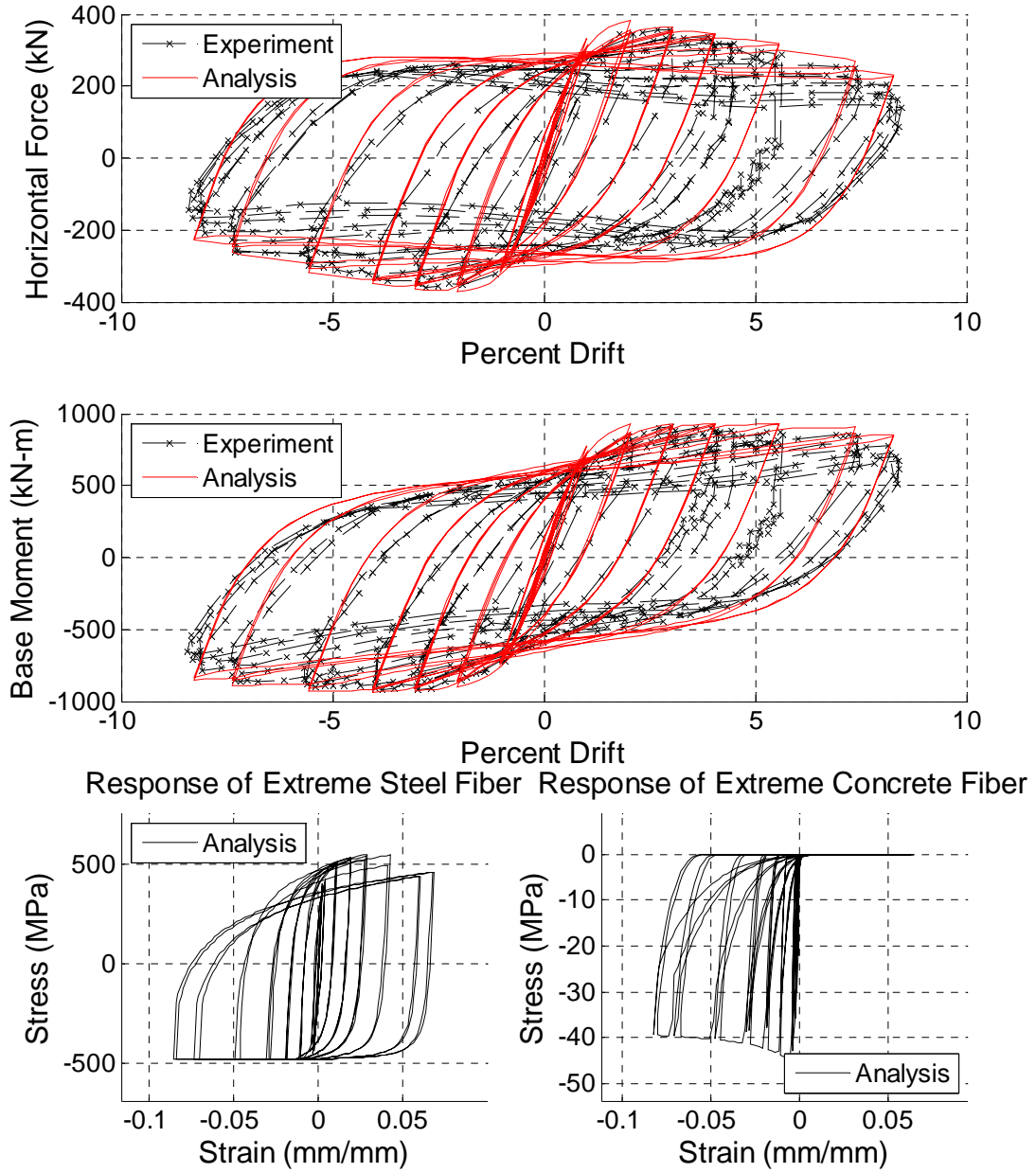


Figure 4-8. Cyclic Local Buckling Calibration Results of Specimen CFST 42

VERIFICATION OF THE FINITE ELEMENT FORMULATION

5.1 Introduction

Results of material and geometric nonlinear analyses using the finite element formulation are presented in this chapter. The analyses herein are intended to provide a comprehensive investigation to the accuracy of the formulation. As such, the members analyzed were chosen to have a broad range of loading and boundary conditions as well as material and geometric properties. Computational results are compared to analytical solutions and experimental results as appropriate. Comparisons are made at not only the element level but section and material level. Where practical, quantitative comparisons were made with the use of various displacement, force, and energy based metrics.

The comparisons have been divided into seven verification sets. The first includes elastic geometrically nonlinear problems. The remaining sets are materially and geometrically nonlinear CCFT experiments grouped by loading condition. In total, 107 experiments have been modeled, including 11 cyclic experiments and 96 monotonic experiments.

5.2 Elastic Geometrically Nonlinear Problems

A series of elastic analyses were performed to verify the accuracy of geometrically nonlinear formulation of the mixed beam element.

5.2.1 Euler Buckling of a Simply Supported Column

The ability of the formulation to detect the Euler buckling load is studied by analyzing a simply supported column. The column is without imperfection and the load is applied concentrically. The critical load of the column is given analytically by Equation 5.1, assuming a effective length factor, K , of 1.

$$P_{cr} = \frac{\pi^2 EI}{(KL)^2} \quad [5.1]$$

In the analysis, the critical load is the load at which the minimum Eigen value of the stiffness matrix becomes zero. The analyses were performed with one to five elements along the height of the column. The number of integration points in each element was found to not significantly affect the results; the results shown are with five integration points per element. The percent error of the computational results (Figure 5-1c) is shown to be small for number of element greater than one.

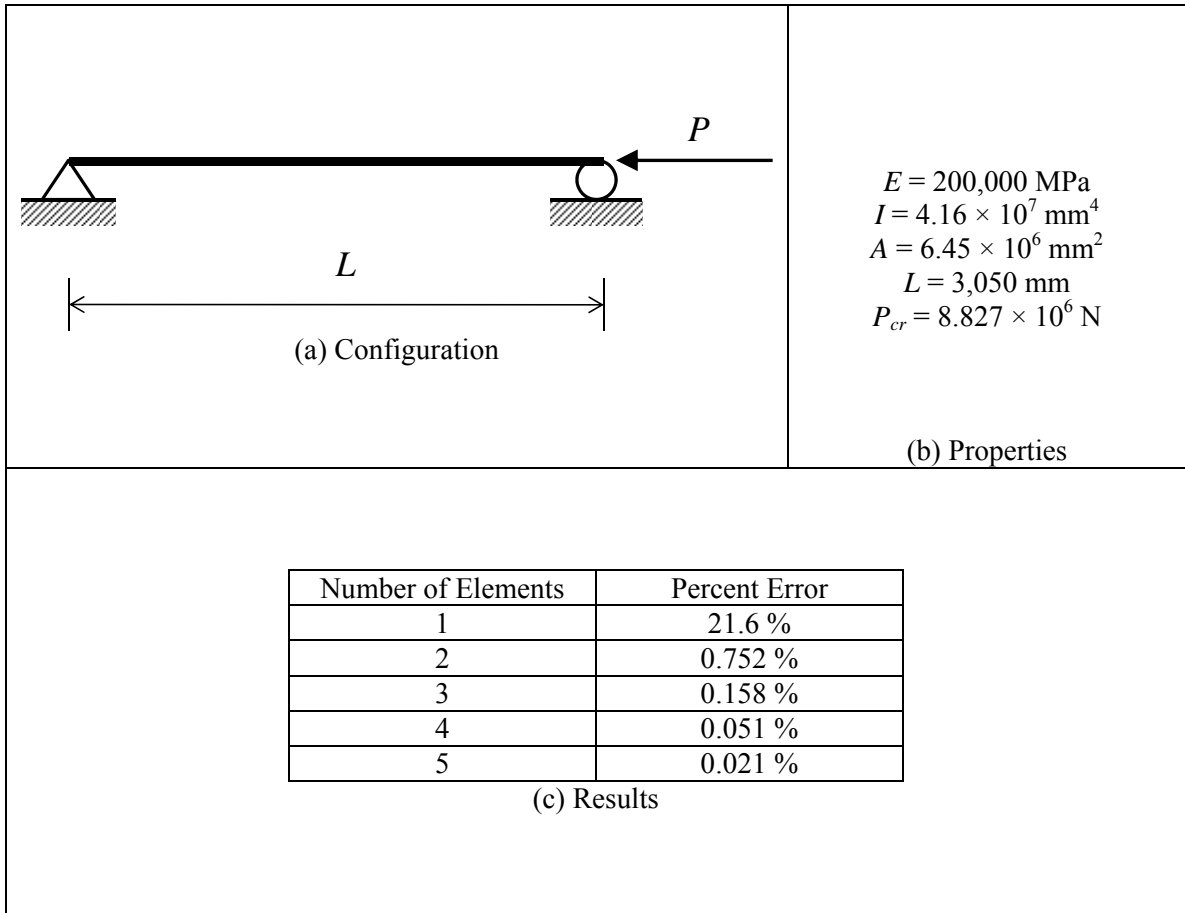


Figure 5-1. Configuration and Results of the Analysis of a Simply Supported Beam under Axial Loading

5.2.2 Cantilever under Axial Loading

To assess the accuracy of the formulation in the post buckling range, the response of a cantilever column under axial loading is studied. The structure, as described in Figure 5-2a, is initially straight. A small bending moment is applied at the free end to introduce a perturbation. Analyses are performed with 3, 5, and 10 elements along the height of the column, each element with 5 integration points. The analysis results are compared to the analytical solution given in Southwell (1941).

The results (Figure 5-2c) demonstrate that the current formulation accurately predicts the behavior. The accuracy increases with the number of elements used, however, the results show good correlation with just 3 elements along the height of the column.

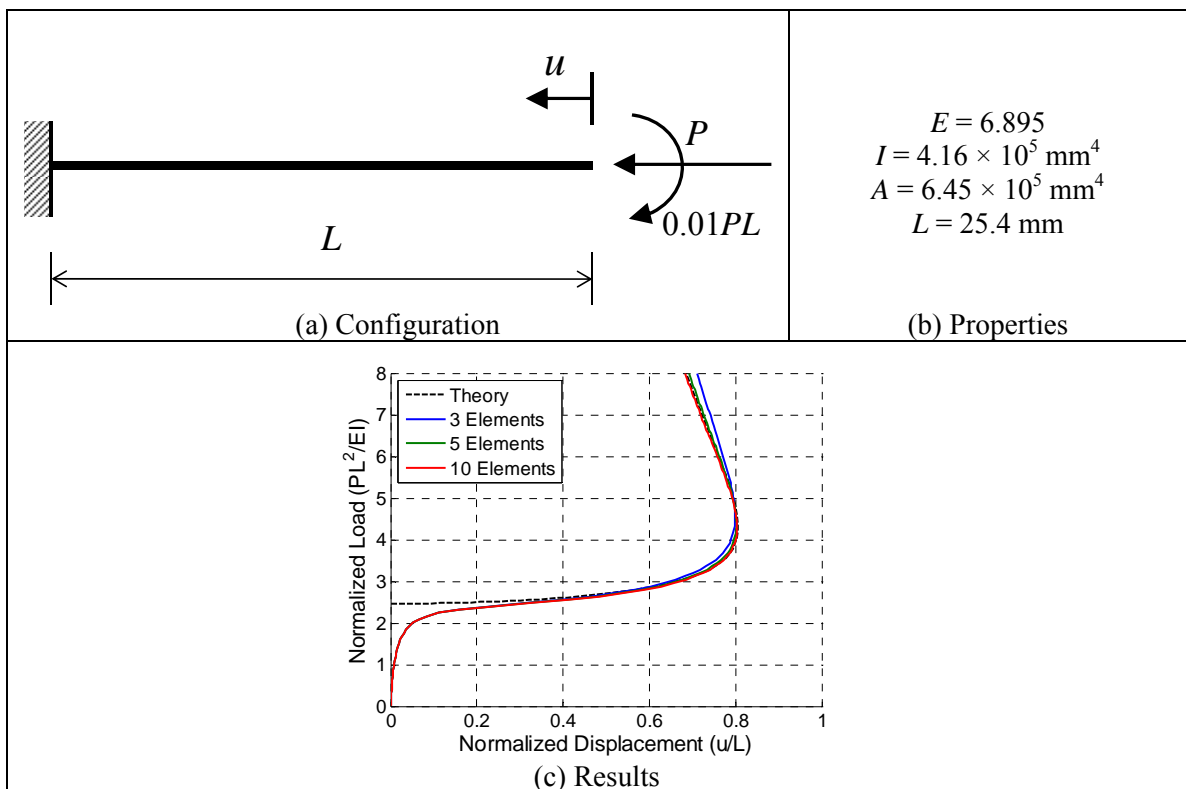


Figure 5-2. Configuration and Results of the Analysis of a Cantilever under Axial Loading

5.2.3 Cantilever under Pure Bending

The ability of the formulation to perform under large displacements and rotations can be examined with the analysis of a cantilever subjected to pure bending (Figure 5-3a). The moment was increased until the cantilever is fully wrapped upon itself. Analyses are performed with 3, 5, and 10 elements along the length of the beam, each element with 5 integration points.

The results (Figure 5-3c) demonstrate that the accuracy increases with the number of elements used, converging to the correct solution. With only three or five elements along the length of the member, the small strain assumption used for the natural deformations is clearly inappropriate for this case of extreme deformation. However, the use of 10 elements along the length of the cantilever provides accurate results.

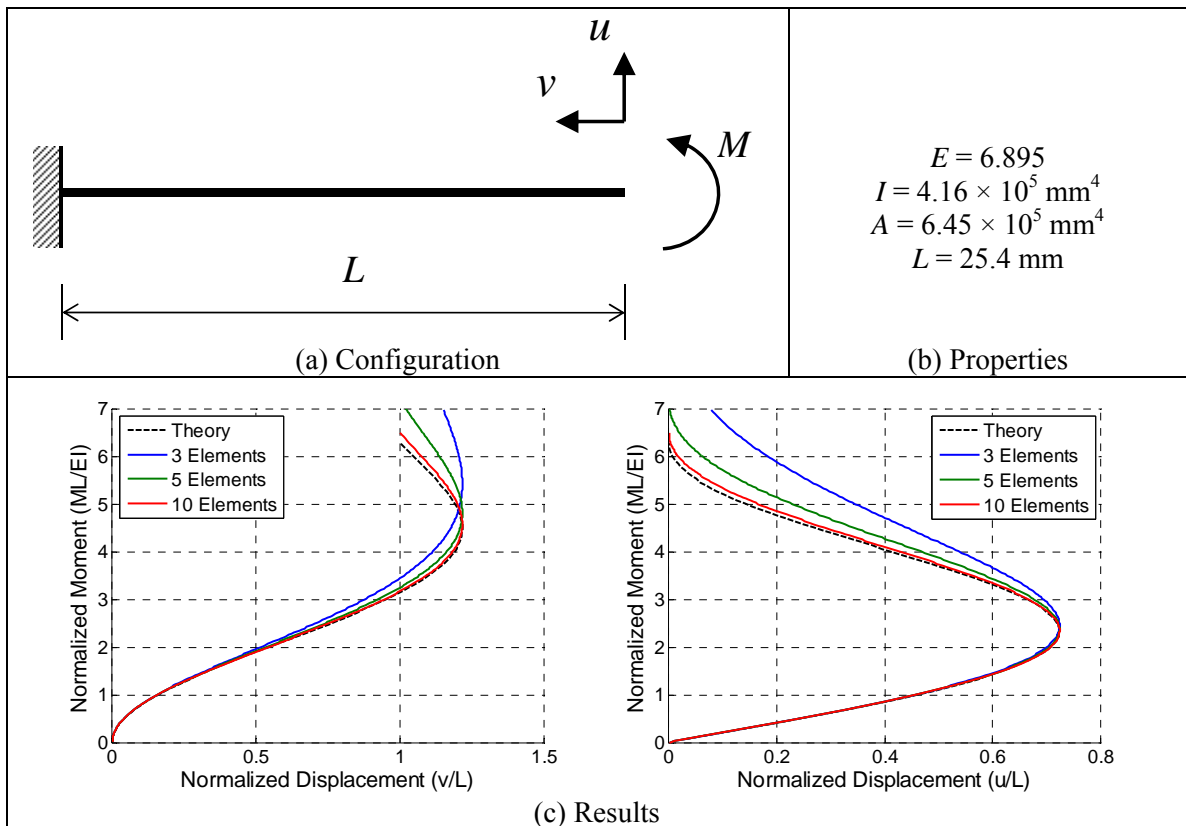


Figure 5-3. Configuration and Results of the Analysis of a Cantilever under Pure Bending

5.2.4 Cantilever under Transverse Tip Loading

To assess the accuracy of the formulation under tension stiffening behavior, the response of a cantilever column under transverse tip loading (Figure 5-4a) is studied. Analyses are performed with 3, 5, and 10 elements along the height of the column, each element with 5 integration points. The analysis results are compared to the analytical solution given in Mattiasson (1981).

The results (Figure 5-4c) demonstrate that the current formulation accurately predicts the behavior. The accuracy increases with the number of elements used, however, the results show good correlation with just 3 elements along the height of the column.

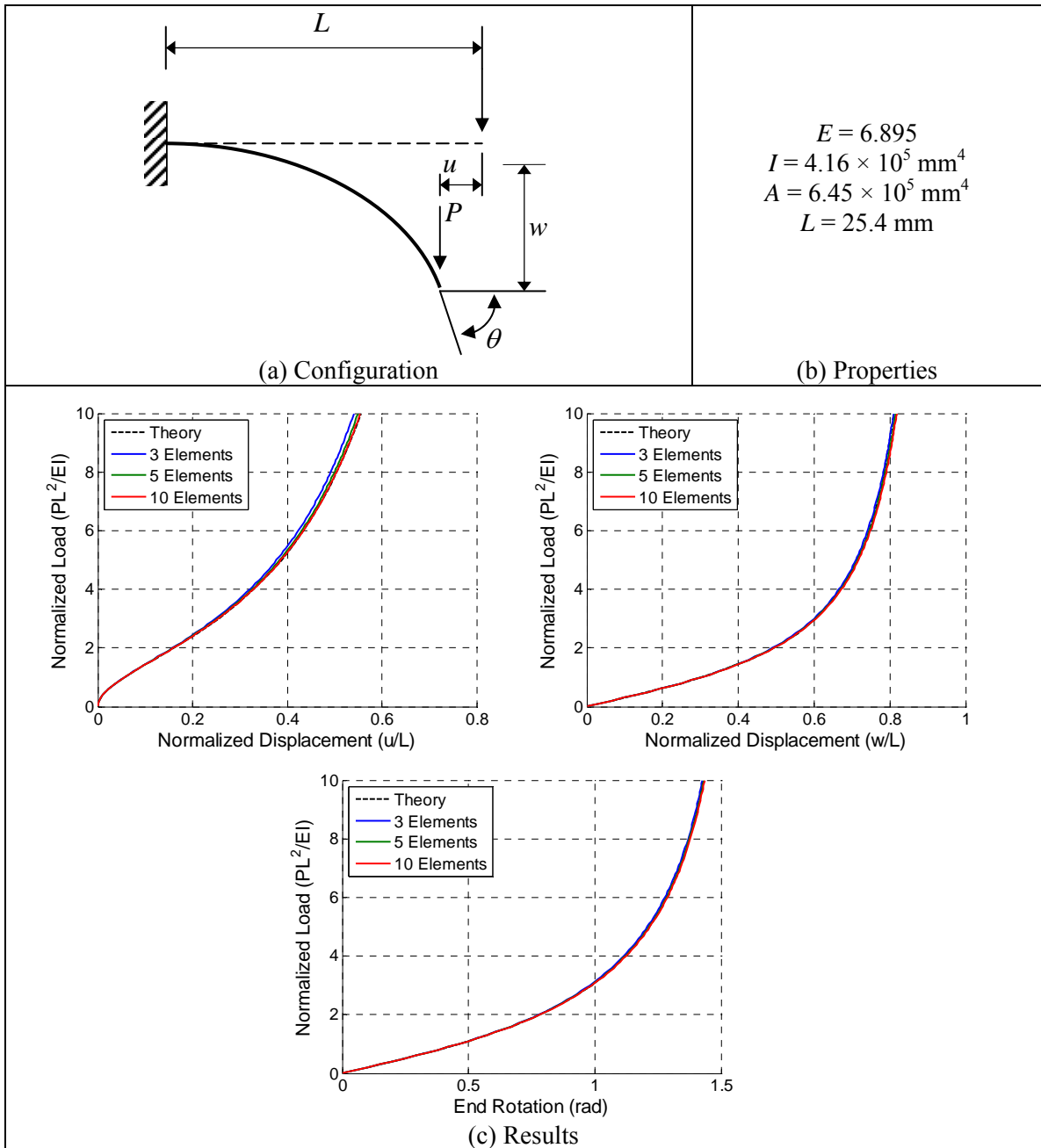


Figure 5-4. Configuration and Results of the Analysis of a Cantilever under Transverse Tip Loading

5.2.5 Right-Angled Simply Supported Frame

The final static nonlinear elastic benchmark problem is the elastic postbuckling analysis of a hinged right-angle frame. The analysis is performed 10 total elements, five along the length of the each member and each element with 5 integration points. The analysis results are compared to the computational solution given in Simo and Vu-Quoc (1986). The results (Figure 5-5c) demonstrate that the current formulation accurately predicts the behavior.

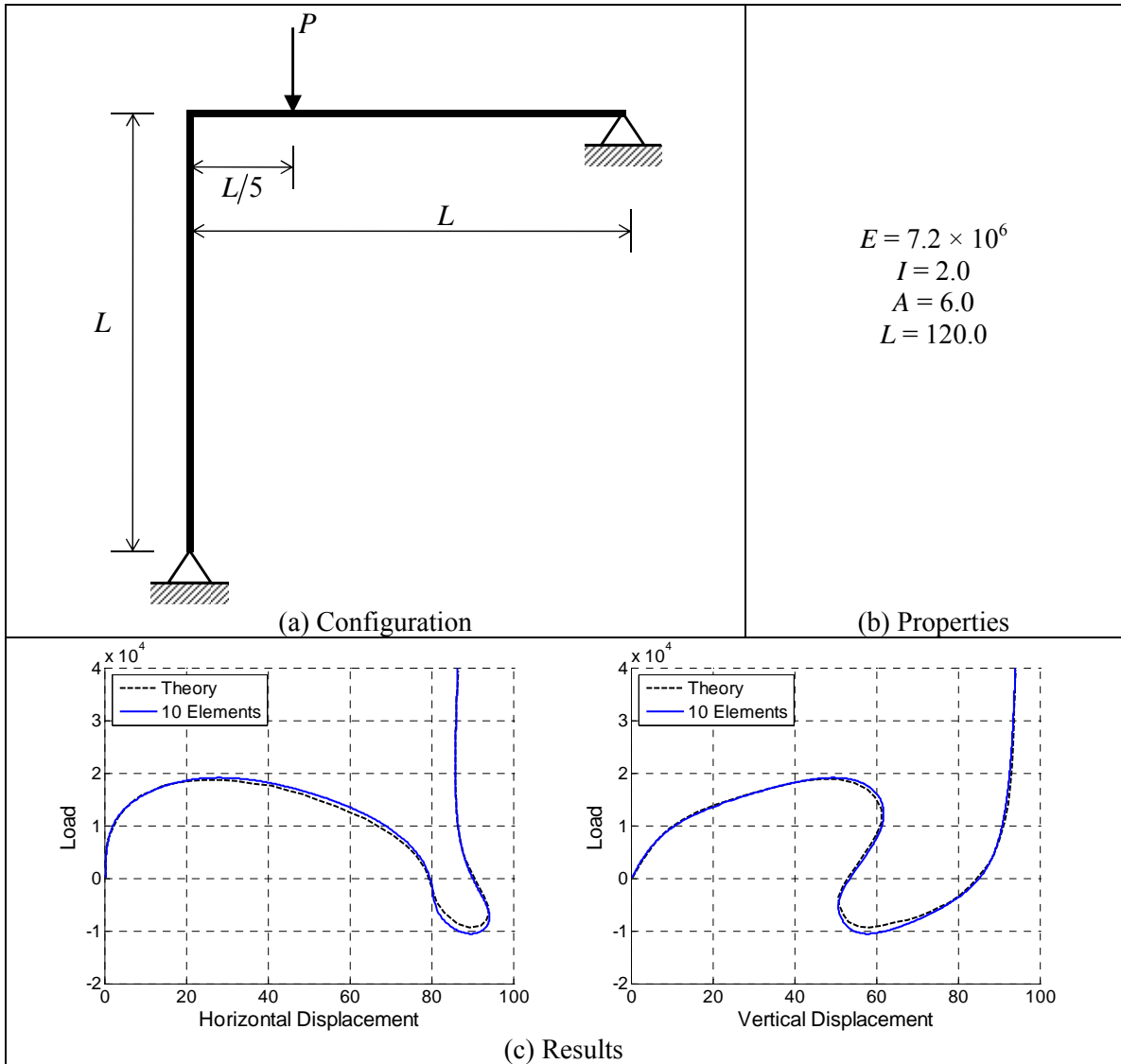


Figure 5-5. Configuration and Results of the Analysis of a Right-Angled Simply Supported Frame

5.2.6 Fixed-Fixed Beam under Dynamic Step-Loading

To assess the accuracy of the formulation under dynamic loading, the fixed-fixed beam subjected to a step loading (Figure 5-6) studied by Hsaio and Jang (1989) is analyzed. Noting symmetry, only half the beam was analyzed. The analysis used the same mesh density, ten elements, and time step, 50 μsec , as Hsaio and Jang (1989). Five integration points were used for each element. Since a consistent mass matrix was not derived for the element, the mass matrix for a linear elastic beam element is used, specifically the mass in the translational directions is $m_{ele}/2$ and the mass in the rotational directions is $m_{ele}L_{ele}^2/420$ (Cook et al. 2002). The system is undamped and time intergration was performed using the Newmark method ($\gamma = 0.50$, $\beta = 0.25$). The results compare well to the computational results of Hsaio and Jang (1989) (Figure 5-6).

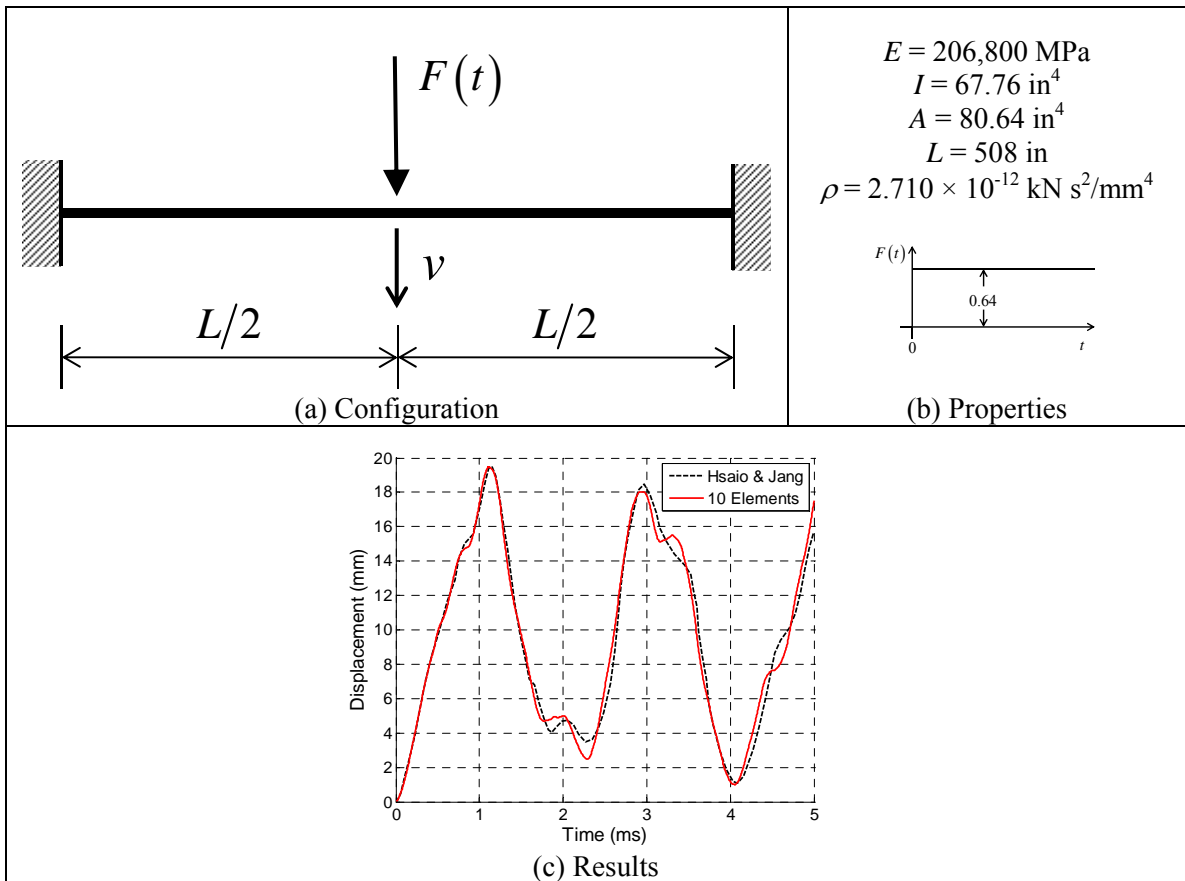


Figure 5-6. Configuration and Results of the Dynamic Analysis of a Fixed-Fixed

5.3 Monotonic Stub Column Experiments

A series of 24 monotonic short concentrically loaded (stub) column tests (setup as shown in Figure 5-7) was used in the calibration of the material constitutive models. An additional series of 24 monotonic stub column tests was compiled to validate the performance of the element formulation.

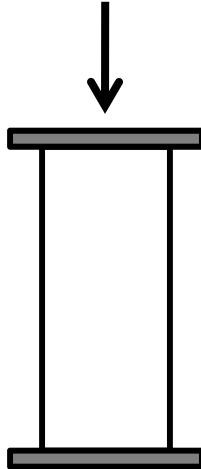


Figure 5-7. Experimental Setup of Stub Column Test

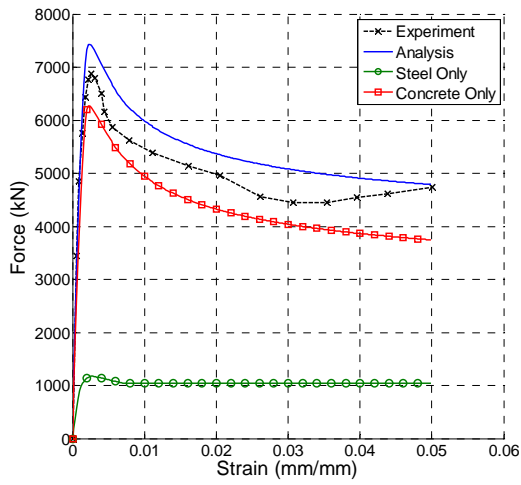
A preliminary mesh refinement study indicated that the results were nearly invariant to the number of elements, number of sections, and fiber discretization. This is likely due to the uniform strain throughout the member. The analyses shown in this section were performed with two elements along the length of the column, with three integration points per member, and a fiber mesh with 8 fibers in the steel tube and 16 fibers in the concrete core. Analyses were run in displacement control, up to the same the peak deformation as experienced in the experiment.

The material and geometric properties of each of the specimens is listed in Table 5.1. Experimental and computational load deformation plots are shown in Figure 5-8 with steel and concrete components for the computational model also shown. Four metrics were computed for comparison of the experimental and computational results. They are: 1) peak load, the largest load attained at any time; 2) strain at peak load; 3) initial stiffness, computed as the secant stiffness between the state of zero load and the state of one-third of the peak load; and 4) area under the curve. These metrics, with corresponding error computations, are listed in Table 5.2.

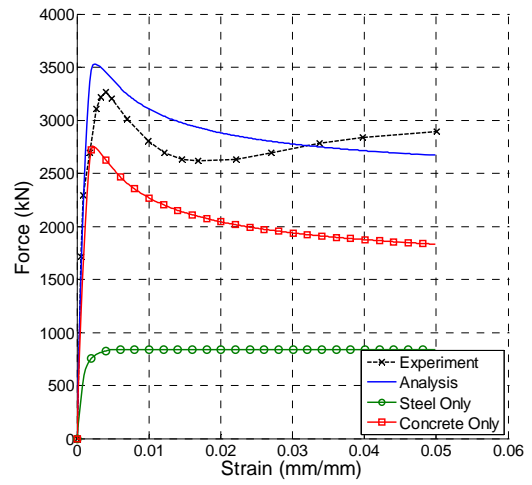
The results indicate very good accuracy in terms of peak load and area under the curve with an average error of less than 10 percent. The strain at peak load was consistently low, with an average error of approximately 35 percent. The error in strain at peak load was especially high for specimens that exhibited a hardening response during the experiment. The initial stiffness was consistently high, with an average error of approximately 65 percent, although some tests overestimate the stiffness while others underestimate it (in addition, as will be seen later, for beam-column tests, the initial stiffness is more often underestimated). As may be seen in Figure 5-8, the general correlation with the experimental response is very good.

Table 5.1. Material and Geometric Properties of the Stub Column Validation Set

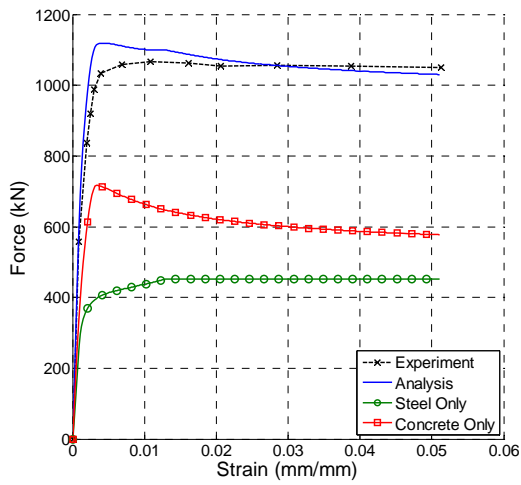
Test #	Author	Year	Specimen	D (mm)	t (mm)	D/t	f _c (MPa)	F _y (MPa)	L (mm)	L/D
1	Yoshioka et al.	1995	CC4-D-4	450.0	2.96	152.0	40.50	283.4	1350	3.00
2	Yoshioka et al.	1995	CC4-C-4	300.2	2.96	101.4	40.50	283.4	901	3.00
3	Yoshioka et al.	1995	CC4-A-4	149.2	2.96	50.4	40.50	283.4	448	3.00
4	Yoshioka et al.	1995	CC8-A-4	108.1	6.47	16.7	40.50	834.5	324	3.00
5	Yamamoto et al.	2002	C30A-4A	318.5	10.30	30.9	52.20	335.0	956	3.00
6	Yamamoto et al.	2002	C10A-2A	101.8	3.20	31.8	23.20	371.0	305	3.00
7	Giakoumelis & Lam	2004	C3	114.4	3.98	28.8	31.40	343.0	300	2.62
8	Giakoumelis & Lam	2004	C11	114.3	3.75	30.5	57.60	343.0	300	2.62
9	Han et al.	2005	CA2-1	100.0	1.87	53.5	85.20	282.0	300	3.00
10	Han et al.	2005	CA4-1	200.0	1.87	107.0	85.20	282.0	600	3.00
11	Han et al.	2005	CC1-1	60.0	2.00	30.0	90.00	404.0	180	3.00
12	Han et al.	2005	CB3-2	150.0	2.00	75.0	85.20	404.0	450	3.00
13	O'Shea & Bridge	2000	S30CS10A	165.0	2.82	58.5	113.60	363.3	578	3.50
14	O'Shea & Bridge	2000	S16CS80A	190.0	1.52	125.0	77.70	306.1	664	3.49
15	O'Shea & Bridge	2000	S10CS80B	190.0	0.86	220.9	74.70	210.7	664	3.49
16	O'Shea & Bridge	2000	S10CS50A	190.0	0.86	220.9	46.00	210.7	659	3.47
17	O'Shea & Bridge	2000	S30CS50B	165.0	2.82	58.5	48.30	363.3	581	3.52
18	O'Shea & Bridge	2000	R12CF1	190.0	1.11	171.2	110.30	203.1	662	3.48
19	O'Shea & Bridge	2000	S20CS50A	190.0	1.94	97.9	46.00	256.4	664	3.49
20	O'Shea & Bridge	2000	S16CS50B	190.0	1.52	125.0	53.50	306.1	665	3.50
21	O'Shea & Bridge	2000	S30CS80A	165.0	2.82	58.5	77.70	363.3	581	3.52
22	Bergmann	1994	RU11	323.9	5.60	57.8	92.30	443.9	1000	3.09
23	Han & Yao	2004	scv2-1	200.0	3.00	66.7	58.50	303.5	600	3.00
24	Han & Yao	2004	sch2-1	200.0	3.00	66.7	58.50	303.5	600	3.00



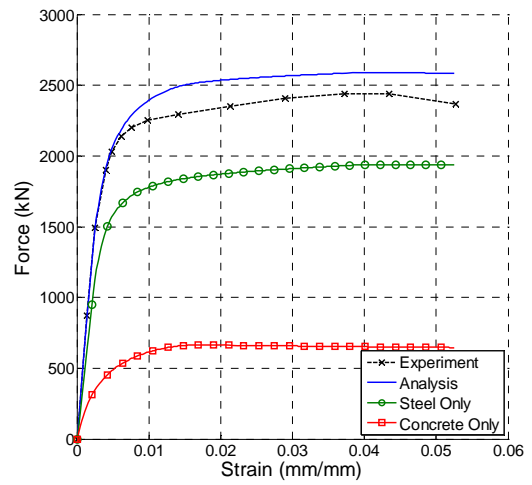
(a) Test #1; Yoshioka et al. 1995; Specimen: CC4-D-4



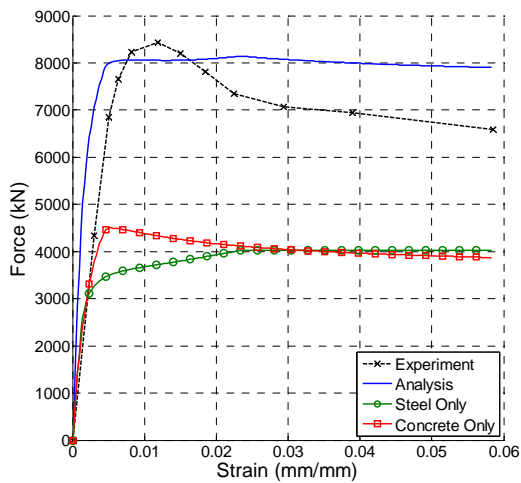
(b) Test #2; Yoshioka et al. 1995; Specimen: CC4-C-4



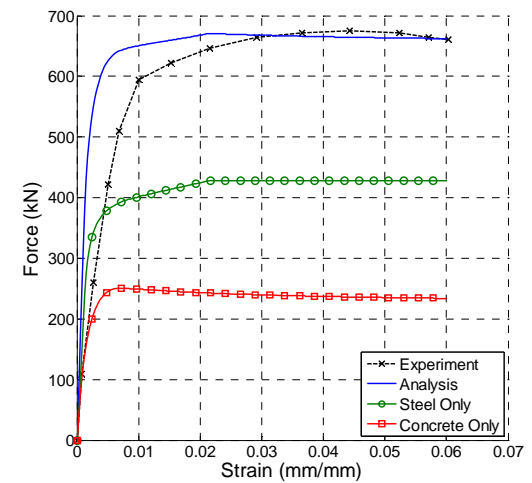
(c) Test #3; Yoshioka et al. 1995; Specimen: CC4-A-4



(d) Test #4; Yoshioka et al. 1995; Specimen: CC8-A-4

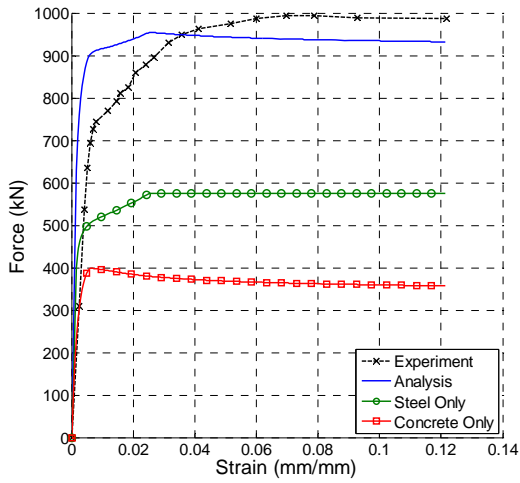


(e) Test #5; Yamamoto et al. 2002; Specimen: C30A-4A

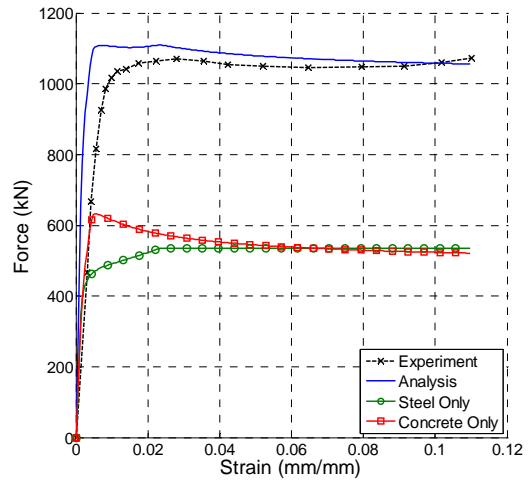


(f) Test #6; Yamamoto et al. 2002; Specimen: C10A-2A

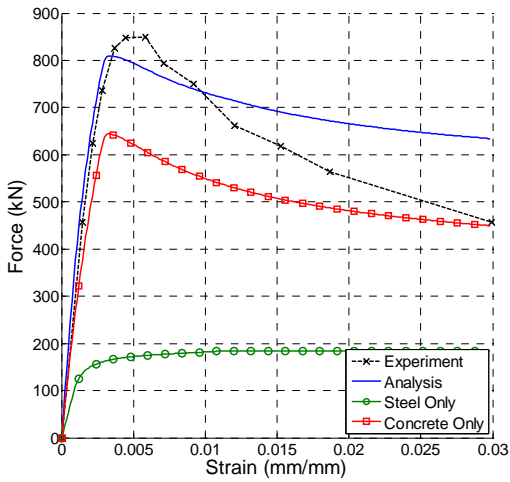
Figure 5-8. Validation Results for Stub Columns



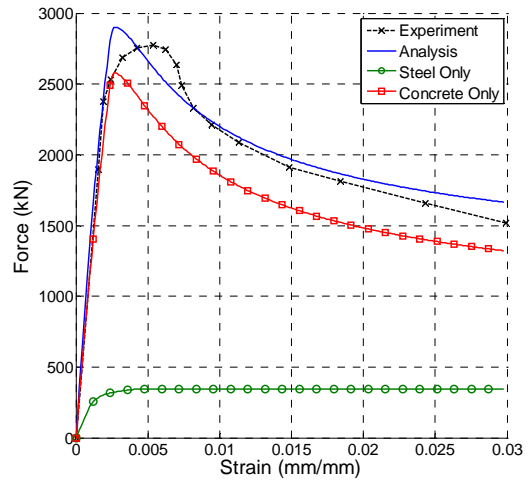
(g) Test #7; Giakoumelis & Lam 2004; Specimen: C3



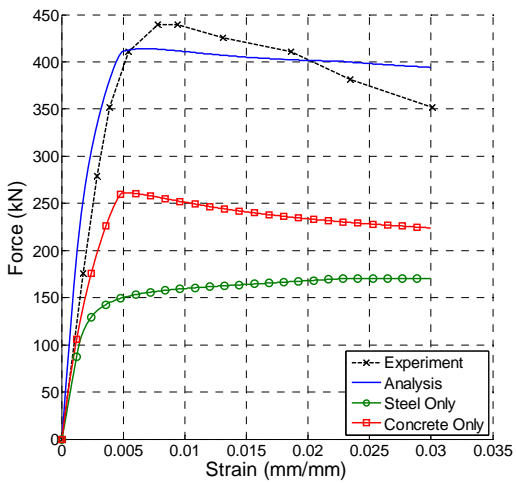
(h) Test #8; Giakoumelis & Lam 2004; Specimen: C11



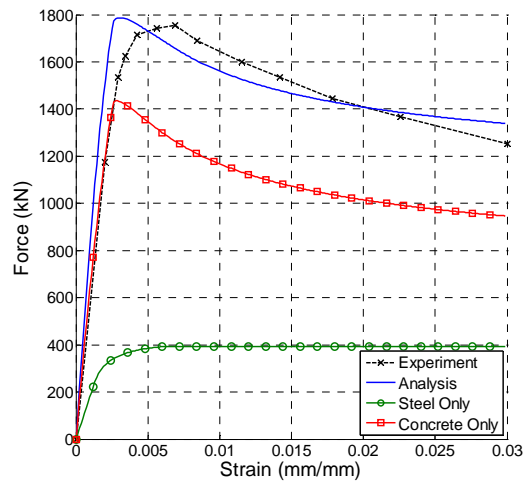
(i) Test #9; Han et al. 2005; Specimen: CA2-1



(j) Test #10; Han et al. 2005; Specimen: CA4-1

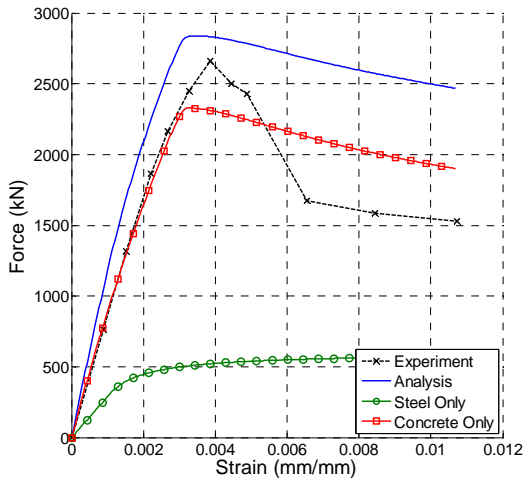


(k) Test #11; Han et al. 2005; Specimen: CC1-1

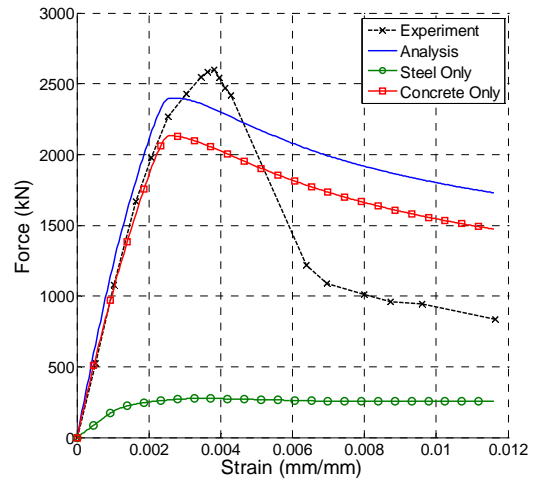


(l) Test #12; Han et al. 2005; Specimen: CB3-2

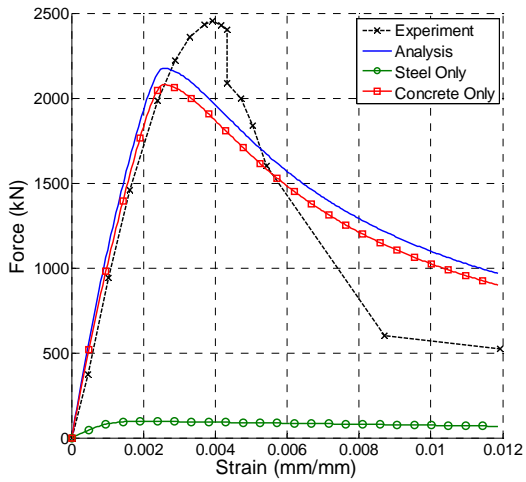
Figure 5-8. Validation Results for Stub Columns (continued)



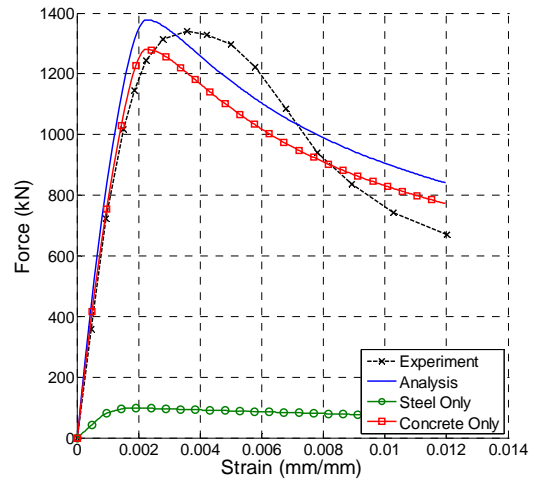
(m) Test #13; O'Shea & Bridge 2000; Specimen: S30CS10A



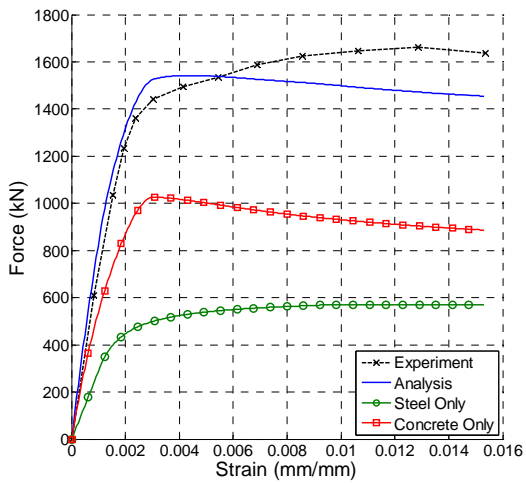
(n) Test #14; O'Shea & Bridge 2000; Specimen: S16CS80A



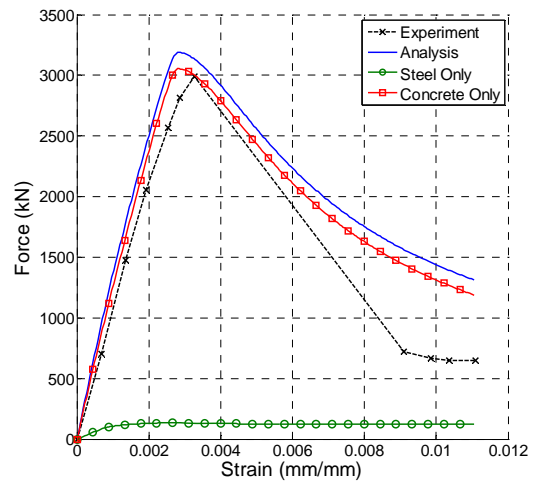
(o) Test #15; O'Shea & Bridge 2000; Specimen: S10CS80B



(p) Test #16; O'Shea & Bridge 2000; Specimen: S10CS50A

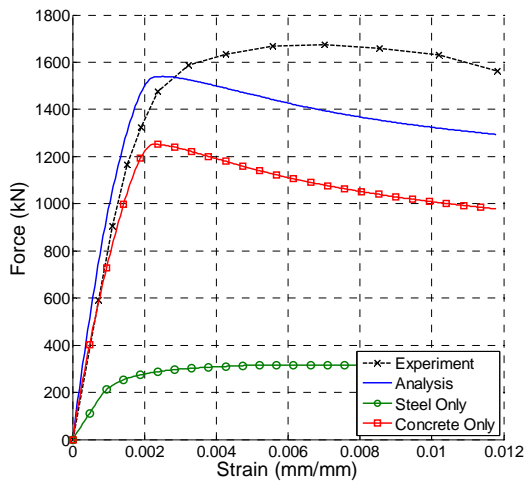


(q) Test #17; O'Shea & Bridge 2000; Specimen: S30CS50B

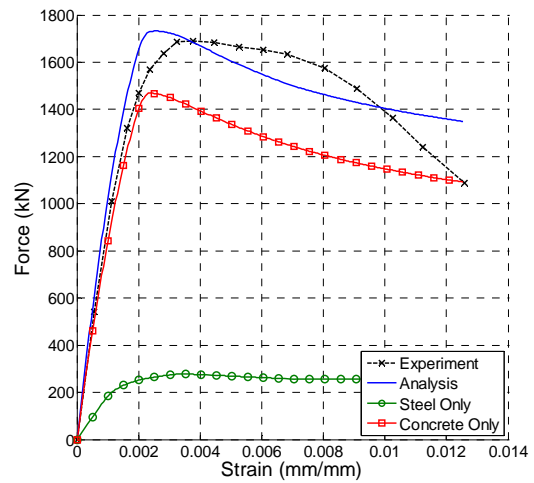


(r) Test #18; O'Shea & Bridge 2000; Specimen: R12CF1

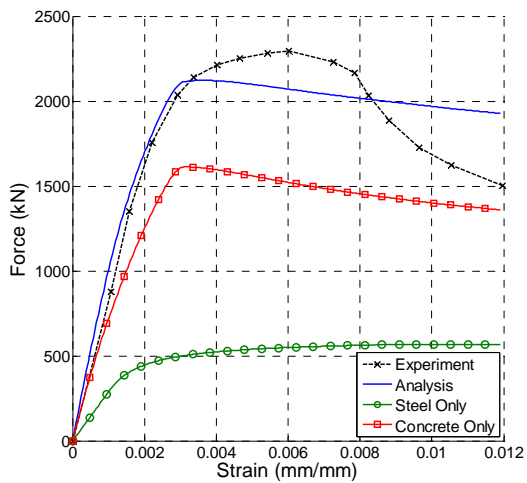
Figure 5-8. Validation Results for Stub Columns (continued)



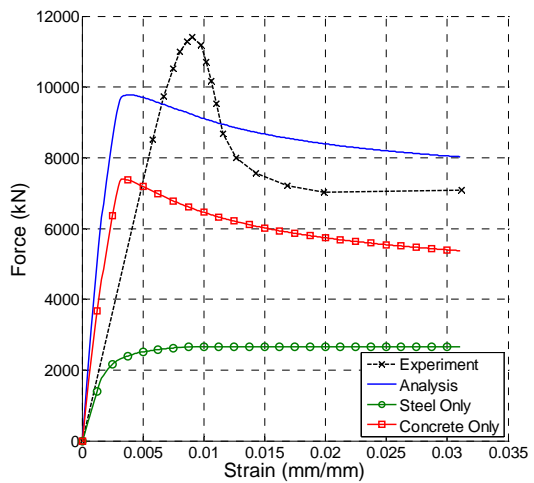
(s) Test #19; O'Shea & Bridge 2000; Specimen: S20CS50A



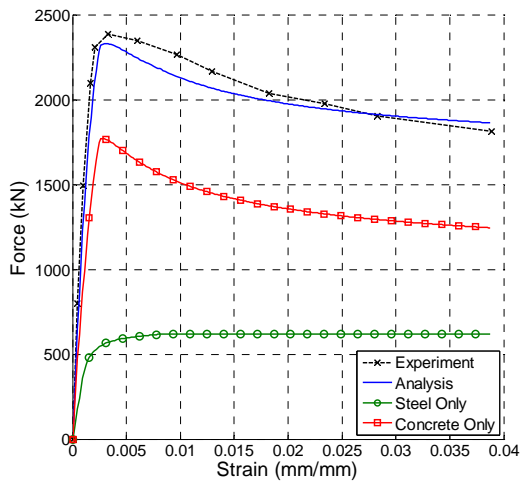
(t) Test #20; O'Shea & Bridge 2000; Specimen: S16CS50B



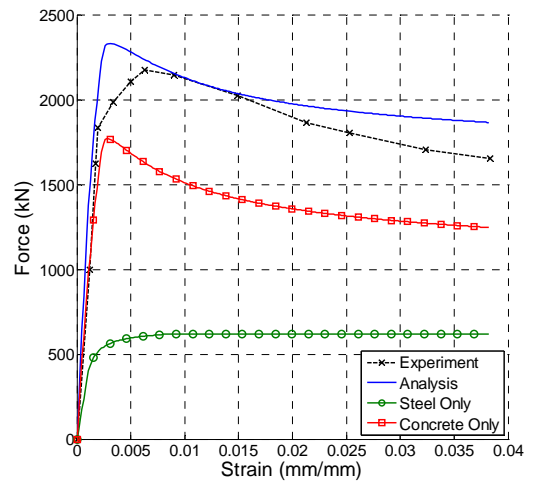
(u) Test #21; O'Shea & Bridge 2000; Specimen: S30CS80A



(v) Test #22; Bergmann 1994; Specimen: RU11



(w) Test #23; Han & Yao 2004; Specimen: scv2-1



(x) Test #24; Han & Yao 2004; Specimen: sch2-1

Figure 5-8. Validation Results for Stub Columns (continued)

Table 5.2. Comparison Metrics for Validation of Stub Columns

Test #	Peak Load (kN)			Strain at Peak Load			Initial Stiffness (kN)			Area under Curve (kN)		
	Expt.	Model	%Error	Expt.	Model	%Error	Expt.	Model	%Error	Expt.	Model	%Error
1	6,876	7,431	8.07%	0.002640	0.002401	-9.05%	6,450,090	5,480,820	-15.03%	246.9	267.9	8.50%
2	3,263	3,528	8.11%	0.004027	0.002405	-40.29%	3,241,150	2,618,210	-19.22%	138.6	142.9	3.11%
3	1,066	1,119	4.94%	0.010798	0.004309	-60.10%	623,879	750,933	20.37%	52.9	53.5	1.17%
4	2,439	2,590	6.21%	0.043436	0.039671	-8.67%	646,948	618,280	-4.43%	119.2	126.5	6.15%
5	8,430	8,144	-3.39%	0.011874	0.023426	97.29%	1,434,340	4,053,090	182.58%	406.3	456.8	12.42%
6	675	671	-0.57%	0.044211	0.021454	-51.47%	102,098	339,746	232.76%	36.8	38.8	5.41%
7	995	955	-3.99%	0.069693	0.025324	-63.66%	121,696	475,501	290.73%	112.0	112.3	0.28%
8	1,072	1,110	3.54%	0.110078	0.023337	-78.80%	151,745	533,662	251.68%	112.0	116.9	4.35%
9	849	809	-4.73%	0.005835	0.003471	-40.51%	314,446	403,409	28.29%	18.1	20.2	11.14%
10	2,777	2,901	4.44%	0.005389	0.002752	-48.94%	1,204,630	1,467,470	21.82%	58.5	59.9	2.41%
11	440	414	-5.88%	0.007814	0.006736	-13.80%	100,871	166,423	64.99%	11.3	11.5	1.70%
12	1,755	1,787	1.82%	0.006907	0.003120	-54.83%	580,334	863,016	48.71%	42.9	43.3	0.92%
13	2,661	2,838	6.65%	0.003866	0.003478	-10.03%	859,890	1,193,350	38.78%	18.6	25.2	35.79%
14	2,602	2,400	-7.75%	0.003816	0.002655	-30.44%	1,040,340	1,261,010	21.21%	16.4	21.9	33.37%
15	2,453	2,176	-11.30%	0.003928	0.002575	-34.45%	895,896	1,160,460	29.53%	14.5	17.0	17.14%
16	1,341	1,378	2.75%	0.003578	0.002257	-36.93%	763,965	956,750	25.23%	11.7	12.3	4.77%
17	1,661	1,542	-7.16%	0.012866	0.004364	-66.08%	730,417	886,166	21.32%	22.5	21.5	-4.59%
18	2,993	3,188	6.51%	0.003278	0.002842	-13.30%	1,072,370	1,393,660	29.96%	17.6	22.4	26.93%
19	1,676	1,539	-8.15%	0.007022	0.002508	-64.29%	810,896	1,082,190	33.46%	17.5	15.6	-10.81%
20	1,691	1,732	2.40%	0.003760	0.002568	-31.70%	957,083	1,096,450	14.56%	17.7	17.9	0.96%
21	2,295	2,122	-7.52%	0.006012	0.003637	-39.50%	824,362	1,041,260	26.31%	21.5	22.0	1.99%
22	11,404	9,777	-14.27%	0.009078	0.003870	-57.37%	1,463,430	4,234,880	189.38%	226.5	260.7	15.12%
23	2,387	2,330	-2.38%	0.003261	0.003113	-4.53%	1,834,870	1,380,760	-24.75%	78.6	76.5	-2.68%
24	2,175	2,330	7.09%	0.006304	0.003070	-51.31%	835,396	1,380,940	65.30%	70.9	75.5	6.54%
Mean			-0.61%			-33.87%			65.56%			7.59%
Standard Deviation			6.68%			35.04%			90.58%			11.29%
Median			0.62%			-39.89%			28.91%			4.56%

5.4 Monotonic Bending Experiments

The uniaxial constitutive relations were derived to mimic the response of short concentrically loaded columns. However, they are assumed to be relevant to the whole spectrum of beam-column behavior. It is thus important to validate the response over the entire spectrum, including the opposite extreme, pure bending. A validation set of 24 CCFT beams subjected to flexure only was compiled. The loading of each of the beams was in one of three different configurations: direct moment, four-point bending, three-point bending (Figure 5-9). Under the direct moment configuration, moments are applied at the member ends and the entire member is subjected to uniform moment. Under the four-point bending configuration, two point loads are applied to the specimen at equal distances in from the member ends, creating a center span with uniform moment. Under the three-point bending configuration, one point load is applied at the midspan of the member; there is no region of uniform moment.

Preliminary mesh refinement studies were performed on each of the three configurations. Similar to those for the stub columns, the studies indicated that the results were nearly invariant to the number of elements and sections. Noting that there is little dependence of the mesh density on the results, the minimum number of elements was chosen for each specimen type. The direct moment analyses were performed with one element along the length of the member; the four-point bending analyses were performed with four elements along the length of the member (so as to be able to assess the response at midspan to compare with the experimental measurements); and the three-point bending analyses were performed with two elements along the length of the member. For all three configurations, each element with three integration points per member. Noting the two-dimensional nature of these tests, the fiber discretization took the form of strips, with 50 strips along the height of the section for each the steel and concrete. The fiber discretization was selected such that it was dense enough to not affect the accuracy of the results within a small tolerance. Analyses were run in displacement control, up to the same the peak deformation as experienced in the experiment.

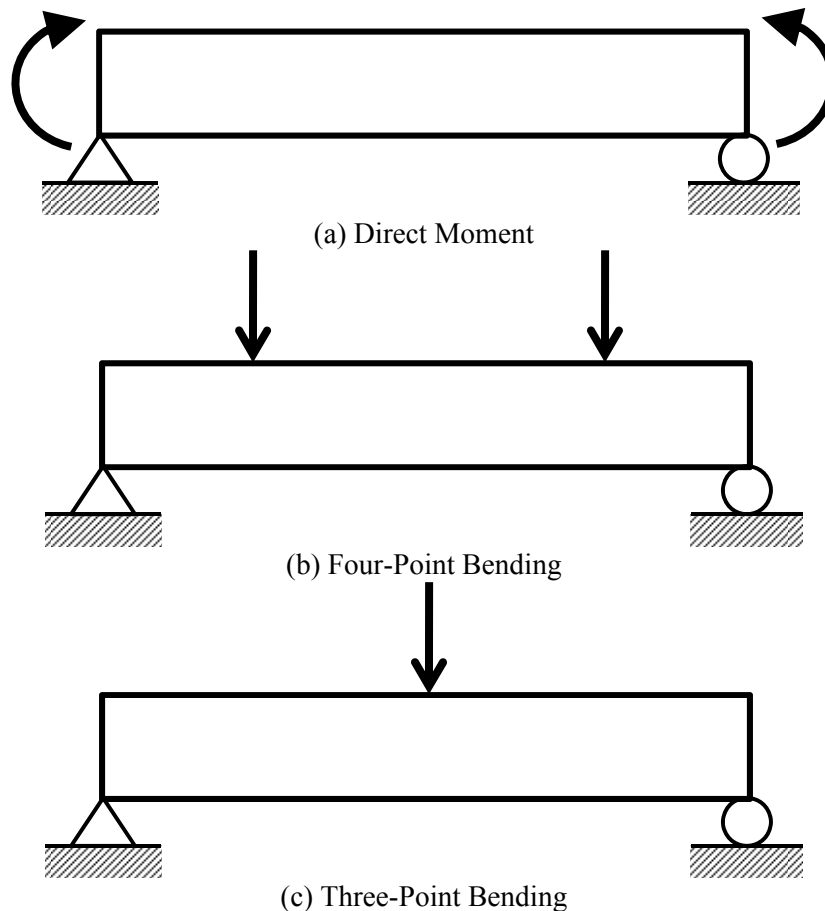


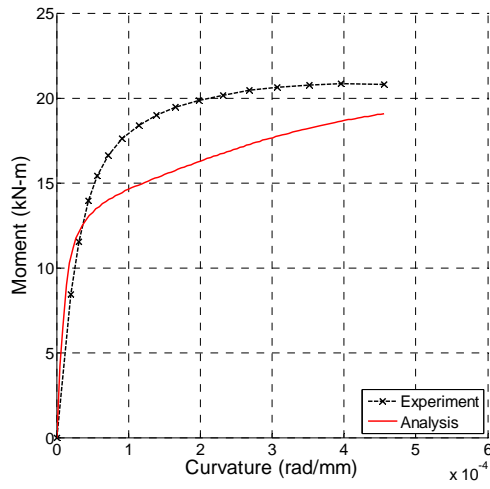
Figure 5-9. Experimental Setup of Pure Bending Tests

The material and geometric properties of each of the specimens is listed in Table 5.3. Experimental and computational moment-curvature or moment-deformation plots are shown in Figure 5-10. Three metrics were computed for comparison of the experimental and computational results. They are: 1) peak moment, the largest moment attained at any time; 2) initial stiffness, computed as the secant stiffness between the state of zero moment and the state of one-third of the peak moment; and 3) area under the curve. Since the peak moment was attained at the end of the test in nearly all cases, the deformation at peak moment was not computed as a metric. These metrics, with corresponding error computations, are listed in Table 5.4.

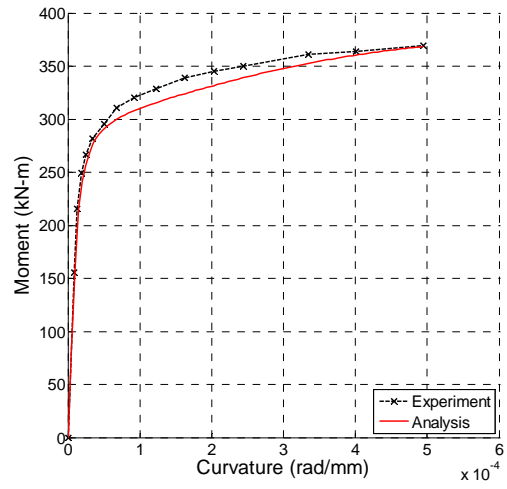
Similar to the stub column tests, both the peak moment and area under the curve show excellent correspondence between the experimental and analytical data each with an average error less than 2 percent. Also similar to the stub column tests is the over estimation of the initial stiffness by the computational model, with an average error of approximately 25 percent, although some tests overestimate the stiffness while others underestimate it.

Table 5.3. Material and Geometric Properties of the Bending Validation Set

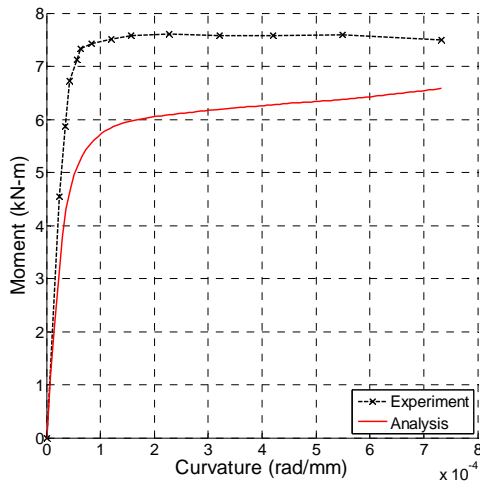
Test #	Author	Year	Specimen	Type of Bending	D (mm)	t (mm)	D/t	f _c (MPa)	F _y (MPa)	Shear Span (mm)	Bending Span (mm)
1	Prion & Bohme	1994	BP3	Direct	152.0	1.70	89.4	73.00	262.0	n/a	300
2	Ichinohe et al.	1991	C06F0M	Direct	300.0	6.23	48.2	58.84	436.3	n/a	600
3	Elchalakani et al.	2001	CBC0-C	Direct	109.9	1.00	109.9	23.40	400.0	n/a	800
4	Elchalakani et al.	2001	CBC0-B	Direct	110.4	1.25	88.3	23.40	400.0	n/a	800
5	Elchalakani et al.	2001	CBC0-A	Direct	110.9	1.50	73.9	23.40	400.0	n/a	800
6	Elchalakani et al.	2001	CBC2	Direct	88.6	2.79	31.8	23.40	432.0	n/a	800
7	Elchalakani et al.	2001	CBC6	Direct	76.2	3.24	23.5	23.40	456.0	n/a	800
8	Elchalakani et al.	2001	CBC1	Direct	101.8	2.53	40.2	23.40	365.0	n/a	800
9	Elchalakani et al.	2001	CBC3	Direct	76.3	2.45	31.2	23.40	415.0	n/a	800
10	Elchalakani et al.	2001	CBC5	Direct	60.7	2.44	24.9	23.40	456.0	n/a	800
11	Wheeler & Bridge	2004	TBP002	Four Point	406.0	6.40	63.4	40.00	351.0	1300	1200
12	Wheeler & Bridge	2004	TBP003	Four Point	406.0	6.40	63.4	55.00	351.0	1300	1200
13	Wheeler & Bridge	2004	TBP005	Four Point	456.0	6.40	71.3	48.00	351.0	1300	1200
14	Wheeler & Bridge	2004	TBP006	Four Point	456.0	6.40	71.3	56.00	351.0	1300	1200
15	Han et al.	2006	CVA-1	Four Point	100.0	1.90	52.6	65.04	282.0	350	700
16	Han et al.	2006	CVB-1	Four Point	200.0	1.90	105.3	65.04	282.0	350	700
17	Han et al.	2006	CB1-1	Four Point	140.0	3.00	46.7	41.20	235.0	210	420
18	Han et al.	2006	CB2-1	Four Point	140.0	3.00	46.7	41.20	235.0	420	840
19	Han et al.	2006	CB4-1	Four Point	180.0	3.00	60.0	50.08	235.0	225	450
20	Han et al.	2006	CB5-1	Four Point	180.0	3.00	60.0	50.08	235.0	450	900
21	Han et al.	2006	CB2-2	Three Point	140.0	3.00	46.7	41.20	235.0	420	n/a
22	Han et al.	2006	CB3-2	Three Point	140.0	3.00	46.7	41.20	235.0	840	n/a
23	Han et al.	2006	CB5-2	Three Point	180.0	3.00	60.0	50.08	235.0	450	n/a
24	Han et al.	2006	CB6-2	Three Point	180.0	3.00	60.0	50.08	235.0	900	n/a



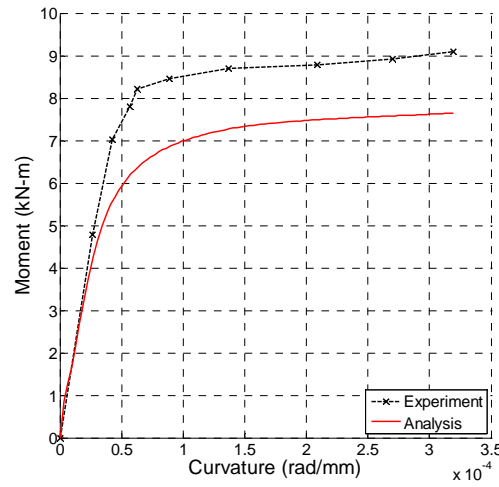
(a) Test #1; Prion & Bohme 1994; Specimen: BP3



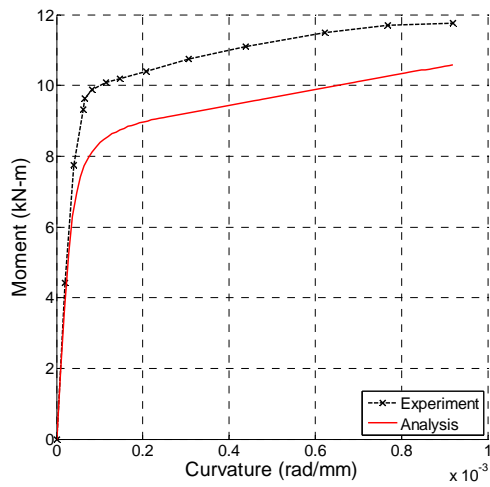
(b) Test #2; Ichinohe et al. 1991; Specimen: C06F0M



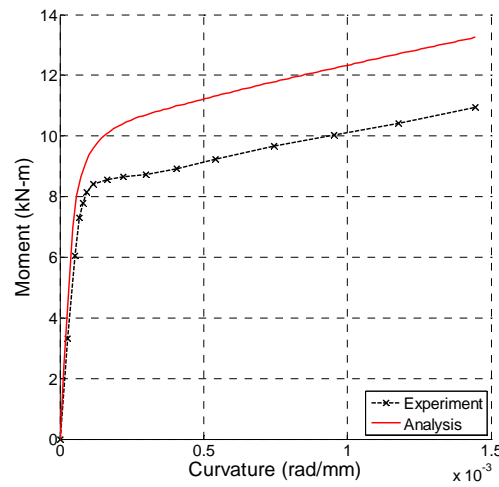
(c) Test #3; Elchalakani et al. 2001; Specimen: CBC0-C



(d) Test #4; Elchalakani et al. 2001; Specimen: CBC0-B

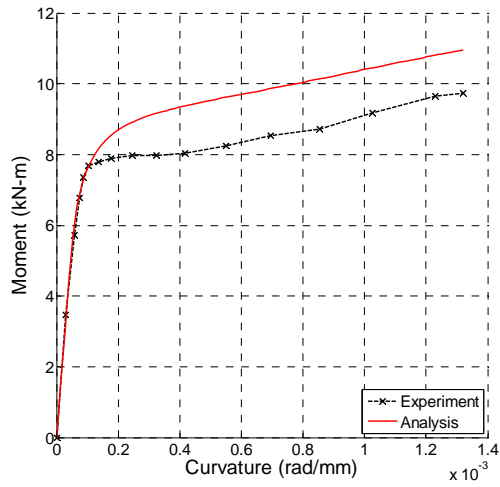


(e) Test #5; Elchalakani et al. 2001; Specimen: CBC0-A

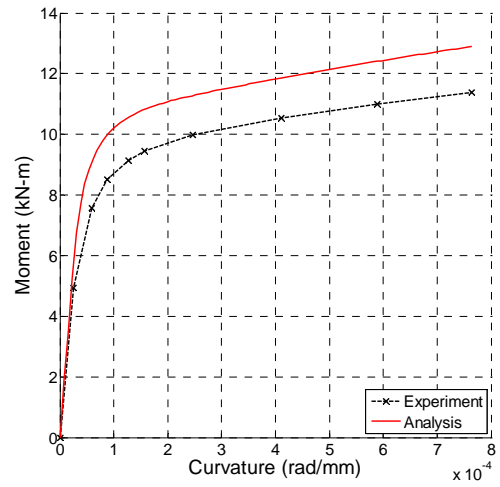


(f) Test #6; Elchalakani et al. 2001; Specimen: CBC2

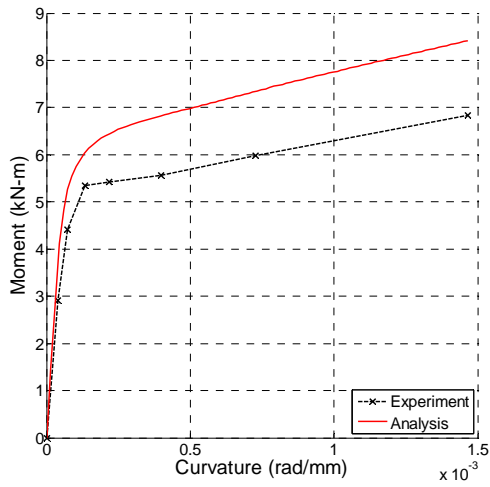
Figure 5-10. Validation Results for Beams



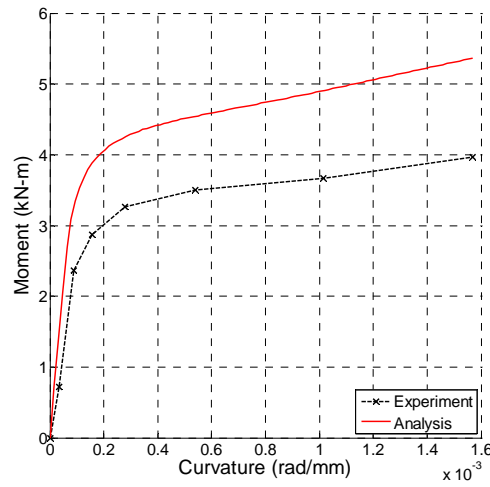
(g) Test #7; Elchalakani et al. 2001; Specimen: CBC6



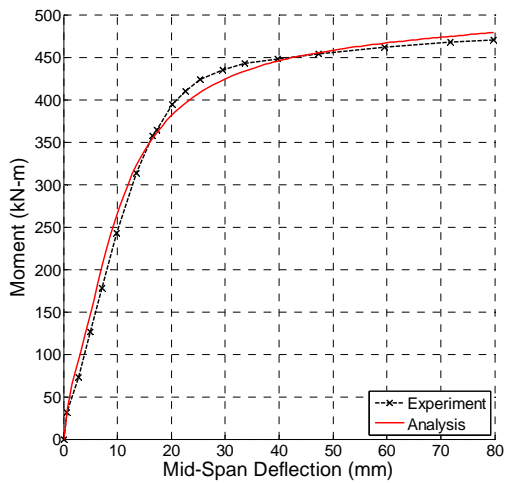
(h) Test #8; Elchalakani et al. 2001; Specimen: CBC1



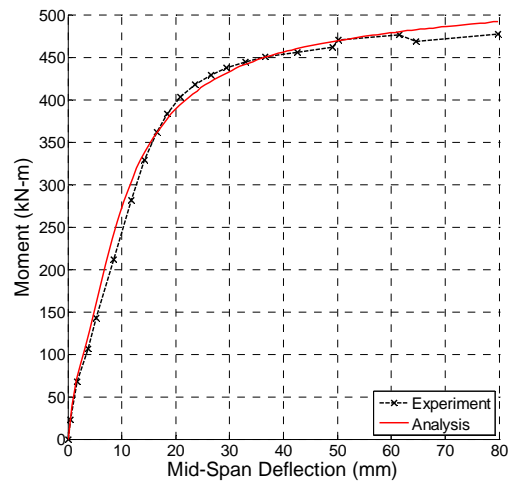
(i) Test #9; Elchalakani et al. 2001; Specimen: CBC3



(j) Test #10; Elchalakani et al. 2001; Specimen: CBC5

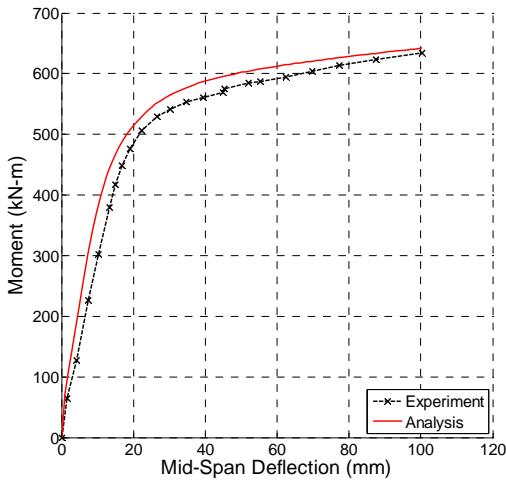


(k) Test #11; Wheeler & Bridge 2004; Specimen: TBP002

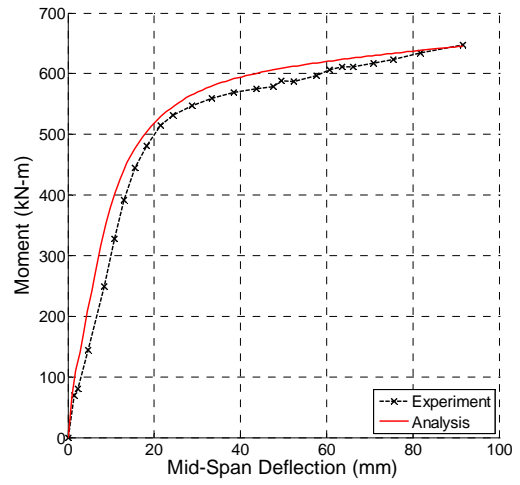


(l) Test #12; Wheeler & Bridge 2004; Specimen: TBP003

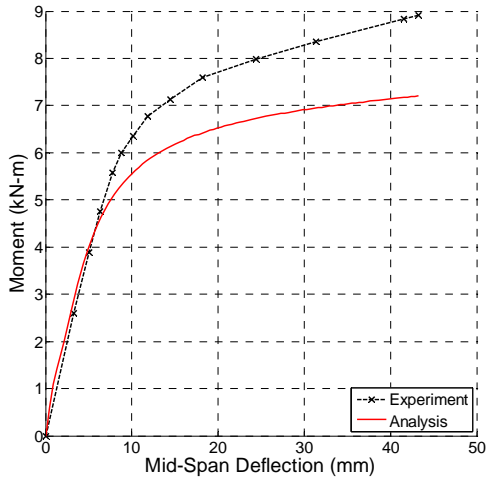
Figure 5-10. Validation Results for Beams (continued)



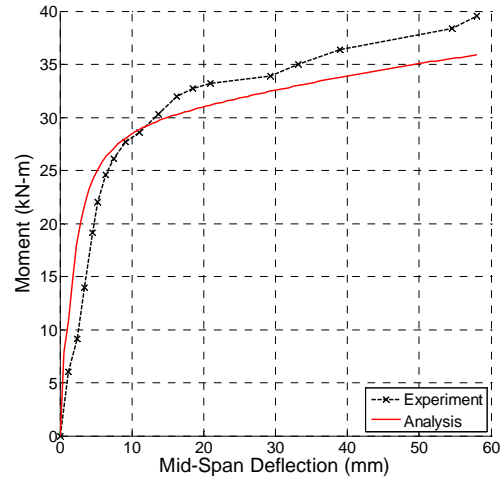
(m) Test #13; Wheeler & Bridge 2004; Specimen: TBP005



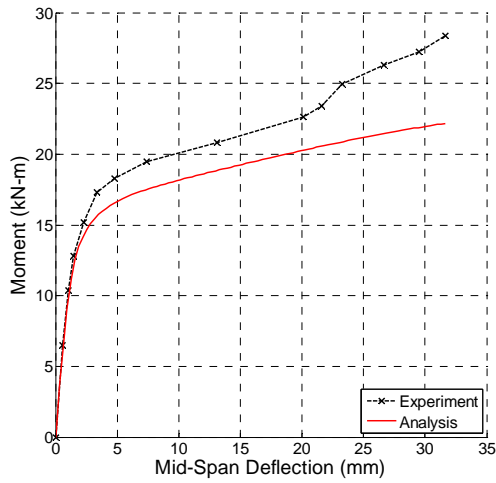
(n) Test #14; Wheeler & Bridge 2004; Specimen: TBP006



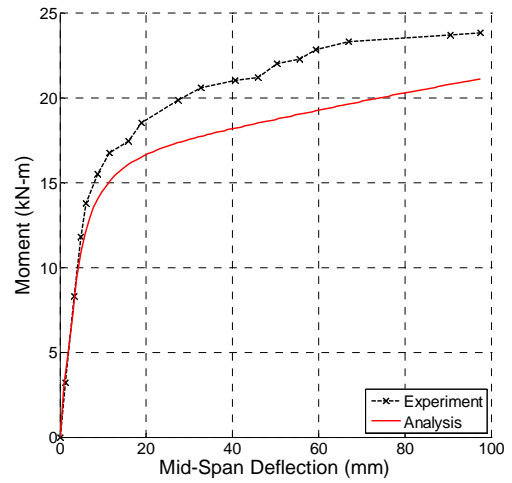
(o) Test #15; Han et al. 2006; Specimen: CVA-1



(p) Test #16; Han et al. 2006; Specimen: CVB-1

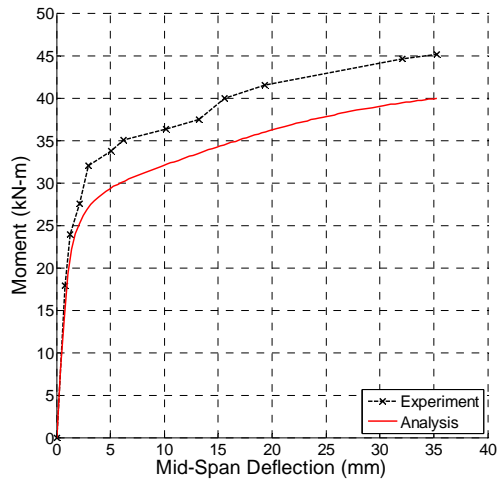


(q) Test #17; Han et al. 2006; Specimen: CB1-1

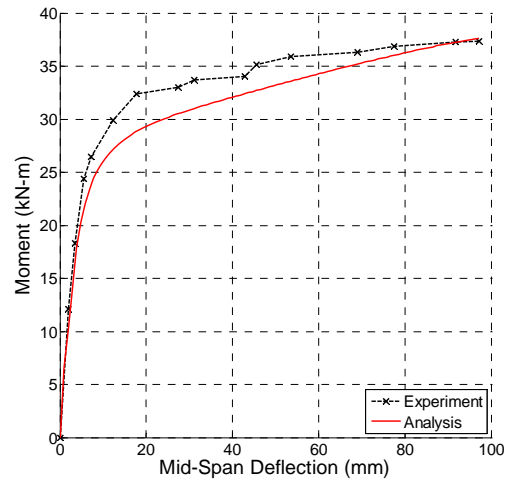


(r) Test #18; Han et al. 2006; Specimen: CB2-1

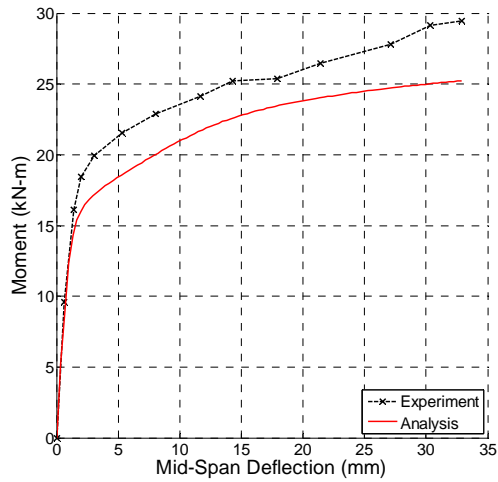
Figure 5-10. Validation Results for Beams (continued)



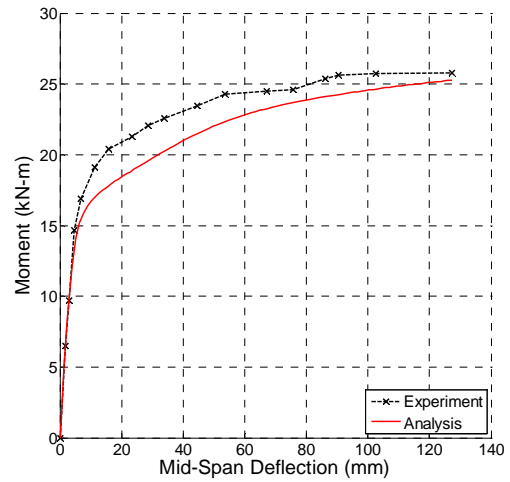
(s) Test #19; Han et al. 2006; Specimen: CB4-1



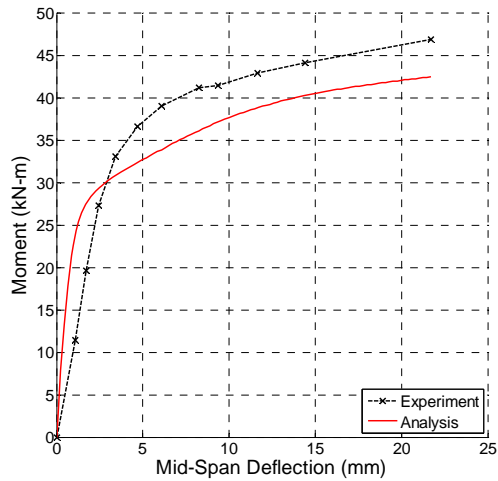
(t) Test #20; Han et al. 2006; Specimen: CB5-1



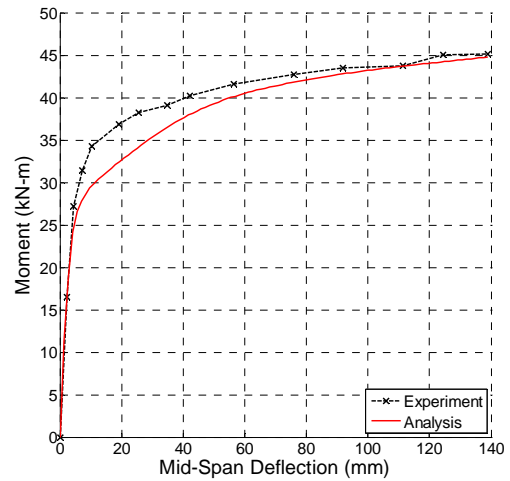
(u) Test #21; Han et al. 2006; Specimen: CB2-2



(v) Test #22; Han et al. 2006; Specimen: CB3-2



(w) Test #23; Han et al. 2006; Specimen: CB5-2



(x) Test #24; Han et al. 2006; Specimen: CB6-2

Figure 5-10. Validation Results for Beams (continued)

Table 5.4. Comparison Metrics for Bending Validation

Test #	Peak Moment (kN-m)			Initial Stiffness (kN-m/mm)			Area under Curve (kN-m/mm)			
	Expt.	Model	% Error	Expt.	Model	% Error	Expt.	Model	% Error	
1	20.83	19.07	-8.45%	425,187	713,183	67.73%	0.008450	0.007322	-13.35%	
2	369.50	368.44	-0.29%	19,016,800	15,994,400	-15.89%	0.166418	0.162167	-2.55%	
3	7.61	6.58	-13.52%	189,652	139,399	-26.50%	0.005367	0.004375	-18.47%	
4	9.09	7.65	-15.87%	181,984	168,539	-7.39%	0.002559	0.002146	-16.12%	
5	11.77	10.58	-10.13%	228,301	194,104	-14.98%	0.009858	0.008533	-13.44%	
6	10.94	13.25	21.18%	119,498	165,021	38.10%	0.013517	0.016463	21.79%	
7	9.74	10.97	12.59%	116,889	111,602	-4.52%	0.010998	0.012476	13.44%	
8	11.38	12.90	13.39%	191,937	229,590	19.62%	0.007561	0.008613	13.93%	
9	6.83	8.42	23.19%	72,287	95,081	31.53%	0.008547	0.010462	22.40%	
10	3.97	5.37	35.27%	24,739	44,100	78.26%	0.005349	0.007150	33.67%	
Test #	Peak Moment (kN-m)			Initial Stiffness (kN-m/mm)			Area under Curve (kN-m-mm)			
	Expt.	Model	% Error	Expt.	Model	% Error	Expt.	Model	% Error	
11	469.98	478.92	1.90%	25.20	29.34	16.43%	31,515	31,723	0.66%	
12	477.08	491.92	3.11%	26.60	30.54	14.81%	32,001	32,496	1.55%	
13	634.52	642.08	1.19%	30.54	43.97	43.95%	52,672	55,256	4.90%	
14	647.95	645.60	-0.36%	30.01	45.01	49.98%	48,151	50,298	4.46%	
15	8.92	7.21	-19.22%	0.78	0.90	15.18%	302	258	-14.49%	
16	39.58	35.87	-9.39%	4.08	8.98	120.38%	1,860	1,798	-3.33%	
17	28.39	22.17	-21.92%	10.24	9.80	-4.37%	678	591	-12.84%	
18	23.80	21.09	-11.37%	2.51	2.46	-1.83%	1,998	1,738	-13.02%	
19	45.12	39.95	-11.47%	23.79	19.89	-16.40%	1,364	1,197	-12.19%	
20	37.36	37.65	0.77%	5.87	5.02	-14.50%	3,245	3,078	-5.13%	
21	29.48	25.23	-14.42%	15.18	13.93	-8.19%	804	716	-11.01%	
22	25.79	25.27	-2.02%	3.38	3.48	2.96%	2,948	2,761	-6.33%	
23	46.86	42.44	-9.44%	11.10	29.67	167.37%	840	783	-6.78%	
24	45.14	44.77	-0.81%	7.41	7.26	-2.00%	5,629	5,413	-3.84%	
<i>Mean</i>			-1.50%				22.91%			
<i>Standard Deviation</i>			14.20%				46.83%			
<i>Median</i>			-1.42%				8.89%			

5.5 Monotonic Proportionally Loaded Beam-Column Experiments

Proportionally loaded beam-column experiments are typically performed to determine the interaction of axial load and bending moment. In most cases the beam-columns are slender enough to experience detrimental second order effects. The eccentricity is introduced by loading the columns off center; the specimens studied in this section have the same eccentricity at both ends (Figure 5-11).

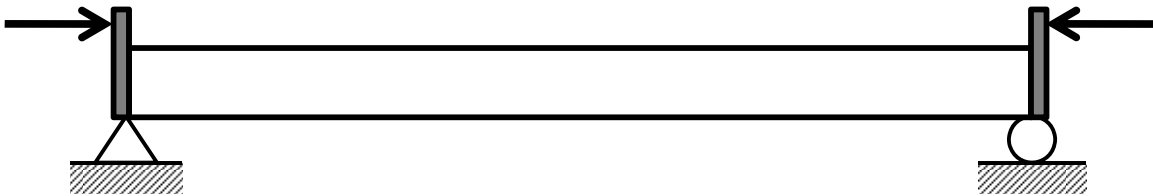


Figure 5-11. Experimental Set of Proportionally Loaded Beam-Column Tests

A preliminary mesh refinement study indicated some variation of the results with the number of elements and sections. This is in contrast to the stub column and bending results and is likely due to the geometric nonlinear effects and variation of strain along the length of the member. The results of a portion of the mesh refinement study are shown in Figure 5-12. The material and geometric properties for this analysis are that of specimen 21 from the proportionally loaded beam-column set. Results are shown for two elements and four elements along the length of the member. The number of integration points was found to have little effect on the results, these analyses have three integration points per element. Also shown are comparable analyses using the displacement-based and force-based elements available in OpenSees (2009). As can be seen, the mixed formulation with two elements yields a peak load near the converged value, but low post-peak strength. With four elements along the length of the member, the results are nearly converged for the entire response. Both the force and displacement formulations with two elements overestimate the strength of the column; however, the force-based element with two elements provides post-peak strength nearly converged. With four elements, the overestimation of the peak strength is less and the post-peak strength is near converged.

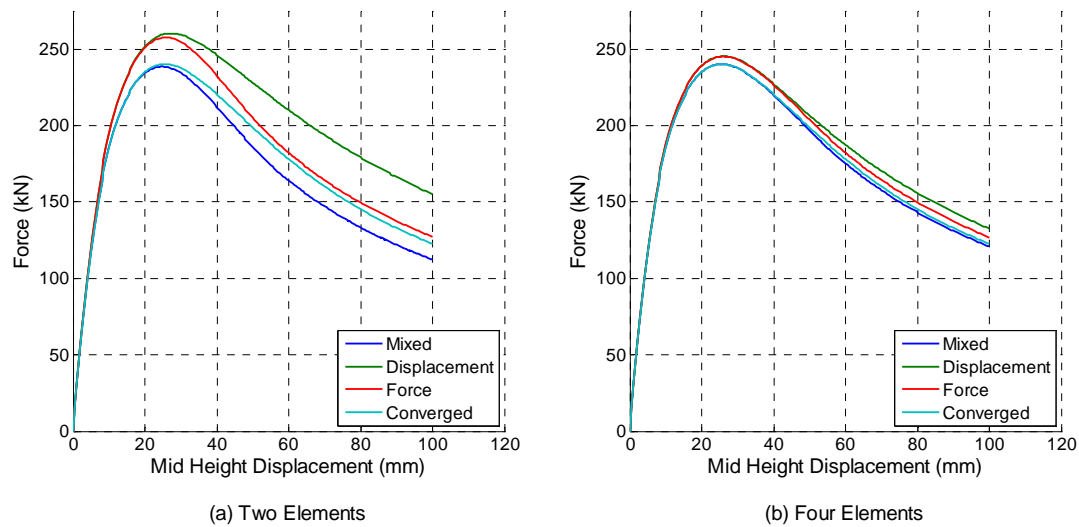


Figure 5-12. Mesh Refinement Study for Proportionally Loaded Beam-Columns

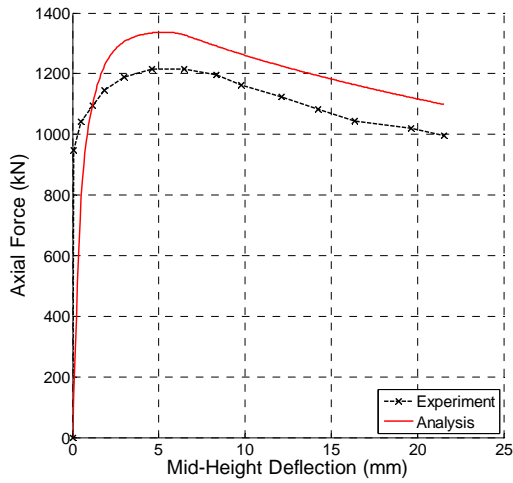
The analyses shown in this section were performed with four elements along the length of the column, with three integration points per member. Noting the two-dimensional nature of these tests, the fiber discretization took the form of strips, with 50 strips along the height of the section for each the steel and concrete. The fiber discretization was selected such that it was dense enough to not affect the accuracy of the results within a small tolerance. Analyses were run in displacement control, up to the same the peak deformation as experienced in the experiment.

The material and geometric properties of each of the specimens is listed in Table 5.5. Experimental and computational load-deformation plots are shown in Figure 5-13. Four metrics were computed for comparison of the experimental and computational results. They are: 1) peak load, the largest load attained at any time; 2) deflection at peak load; 3) initial stiffness, computed as the secant stiffness between the state of zero load and the state of one-third of the peak load. 4) area under the curve. These metrics, with corresponding error computations, are listed in Table 5.6.

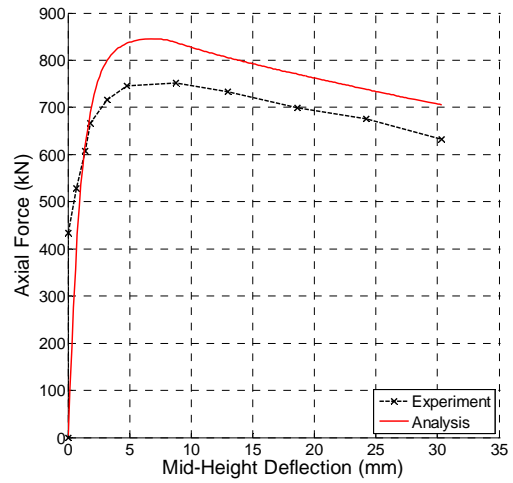
The peak load and area under the curve show excellent correspondence between the experimental and analytical results with an average error of less than 5 percent for each. Opposite to that of the stub column and bending test comparisons, the initial stiffness is underestimated by approximately 20 percent on average in these beam-column comparisons. The deformation at the peak load shows good correspondence, with an average error of approximately 15 percent.

Table 5.5. Material and Geometric Properties of the Proportionally Loaded Column Validation Set

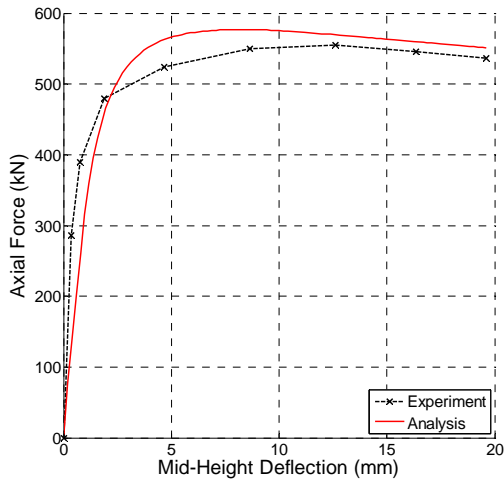
Test #	Author	Year	Specimen	D (mm)	t (mm)	D/t	f _c (MPa)	F _v (MPa)	L (mm)	L/D	e (mm)	e/D
1	Matsui & Tsuda	1996	C4-1	165.2	4.50	36.7	31.87	413.8	661	4.00	20.7	0.125
2	Matsui & Tsuda	1996	C4-3	165.2	4.50	36.7	31.87	413.8	661	4.00	62.0	0.375
3	Matsui & Tsuda	1996	C4-5	165.2	4.50	36.7	31.87	413.8	661	4.00	103.2	0.625
4	Matsui & Tsuda	1996	C12-1	165.2	4.50	36.7	31.87	413.8	1982	12.00	20.7	0.125
5	Matsui & Tsuda	1996	C12-3	165.2	4.50	36.7	31.87	413.8	1982	12.00	62.0	0.375
6	Matsui & Tsuda	1996	C12-5	165.2	4.50	36.7	31.87	413.8	1982	12.00	103.2	0.625
7	Matsui & Tsuda	1996	C24-1	165.2	4.50	36.7	31.87	413.8	3965	24.00	20.7	0.125
8	Matsui & Tsuda	1996	C24-3	165.2	4.50	36.7	31.87	413.8	3965	24.00	62.0	0.375
9	Matsui & Tsuda	1996	C24-5	165.2	4.50	36.7	31.87	413.8	3965	24.00	103.2	0.625
10	Kilpatrick & Rangan	1999	SC-0	76.0	2.20	34.5	58.00	435.0	802	10.55	15.0	0.197
11	Kilpatrick & Rangan	1999	SC-1	76.0	2.20	34.5	58.00	435.0	1032	13.58	15.0	0.197
12	Kilpatrick & Rangan	1999	SC-2	76.0	2.20	34.5	58.00	435.0	1262	16.61	15.0	0.197
13	Kilpatrick & Rangan	1999	SC-3	76.0	2.20	34.5	58.00	435.0	1487	19.57	15.0	0.197
14	Kilpatrick & Rangan	1999	SC-4	76.0	2.20	34.5	58.00	435.0	1717	22.59	15.0	0.197
15	Kilpatrick & Rangan	1999	SC-5	76.0	2.20	34.5	58.00	435.0	1947	25.62	15.0	0.197
16	Kilpatrick & Rangan	1999	SC-6	76.0	2.20	34.5	58.00	435.0	2172	28.58	15.0	0.197
17	Kilpatrick & Rangan	1999	SC-7	76.0	2.20	34.5	58.00	435.0	2402	31.61	15.0	0.197
18	Kilpatrick & Rangan	1999	SC-9	101.7	2.40	42.4	58.00	410.0	1947	19.14	10.0	0.098
19	Kilpatrick & Rangan	1999	SC-10	101.7	2.40	42.4	58.00	410.0	1947	19.14	15.0	0.147
20	Kilpatrick & Rangan	1999	SC-11	101.7	2.40	42.4	58.00	410.0	1947	19.14	20.0	0.197
21	Kilpatrick & Rangan	1999	SC-12	101.7	2.40	42.4	58.00	410.0	1947	19.14	25.0	0.246
22	Kilpatrick & Rangan	1999	SC-13	101.7	2.40	42.4	58.00	410.0	1947	19.14	30.0	0.295
23	Kilpatrick & Rangan	1999	SC-14	101.7	2.40	42.4	58.00	410.0	1947	19.14	40.0	0.393
24	Kilpatrick & Rangan	1999	SC-15	101.7	2.40	42.4	58.00	410.0	1947	19.14	50.0	0.492



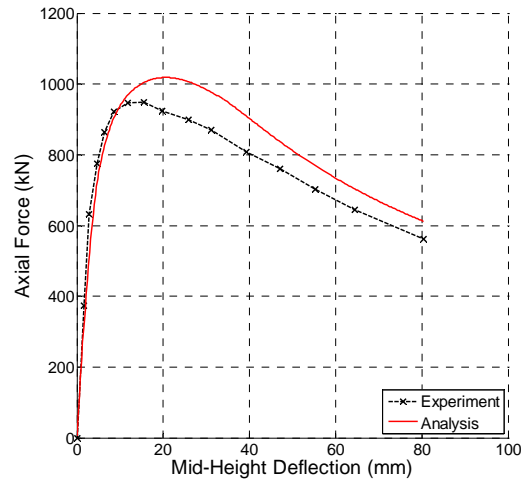
(a) Test #1; Matsui & Tsuda 1996; Specimen: C4-1



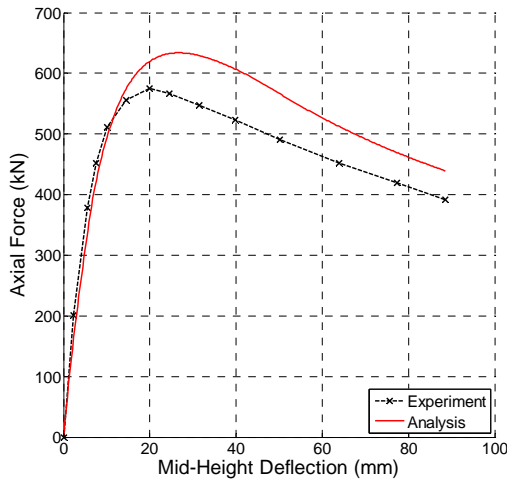
(b) Test #2; Matsui & Tsuda 1996; Specimen: C4-3



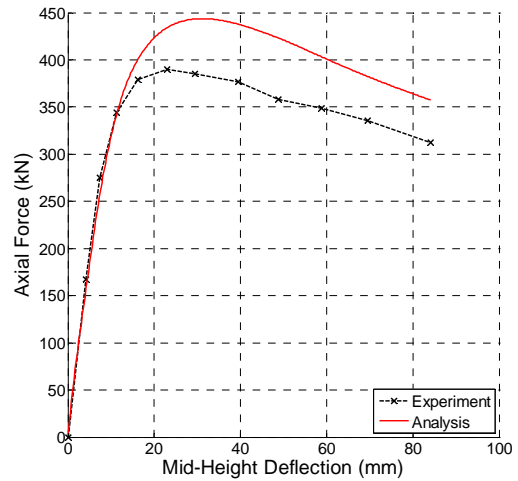
(c) Test #3; Matsui & Tsuda 1996; Specimen: C4-5



(d) Test #4; Matsui & Tsuda 1996; Specimen: C12-1

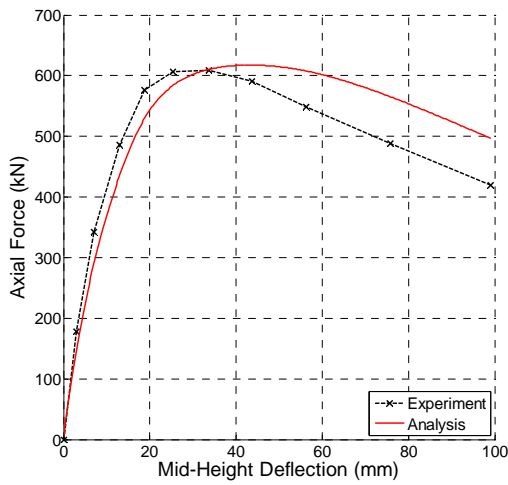


(e) Test #5; Matsui & Tsuda 1996; Specimen: C12-3

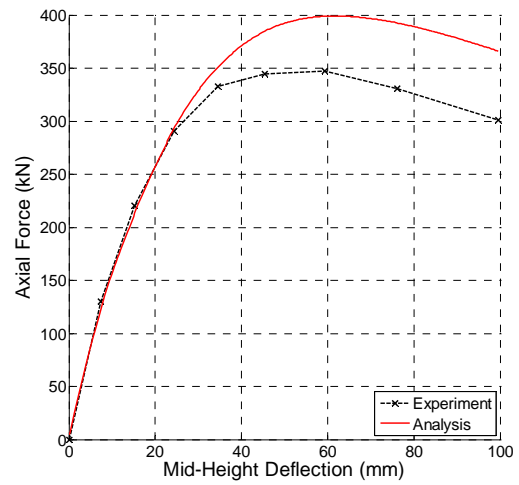


(f) Test #6; Matsui & Tsuda 1996; Specimen: C12-5

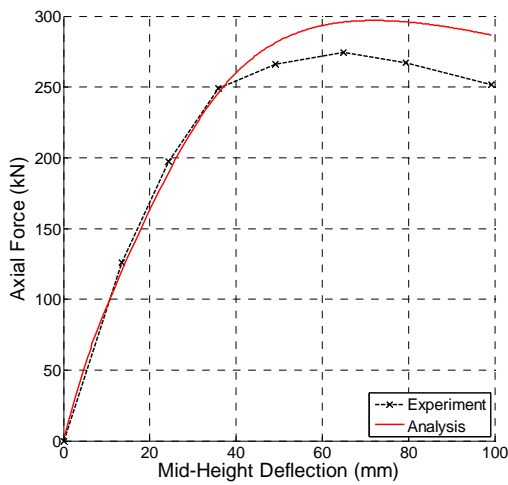
Figure 5-13. Validation Results for Proportionally Loaded Beam-Columns



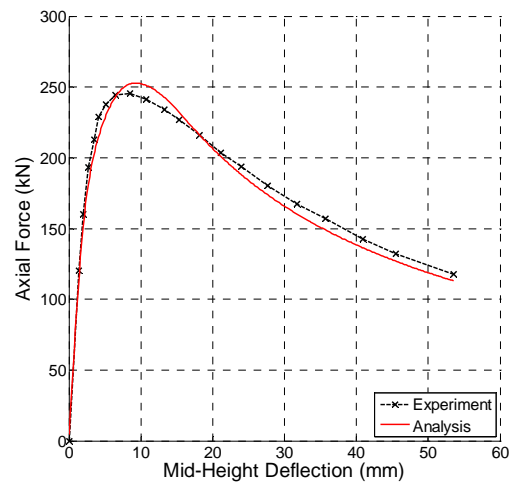
(g) Test #7; Matsui & Tsuda 1996; Specimen: C24-1



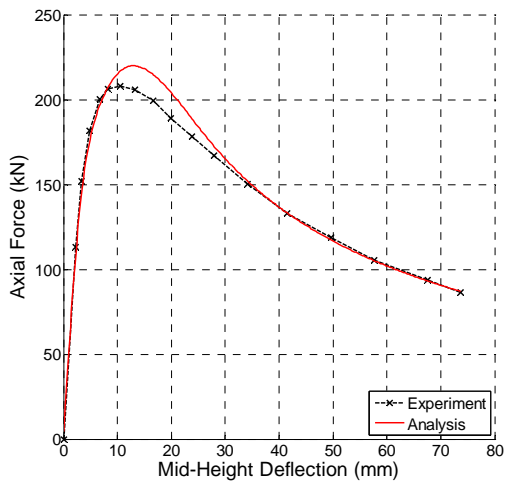
(h) Test #8; Matsui & Tsuda 1996; Specimen: C24-3



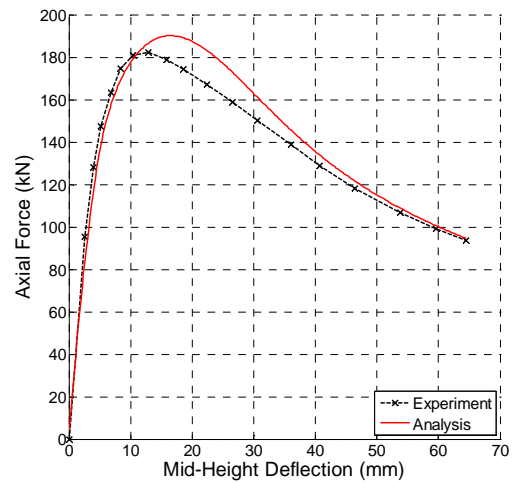
(i) Test #9; Matsui & Tsuda 1996; Specimen: C24-5



(j) Test #10; Kilpatrick & Rangan 1999; Specimen: SC-0

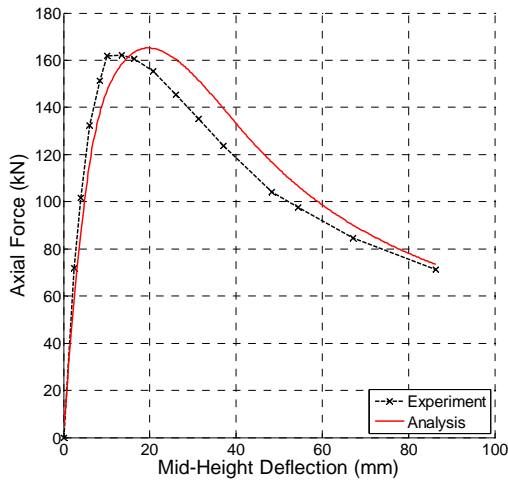


(k) Test #11; Kilpatrick & Rangan 1999; Specimen: SC-1

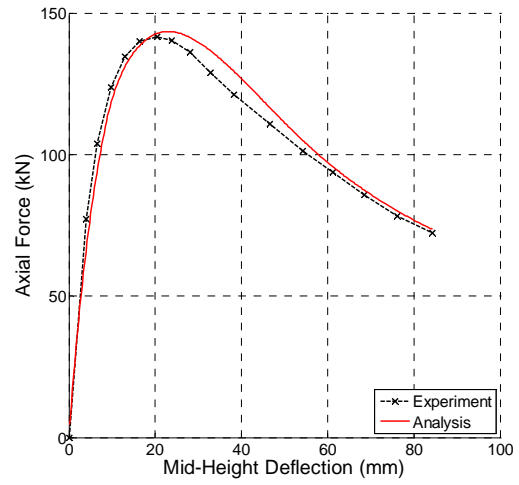


(l) Test #12; Kilpatrick & Rangan 1999; Specimen: SC-2

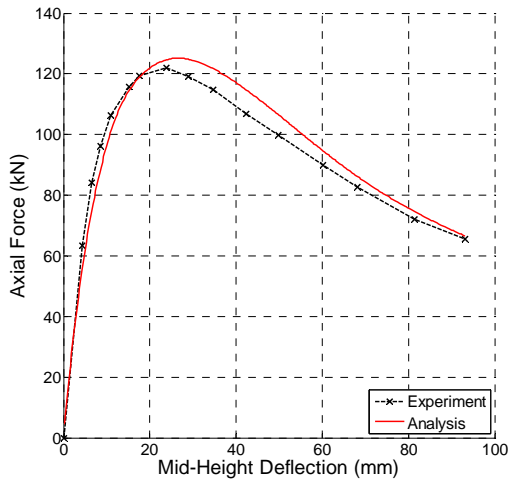
Figure 5-13. Validation Results for Proportionally Loaded Beam-Columns (continued)



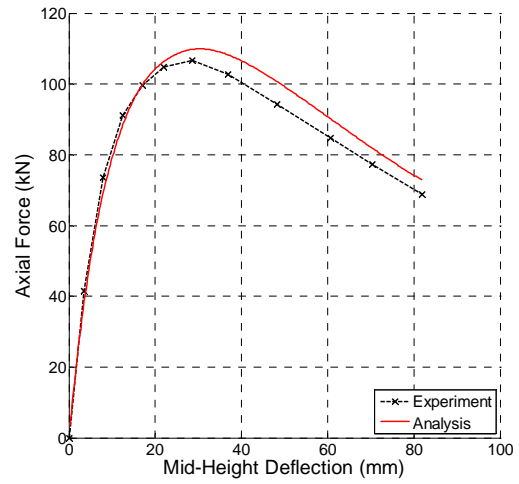
(m) Test #13; Kilpatrick & Rangan 1999; Specimen: SC-3



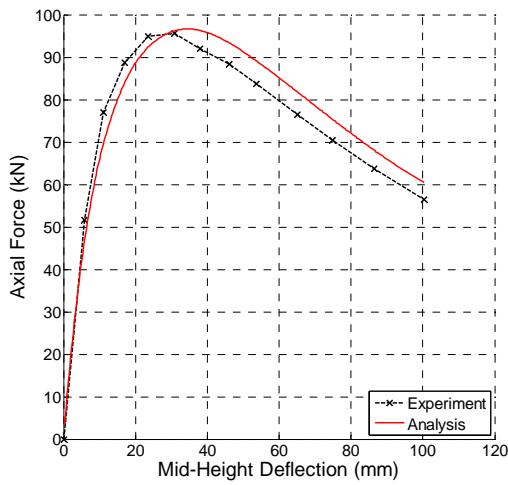
(n) Test #14; Kilpatrick & Rangan 1999; Specimen: SC-4



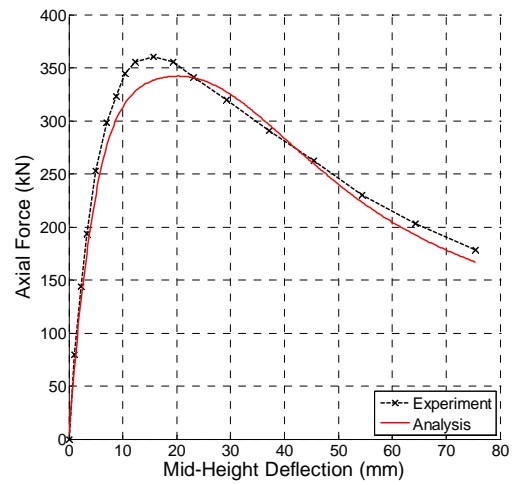
(o) Test #15; Kilpatrick & Rangan 1999; Specimen: SC-5



(p) Test #16; Kilpatrick & Rangan 1999; Specimen: SC-6

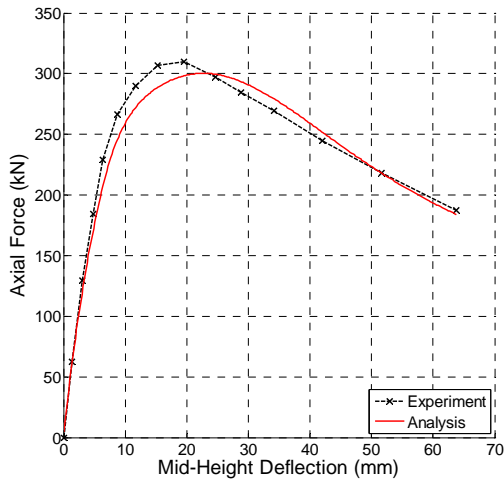


(q) Test #17; Kilpatrick & Rangan 1999; Specimen: SC-7

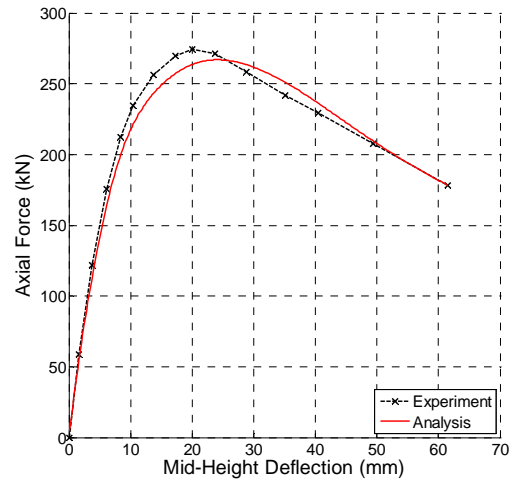


(r) Test #18; Kilpatrick & Rangan 1999; Specimen: SC-9

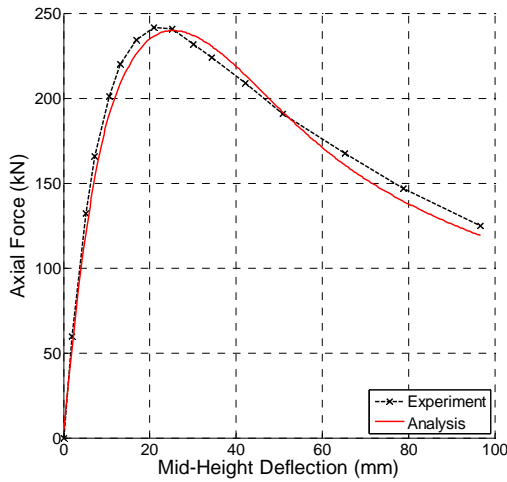
Figure 5-13. Validation Results for Proportionally Loaded Beam-Columns (continued)



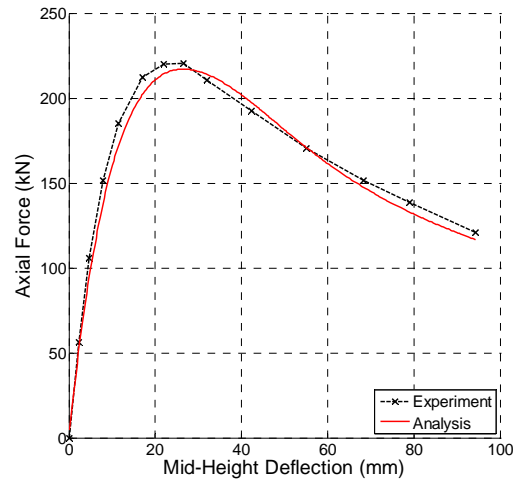
(s) Test #19; Kilpatrick & Rangan 1999; Specimen: SC-10



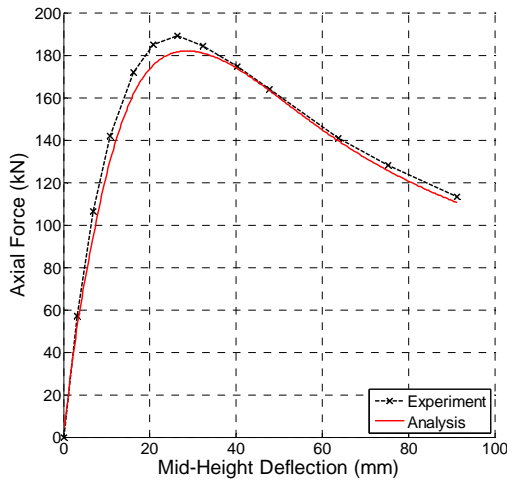
(t) Test #20; Kilpatrick & Rangan 1999; Specimen: SC-11



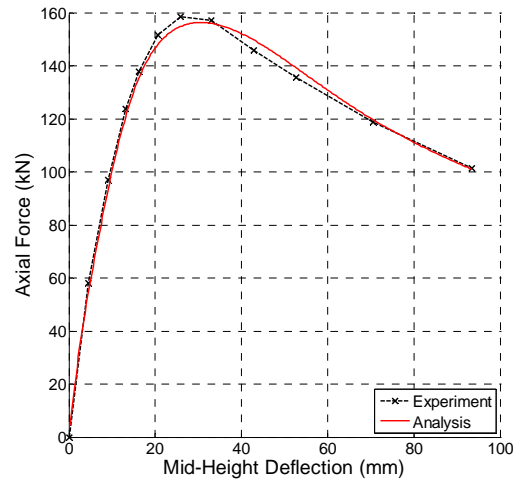
(u) Test #21; Kilpatrick & Rangan 1999; Specimen: SC-12



(v) Test #22; Kilpatrick & Rangan 1999; Specimen: SC-13



(w) Test #23; Kilpatrick & Rangan 1999; Specimen: SC-14



(x) Test #24; Kilpatrick & Rangan 1999; Specimen: SC-15

Figure 5-13. Validation Results for Proportionally Loaded Beam-Columns (continued)

Table 5.6. Comparison Metrics for Proportionally Loaded Beam-Column Data

Test #	Peak Load (kN)			Strain at Peak Load (mm)			Initial Stiffness (kN/mm)			Area under Curve (kN-mm)		
	Expt.	Model	% Error	Expt.	Model	% Error	Expt.	Model	% Error	Expt.	Model	% Error
1	1,215.1	1,337.2	10.05%	6.472	5.309	-17.97%	19,736.8	1,799.4	-90.88%	23,993	25,846	7.73%
2	751.7	845.6	12.49%	8.779	6.824	-22.27%	10,590.6	603.7	-94.30%	21,102	23,027	9.12%
3	555.1	577.2	3.98%	12.605	8.241	-34.62%	839.4	342.7	-59.18%	10,229	10,478	2.44%
4	947.8	1,018.3	7.43%	15.605	20.620	32.14%	241.1	194.5	-19.35%	61,013	65,837	7.91%
5	575.6	633.8	10.12%	19.873	26.557	33.63%	88.2	66.6	-24.48%	41,725	46,162	10.63%
6	389.6	443.7	13.89%	22.937	31.123	35.69%	40.3	37.9	-5.86%	28,329	31,924	12.69%
7	608.6	617.5	1.46%	33.687	43.283	28.49%	56.9	45.8	-19.50%	49,693	52,584	5.82%
8	347.2	399.1	14.94%	59.383	61.776	4.03%	17.6	16.3	-7.10%	28,974	32,558	12.37%
9	274.3	297.0	8.26%	64.996	72.078	10.90%	9.4	9.4	-0.05%	21,917	23,294	6.29%
10	245.3	252.7	3.05%	8.490	9.271	9.20%	89.0	86.8	-2.53%	9,536	9,362	-1.82%
11	208.0	219.9	5.73%	10.522	13.008	23.63%	51.2	51.7	1.10%	10,457	10,673	2.07%
12	182.1	190.1	4.42%	12.887	16.534	28.30%	37.8	34.1	-9.82%	8,760	9,064	3.47%
13	162.1	165.2	1.91%	13.414	19.561	45.82%	30.0	24.3	-19.16%	9,606	10,090	5.03%
14	141.6	143.5	1.33%	20.445	23.057	12.77%	19.7	18.0	-8.61%	8,941	9,113	1.93%
15	122.0	125.2	2.63%	23.791	26.696	12.21%	14.6	13.8	-5.27%	8,641	8,905	3.05%
16	106.6	109.9	3.08%	28.657	30.286	5.68%	12.0	11.0	-8.11%	7,066	7,342	3.91%
17	95.6	96.6	1.07%	30.925	34.463	11.44%	9.0	8.9	-0.78%	7,576	7,809	3.08%
18	360.7	342.1	-5.16%	15.655	20.132	28.60%	66.7	59.9	-10.22%	20,090	19,503	-2.92%
19	309.7	300.3	-3.01%	19.546	22.749	16.38%	43.8	41.1	-6.13%	15,551	15,399	-0.97%
20	274.6	267.0	-2.80%	20.016	24.198	20.89%	33.8	31.6	-6.62%	13,467	13,378	-0.66%
21	241.4	239.8	-0.67%	20.897	25.456	21.81%	27.2	25.7	-5.82%	17,354	17,001	-2.03%
22	220.6	217.1	-1.58%	26.583	26.397	-0.70%	23.6	21.5	-8.72%	15,690	15,400	-1.85%
23	189.1	182.0	-3.75%	26.442	28.596	8.15%	17.2	15.9	-7.85%	13,315	12,962	-2.66%
24	158.5	156.3	-1.38%	25.923	30.537	17.80%	13.0	12.3	-5.32%	11,591	11,602	0.10%
Mean			3.64%			13.83%			-17.69%			3.53%
Standard Deviation			5.69%			18.89%			26.05%			4.76%
Median			2.84%			14.58%			-7.98%			3.06%

5.6 Monotonic Non-Proportionally Loaded Beam-Column Experiments

Non-proportional loading better represents the loading of beam-columns in moment resisting frames in earthquakes than proportional loading. For the case of the specimens examined in this section, the axial load is first applied and then a bending moment is applied at each end (Figure 5-14). Under this configuration, the ability of the formulation to model a load reversal is also tested, as some of the fibers are first in compression then in tension.

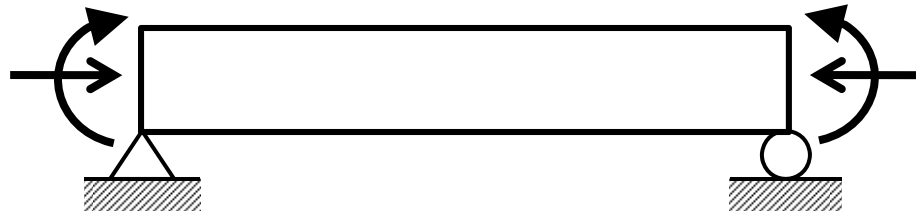


Figure 5-14. Experimental Setup of Non-Proportionally Loaded Beam-Column Tests

A preliminary mesh refinement study indicated significant variation of the results with the number of elements and sections. The results of a portion of the mesh refinement study are shown in Figure 5-15. The material and geometric properties for this analysis are that of specimen 12 from the proportionally loaded beam-column set. Results are shown for one, three, and five elements along the length of the member; the number of integration points for all analyses was three. The pre-peak behavior is the same for all three analyses. The post-peak behavior is strongly dependent on the number of elements, with steeper descending branches seen from denser meshes.

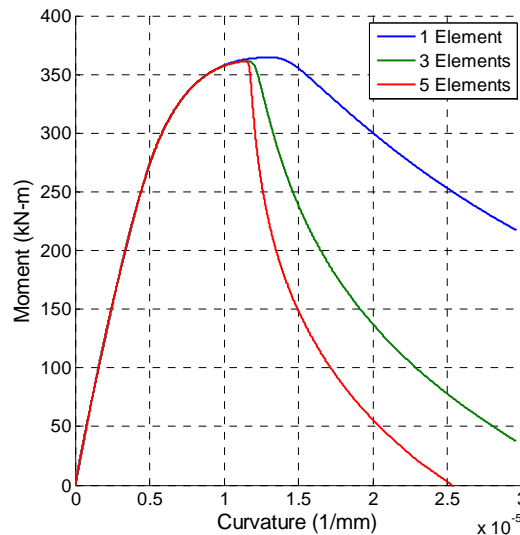


Figure 5-15. Mesh Refinement Study for Non-Proportionally Loaded Beam-Columns

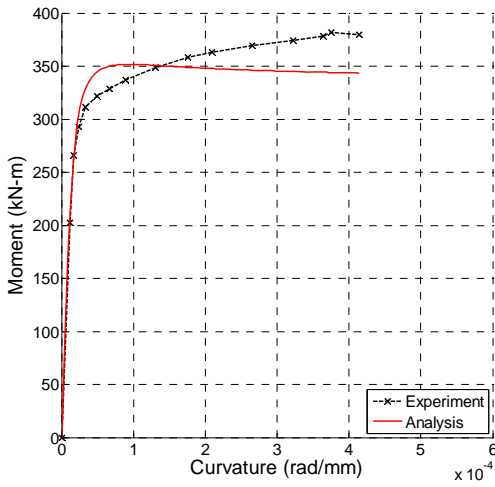
The behavior seen in Figure 5-15 is likely due to localization, a phenomenon where softening at the section level causes a loss of objectivity. Under high axial loads, the section response does experience softening. Localization has been studied for force-based elements (Coleman and Spacone 2001; Scott and Fenves 2006). Two general solutions have been proposed, the first is the alteration of the softening slope of the constitutive relations, and the second is to ensure that the numerical integration is performed such that the softening effects are distributed along the appropriate length of the member, i.e., the plastic hinge length. Thus, the mesh density of the analyses presented in this section was selected such that the length influenced by the integration points is approximately the same as the plastic hinge length, assumed to be approximately the diameter of the section. As such, the analyses were performed with one element along the length of the column and three integration points. Noting the two-dimensional nature of these tests, the fiber discretization took the form of strips, with 50 strips along the height of the section for each the steel and concrete. The fiber discretization was selected such that it was dense enough to not affect the accuracy of the results within a small tolerance. Analyses were run in displacement control, up to the same peak deformation as experienced in the experiment.

The material and geometric properties of each of the specimens is listed in Table 5.7. Experimental and computational load-deformation plots are shown in Figure 5-16. Four metrics were computed for comparison of the experimental and computational results. They are: 1) peak moment, the largest moment attained at any time; 2) curvature at peak moment; 3) initial stiffness, computed as the secant stiffness between the state of zero moment and the state of one-third of the peak moment. 4) area under the curve. These metrics, with corresponding error computations, are listed in Table 5.8.

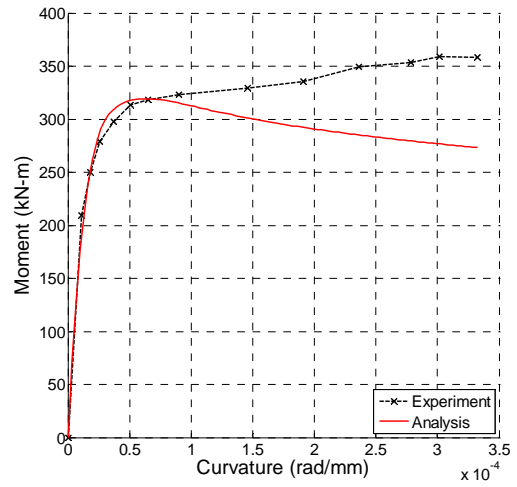
The peak moment and area under the curve show excellent correspondence with an average error of less than 5 percent each. The curvature at peak moment is underestimated on average by approximately 40 percent while the initial stiffness shows good correspondence, with an over approximation of approximately 10 percent.

Table 5.7. Material and Geometric Properties of the Non-Proportionally Loaded Column Validation Set

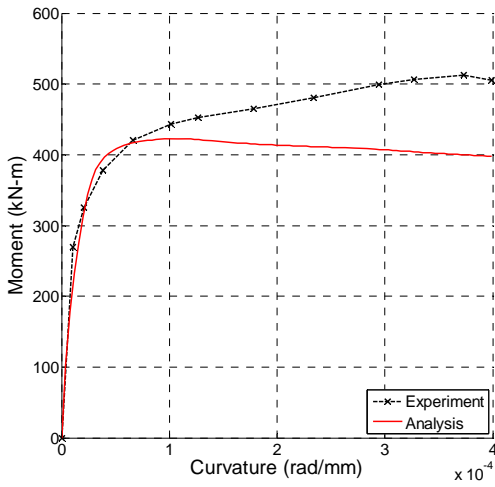
Test #	Author	Year	Specimen	D (mm)	t (mm)	D/t	f _c (MPa)	F _v (MPa)	L (mm)	L/D	P (kN)	P/P _o
1	Ichinohe et al.	1991	C06F3M	300.0	5.83	51.5	64.33	420.2	600	2.0	1,932	0.30
2	Ichinohe et al.	1991	C06F5M	300.0	5.83	51.5	61.88	420.2	600	2.0	3,217	0.51
3	Ichinohe et al.	1991	C08F5M	300.0	8.40	35.7	65.31	400.7	600	2.0	3,481	0.48
4	Ichinohe et al.	1991	C12F5M	300.0	11.70	25.6	66.19	380.0	600	2.0	4,070	0.51
5	Nishiyama et al.	2002	EC4-A-4-035	150.0	2.96	50.7	39.90	283.0	450	3.0	363	0.35
6	Nishiyama et al.	2002	EC4-A-4-06	150.0	2.96	50.7	39.90	283.0	450	3.0	612	0.59
7	Nishiyama et al.	2002	EC4-C-2-035	300.0	2.96	101.4	24.50	283.0	900	3.0	832	0.34
8	Nishiyama et al.	2002	EC4-C-4-03	300.0	2.96	101.4	40.70	283.0	900	3.0	1,064	0.30
9	Nishiyama et al.	2002	EC4-C-4-04	300.0	2.96	101.4	40.70	283.0	900	3.0	1,418	0.40
10	Nishiyama et al.	2002	EC4-C-8-045	300.0	2.96	101.4	78.10	283.0	900	3.0	2,739	0.45
11	Nishiyama et al.	2002	EC4-D-4-04	450.0	2.96	152.0	39.90	283.0	1350	3.0	2,943	0.40
12	Nishiyama et al.	2002	EC4-D-4-06	450.0	2.96	152.0	40.70	283.0	1350	3.0	4,488	0.60
13	Nishiyama et al.	2002	EC6-A-4-02	122.0	4.54	26.9	39.90	579.0	366	3.0	274	0.20
14	Nishiyama et al.	2002	EC6-A-4-06	122.0	4.54	26.9	39.90	579.0	366	3.0	822	0.60
15	Nishiyama et al.	2002	EC6-C-2-06	239.0	4.54	52.6	24.50	579.0	717	3.0	1,772	0.60
16	Nishiyama et al.	2002	EC6-C-4-06	239.0	4.54	52.6	39.90	579.0	717	3.0	2,156	0.60
17	Nishiyama et al.	2002	EC6-C-8-03	239.0	4.54	52.6	77.60	579.0	717	3.0	1,547	0.30
18	Nishiyama et al.	2002	EC6-C-8-06	239.0	4.54	52.6	77.60	579.0	717	3.0	3,095	0.60
19	Nishiyama et al.	2002	EC6-C-4-025	239.0	4.54	52.6	40.70	579.0	717	3.0	907	0.25
20	Nishiyama et al.	2002	EC8-A-4-06	108.0	6.47	16.7	39.90	834.0	324	3.0	1,203	0.60
21	Nishiyama et al.	2002	EC8-C-4-015	222.0	6.47	34.3	39.90	834.0	666	3.0	753	0.15
22	Nishiyama et al.	2002	EC8-C-4-06	222.0	6.47	34.3	39.90	834.0	666	3.0	3,014	0.60
23	Nishiyama et al.	2002	EC8-C-4-03	222.0	6.47	34.3	40.70	834.0	666	3.0	1,515	0.30
24	Nishiyama et al.	2002	EC8-C-8-07	222.0	6.47	34.3	77.60	834.0	666	3.0	4,422	0.70



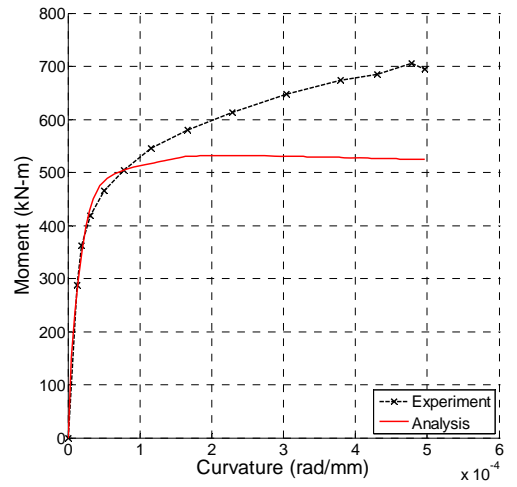
(a) Test #1; Ichinohe et al. 1991; Specimen: C06F3M



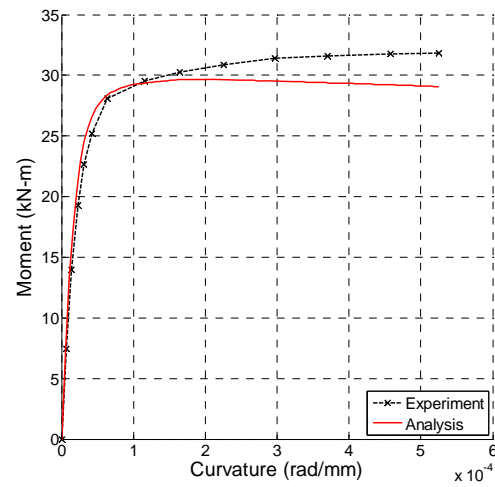
(b) Test #2; Ichinohe et al. 1991; Specimen: C06F5M



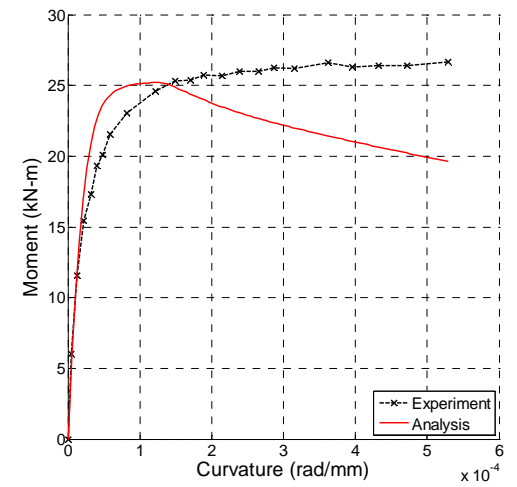
(c) Test #3; Ichinohe et al. 1991; Specimen: C08F5M



(d) Test #4; Ichinohe et al. 1991; Specimen: C12F5M

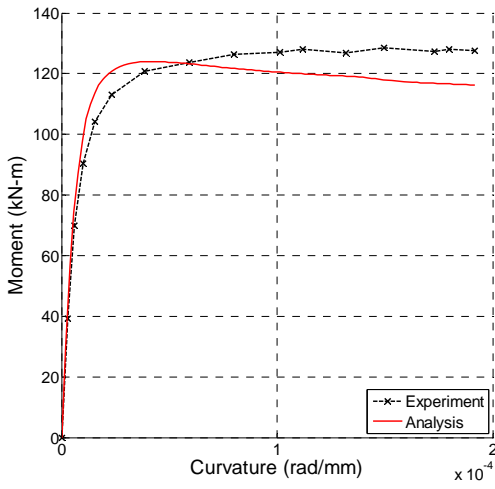


(e) Test #5; Nishiyama et al. 2002; Specimen: EC4-A-4-035

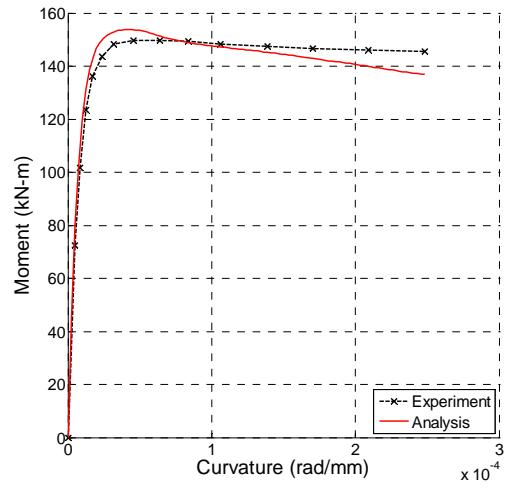


(f) Test #6; Nishiyama et al. 2002; Specimen: EC4-A-4-06

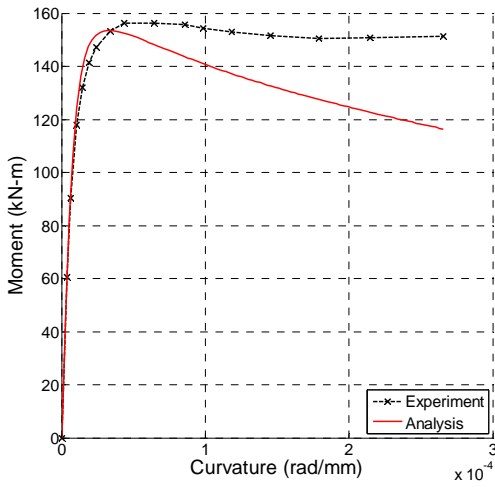
Figure 5-16. Validation Results for Non-Proportionally Loaded Beam-Columns



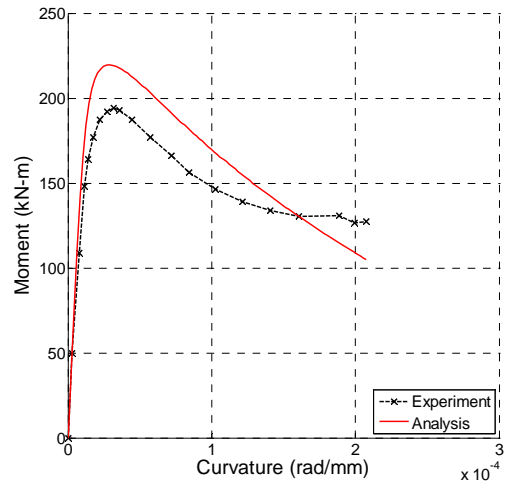
(g) Test #7; Nishiyama et al. 2002; Specimen: EC4-C-2-035



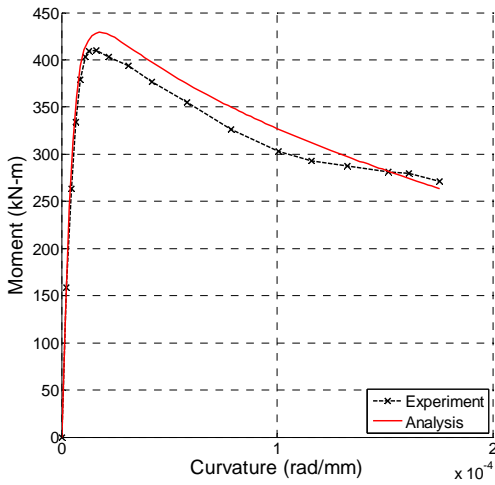
(h) Test #8; Nishiyama et al. 2002; Specimen: EC4-C-4-03



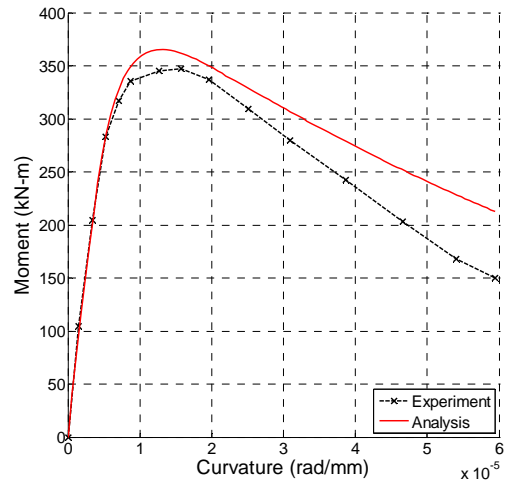
(i) Test #9; Nishiyama et al. 2002; Specimen: EC4-C-4-04



(j) Test #10; Nishiyama et al. 2002; Specimen: EC4-C-8-045

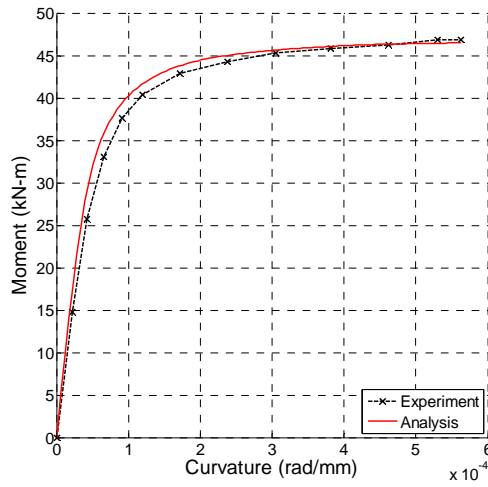


(k) Test #11; Nishiyama et al. 2002; Specimen: EC4-D-4-04

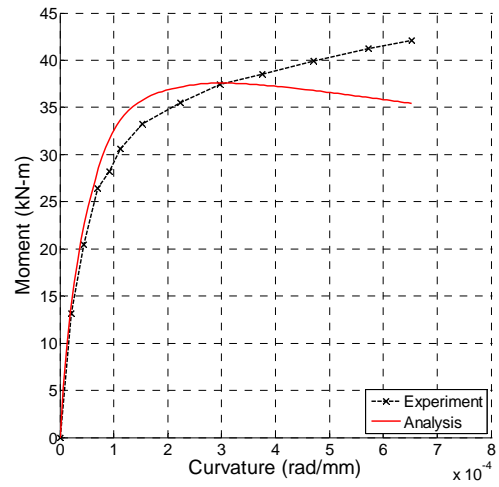


(l) Test #12; Nishiyama et al. 2002; Specimen: EC4-D-4-06

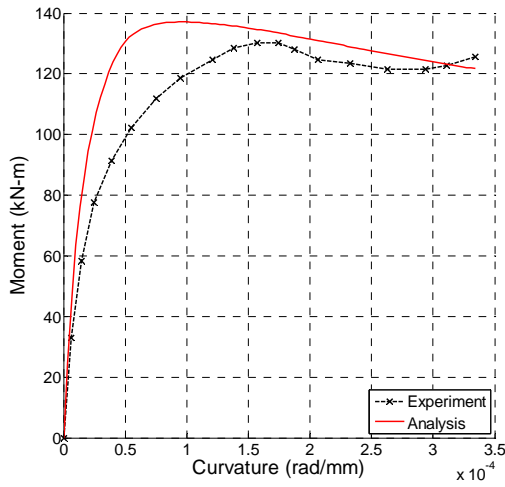
Figure 5-16. Validation Results for Non-Proportionally Loaded Beam-Columns (cont'd)



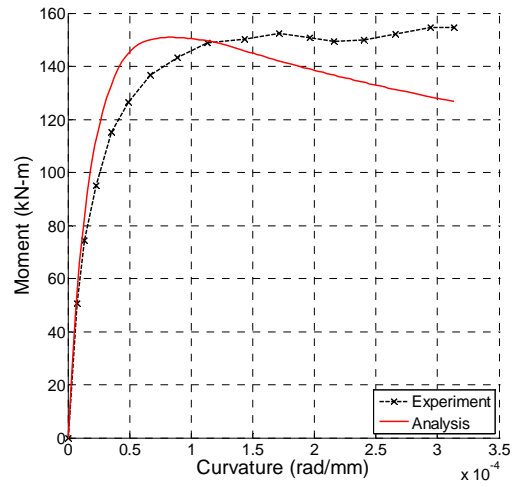
(m) Test #13; Nishiyama et al. 2002; Specimen: EC6-A-4-02



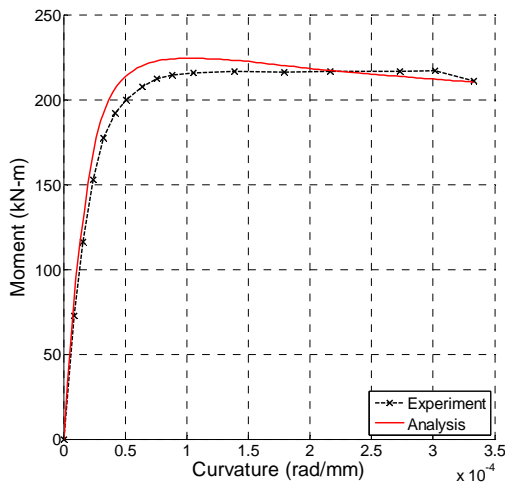
(n) Test #14; Nishiyama et al. 2002; Specimen: EC6-A-4-06



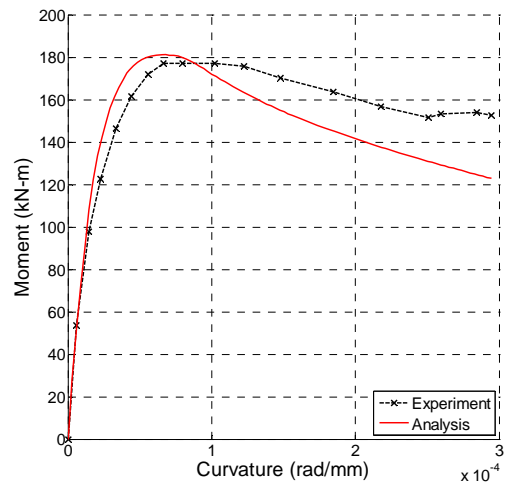
(o) Test #15; Nishiyama et al. 2002; Specimen: EC6-C-2-06



(p) Test #16; Nishiyama et al. 2002; Specimen: EC6-C-4-06

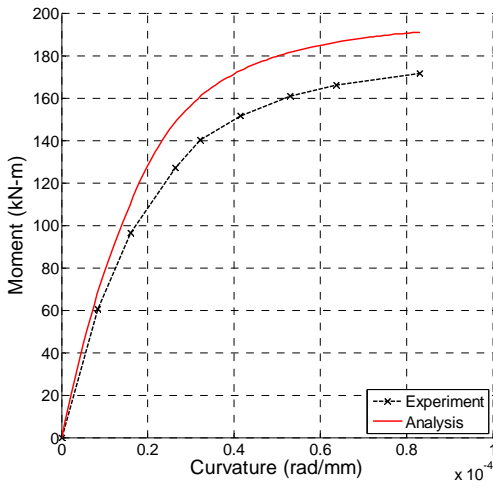


(q) Test #17; Nishiyama et al. 2002; Specimen: EC6-C-8-03

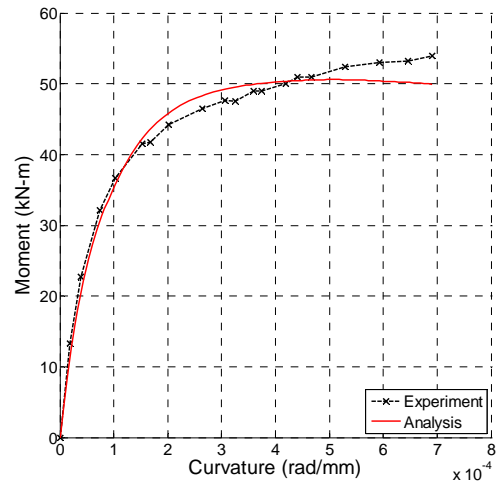


(r) Test #18; Nishiyama et al. 2002; Specimen: EC6-C-8-06

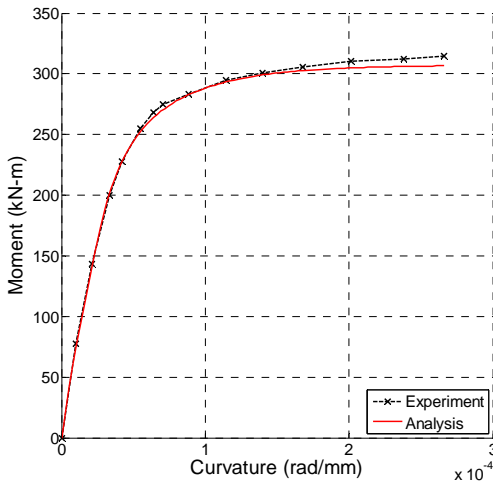
Figure 5-16. Validation Results for Non-Proportionally Loaded Beam-Columns (cont'd)



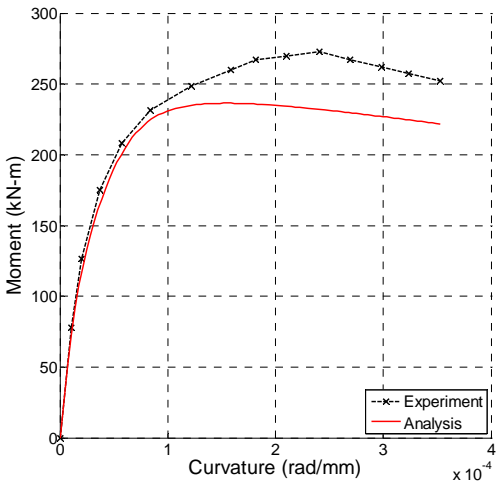
(s) Test #19; Nishiyama et al. 2002; Specimen: EC6-C-4-025



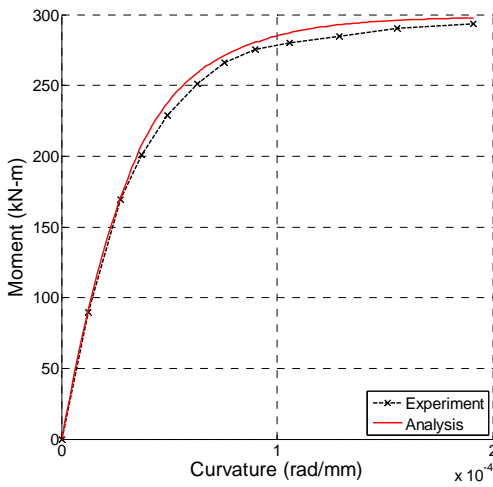
(t) Test #20; Nishiyama et al. 2002; Specimen: EC8-A-4-06



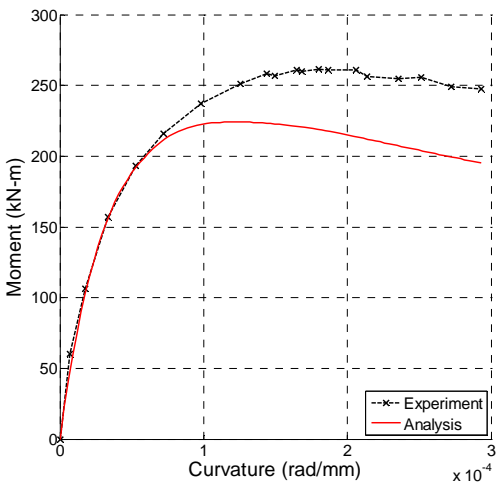
(u) Test #21; Nishiyama et al. 2002; Specimen: EC8-C-4-015



(v) Test #22; Nishiyama et al. 2002; Specimen: EC8-C-4-06



(w) Test #23; Nishiyama et al. 2002; Specimen: EC8-C-4-03



(x) Test #24; Nishiyama et al. 2002; Specimen: EC8-C-8-07

Figure 5-16. Validation Results for Non-Proportionally Loaded Beam-Columns (cont'd)

Table 5.8. Comparison Metrics for Non-Proportionally Loaded Beam-Column Data

Test #	Peak Moment (kN-m)			Curvature at Peak Moment (1/mm)			Initial Stiffness (kN-m/mm)			Area under Curve (kN-m/mm)		
	Expt.	Model	% Error	Expt.	Model	% Error	Expt.	Model	% Error	Expt.	Model	% Error
1	381.9	351.7	-7.90%	3.76E-04	9.11E-05	-75.75%	1.80E+07	2.18E+07	20.75%	0.1441	0.1397	-3.05%
2	358.6	319.2	-10.99%	3.02E-04	6.31E-05	-79.06%	1.86E+07	2.02E+07	8.72%	0.1075	0.0954	-11.25%
3	512.3	422.7	-17.49%	3.73E-04	1.04E-04	-72.20%	2.53E+07	2.35E+07	-7.16%	0.1807	0.1586	-12.20%
4	705.4	532.0	-24.59%	4.79E-04	2.19E-04	-54.34%	2.27E+07	2.75E+07	21.30%	0.2941	0.2520	-14.29%
5	31.8	29.7	-6.71%	5.25E-04	1.89E-04	-64.00%	1.04E+06	1.32E+06	26.64%	0.0155	0.0149	-3.96%
6	26.6	25.2	-5.40%	5.29E-04	1.22E-04	-77.00%	1.03E+06	1.03E+06	0.02%	0.0130	0.0116	-10.80%
7	128.4	124.0	-3.47%	1.50E-04	4.21E-05	-71.83%	1.38E+07	1.50E+07	8.99%	0.0231	0.0224	-3.13%
8	149.8	153.7	2.65%	6.38E-05	4.22E-05	-33.86%	1.50E+07	1.70E+07	13.34%	0.0356	0.0353	-0.86%
9	156.2	153.6	-1.72%	6.46E-05	3.19E-05	-50.67%	1.58E+07	1.66E+07	4.75%	0.0394	0.0351	-11.03%
10	194.3	219.6	13.05%	3.16E-05	2.91E-05	-8.06%	1.57E+07	1.85E+07	17.68%	0.0307	0.0333	8.58%
11	409.8	429.1	4.71%	1.60E-05	1.75E-05	9.37%	6.96E+07	7.46E+07	7.14%	0.0564	0.0590	4.62%
12	347.1	365.2	5.21%	1.58E-05	1.31E-05	-16.96%	6.68E+07	6.35E+07	-5.02%	0.0152	0.0169	11.61%
13	46.8	46.5	-0.78%	5.30E-04	5.63E-04	6.07%	6.74E+05	8.10E+05	20.28%	0.0232	0.0237	2.02%
14	42.1	37.6	-10.72%	6.52E-04	3.00E-04	-54.00%	5.97E+05	7.00E+05	17.25%	0.0229	0.0224	-2.39%
15	130.2	137.2	5.36%	1.57E-04	9.69E-05	-38.36%	4.57E+06	7.02E+06	53.57%	0.0382	0.0419	9.61%
16	154.6	150.9	-2.40%	3.14E-04	8.47E-05	-73.00%	6.72E+06	7.49E+06	11.47%	0.0436	0.0422	-3.29%
17	217.2	224.4	3.28%	3.02E-04	1.03E-04	-65.76%	8.60E+06	9.80E+06	14.01%	0.0678	0.0693	2.31%
18	177.0	181.1	2.29%	6.65E-05	6.78E-05	1.91%	8.55E+06	8.47E+06	-0.95%	0.0461	0.0433	-6.18%
19	171.6	191.0	11.30%	8.31E-05	8.31E-05	0.00%	7.19E+06	8.27E+06	14.92%	0.0110	0.0125	13.96%
20	53.9	50.6	-6.15%	6.90E-04	5.11E-04	-26.00%	6.39E+05	5.68E+05	-11.13%	0.0310	0.0307	-0.82%
21	314.4	306.7	-2.46%	2.66E-04	2.66E-04	0.00%	7.13E+06	6.96E+06	-2.45%	0.0720	0.0712	-1.06%
22	272.7	236.4	-13.32%	2.40E-04	1.55E-04	-35.48%	7.08E+06	6.72E+06	-5.00%	0.0835	0.0753	-9.83%
23	293.6	297.7	1.42%	1.91E-04	1.91E-04	0.00%	7.08E+06	7.32E+06	3.31%	0.0463	0.0475	2.61%
24	261.4	224.3	-14.19%	1.80E-04	1.23E-04	-31.60%	6.62E+06	6.42E+06	-3.03%	0.0661	0.0578	-12.53%
Mean			-3.29%			-37.94%			9.56%			-2.14%
Standard Deviation			9.01%			30.90%			13.99%			8.04%
Median			-2.43%			-36.92%			8.85%			-2.72%

5.7 Cyclic Pure Bending Experiments

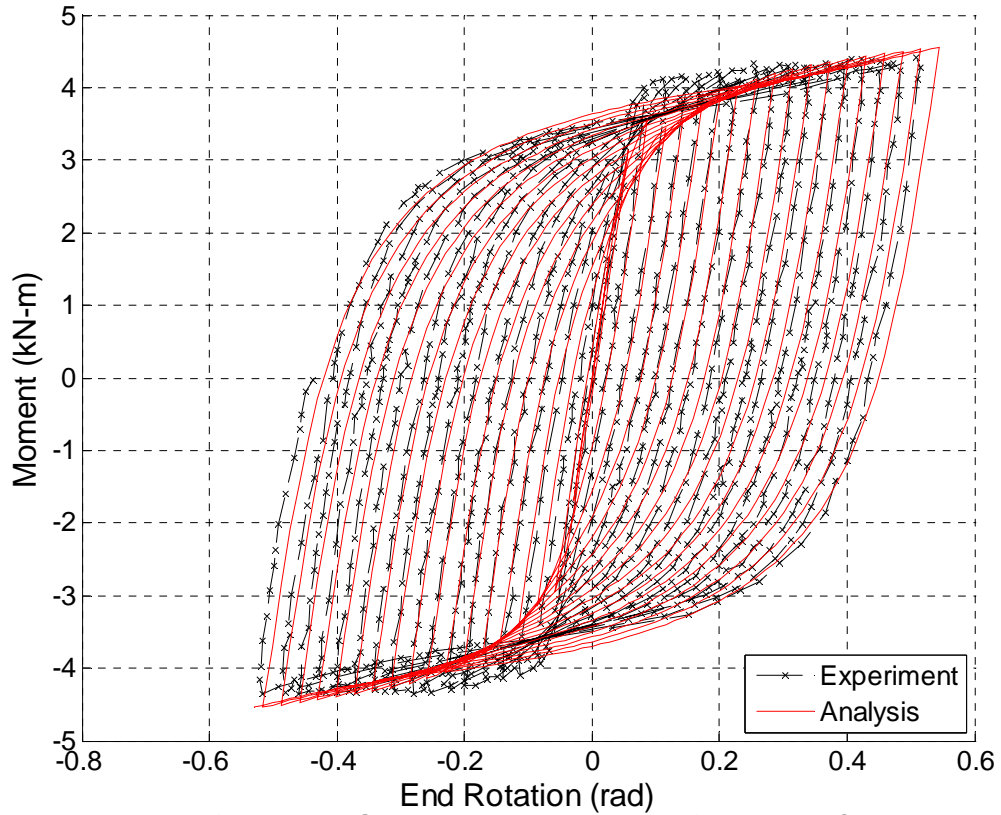
The ability of the formulation to accurately model the behavior of cyclically loaded specimens is examined in this section. These analyses are similar to those performed in for the validation of the monotonic pure bending experiments. The setup is identical to that of the direct moment tests of that section (Figure 5-9(a)). A similar mesh density was also used, namely, two elements along the length and three integration points for each element. Noting the two dimensional nature of these tests, the fiber discretization took the form of strips, with 50 strips along the height of the section for each the steel and concrete. Analyses were run in displacement control, following the same deformation pattern as experienced in the experiment.

The material and geometric properties of each of the specimens is listed in Table 5.9. Experimental and computational load-deformation plots are shown in Figure 5-17. Also shown in Figure 5-17 are the stress-strain response obtained from the analyses for the extreme fibers of both the steel and concrete located at midspan of the beam.

Table 5.9. Material and Geometric Properties of Cyclic Pure Bending Specimens

Test #	Author	Year	Specimen	D (mm)	t (mm)	D/t	f'_c (MPa)	F_y (MPa)	Bending Span (mm)
1	Elchalakani & Zhao	2008	F19I1	60.4	2.95	20.5	23.08	413.0	800
2	Elchalakani & Zhao	2008	F11I1	87.3	2.28	38.3	23.08	473.0	800
3	Elchalakani & Zhao	2008	F04I1	110.4	1.25	88.3	23.08	430.0	800
4	Elchalakani & Zhao	2008	F01I1	109.3	1.05	104.1	23.08	457.0	800
5	Elchalakani & Zhao	2008	F16I1	89.1	3.09	28.8	23.08	473.0	800
6	Elchalakani & Zhao	2008	F15I1-S	76.1	2.35	32.4	23.08	370.0	800
7	Elchalakani & Zhao	2008	F14I3	89.3	2.52	35.5	23.08	378.0	800

Test #1; Elchalakani & Zhao 2008; Specimen: F1911



Response of Extreme Steel Fiber Response of Extreme Concrete Fiber

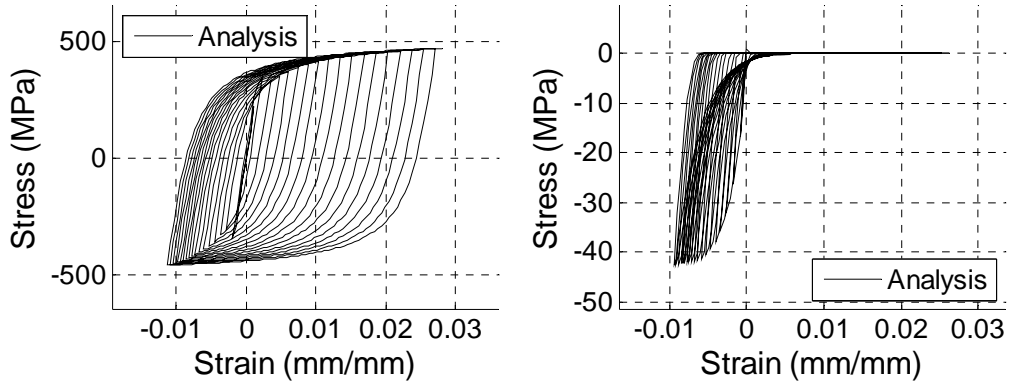
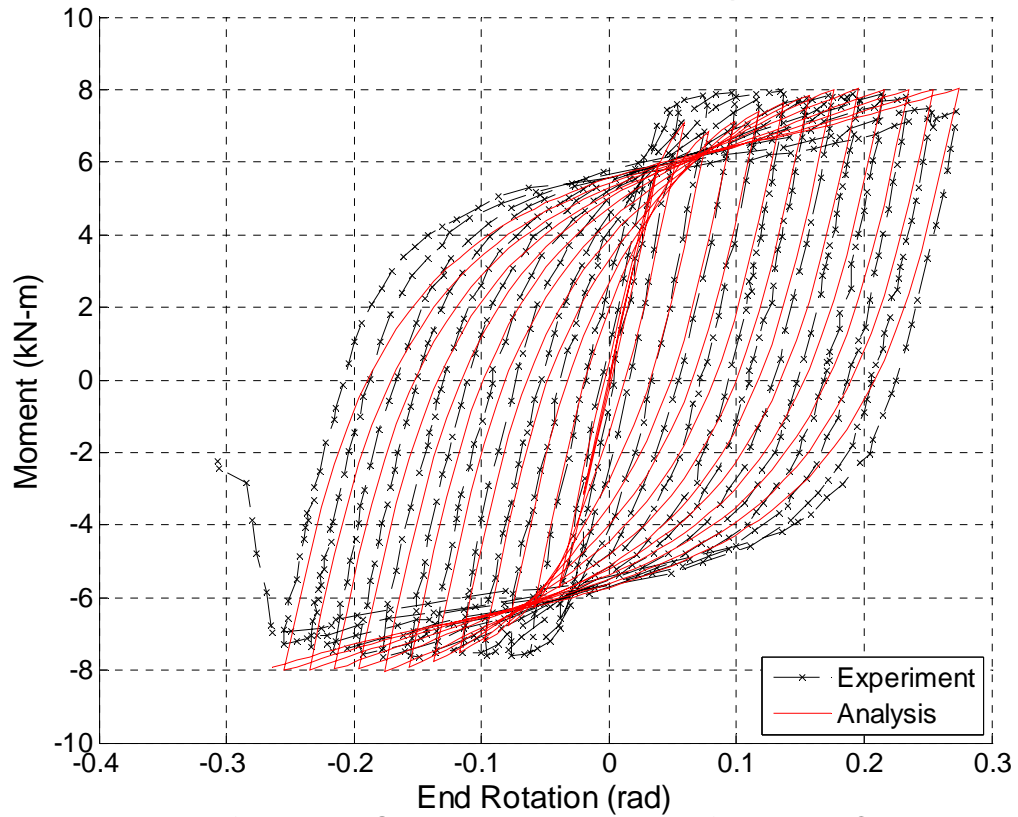


Figure 5-17. Validation Results for Cyclic Pure Bending

Test #2; Elchalakani & Zhao 2008; Specimen: F1111



Response of Extreme Steel Fiber Response of Extreme Concrete Fiber

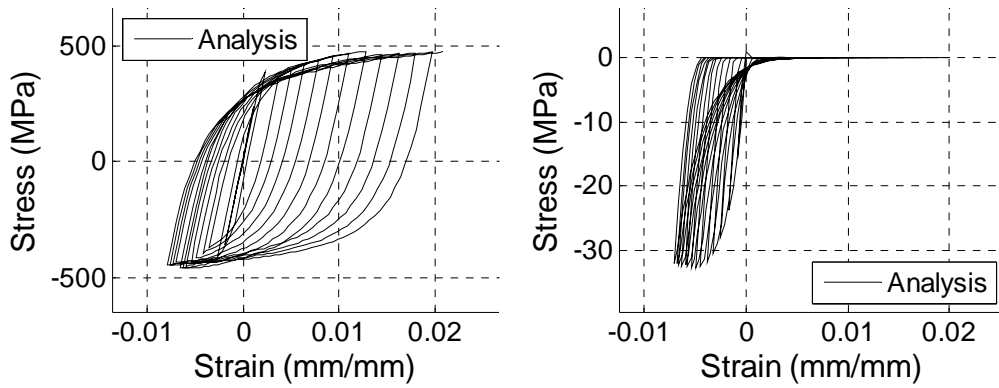
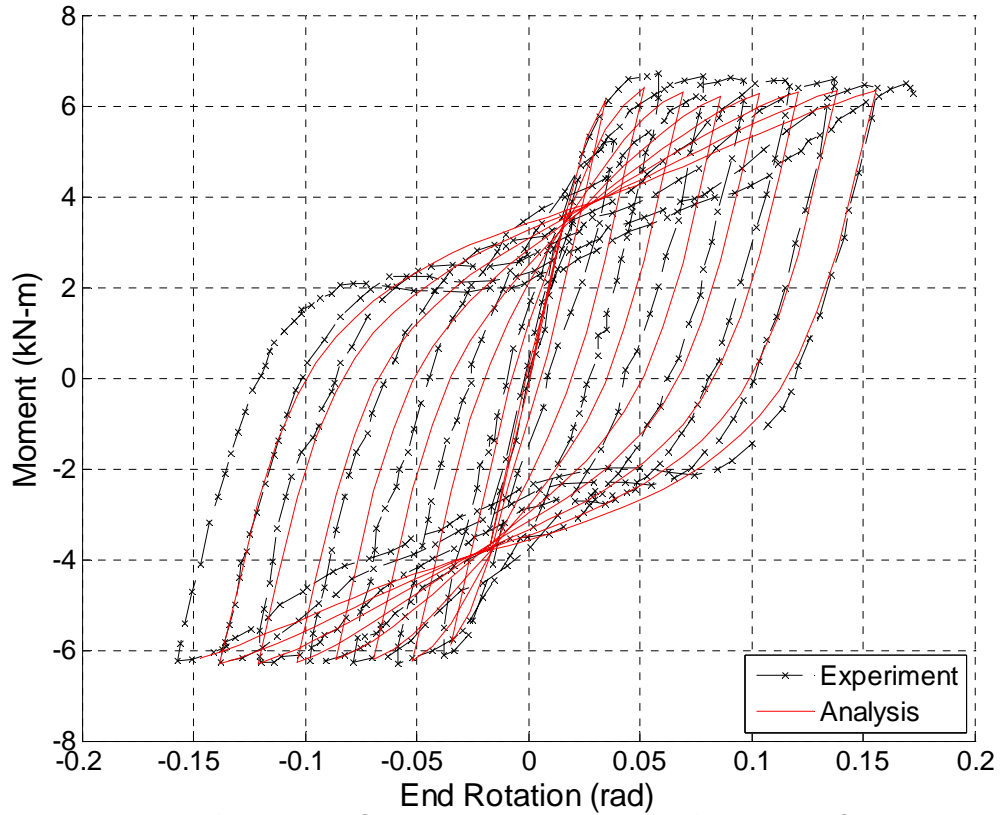


Figure 5-17. Validation Results for Cyclic Pure Bending (continued)

Test #3; Elchalakani & Zhao 2008; Specimen: F0411



Response of Extreme Steel Fiber Response of Extreme Concrete Fiber

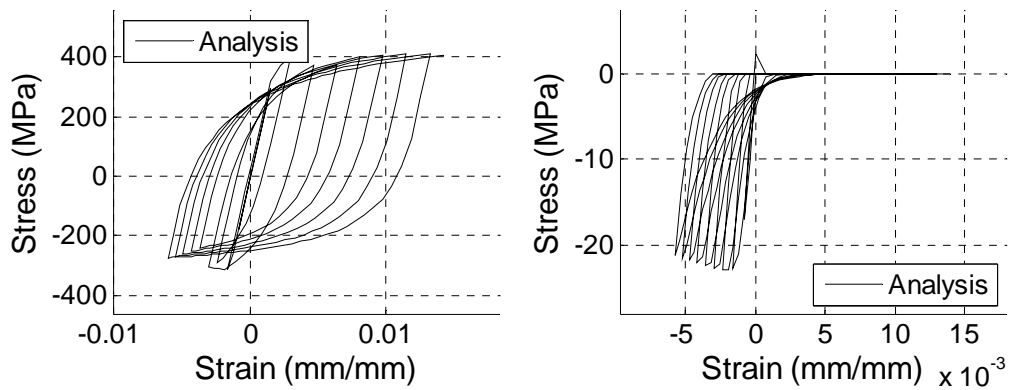
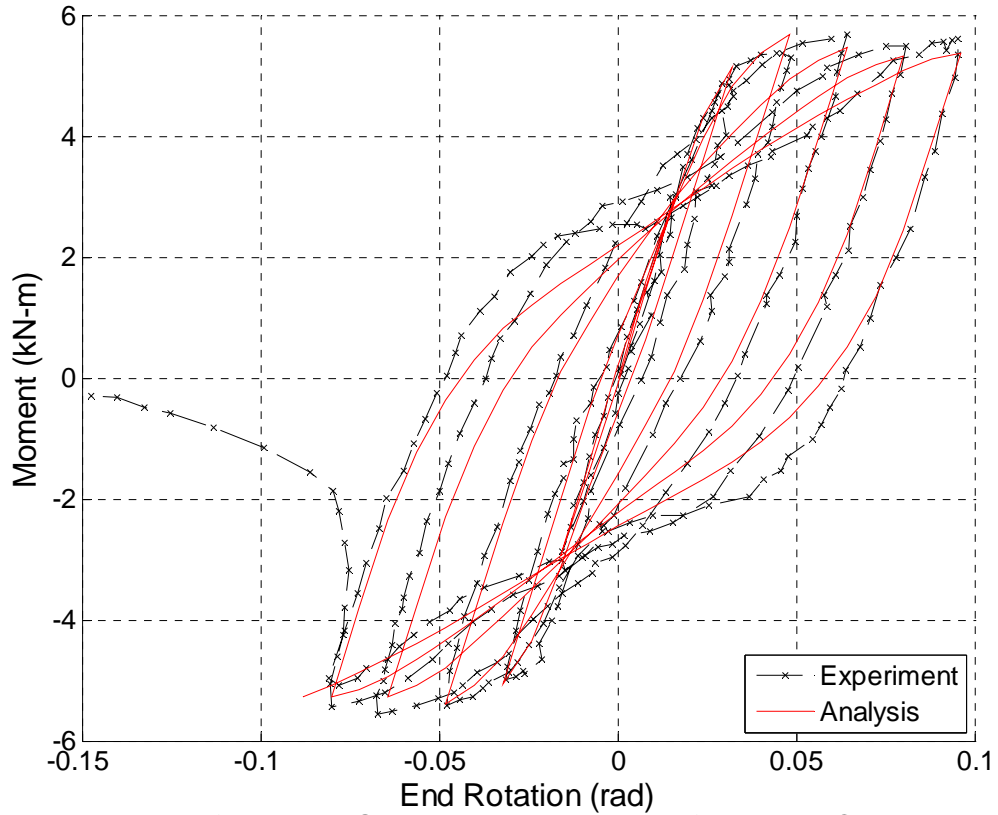


Figure 5-17. Validation Results for Cyclic Pure Bending (continued)

Test #4; Elchalakani & Zhao 2008; Specimen: F0111



Response of Extreme Steel Fiber Response of Extreme Concrete Fiber

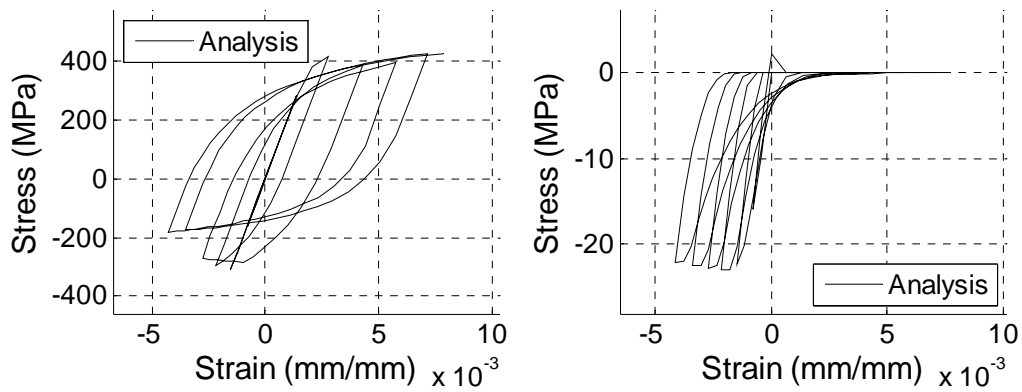
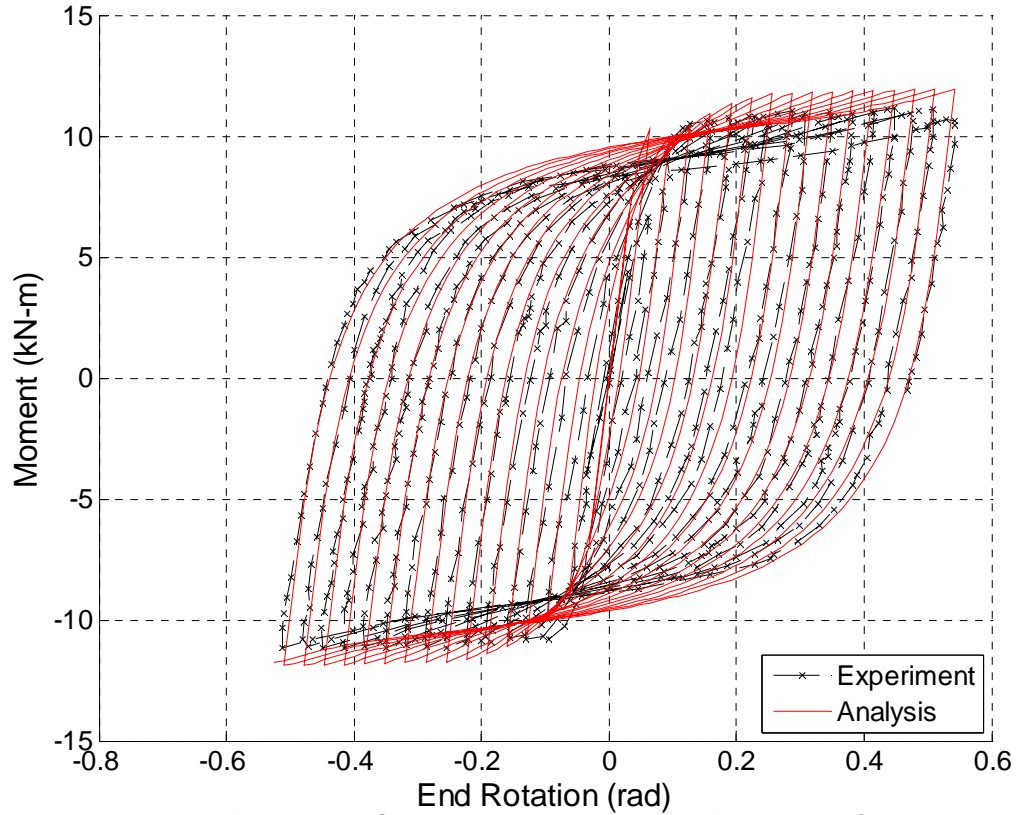


Figure 5-17. Validation Results for Cyclic Pure Bending (continued)

Test #5; Elchalakani & Zhao 2008; Specimen: F1611



Response of Extreme Steel Fiber Response of Extreme Concrete Fiber

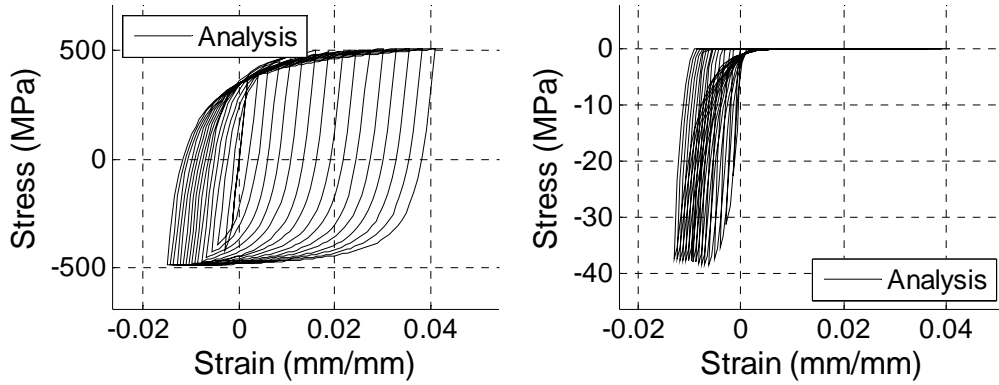
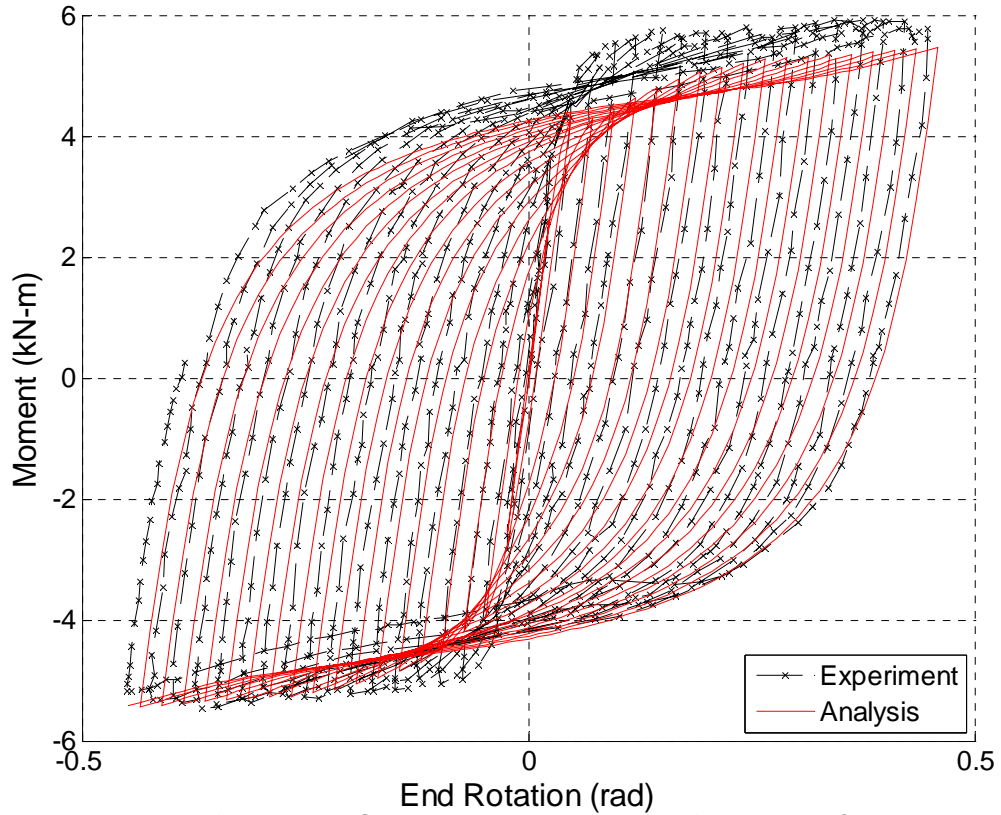


Figure 5-17. Validation Results for Cyclic Pure Bending (continued)

Test #6; Elchalakani & Zhao 2008; Specimen: F15I1-S



Response of Extreme Steel Fiber Response of Extreme Concrete Fiber

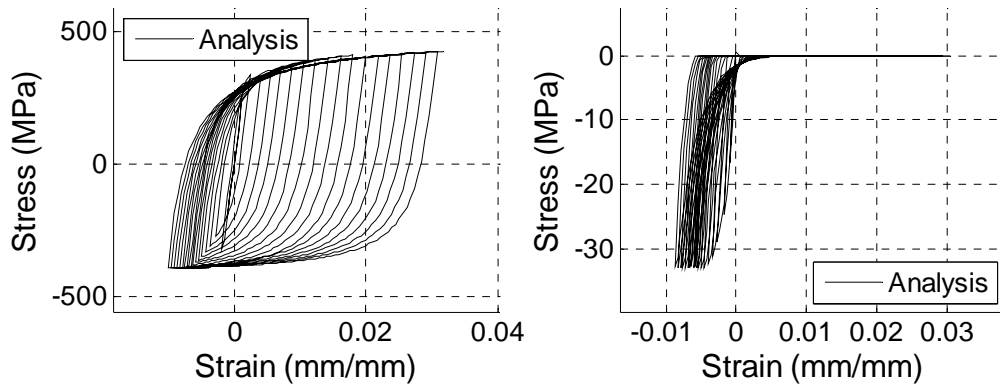
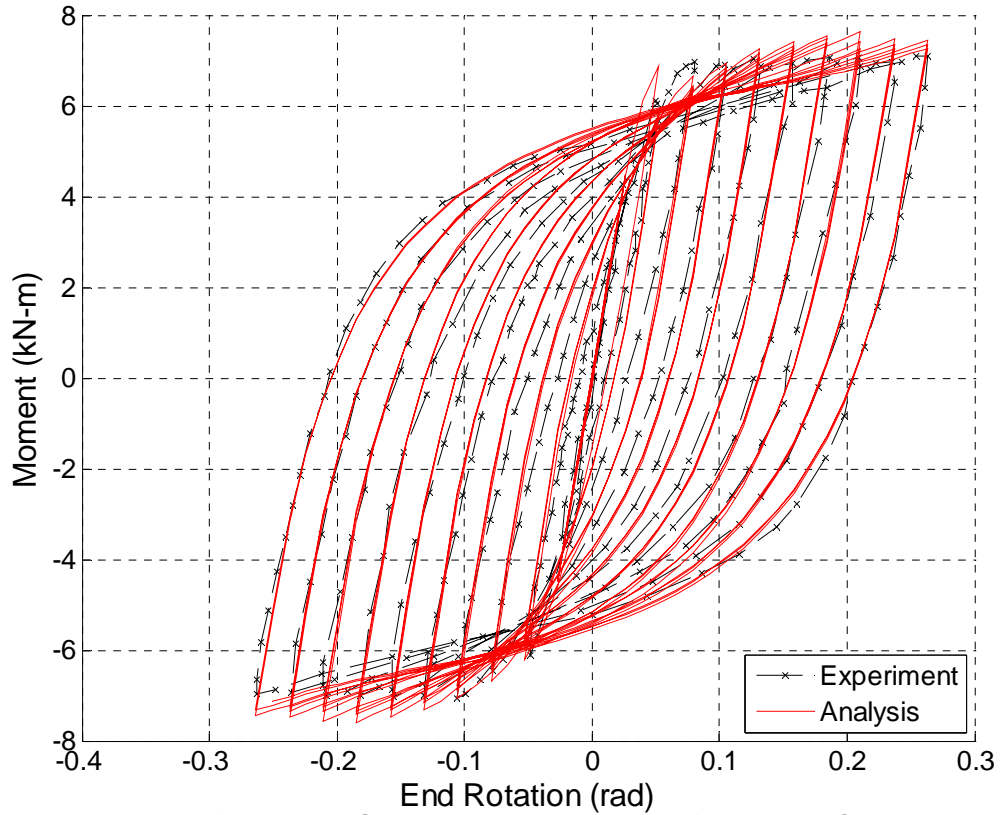


Figure 5-17. Validation Results for Cyclic Pure Bending (continued)

Test #7; Elchalakani & Zhao 2008; Specimen: F14I3



Response of Extreme Steel Fiber Response of Extreme Concrete Fiber

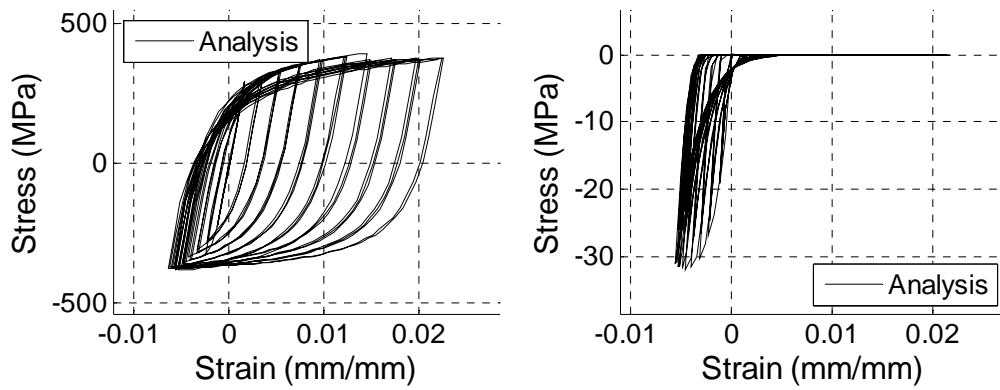


Figure 5-17. Validation Results for Cyclic Pure Bending (continued)

5.8 Cyclic Slender Beam-Column Experiments

The final verification study compares computational results to the results from a series of full-scale concrete-filled steel tube (CFT) beam-column tests performed at the NEES MAST Laboratory at the University of Minnesota (Perea 2009; Denavit et al. 2009; Leon et al. 2009). The test series included both RCFT and CCFT members; comparisons to the CCFT members are made here.

The MAST Laboratory allows for six degrees-of-freedom (DOF) control through a rigid steel crosshead. For the main portion of testing, most specimens were kept in a fixed-free ($K=2$) configuration, achieved as follows. The beam-column bases are welded to a base plate which is bolted to the testing floor, providing a fixed connection. The beam-column tops are welded to a base plate with a hole for placing the concrete, which is bolted to the crosshead. The free condition is provided by control of the crosshead; allowing horizontal displacements and setting bending moments at the top to zero. Twist is constrained to zero due to the low torsional stiffness of the specimens.

The loading protocol for each specimen is divided into several load cases. The first three load cases are the same for each of the specimens. The first load case subjects the specimen to concentric load. The horizontal DOFs are held at zero force, allowing the specimen to displace transversely. The vertical DOF is loaded under displacement control until a critical load is reached or until actuator load limits are reached. The second and third load cases subject the specimen to constant axial load (with different values being used between the second and third load cases) and cyclic transverse displacements, causing uniaxial flexure. The vertical DOF is under load control while the horizontal DOFs are under displacement control. The fourth and later load cases varied among the specimens. Some of the specimens were subjected to a biaxial cyclic loading. For this load case the control was similar to that of the second and third load cases except that the horizontal displacements were moved in a figure eight pattern (e.g., Figure 5-20(e)), causing biaxial flexure. Comparisons between experimental and computational results for these load cases are shown below. Other load cases, which are not analyzed in this work include: 1) Sets of “probes” of the interaction surface. While holding a constant axial load, the horizontal displacements are increased with a fixed ratio of X to Y displacement until a critical flexural strength is reached, at which point the horizontal displacements are reversed. The process is then repeated for several additional X/Y displacement combinations. 2) Cyclic torsional loading at different levels of axial loading. 3) Concentric loading, uniaxial cyclic, and biaxial cyclic in a configuration having a fixed base and with the top fixed against rotation but free to translate (thus $K = 1$ with the CFT subjected to reverse curvature flexure).

Four of the specimens tested (Specimens 6, 7, 11, and 15) will be presented in this work.

The measured material and geometric properties of the specimens are listed in Table

5.10, the initial out-of-plumbness and loading direction unit vectors are listed in Table 5.11, while the specific loading history of each specimen and applicable axial load for each load case is listed in

Table 5.12.

Table 5.10. Material and Geometric Properties of the Slender Beam-Column Specimens

#	Specimen Name	D (mm)	t (mm)	D/t	f'_c (MPa)	F_y (MPa)	L (mm)	L/D
6	6-CCFT12.75x0.25-18ft-12ksi	324	5.80	55.8	91.01	337.2	5499	16.98
7	7-CCFT20x0.25-18ft-12ksi	508	5.98	84.9	91.01	328.2	5534	10.89
11	11-CCFT20x0.25-26ft-5ksi	508	5.98	84.9	55.85	305.4	7995	15.74
15	15-CCFT20x0.25-26ft-12ksi	508	5.98	84.9	79.98	293.0	7976	15.70

Table 5.11. Initial Out-of-Plumbness and Loading Direction Unit Vectors of the Slender Beam-Column Specimens

Test #	Initial Out-of-Plumbness		Direction of Motion: Load Case 1		Direction of Motion: Load Case 2 & 3	
	X (mm)	Y (mm)	X	Y	X	Y
6	9.1	-6.1	-0.2978	-0.9546	0.2750	0.9615
7	-7.6	-11.9	-0.4477	-0.8942	0.4414	0.8973
11	15.0	-54.1	0.1934	-0.9811	0.2587	-0.9660
15	6.1	41.1	0.5319	0.8468	0.7071	0.7071

Table 5.12. Loading Protocols of the Slender Beam-Column Specimens

Load Case	Description	Axial Load (kN)	Load Case	Description	Axial Load (kN)
<i>Specimen 06</i>			<i>Specimen 11</i>		
LC1	Concentric Loading	n/a	LC1	Concentric Loading	n/a
LC2	Uniaxial Cyclic	1,334	LC2	Uniaxial Cyclic	2,669
LC3	Uniaxial Cyclic	667	LC3	Uniaxial Cyclic	1,334
			LC4	Biaxial Cyclic	2,002
			LC5	Biaxial Cyclic	667
<i>Specimen 07</i>			<i>Specimen 15</i>		
LC1	Concentric Loading	n/a	LC1	Concentric Loading	n/a
LC2	Uniaxial Cyclic	4,448	LC2	Uniaxial Cyclic	1,779
LC3	Uniaxial Cyclic	2,224	LC3	Uniaxial Cyclic	3,559
LC4	Biaxial Cyclic	5,560	LC4	Biaxial Cyclic	890
			LC5	Biaxial Cyclic	2,669

The column was modeled with four elements along the length of the column, each with four integration points. A dense fiber discretization was used with 8 fibers in the radial direction for the concrete core and 2 fibers in the radial direction for the steel tube and 30 fibers around the circumference for both materials. The out-of-plumbness of the specimens (

Table 5.11) was modeled directly by defining the initial nodal coordinates. The base was fully fixed against translation and rotation.

Observations of the experimental data indicate that non-negligible friction existed in the crosshead. An assessment of the crosshead friction can be made with the experimental data at displacement reversals in second and third load cases. Upon these reversals, a very stiff response is seen, resulting in a jump in transverse load of approximately 8.9 kN (2

kips), which is likely due to friction in the loading system rather than specimen behavior. To account for this friction, zero length springs were added at the top of the column in the transverse (X and Y) directions as shown schematically in Figure 5-18. The constitutive model associated with the zero length springs was elastic-perfectly plastic with a yield force of 4.45 kN (1 kip, half of the value in transverse load observed in friction-related response in the experimental data). The stiffness of the elastic portion was selected such that the transition from positive to negative yielding occurred at a displacement less than the displacement step size used in the analysis, thus minimizing the influence of the spring on the nonlinear solution. Also, these springs were not used in the first load case. While friction in the crosshead is presumed to still be significant in the first load case, it is not modeled since the zero length springs described above, which are appropriate for the later load cases, lead to inappropriate results for the first load case, and a more accurate model is not readily attainable. For the first load case, the control of the specimen in the transverse directions was different as compared to the remainder of each experiment (i.e., for the first load case, the transverse directions were in force control rather than displacement control). These forces were controlled to be zero, and thus the spring force provided an artificial constraint that inappropriately dominated the results. Other than not being present in the first load case of each specimen, the springs modeling crosshead friction were included throughout the loading history and for all specimens.

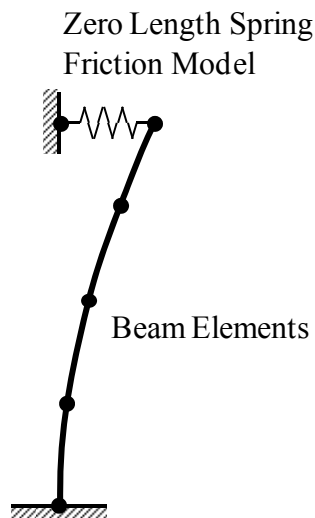


Figure 5-18. Schematic Representation of Friction Model

The analysis of the first load case, consisting of concentric loading, was completed in displacement control, up to the displacements experienced experimentally by the specimen. This was in contrast to the control method used in the experiment, as described above. The differences in control were necessary because of the differences in the capabilities and stability of the experimental loading system as compared to the computational model; however, comparable results were obtained. To ensure that the direction of motion in the analysis was the same as that of the specimen, a stiff spring was introduced perpendicular to the observed direction of motion. This spring was removed upon completion of the first load case. The later load cases, including both uniaxial cyclic and biaxial cyclic loading, used the same control as in the experiment: the

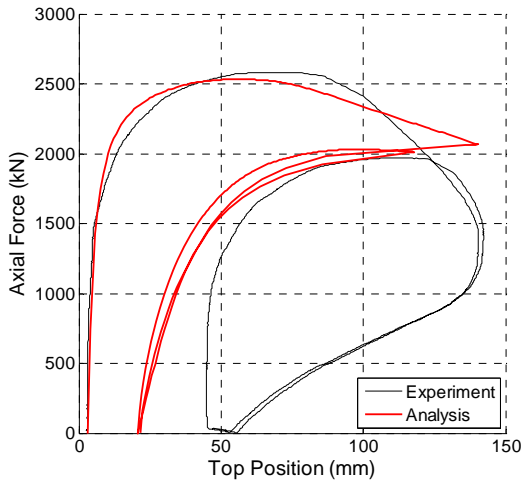
horizontal DOFs were under displacement control while the vertical DOF was under force control. The two displacement histories and one loading history were defined to match what the specimen experienced during the test.

For both the concentric loading and the uniaxial cyclic load cases, the motion of the column was such that the flexural response was uniaxial. However, as in the experiment, the motion was not along one of the coordinate axes. For this reason, unit vectors were defined in the direction of motion for each load case (

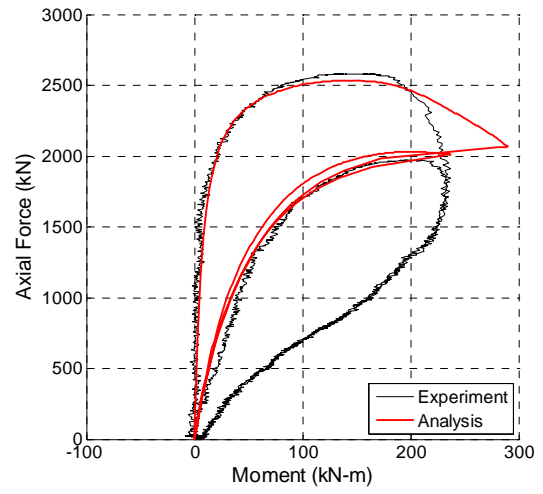
Table 5.11). The displacements, forces, and moments shown in the following figures show the projection of the various quantities on the appropriate unit vector (a unit vector perpendicular to the motion for the moments). Several specimens will be presented individually.

Specimen 6: The experimental and computational results for Specimen 6 are presented in Figure 5-19. For the first cycle of first load case, the computational model accurately captured the initial stiffness and peak load. The post-peak behavior and unloading behavior, however, do not correspond well. For the second cycle, the peak load and axial load-moment response correspond well, but horizontal displacement, post-peak and unloading do not. One possible cause of this is that for this load case, the horizontal DOFs were in load control set to zero force, however, due to the flexibility of the specimens in the horizontal direction, especially near the limit point, the accuracy of the control (on the order of 5 kN) likely induced significant loading on the column which will affect the response. The analyses, on the other hand, are capable of maintaining perfect control.

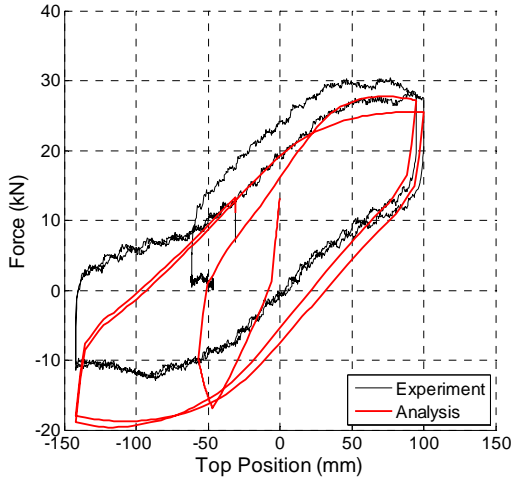
In each of the uniaxial cyclic load cases, two cycles were performed at a deformation level large enough to show softening in the horizontal force-displacement response. At each reversal, a very stiff response is seen in the experimental results (Figure 5-19(c-f)). This is the result of friction in the loading crosshead, and the zero-length springs added to the model capture this behavior well. The computational model provides a good estimation of the peak force and moment as well as the stiffness.



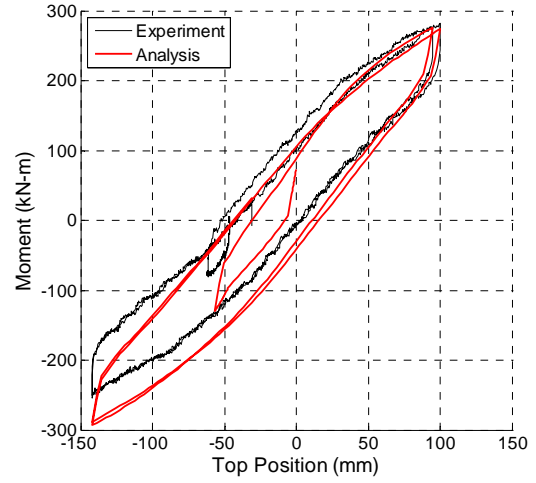
(a) Load Case 1: Concentric Loading



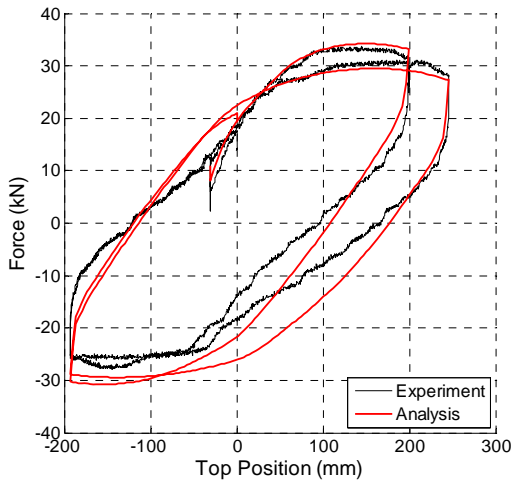
(b) Load Case 1: Concentric Loading



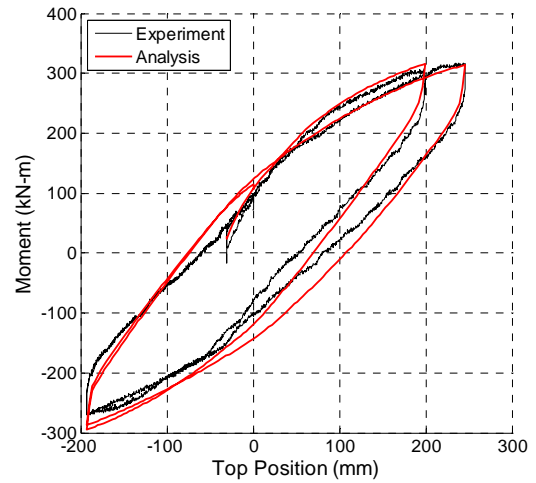
(c) Load Case 2: Uniaxial Cyclic



(d) Load Case 2: Uniaxial Cyclic



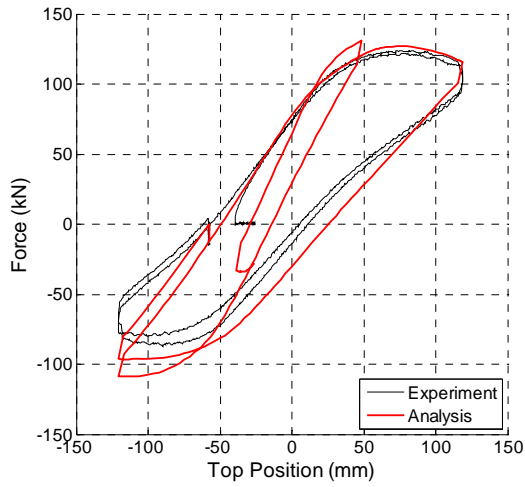
(e) Load Case 3: Uniaxial Cyclic



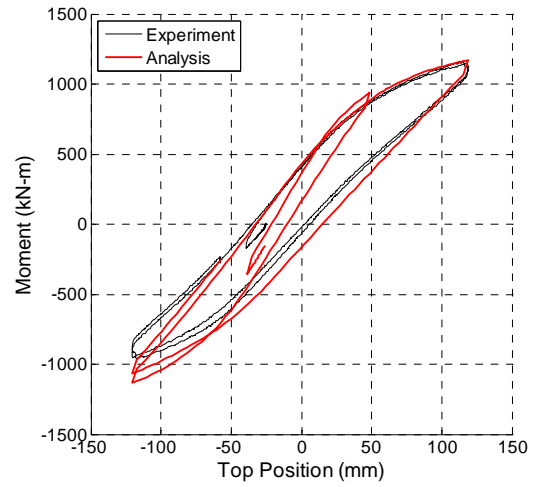
(f) Load Case 3: Uniaxial Cyclic

Figure 5-19. Validation Results for Slender Beam-Column Specimen 6

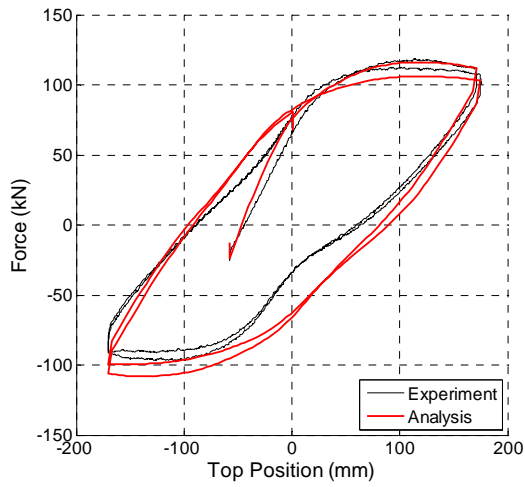
Specimen 7: The experimental and computational results for Specimen 7 are presented in Figure 5-20. The axial strength of Specimen 7 was higher than that of the other specimens. When the first load case was performed, however, the force limits of the actuators were reached and significant nonlinearity was not observed. For that reason, the results have been excluded from this discussion. Similar to Specimen 6, the uniaxial cyclic load cases show good correspondence between the experimental and analytical results. The jumps in load due to friction in the loading crosshead are less noticeable due to the higher forces attained during the test. The fourth load case subjected the column to a biaxial displacement history. The computational model accurately predicted the stable response for the smaller excursions and the unstable response for the large excursions (as indicated by the slope of the horizontal force-displacement response). However, the forces from the computational model for the largest excursion are significantly low. The cause for this discrepancy is unclear and will be the subject of future research. Specimen 11 tends to show better correlation during the biaxial loading (see below). The reason for the discrepancies could relate to friction forces or other eccentricities in the experiment that offset the results systematically and that are not modeled in the analysis, or to the computational model for cyclic concrete crushing or local buckling not addressing the response with sufficient accuracy.



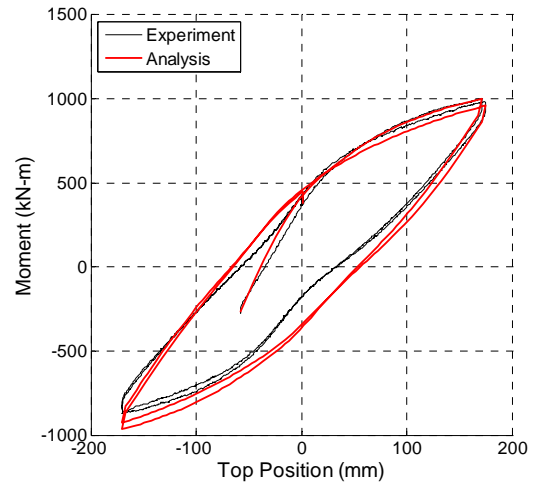
(a) Load Case 2: Uniaxial Cyclic



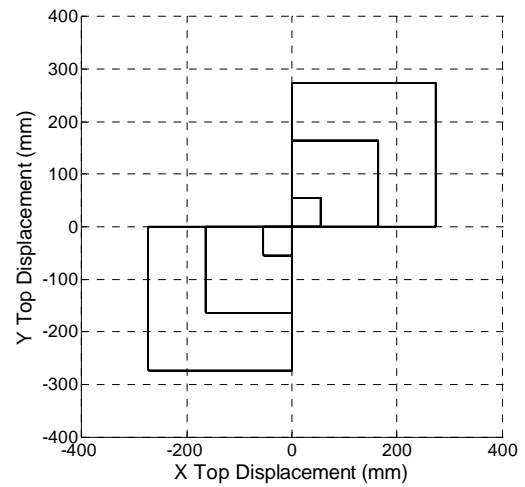
(b) Load Case 2: Uniaxial Cyclic



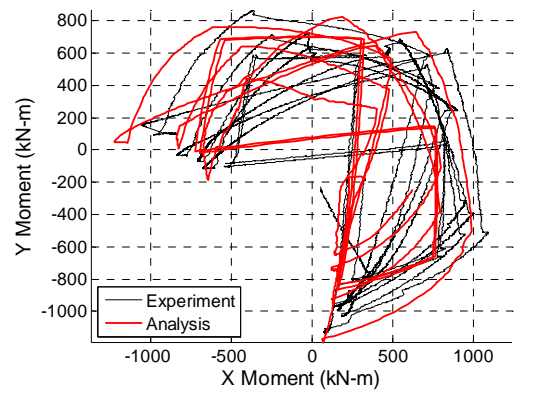
(c) Load Case 3: Uniaxial Cyclic



(d) Load Case 3: Uniaxial Cyclic

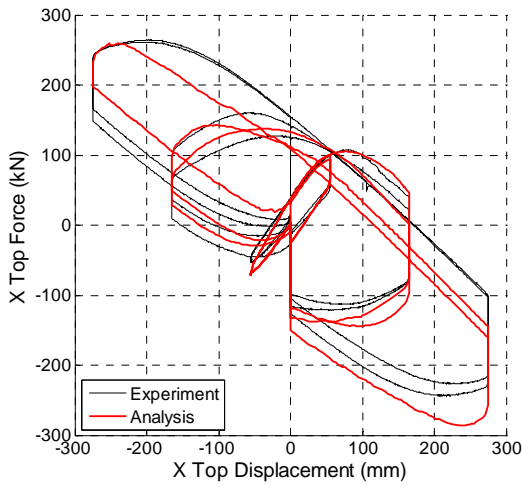


(e) Load Case 4: Biaxial Cyclic

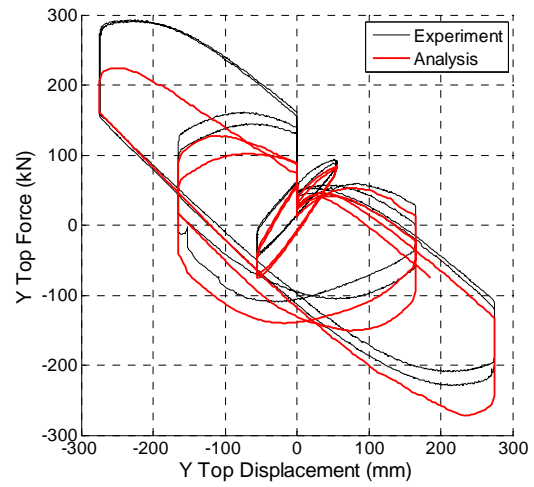


(f) Load Case 4: Biaxial Cyclic

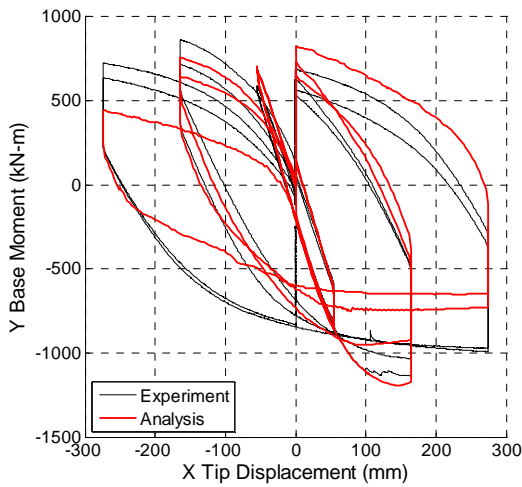
Figure 5-20. Validation Results for Slender Beam-Column Specimen 7



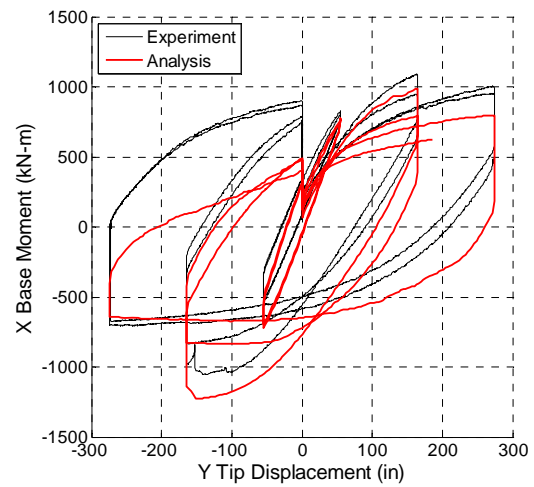
(g) Load Case 4: Biaxial Cyclic



(h) Load Case 4: Biaxial Cyclic



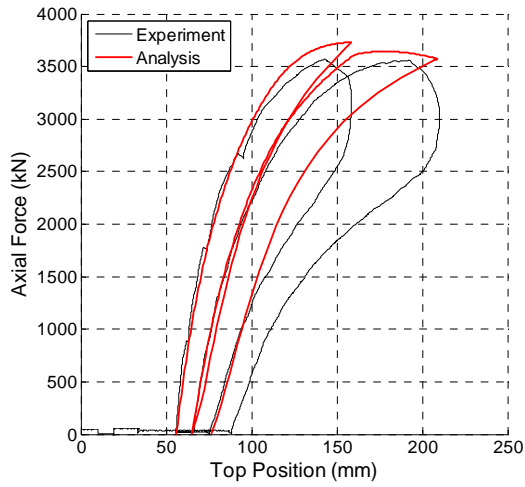
(i) Load Case 4: Biaxial Cyclic



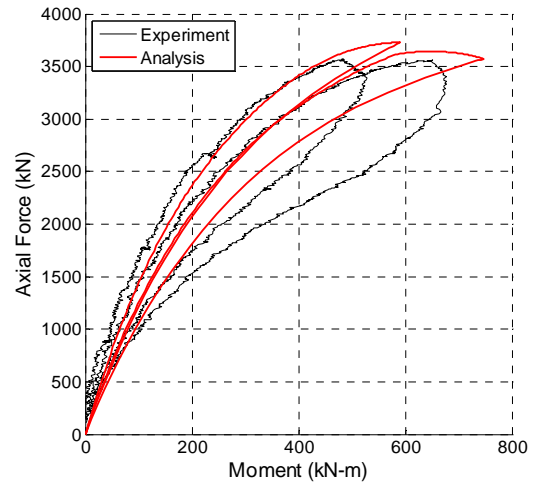
(j) Load Case 4: Biaxial Cyclic

Figure 5-20. Validation Results for Slender Beam-Column Specimen 7 (continued)

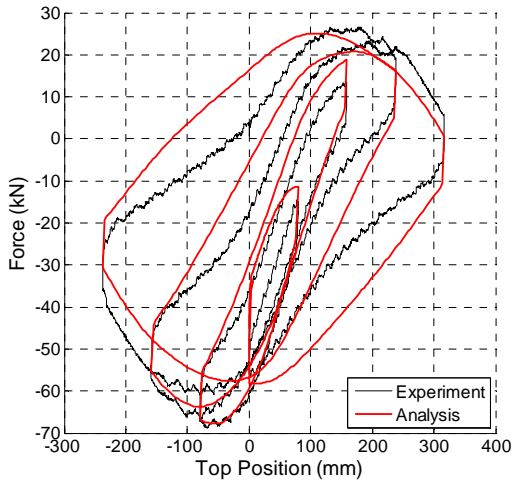
Specimen 11 and Specimen 15: The experimental and computational results for Specimen 11 and Specimen 15 are presented in Figure 5-21 and Figure 5-22, respectively. Both Specimen 11 and Specimen 15 were subjected to two cycles of concentric loading, an increasing uniaxial cyclic loading at two axial load levels, and biaxial cyclic loading at two axial load levels. Similar correspondence is observed for these specimens in comparison to the previous specimens.



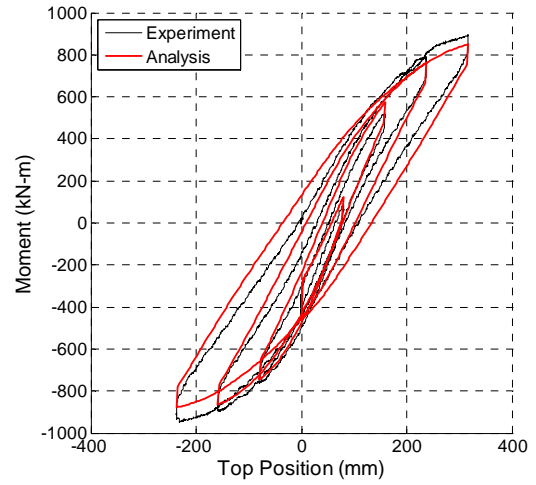
(a) Load Case 1: Concentric Loading



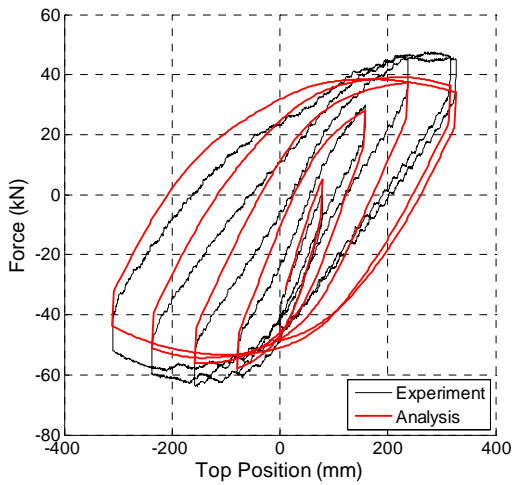
(b) Load Case 1: Concentric Loading



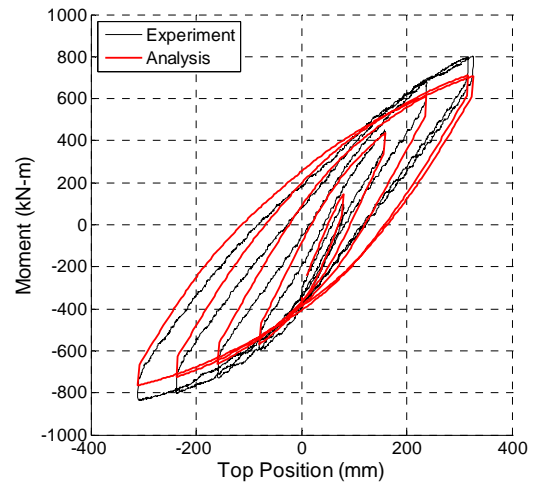
(c) Load Case 2: Uniaxial Cyclic



(d) Load Case 2: Uniaxial Cyclic

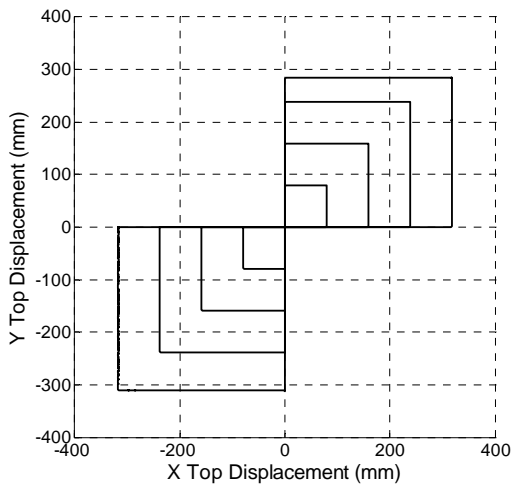


(e) Load Case 3: Uniaxial Cyclic

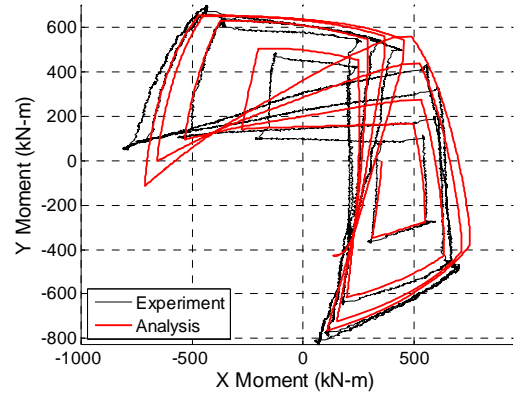


(f) Load Case 3: Uniaxial Cyclic

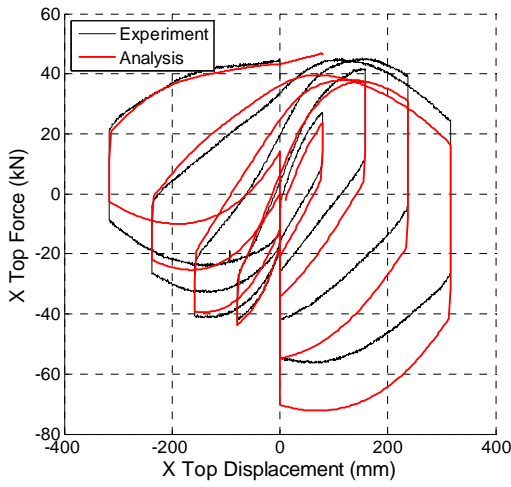
Figure 5-21. Validation Results for Slender Beam-Column Specimen 11



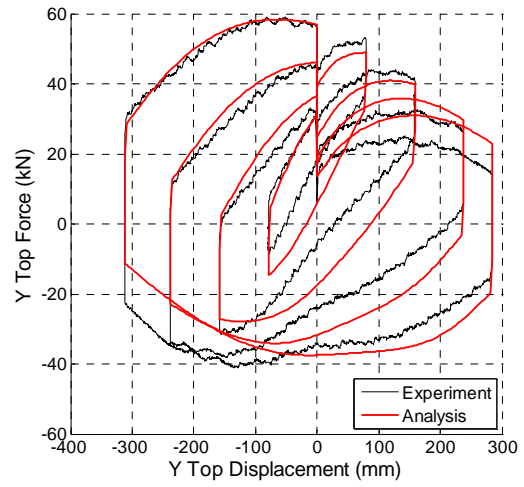
(g) Load Case 4: Biaxial Cyclic



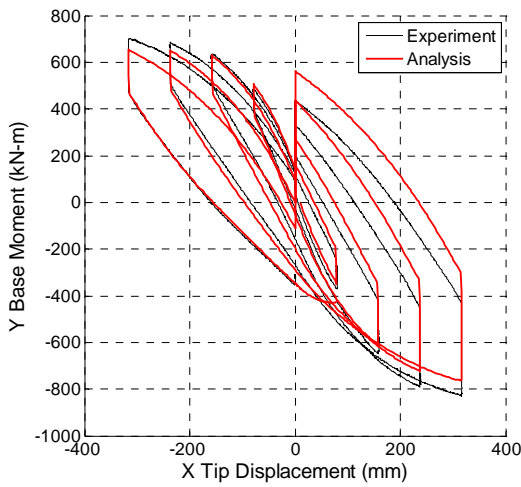
(h) Load Case 4: Biaxial Cyclic



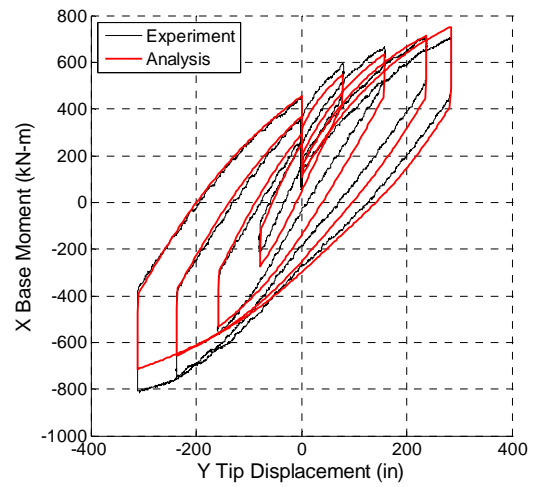
(i) Load Case 4: Biaxial Cyclic



(j) Load Case 4: Biaxial Cyclic

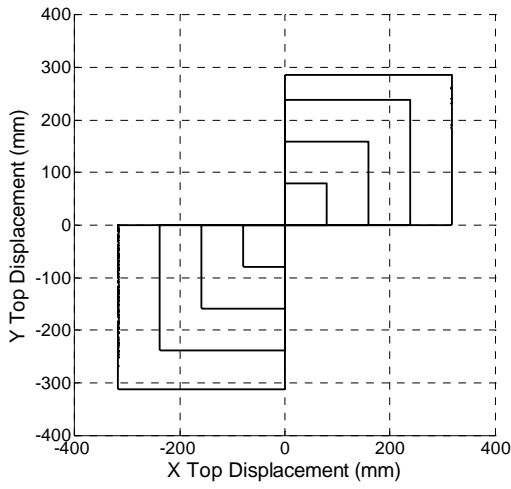


(k) Load Case 4: Biaxial Cyclic

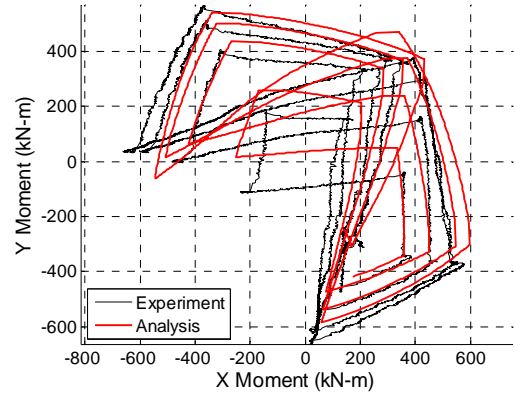


(l) Load Case 4: Biaxial Cyclic

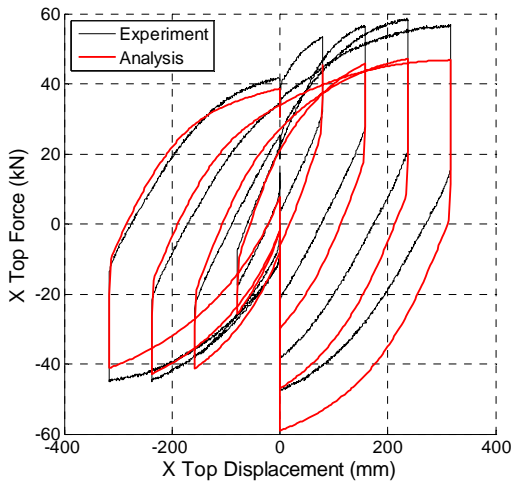
Figure 5-21. Validation Results for Slender Beam-Column Specimen 11 (continued)



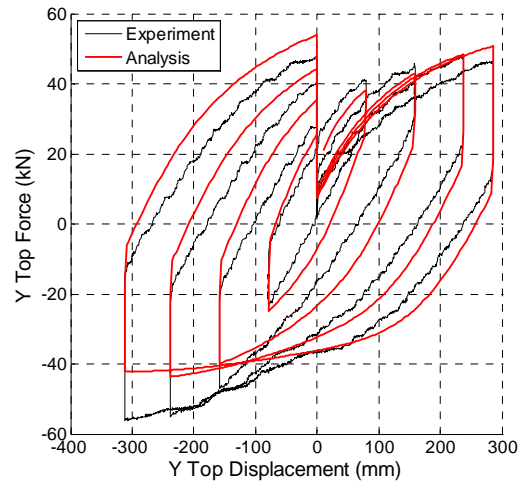
(m) Load Case 5: Biaxial Cyclic



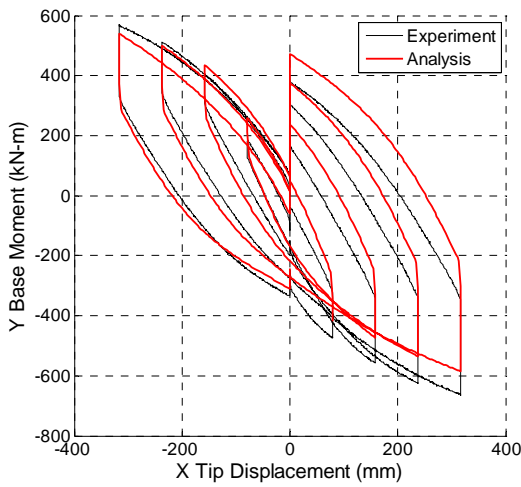
(n) Load Case 5: Biaxial Cyclic



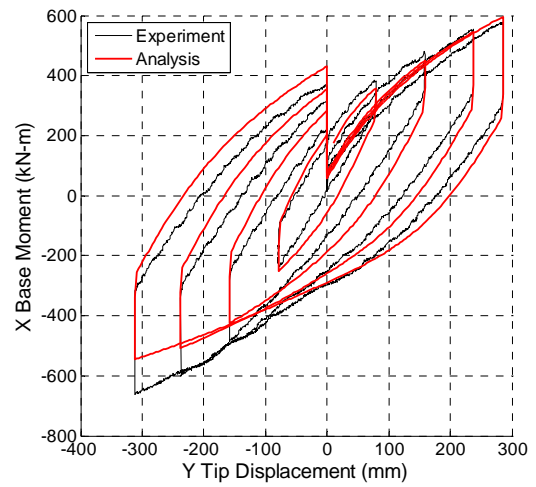
(o) Load Case 5: Biaxial Cyclic



(p) Load Case 5: Biaxial Cyclic

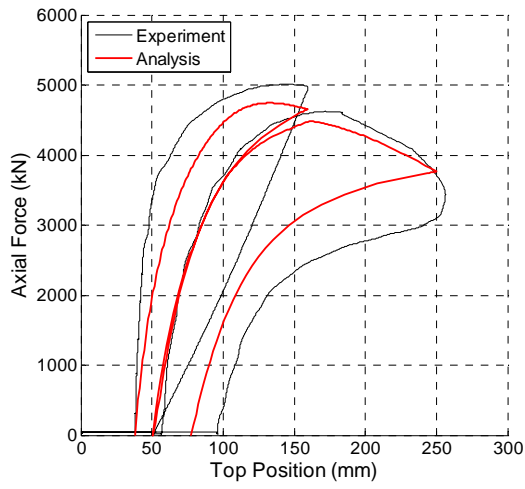


(q) Load Case 5: Biaxial Cyclic

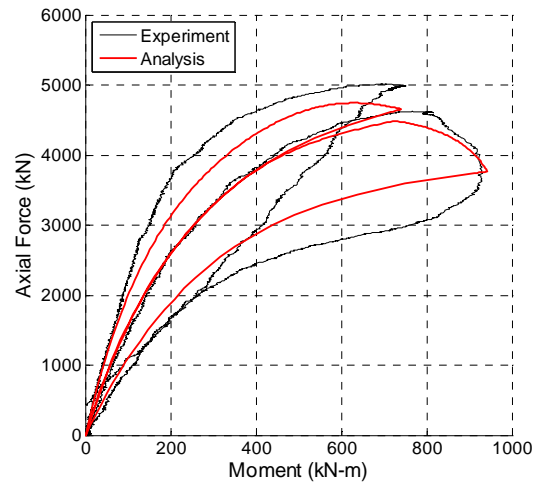


(r) Load Case 5: Biaxial Cyclic

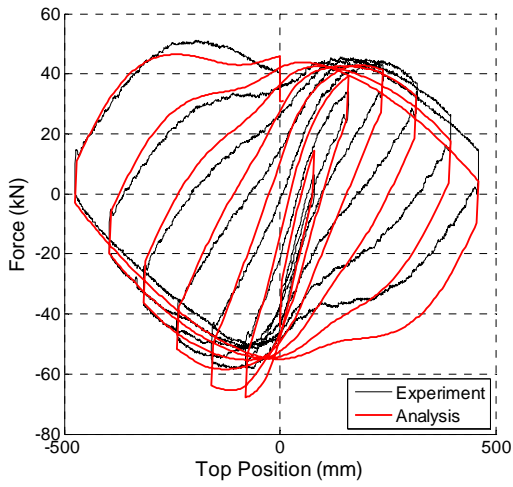
Figure 5-21. Validation Results for Slender Beam-Column Specimen 11 (continued)



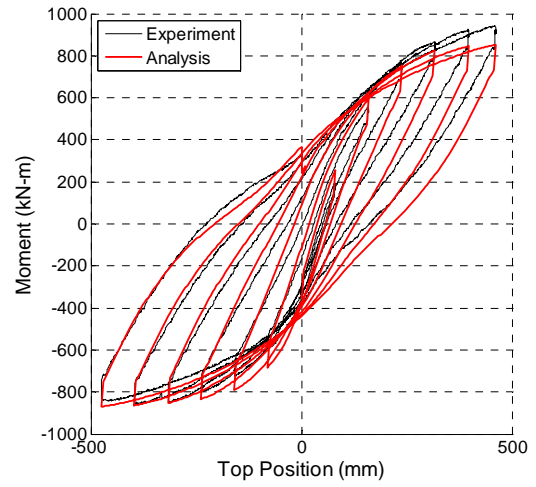
(a) Load Case 1: Concentric Loading



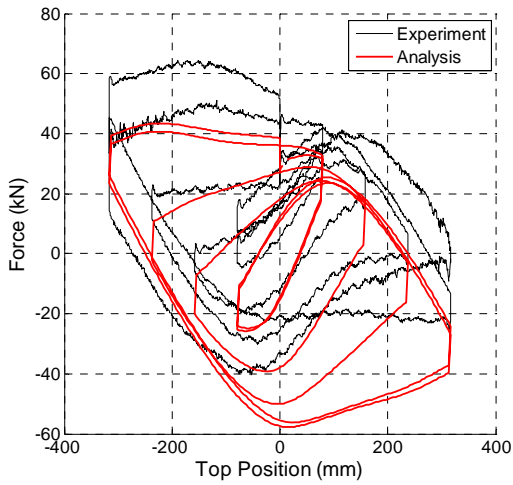
(b) Load Case 1: Concentric Loading



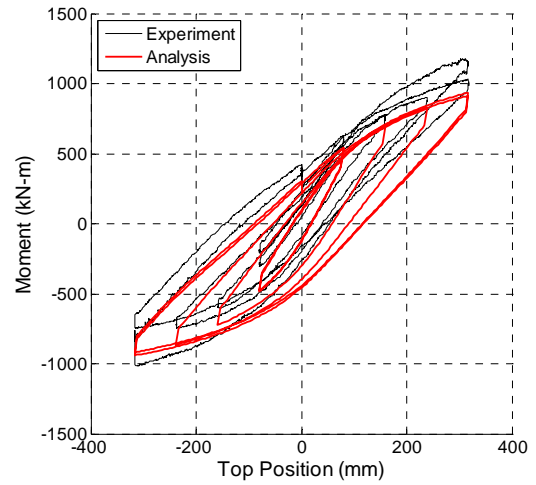
(c) Load Case 2: Uniaxial Cyclic



(d) Load Case 2: Uniaxial Cyclic

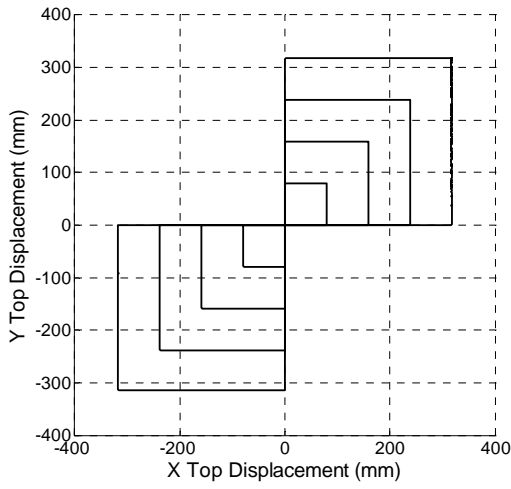


(e) Load Case 3: Uniaxial Cyclic

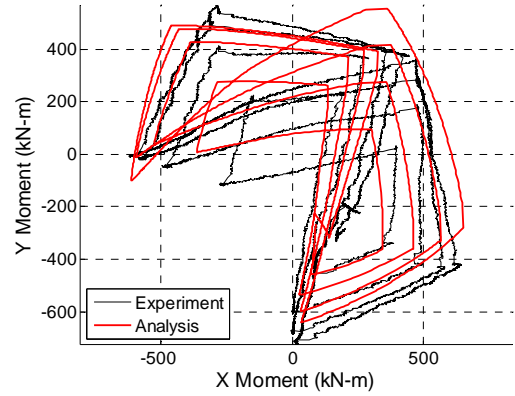


(f) Load Case 3: Uniaxial Cyclic

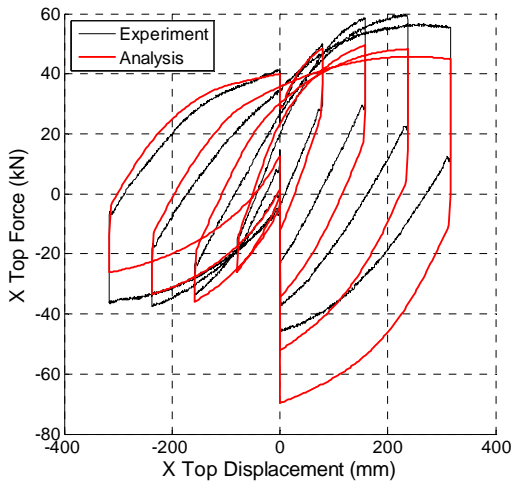
Figure 5-22. Validation Results for Slender Beam-Column Specimen 15



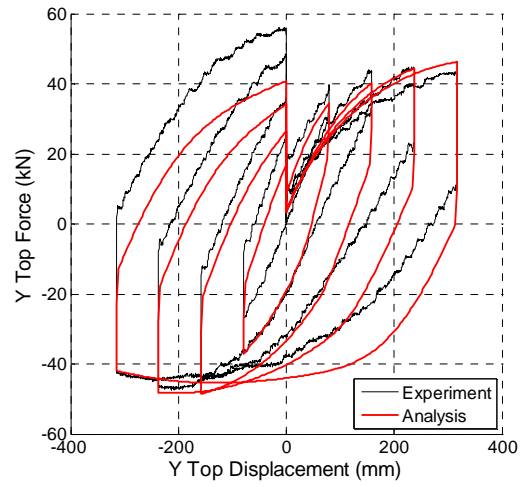
(g) Load Case 4: Biaxial Cyclic



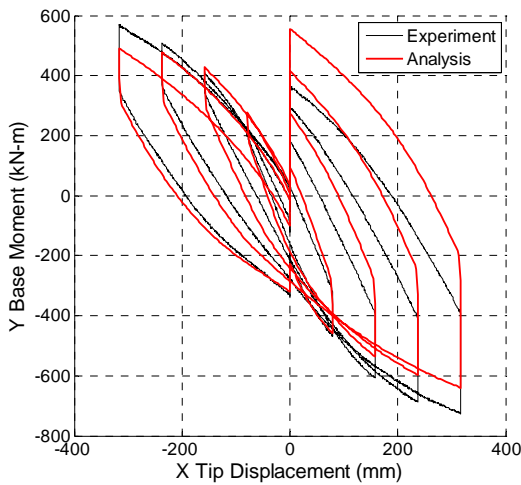
(h) Load Case 4: Biaxial Cyclic



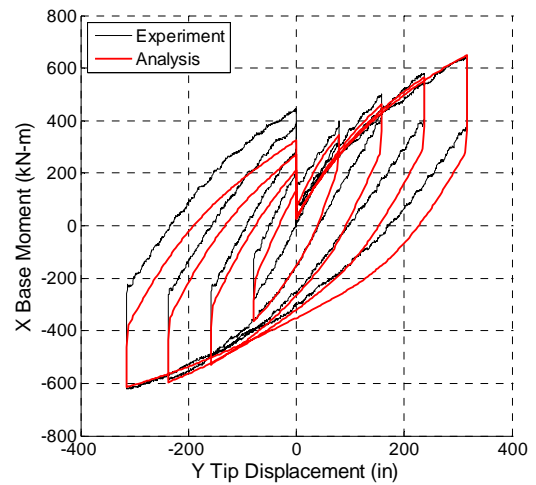
(i) Load Case 4: Biaxial Cyclic



(j) Load Case 4: Biaxial Cyclic

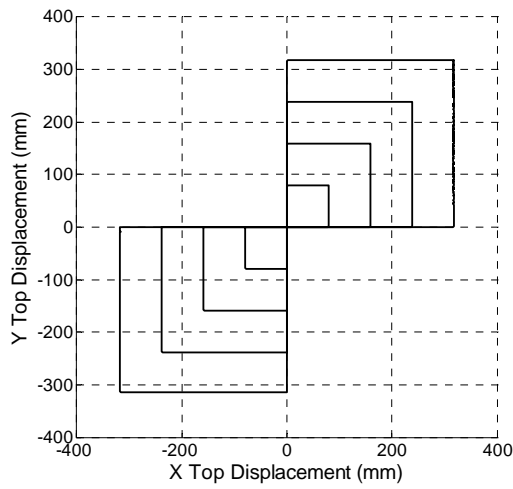


(k) Load Case 4: Biaxial Cyclic

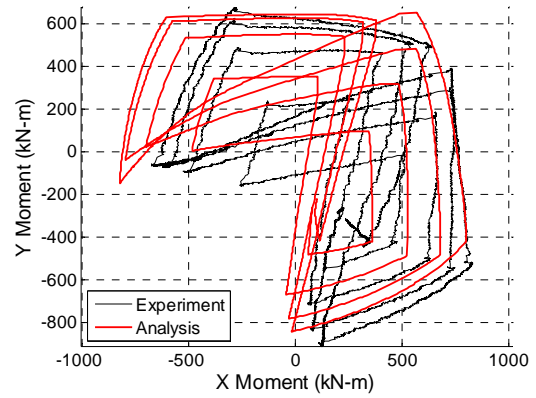


(l) Load Case 4: Biaxial Cyclic

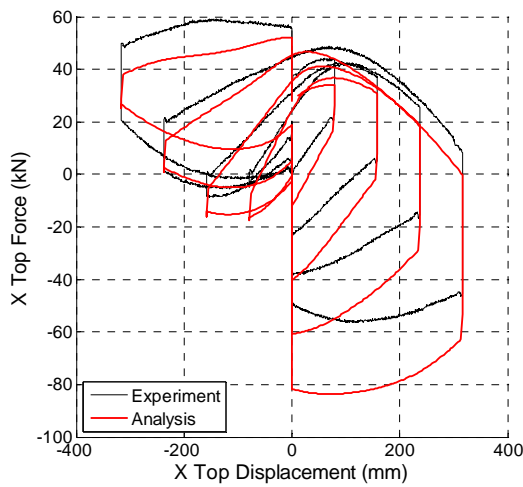
Figure 5-22. Validation Results for Slender Beam-Column Specimen 15 (continued)



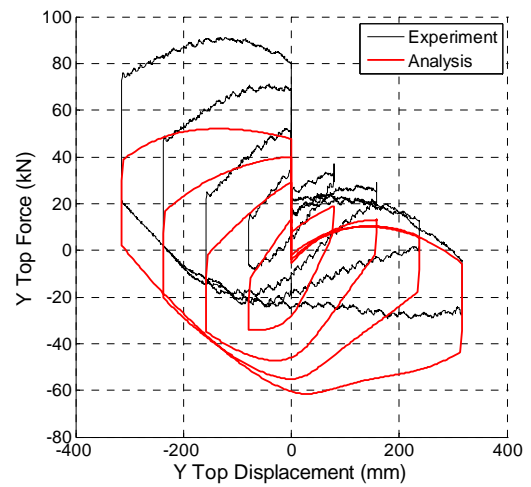
(m) Load Case 5: Biaxial Cyclic



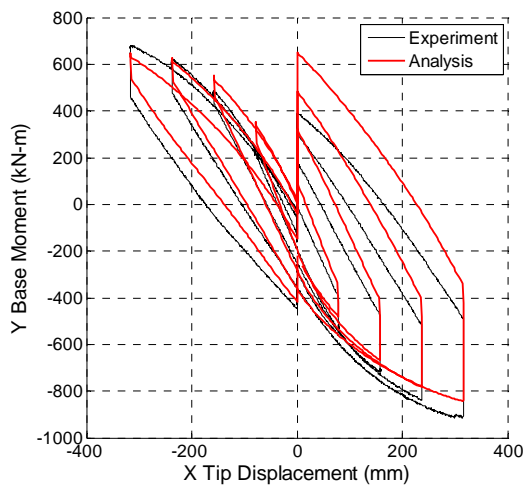
(n) Load Case 5: Biaxial Cyclic



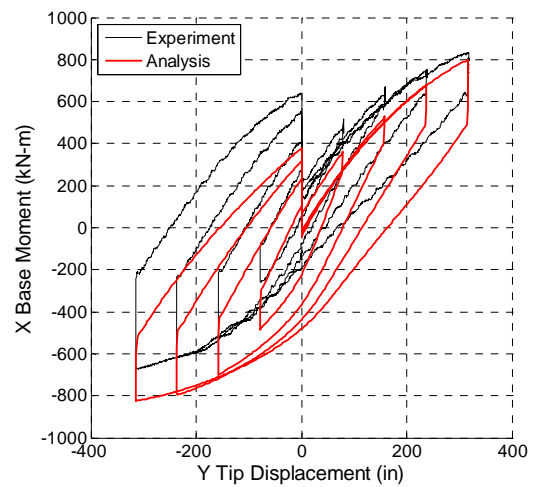
(o) Load Case 5: Biaxial Cyclic



(p) Load Case 5: Biaxial Cyclic



(q) Load Case 5: Biaxial Cyclic



(r) Load Case 5: Biaxial Cyclic

Figure 5-22. Validation Results for Slender Beam-Column Specimen 15 (continued)

5.9 Comparison to Existing Models

As a final evaluation, comparisons are made between the current model and several existing computational models. The results of analyses of Specimen 11, described in the previous section, are the basis of comparison. The current model, with a mixed beam element and comprehensive cyclic constitutive models, are compared to displacement-based and force-based beam elements using uniaxial material models based on constitutive relations from the literature.

Cyclic steel and concrete constitutive models based on the work of Sakino et al. (2004) were used in some of the analyses presented in this section. The Concrete04 material of OpenSees (OpenSees 2009) was used for the concrete core, and input parameters were selected to match the model for the monotonic compressive response of the concrete core of CFT members presented by Sakino et al. (2004). However, the post-peak curve described by Sakino et al. (2004) is not identical to that of the Concrete04 material. For that reason, the strain at peak stress was increased by 5% in the Concrete04 model; this modification provided a good agreement between the Concrete04 model and the formulation presented by Sakino et al. (2004) over the range of zero strain up to ten times the strain at peak stress [i.e., the parameter used to describe the strain at peak stress in the Concrete04 material was taken as 1.05 times the strain at peak stress as described in Sakino et al. (2004), so that the monotonic compressive response of the Concrete04 material mimics that of the formulation presented in Sakino et al. (2004)]. The tensile response of the concrete core was assumed to be zero and the cyclic response was taken as standard for the Concrete04 material.

The ElasticPP material (OpenSees 2009) was used for the steel tube. Sakino et al. (2004) presents a model for the monotonic compressive response of the steel tube of CFT members. Unlike the concrete model, the monotonic compressive response of the model available in OpenSees is identical to that of Sakino et al. (2004). The tensile response was assumed to be elastic-perfectly plastic, with a yield stress equal to 1.08 times the nominal yield stress. This value was chosen through the use of a von Mises failure criterion coupled with the value of hoop stress assumed in Sakino et al. (2004). The cyclic response was taken as standard for the ElasticPP material. It is noteworthy that these models can be defined at runtime with standard OpenSees, without the need for development (coding) or compiling special material models or a special version of OpenSees.

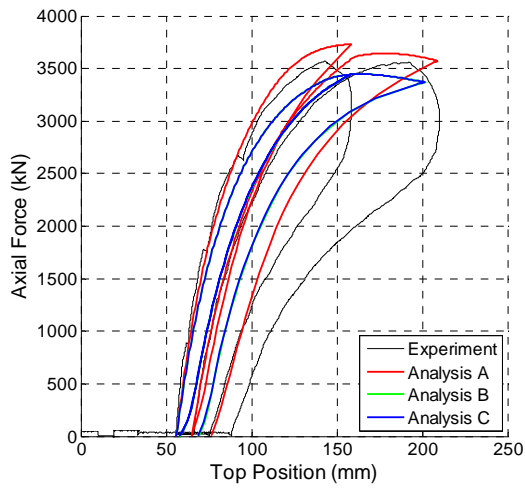
In Figure 5-23 the experimental results and three sets of computational results are presented. The computational results are labeled as follows:

- “**Analysis A**”, the mixed beam element formulation presented in this work, using the constitutive relations presented in this work.
- “**Analysis B**”, the displacement-based beam element formulation available in OpenSees (OpenSees 2009), using the uniaxial material models based on the constitutive relations of Sakino et al. (2004) described above.

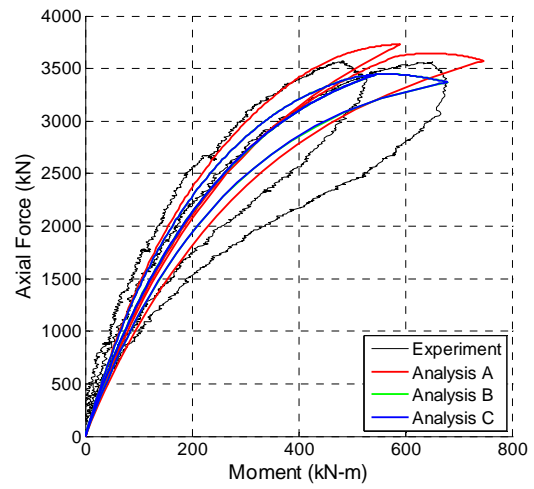
- “**Analysis C**”, the force-based beam element formulation available in OpenSees (Scott et al. 2008; OpenSees 2009), using the uniaxial material models based on the constitutive relations of Sakino et al. (2004) described above.

The analyses were identical to the previous section with the exception of the choice of element and uniaxial material model (i.e., the number of elements, fiber discretization, friction model, initial imperfections, geometric transformation, and related model characteristics remained the same as in the previous section and between analyses).

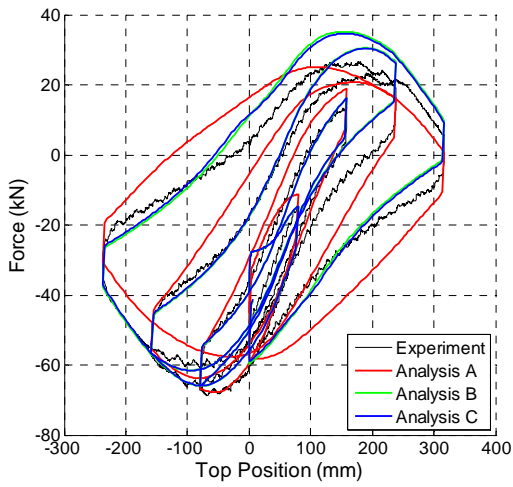
The results of the analyses show that for the early load cases, all three analyses perform satisfactorily, with the analyses using the constitutive models by Sakino et al. (2004) performing slightly better. In the later load histories, a significant difference between the analyses arises. As the loading progresses, damage accumulates in the specimen, and the current model is more capable of predicting this behavior than the existing model.



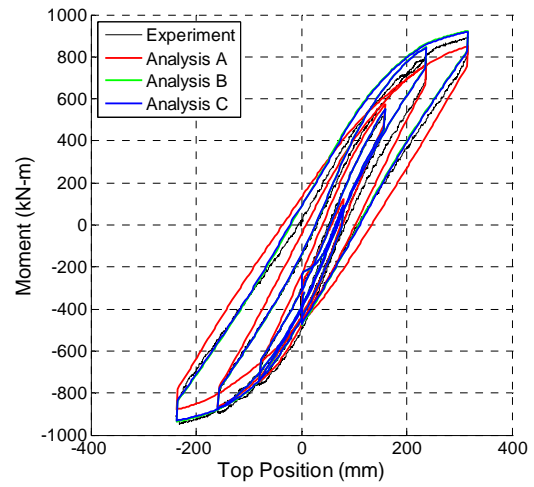
(a) Load Case 1: Concentric Loading



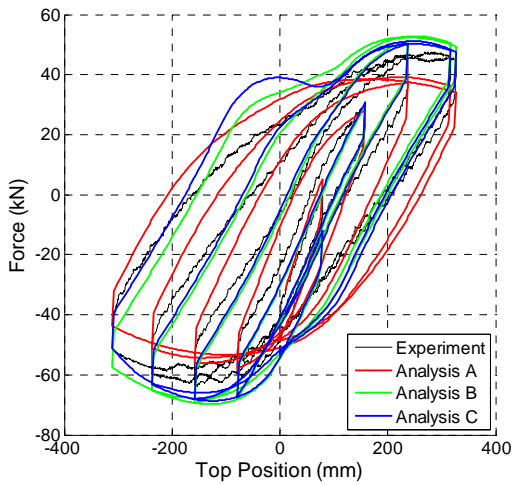
(b) Load Case 1: Concentric Loading



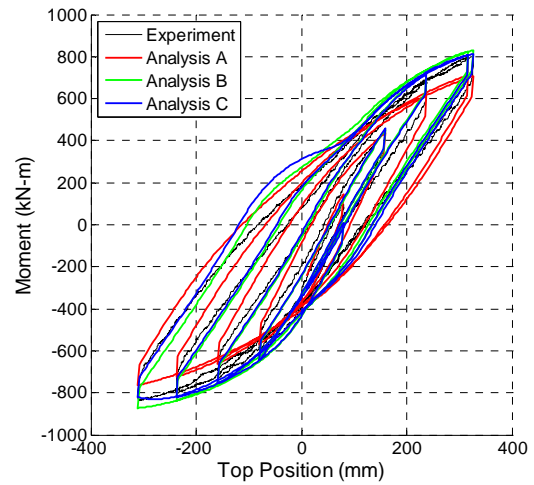
(c) Load Case 2: Uniaxial Cyclic



(d) Load Case 2: Uniaxial Cyclic

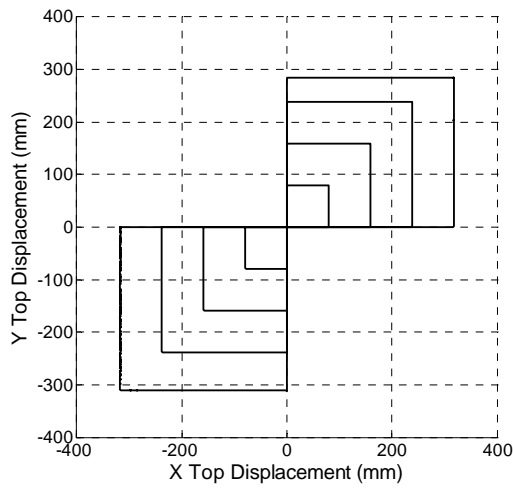


(e) Load Case 3: Uniaxial Cyclic

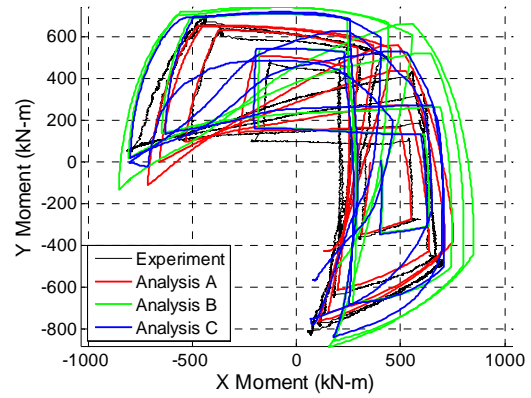


(f) Load Case 3: Uniaxial Cyclic

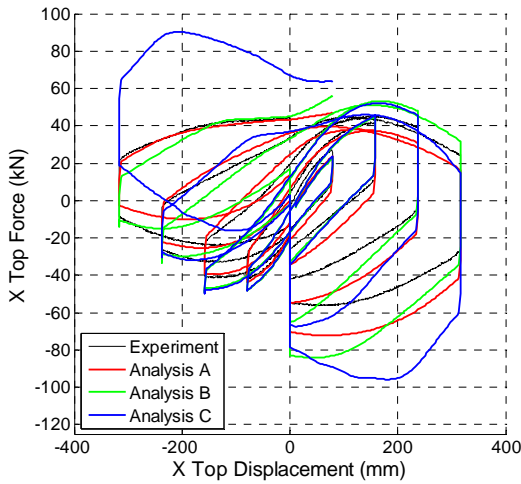
Figure 5-23. Analysis Comparison Results



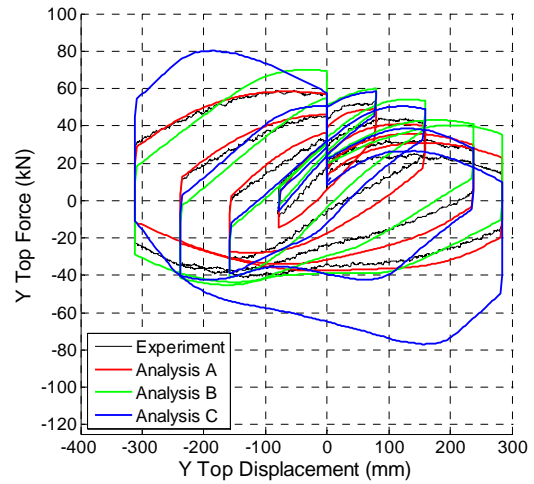
(g) Load Case 4: Biaxial Cyclic



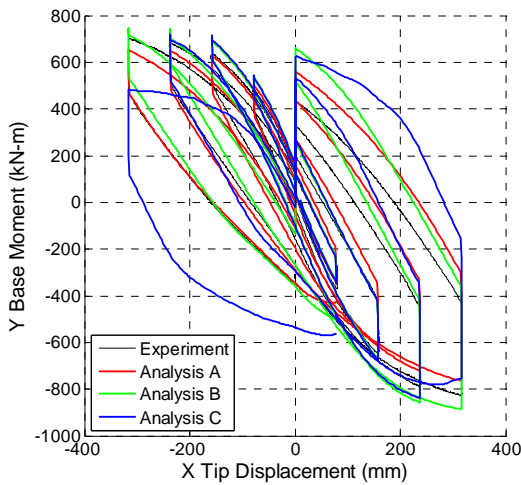
(h) Load Case 4: Biaxial Cyclic



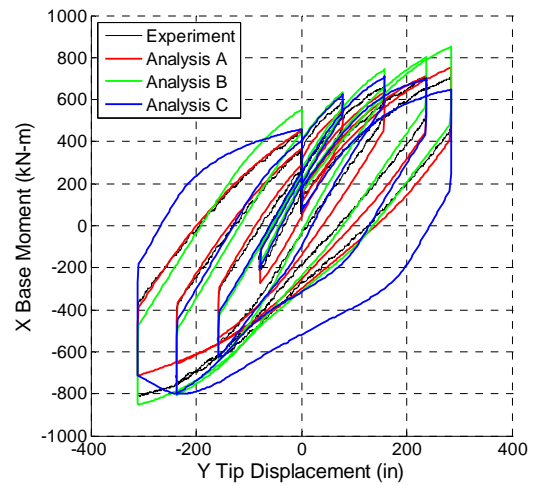
(i) Load Case 4: Biaxial Cyclic



(j) Load Case 4: Biaxial Cyclic

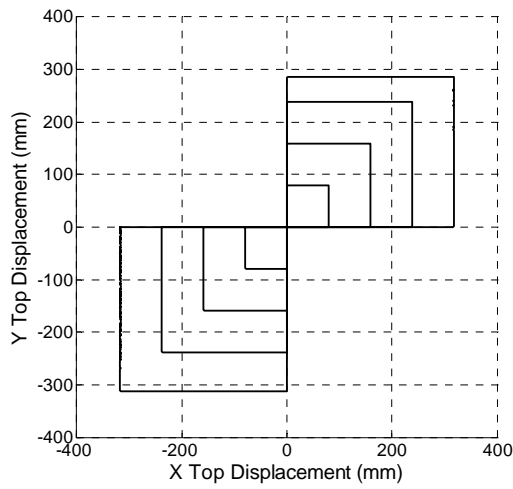


(k) Load Case 4: Biaxial Cyclic

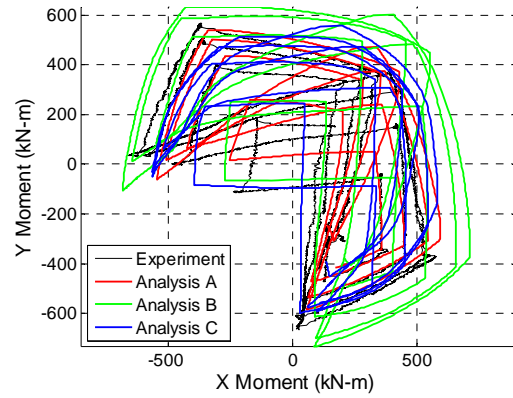


(l) Load Case 4: Biaxial Cyclic

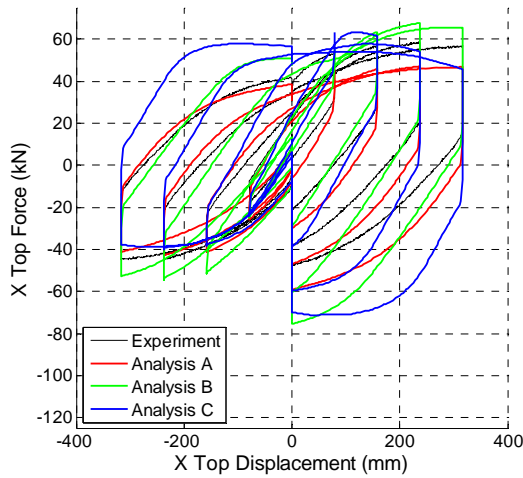
Figure 5-23. Analysis Comparison Results (continued)



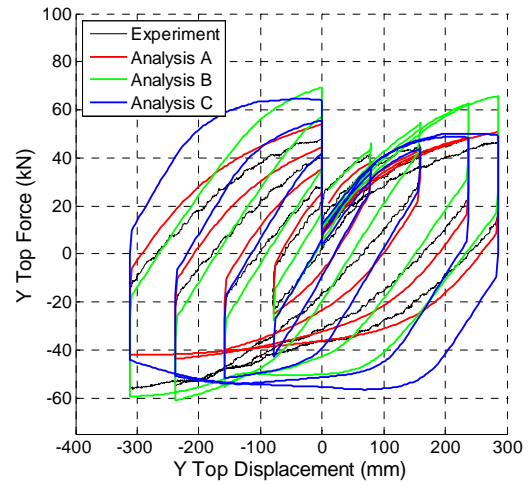
(m) Load Case 5: Biaxial Cyclic



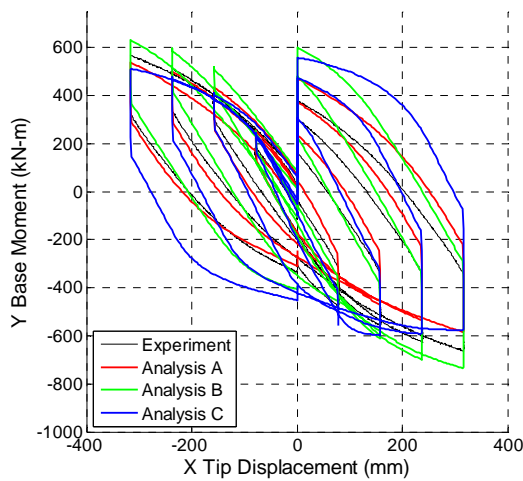
(n) Load Case 5: Biaxial Cyclic



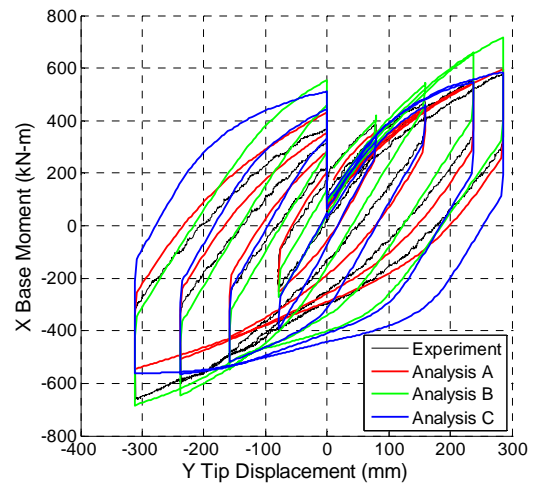
(o) Load Case 5: Biaxial Cyclic



(p) Load Case 5: Biaxial Cyclic



(q) Load Case 5: Biaxial Cyclic



(r) Load Case 5: Biaxial Cyclic

Figure 5-23. Analysis Comparison Results (continued)

CONCLUSIONS

A mixed finite element formulation was developed for the three-dimensional analysis of CCFT members and frames. The element was derived in the corotational frame utilizing the Total Lagrangian approach to reference forces and deformations. Material inelasticity is tracked with fiber cross sections located at integration points along the length of the element. The formulation was implemented within the OpenSees framework making available a wide variety of other elements, material models, and solution techniques.

Comprehensive uniaxial cyclic constitutive relations were developed for the concrete core and steel tube. These models account for the salient features of each material and the interaction between the two, including: cracking and confinement of the concrete core and gradual yielding and local of the steel tube. A rule-based approach is used for the cyclic behavior of the concrete core while a bounding surface plasticity formulation is used for the cyclic behavior of the steel tube.

The formulation was validated against a wide range of monotonic and cyclic experiments, including short columns, beams, and proportionally and non-proportionally loaded beams columns. Several elastic problems were also analyzed to validate the geometrically nonlinear formulation. The studies showed that accurate results can be obtained for CCFT members and frames subjected to a variety of loading conditions.

The formulation is suitable for use for many future investigations into the behavior of CCFT members. Possible studies include: 1) Nonlinear incremental dynamic analyses of moment resisting and braced frames to determine appropriate seismic response factors (e.g., R , C_d , and Ω_o). 2) Parametric studies to assess beam-column interaction strength and to establishing guidelines for the computation of equivalent composite beam-column rigidity. 3) Detailed investigation of beam-column behavior including the evolution of section and beam-column strength of CCFT members.

REFERENCES

- Alemdar, B. N. (2001). "Distributed Plasticity Analysis of Steel Building Structural Systems," Ph.D. dissertation, School of Civil and Environmental Engineering, Georgia Institute of Technology, Atlanta, GA, July.
- Alemdar, B. N. and White, D. W. (2005). "Displacement, Flexibility, and Mixed Beam-Column Finite Element Formulations for Distributed Plasticity Analysis," *Journal of Structural Engineering*, ASCE, Vol. 131, No. 12, pp. 1811-1819.
- Aval, S. B. B., Saadeghvaziri, M. A., and Golafshani, A. A. (2002). "Comprehensive Composite Inelastic Fiber Element for Cyclic Analysis of Concrete-Filled Steel Tube Columns," *Journal of Engineering Mechanics*, ASCE, Vol. 128, No. 4, pp. 428-437.
- Bergmann, R. (1994). "Load Introduction in Composite Columns Filled with High Strength Concrete," in *Tubular Structures VI, Proceedings of 6th International Symposium on Tubular Structures*, Melbourne, Australia, December, pp. 373-380.
- Blanks, R. F. and McNamara, C. C. (1935). "Mass Concrete Tests In Large Cylinders," *Journal of the American Concrete Institute*, Vol. 31, No. 1, pp. 280-303.
- Bradford, M. A., Loh, H. Y., and Uy, B. (2002). "Slenderness Limits for Filled Circular Steel Tubes," *Journal of Constructional Steel Research*, Vol. 58, No. 2, pp. 243-252.
- Chang, G. A. and Mander, J. B. (1994). "Seismic Energy Based Fatigue Damage Analysis of Bridge Columns: Part I - Evaluation of Seismic Capacity," Report No. NCEER-94-0006, National Center for Earthquake Engineering Research, State University of New York, Buffalo, NY.
- Coleman, J. and Spacone, E. (2001). "Localization Issues in Force-Based Frame Elements," *Journal of Structural Engineering*, ASCE, Vol. 127, No. 11, pp. 1257-1265.
- Cook, R. D., Malkus, D. S., Plesha, M. E. and Witt, R. J. (2002). *Concepts and Applications of Finite Element Analysis*, John Wiley & Sons, New York, NY.
- Denavit, M. D., Hajjar, J. F., Perea, T., Leon, R. T. (2009). "Seismic Multi-Axial Behavior of Concrete-Filled Steel Tube Beam-Columns" in *Proceedings of the 2009 Asian-Pacific Network of Centers for Earthquake Engineering Research (ANCER) Workshop*, Urbana, Illinois, August.
- de Souza, R. M. (2000). "Force-Based Finite Element for Large Displacement Inelastic Analysis of Frames," Ph.D. dissertation, University of California, Berkeley, CA.

- Elchalakani, M., Zhao, X. L., and Grzebieta, R. H. (2001). "Concrete-Filled Circular Steel Tubes Subjected to Pure Bending," *Journal of Constructional Steel Research*, Vol. 57, No. 11, pp. 1141-1168.
- Elchalakani, M., Zhao, X. L., (2008). "Concrete-Filled Cold-Formed Circular Steel Tubes Subjected to Variable Amplitude Cyclic Pure Bending," *Engineering Structures*, Vol. 30, No. 2, pp. 287-299.
- Elremaily, A. and Azizinamini, A. (2002). "Behavior and Strength of Circular Concrete-filled Tube Columns," *Journal of Constructional Steel Research*, Vol. 58, No. 12, pp. 1567-1591.
- El-Tawil, S. and Deierlein, G. G. (2001). "Nonlinear Analysis of Mixed Steel-Concrete Frames. I: Element Formulation," *Journal of Structural Engineering*, ASCE, Vol. 127, No. 6, pp. 647-655.
- FEMA (2008). Quantification of Building Seismic Performance Factors ATC-63 Project Report - 90% Draft, FEMA P695, Federal Emergency Management Agency, Washington, D.C.
- Fukumoto, Y. and Kusama H. (1985). "Local Instability Tests of Plate Elements Under Cyclic Uniaxial Loading," *Journal of Structural Engineering*, ASCE, Vol. 111, No. 5, pp. 1051-1067.
- Giakoumelis, G. and Lam, D., (2004). "Axial Capacity of Circular Concrete-Filled Tube Columns," *Journal of Constructional Steel Research*, Vol. 60, No. 7, pp. 1049-1068.
- Gourley, B. C. and Hajjar, J. F. (1994). "Cyclic Nonlinear Analysis of Three-Dimensional Concrete-Filled Steel Tube Beam-Columns and Composite Frames," Report No. ST-94-3, Department of Civil Engineering, University of Minnesota, Minneapolis, MN, February.
- Gourley, B. C., Tort, C., Denavit, M. D., Schiller, P. H., and Hajjar, J. F. (2008). "A Synopsis of Studies of the Monotonic and Cyclic Behavior of Concrete-Filled Steel Tube Beam-Columns," Report No. NSEL-008, Newmark Structural Laboratory Report Series (ISSN 1940-9826), Department of Civil and Environmental Engineering, University of Illinois at Urbana-Champaign, Urbana, Illinois, April.
- Hajjar, J. F. and Gourley, B. C. (1996). "Representation of Concrete-Filled Steel Tube Cross-Section Strength," *Journal of Structural Engineering*, ASCE, Vol. 122, No. 11, pp. 1327-1336.
- Hajjar, J. F. and Gourley, B. C. (1997). "A Cyclic Nonlinear Model for Concrete-Filled Tubes. I: Formulation," *Journal of Structural Engineering*, ASCE, Vol. 123, No. 6 pp. 736-744.

- Hajjar, J. F., Molodan, A., and Schiller, P. H. (1998). "A Distributed Plasticity Model for Cyclic Analysis of Concrete-Filled Steel Tube Beam-Columns and Composite Frames," *Engineering Structures*, Vol. 20, Nos. 4-6, April-June, pp. 398-412.
- Han, L. H., Lu, H., Yao, G.-H., Liao, F.-Y. (2006). "Further Study on the Flexural Behaviour of Concrete-Filled Steel Tubes," *Journal of Constructional Steel Research*, Vol. 62, No. 6, pp. 554-565.
- Han, L. H. and Yao, G. H. (2004). "Experimental Behaviour of Thin-Walled Hollow Structural Steel (HSS) Columns Filled with Self-Consolidating Concrete (SCC)," *Thin-Walled Structures*, Vol. 42, No. 9, pp. 1357-1377.
- Han, L.-H., Yao, G.-H., and Zhao, X.-L. (2005). "Tests and Calculations for Hollow Structural Steel (HSS) Stub Columns Filled with Self-Consolidating Concrete (SCC)," *Journal of Constructional Steel Research*, Vol. 61, No. 9, pp. 1241-1269.
- Hatzigeorgiou, G. D. (2008a). "Numerical model for the behavior and capacity of circular CFT columns, Part I: Theory," *Engineering Structures*, Vol. 30, No. 6, pp.1573-1578.
- Hatzigeorgiou, G. D. (2008b). "Numerical model for the behavior and capacity of circular CFT columns, Part II: Verification and extension," *Engineering Structures*, Vol. 30, No. 6, pp. 1579-1589.
- Hjelmstad, K. D. and Taciroglu, E. (2003). "Mixed Variational Methods for Finite Element Analysis of Geometrically Non-Linear, Inelastic Bernoulli-Euler Beams," *Communications in Numerical Methods in Engineering*, Vol. 19, No. 10, pp. 809-832.
- Hsiao, K.-M. and Jang J.-Y. (1989). "Nonlinear dynamic analysis of elastic frames," *Computers & Structures*, Vol. 33, No. 4, pp. 1057-1063.
- Hu, H.-T., Huang, C.-S., Wu, M.-H., and Wu, Y.-M. (2003). "Nonlinear Analysis of Axially Loaded Concrete-Filled Tube Columns with Confinement Effect," *Journal of Structural Engineering*, ASCE, Vol. 129, No. 10, pp. 1322-1329.
- Ichinohe, Y., Matsutani, T., Nakajima, M., Ueda, H., and Takada, K. (1991) "Elasto-Plastic Behavior of Concrete Filled Steel Circular Columns," Proceedings of the Third International Conference on Steel-Concrete Composite Structures, Fukuoka, Japan, September 26-29, 1991, pp. 131-136
- Inai, E., Mukai, A., Kai, M., Tokinoya, H., Fukumoto, T. Mori, K. (2004). "Behavior of Concrete-Filled Steel Tube Beam Columns," *Journal of Structural Engineering*, ASCE, Vol. 130, No. 2, pp. 189-202.
- Johansson, M. and Gylltoft, K. (2002). "Mechanical Behavior of Circular Steel-Concrete Composite Stub Columns," *Journal of Structural Engineering*, ASCE, Vol. 128, No. 8, pp. 1073-1081.

- Kilpatrick, A. E. and Rangan, B. V. (1999). "Tests on High-Strength Concrete-Filled Steel Tubular Columns," *ACI Structural Journal*, Vol. 96, No. 2, pp. 268-274.
- Kim, J.-K., Yi, S.-T., Park, C.-K. and Eo, S.-H. (1999). "Size Effect on Compressive Strength of Plain and Spirally Reinforced Concrete Cylinders," *ACI Structural Journal*, Vol. 96, No. 1, pp. 88-94.
- Leon, R. T., Perea, T., Hajjar, J.F., and Denavit, M. D., (2009). "Determination of Buckling Loads from Triaxial Load Tests of Slender Concrete-Filled Tube Beam-Columns," *Proceedings of the 3rd International Conference on Advances in Experimental Structural Engineering*. San Francisco, California, USA.
- Mamaghani, I. H. P., Usami, T., and Mizuno, E. (1996). "Cyclic Elastoplastic Behavior of Steel Structures: Theory and Experiment," Department of Civil Engineering, Report No. 9601, Nagoya, Japan, March.
- Mander, J. B., Priestley, M. J. N., and Park, R. (1988). "Theoretical Stress-Strain Model for Confined Concrete," *Journal of Structural Engineering*, Vol. 114, No. 8, pp. 1804-1826.
- Marson, J. and Bruneau, M. (2004). "Cyclic Testing of Concrete-Filled Circular Steel Bridge Piers having Encased Fixed-Based Detail," *Journal of Bridge Engineering*, ASCE, Vol. 9, No. 1, pp. 14-23.
- Matsui, C. and Tsuda, K. (1996). "Strength and Behavior Of Slender Concrete Filled Steel Tubular Columns," in *Proceedings of The Second International Symposium on Civil Infrastructure Systems*, ed. P. T. Y Chang, L. W Lu, and L. Wei, Hong Kong, China.
- Mattiasson, K. (1981). "Numerical Results from Large Deflection Beam and Frame Problems Analyzed by Means of Elliptic Integrals," *International Journal for Numerical Methods in Engineering*, Vol. 17, No. 1, pp. 145-153.
- Nishiyama, I., Morino, S., Sakino, K., Nakahara, H., Fujimoto, T., Mukai, A., Inai, E., Kai, M., Tokinoya, H., Fukumoto, T., Mori, K., Yoshioka, K., Mori, O., Yonezawa, K., Uchikoshi, M., and Hayashi, Y. (2002). "Summary of Research on Concrete-Filled Structural Steel Tube Columns System Carried Out Under The US-Japan Cooperative Research Program on Composite and Hybrid Structures," BRI Research Paper No. 147, Building Research Institute, Japan, January.
- Nukala, P. K. V. V. and White, D. W., (2004a) "A Mixed Finite Element for Three-Dimensional Nonlinear Analysis of Steel Frames," *Computer Methods in Applied Mechanics and Engineering*, Vol. 193, No. 23-26, pp. 2507-2545.
- Nukala, P. K. V. V. and White, D. W., (2004b). "Variationally Consistent State Determination Algorithms for Nonlinear Mixed Beam Finite Elements," *Computer Methods in Applied Mechanics and Engineering*, Vol. 193, No. 33-35, pp. 3647-3666.

- OpenSees (2009). "Open System for Earthquake Engineering Simulation," Open source software, <http://opensees.berkeley.edu>.
- O'Shea, M. D. and Bridge R. (1997a). "Local Buckling of Thin-Walled Circular Steel Sections With or Without Internal Restraint," Report No. R740, Department of Civil Engineering, The University of Sydney, Sydney, Australia, April.
- O'Shea, M. D. and Bridge R. (1997b). "Tests on Circular Thin-Walled Steel Tubes Filled with Very High Strength Concrete," Report No. R754, Department of Civil Engineering, The University of Sydney, Sydney, Australia, November.
- O'Shea, M. D. and Bridge R. (1997c). "Tests on Circular Thin-Walled Steel Tubes Filled with Medium and High Strength Concrete," Report No. R755, Department of Civil Engineering, The University of Sydney, Sydney, Australia, November.
- Perea, T. (2009). "Analytical and Experimental Study on Composite Concrete-Filled Steel Tube Beam-Columns," Ph.D. dissertation, School of Civil and Environmental Engineering, Georgia Institute of Technology, Atlanta, Georgia, in preparation.
- Prion, H. G. L. and Boehme, J. (1994). "Beam-Column Behaviour of Steel Tubes Filled with High Strength Concrete," *Canadian Journal of Civil Engineering*, Vol. 21, No. 2, pp. 207-218.
- Richart, F. E., Brandtzaeg, A., and Brown, R.L. (1929). "The Failure of Plain and Spirally Reinforced Columns in Compression," Bulletin No. 190, University of Illinois Engineering Experimental Station, Urbana, Illinois, January.
- Roeder, C. W., Cameron B., and Brown, C. B. (1999). "Composite Action in Concrete Filled Tubes," *Journal of Structural Engineering*, ASCE, Vol. 125, No. 5, pp. 477-484.
- Sakino, K., Nakahara, H., Morino, S., and Nishiyama, I. (2004). "Behavior of Centrally Loaded Concrete-Filled Steel-Tube Short Columns," *Journal of Structural Engineering*, ASCE, Vol. 130, No. 2, pp. 180-188.
- Sakino, K., Tomii, M., and Watanabe, K. (1985). "Sustaining Load Capacity of Plain Concrete Stub Columns Confined by Circular Steel Tube," Proceedings of the International Specialty Conference on Concrete Filled Steel Tubular Structures, Harbin, China, August 1985, pp. 112-118.
- Schneider, S. P. (1998). "Axially Loaded Concrete-Filled Steel Tubes," *Journal of Structural Engineering*, ASCE, Vol. 124, No. 10, pp. 1125-1138.
- Scott, M. H. and Fenves, G. L., (2006). "Plastic Hinge Integration Methods for Force-Based Beam-Column Elements," *Journal of Structural Engineering*, ASCE, Vol. 132, No. 2, pp. 244-252.

- Scott, M. H., Fenves, G. L., McKenna, F., and Filippou, F. C. (2008). "Software Patterns for Nonlinear Beam-Column Models," *Journal of Structural Engineering*, ASCE, Vol. 134, No. 4, pp. 562-571.
- Simo, J. C. and Vu-Quoc, L. (1986). "A Three-Dimensional Finite-Strain Rod Model. Part II: Computational Aspects," *Computer Methods in Applied Mechanics and Engineering*, Vol. 58, No. 1, pp. 79-116.
- Southwell, R. V. (1941). *Introduction to the Theory of Elasticity for Engineers and Physicists*, Oxford University Press.
- Shams, M. and Saadeghvaziri, M. A. (1999). "Nonlinear Response of Concrete-Filled Steel Tubular Columns under Axial Loading," *ACI Structural Journal*, Vol. 96, No. 6.
- Shen, C., Mamaghani, I. H. P., Mizuno, E., and Usami, T. (1995). "Cyclic Behavior of Structural Steels. II: Theory," *Journal of Engineering Mechanics*, ASCE, Vol. 121, No. 11, pp. 1165-1172.
- Susantha, K. A. S., Ge, H., and Usami, T. (2001). "Uniaxial Stress-Strain Relationship of Concrete Confined by Various Shaped Steel Tubes," *Engineering Structures*, Vol. 23, No. 10, pp. 1331-1347.
- Tort, C. and Hajjar, J. F. (2007). "Reliability-Based Performance-Based Design of Rectangular Concrete-Filled Steel Tube (RCFT) Members and Frames," Structural Engineering Report No. ST-07-1, Department of Civil Engineering, University of Minnesota, Minneapolis, Minnesota, August.
- Tsai, W. T. (1988). "Uniaxial Compressional Stress-Strain Relation of Concrete," *Journal of Structural Engineering*, ASCE, Vol. 114, No. 9, pp. 2133-2136.
- Varma, A. H., Ricles, J. M., Sause, R., Lu, L.-W. (2002). "Seismic Behavior and Modeling of High-Strength Composite Concrete-Filled Steel Tube (CFT) Beam-Columns," *Journal of Constructional Steel Research*, Vol. 58, pp. 725-758.
- Wheeler, A. and Bridge, R. (2004). "The Behaviour Of Circular Concrete-Filled Thin-Walled Steel Tubes In Flexure," in *Proceedings of the 5th International Conference on Composite Construction in Steel and Concrete V*, ed. R. T Leon and J. Lange, Mpumalanga, South Africa.
- Yamamoto, T., Kawaguchi, J., and Morino, S. (2002). "Experimental Studies of Scale Effects on the Compressive Behavior of Short Concrete-Filled Steel Tube Columns," *Composite Construction in Steel and Concrete IV*, Proceedings of the United Engineering Foundation Conference on Composite Construction in Steel and Concrete IV, Banff, Alberta, Canada, May 28-June 2, 2000 pp. 879-890

- Yang, Y. and Leu, L. (1991). "Force Recovery Procedures in Nonlinear Analysis," 4. *International Conference on Civil and Structural Engineering Computing*, Vol. 1, Sept. 19-21, 1989, London, UK, pp. 275-280.
- Yoshioka, K., Inai, E., Hukumoto, N., Kai, M., Murata, Y., Noguchi, T., Tanaka, Y., Tokinoya, H., and Mukai, A. (1995). "Compressive Tests on CFT Short Columns Part 1: Circular CFT Columns," Proceedings of the Second Joint Technical Coordinating Committee (JTCC) on Composite and Hybrid Structures, Hawaii, 26-28 June 1995.

List of Recent NSEL Reports

<i>No.</i>	<i>Authors</i>	<i>Title</i>	<i>Date</i>
008	Gourley, B.C., Tort, C., Denavit, M.D., Schiller, P.H., and Hajjar, J.F.	A Synopsis of Studies of the Monotonic and Cyclic Behavior of Concrete-Filled Steel Tube Members, Connections, and Frames	April 2008
009	Xu, D. and Hjelmstad, K.D.	A New Node-to-node Approach to Contact/Impact Problems for Two Dimensional Elastic Solids Subject to Finite Deformation	May 2008
010	Zhu, J. and Popovics, J.S.	Non-contact NDT of Concrete Structures Using Air Coupled Sensors	May 2008
011	Gao, Y. and Spencer, B.F.	Structural Health Monitoring Strategies for Smart Sensor Networks	May 2008
012	Andrews, B., Fahnestock, L.A. and Song, J.	Performance-based Engineering Framework and Ductility Capacity Models for Buckling-Restrained Braces	July 2008
013	Pallarés, L. and Hajjar, J.F.	Headed Steel Stud Anchors in Composite Structures: Part I – Shear	April 2009
014	Pallarés, L. and Hajjar, J.F.	Headed Steel Stud Anchors in Composite Structures: Part II – Tension and Interaction	April 2009
015	Walsh, S. and Hajjar, J.F.	Data Processing of Laser Scans Towards Applications in Structural Engineering	June 2009
016	Reneckis, D. and LaFave, J.M.	Seismic Performance of Anchored Brick Veneer	Aug. 2009
017	Borello, D.J., Denavit, M.D., and Hajjar, J.F.	Behavior of Bolted Steel Slip-critical Connections with Fillers	Aug. 2009
018	Rice, J.A. and Spencer, B.F.	Flexible Smart Sensor Framework for Autonomous Full-scale Structural Health Monitoring	Aug. 2009
019	Sim, S.-H. and Spencer, B.F.	Decentralized Strategies for Monitoring Structures using Wireless Smart Sensor Networks	Nov. 2009
020	Kim, J. and LaFave, J.M.	Joint Shear Behavior of Reinforced Concrete Beam-Column Connections subjected to Seismic Lateral Loading	Nov. 2009
021	Linderman, L.E., Rice, J.A., Barot, S., Spencer, B.F., and Bernhard, J.T.	Characterization of Wireless Smart Sensor Performance	Feb. 2010
022	Miller, T.I. and Spencer, B.F.	Solar Energy Harvesting and Software Enhancements for Autonomous Wireless Smart Sensor Networks	March 2010
023	Denavit, M.D. and Hajjar, J.F.	Nonlinear Seismic Analysis of Circular Concrete-Filled Steel Tube Members and Frames	March 2010